Self-assembly of amphiphilic oligo(phenylene ethynylene)-based (bi)pyridine ligands and their Pt(II) and Pd(II) complexes

Dissertation zur Erlangung des
naturwissenschaftlichen Doktorgrades
der Julius-Maximilians-Universität Würzburg

vorgelegt von
Christina Rest
aus Aschaffenburg

Würzburg 2015

Eingereicht bei der Fakultät für Chemie und Pharmazie am:

18.12.2015

Gutachter der schriftlichen Arbeit:
1. Gutachter: Prof. Dr. Gustavo Fernández
2. Gutachter: Prof. Dr. Frank Würthner

Prüfer des öffentlichen Promotionskolloquiums:
1. Prüfer: Prof. Dr. Gustavo Fernández
2. Prüfer: Prof. Dr. Frank Würthner
3. Prüfer: Prof. Dr. Ingo Fischer

Datum des öffentlichen Promotionskolloquiums:

22.04.2016

Doktorurkunde ausgehändigt am:

____

Danksagung

Mein besonderer Dank gilt Herrn Prof. Dr. Gustavo Fernández sowie Herrn Prof. Dr. Frank Würthner für die hervorragende wissenschaftliche Betreuung während meiner Promotionszeit, die hilfreichen fachlichen Diskussionen und Anregungen sowie die ausgezeichneten Arbeitsbedingungen. Bei Herrn Prof. Dr. Gustavo Fernández möchte ich mich hierbei für die intensive Unterstützung und das stete Vertrauen in meine Arbeit bedanken.

Bei Herrn Dr. Vladimir Stepanenko bedanke ich mich herzlich für die zahlreichen mikroskopischen Untersuchungen der Verbindungen **2-5** mittels AFM und SEM sowie die hilfreichen Gespräche, die einen wertvollen Beitrag zu dieser Doktorarbeit leisten.

Bei Herrn Dr. Matthias Grüne sowie Frau Elfriede Ruckdeschel möchte ich mich für die Durchführung von NMR-Experimenten und die hervorragende fachliche Unterstützung bedanken. Herrn Dr. Michael Büchner, Herrn Fritz Dadrich und Frau Antje Hautzinger danke ich für die Aufnahme der Massenspektren. Zudem bedanke ich mich bei Frau Liselotte Michels und Frau Sabine Timmroth für die Durchführung der Elementaranalysen am Institut für Anorganische Chemie.

Herrn Dr. Xin Zhang danke ich für die Einarbeitung in die Transmissionselektronen-Mikroskopie sowie seine Hilfe bei den TEM-Aufnahmen der Verbindungen **1** und **4**. In diesem Zusammenhang möchte ich mich bei Herrn Prof. Dr. Georg Krohne sowie Frau Daniela Bunsen und Frau Claudia Gehrig für die Möglichkeit bedanken das Transmissionselektronen-Mikroskop im Biozentrum zu benutzen. Vielen Dank für die freundliche Hilfe bei Fragen und Problemen.

Zudem möchte ich Frau Dr. Katharina Fucke (Kristallstruktur von Pt(II) Komplex **2**) sowie Herrn Dr. David Schmidt (Kristallstruktur von Pd(II) Komplex **3**) für das Lösen der präsentierten Kristallstrukturen und die hilfreichen Erklärungen danken.

Herrn David Bialas danke ich für seine Hilfe bei den durchgeführten AM1 Rechnungen, sowie seine Unterstützung beim Erstellen der graphischen Modelle in Fig. 42 sowie Fig. 118. Für die graphische Darstellung von Fig. 66 sowie Fig. 106 danke ich Frau Ana Reviejo Guzmán.

Des Weiteren danke ich Herrn Dr. Chantu Saha-Möller und Herrn Dr. Matthias Stolte für die Hilfe bei verschiedenen organisatorischen sowie fachlichen Belangen. Herrn Dr. Soichiro Ogi danke ich für die hilfreichen wissenschaftlichen Gespräche. Vielen Dank auch an Herrn Joachim Bialas für seine Hilfsbereitschaft im Laboralltag, sowie seine fortwährend gute Laune. Frau Christiana Toussaint und Frau Anette Häfner danke ich für ihre nette Hilfe bei bürokratischen Angelegenheiten.

Meinen Bachelorstudenten Herrn Alex Rödle und Frau Anja Martin, mit denen ich sehr gerne zusammen gearbeitet habe, danke ich für ihr Engagement und die gute synthetische Unterstützung.

Bei dem gesamten Arbeitskreis Würthner (mit den Arbeitsgruppen Beuerle und Fernández) möchte ich mich für die freundschaftliche Zusammenarbeit, das schöne Arbeitsklima und die stete Hilfsbereitschaft bedanken. Mein herzlicher Dank gilt neben den aktuellen Mitgliedern auch allen Ehemaligen mit denen ich zusammen arbeiten durfte; insbesondere möchte ich hierbei Herrn Dr. Sabin Suraru und Herrn Dr. Marcel Gsänger nennen.

Mein besonderer Dank gilt Frau Jennifer Begall für ihre zuverlässige Arbeit und Hilfsbereitschaft während meiner Doktorarbeit. Hierbei möchte ich mich neben der Unterstützung im Labor auch für die tolle Freundschaft bedanken. Weiterhin möchte ich mich bei Johannes für seine Hilfe und Unterstützung bedanken.

Der größte Dank gilt meiner Familie für ihre uneingeschränkte Unterstützung, Geduld und Kraft während meines gesamten Studiums. Danke für den wunderbaren Rückhalt in den letzten Jahren, ohne den dies Alles nicht möglich gewesen wäre.

List of Abbreviations

Ar	argon atmosphere
AFM	atomic force microscopy
AM1	Austin model 1
BODIPY	boron-dipyrromethene
BTA	benzene-1,3,5-tricarboxyamide
BuOH	butanol
CA	citronellic acid
CyA	cyanuric acid
CD	circular dichroism
cgc	critical gelation concentration
d	doublet
dd	doublet of doublets
DBN	diazabicyclo[4.3.0]non-5-ene
DBU	1,8-diazabicyclo[5.4.0]undec-7-ene
DFT	density functional theory
DLS	dynamic light scattering
DMF	dimethylformamide
DMSO	dimethyl sulfoxide
DOSY	diffusion ordered spectroscopy
DPA	diphenylacetylene
DPB	diphenylbutadiyne
DP_N	degree of polymerization
DTPA	diethylenetriaminepentaacetic acid
EHUT	2,4-bis(2-ethylhexylureido)toluene
ESI	electrospray ionization
EtOH	ethanol
eq.	equation
equiv.	equivalent
Fig.	figure
FTIR	Fourier transform infrared
HOPG	highly ordered pyrolytic graphite

HRMS	high-resolution mass spectrometry
HRTEM	high-resolution transmission electron microscopy
ILCT	intraligand charge transfer
ITC	isothermal titration calorimetry
m	multiplet
M	molar
MALDI	matrix-assisted laser desorption/ionization
MC	merocyanine
MCH	methylcyclohexane
MeOH	methanol
MHz	megahertz
min	minute
MLCT	metal-to-ligand charge transfer
nm	nanometre
NMR	nuclear magnetic resonance
OPE	oligo(phenylene ethynylene)
OPV	oligo(phenylene vinylene)
PBI	perylene bisimide
POM	polarized optical microscopy
r.t.	room temperature
ref.	reference
ROESY	rotating-frame Overhauser effect spectroscopy
rpm	revolutions per minute
s	singlet
SANS	small-angle neutron scattering
sec	second
SEM	scanning electron microscopy
STM	scanning tunnelling microscopy
TEM	transmission electron microscopy
TFA	trifluoroacetic acid
TGA	thermogravimetric analysis
THF	tetrahydrofuran
TIPS	triisopropylsilyl
TLC	thin-layer chromatography

TMS	trimethylsilyl
TMSA	trimethylsilyl acetylene
UV/Vis	ultraviolet/visible
WAXS	wide-angle X-ray scattering

Table of Contents

Chapter 1

-

Introduction and aim of the thesis

Supramolecular chemistry has been defined by J. M. Lehn in 1978 as the “chemistry of molecular assemblies and of the intermolecular bond”.[1] This field of research focuses on “the chemistry beyond the molecule” and aims at creating organized structures that are held together by non-covalent forces between two or more subunits.[2] Self-assembly into fascinating, highly ordered architectures also plays a key role in many natural systems.[3] A particularly relevant example in this regard is represented by the growth of double-stranded DNA that is based on complementary base pairing. The interplay of dynamic assembly and disassembly includes correction mechanisms resulting in an almost perfect non-covalent structure.[3] Similarly, the arrangement of lipid molecules in aqueous medium results in a fascinating, non-covalently stabilized system. The amphiphilic subunits create a bilayer membrane that can separate the aqueous environments inside and outside a cell from each other.[4,5]

As shown by these intriguing examples, natural supramolecular processes represent the starting point towards the creation of increasingly more complex self-assembled structures by small, artificial building blocks.[3,6] In this regard, a main focus of supramolecular chemists is on the formation of non-covalent arrangements by amphiphilic components in aqueous media.[7] The appropriate design of amphiphilic building blocks allows the creation of manifold architectures of different size and shape, ranging from small spherical micelles up to extended lamellar assemblies. Among common amphiphiles, *metallosupramolecular π-amphiphiles* are becoming particularly attractive in the supramolecular field of research.[8] This term includes molecular structures that combine amphiphilicity, an aromatic π-surface and a ligating moiety coordinated to a metal ion. The metal centre can provide innovative properties to the system. Firstly, it can benefit from the geometric versatility of the metal ion with a tetrahedral or square-planar coordination pattern for four ligands, while six-fold coordinated systems mainly exhibit an octahedral geometry.[9] Moreover, the metal centre can introduce promising photophysical properties[10-14] that cannot be observed for the free ligand. A further, particularly relevant characteristic of *metallosupramolecular π-amphiphiles* that is not present in conventional organic amphiphiles or surfactants is the possibility of the participation of the metal ion in metal-metal interactions. These attractive forces can contribute to the stability of the supramolecular structure, as primarily reported for Pt(II) complexes.[15-20]

This work aims at complementing the field of amphiphilic systems by the construction of *metallosupramolecular π-amphiphiles* comprising metal ions with square-planar geometry. The designed amphiphilic molecules are based on an aromatic scaffold that is attached to a ligating moiety to allow their coordination to metal ions. In this way, Pt(II) and Pd(II) metal complexes have been synthesized, whose amphiphilic nature provides solubility in polar solvents or water. As basic unit for the target compounds an oligo(phenylene ethynylene) (OPE) scaffold was chosen since this aromatic core shows a relatively rigid, conjugated surface, yet maintaining a certain rotational flexibility between the rings.[21] These features fulfil the conditions for aromatic interactions between the extended π-surfaces. The amphiphilic character of the ligands was achieved by attaching hydrophilic glycol chains to the terminal phenylene rings. Finally, a pyridine and bipyridine moiety, respectively, allows their coordination to different metal centres as mono- and bidentate ligands.

Following this synthetic plan, two new amphiphilic OPE derivatives substituted with a pyridine (**1**) or bipyridine (**4**) unit were designed (Chart 1). Amphiphile **1** acts as a ligand that is able to coordinate to square-planar Pt(II) and Pd(II) centres, leading to two new Pt(II) (**2**) and Pd(II) (**3**) complexes with *trans*-conformation. In this regard, the self-assembly behaviour and the underlying aggregation mechanisms of ligand **1** and its corresponding complexes have been investigated. Furthermore, detailed studies on the related complexes **2** and **3** can answer the question about the influence of the metal centre on their supramolecular behaviour.

Chart 1 Target amphiphilic ligands **1** and **4** and their corresponding metal complexes **2-3** and **5**, investigated in this thesis.

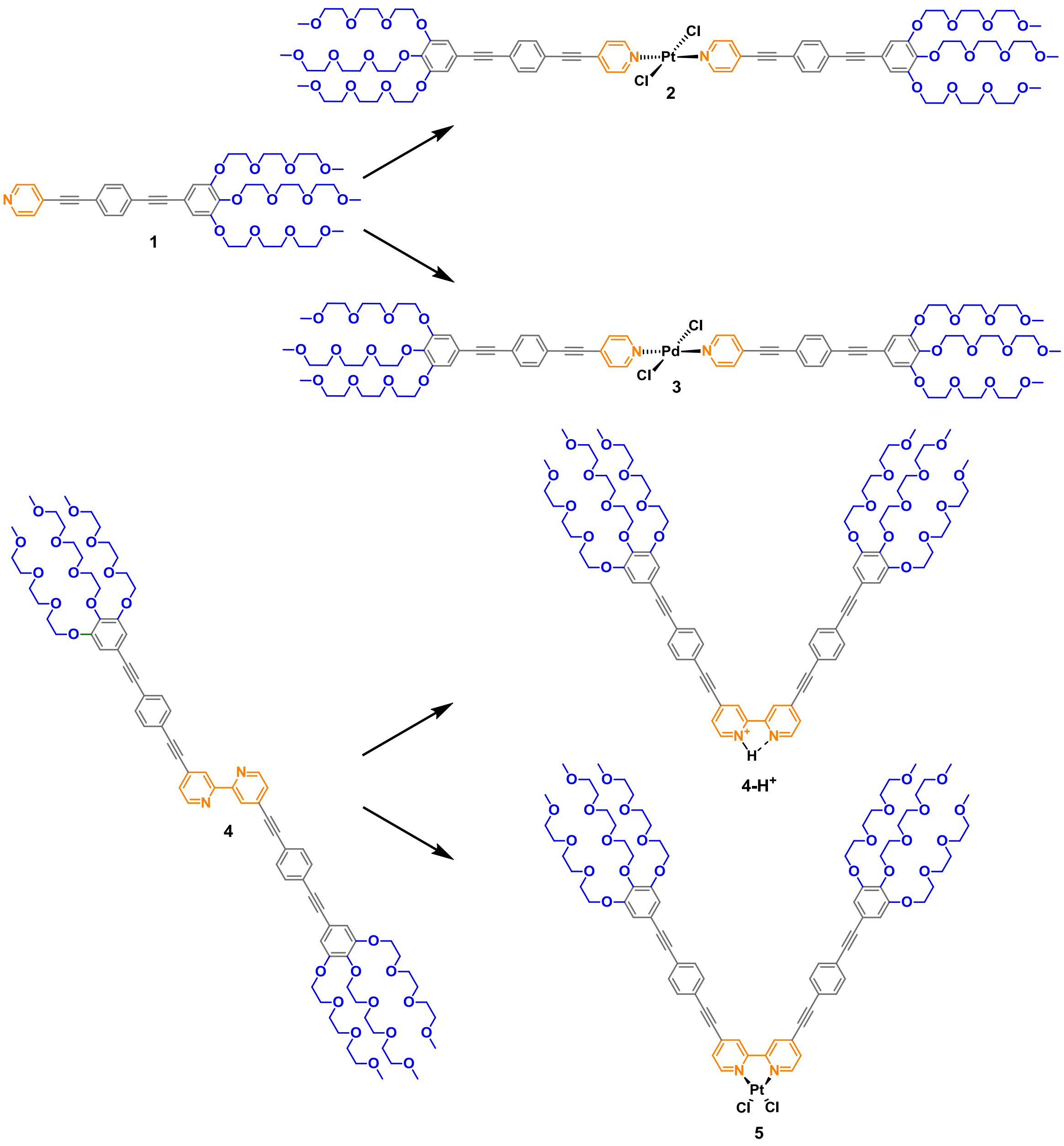

In addition, for the bipyridine-based derivative **4** the aggregation pathway in aqueous solution will be revealed. Taking this ligand for the complexation of a Pt(II) centre, the target complex **5** with *cis*-geometry is realized (Chart 1). The ligating ability of **4** is further exploited to analyse the pH-responsiveness of the system. In this regard, the effect of the addition of acid on the self-assembly of **4** in organic and aqueous medium has been investigated. The detailed studies on the ligand **4**, its H^+-adduct **4-H**$^+$ and the corresponding Pt(II) complex **5** can clarify the impact of the molecular conformation and its electronic structure on the non-covalently formed assemblies.

In the following chapter of this thesis (*Chapter 2*), a comprehensive literature survey on the importance of cooperative effects in self-assembled systems will be presented. Initially, a definition of the term *cooperativity* is given, while afterwards different mechanisms for the formation of supramolecular polymers will be presented. In this regard, the non-cooperative isodemic model, as well as different cooperative aggregation models are discussed. In the main part of *Chapter 2*, examples of cooperative supramolecular systems will be classified depending on the non-covalent forces that drive their self-assembly.

In *Chapter 3*, the results achieved during the laboratory work for the target compounds **1**-**5** will be presented and discussed. Related to the investigated system, this chapter is divided into two parts:

Part I includes the work on the amphiphilic pyridine-based ligand **1** and its corresponding Pt(II) and Pd(II) complexes **2** and **3**, respectively. For OPE derivative **1**, the aggregation mechanism in solution is investigated and the created assemblies visualized by microscopic imaging. For the *trans*-complexes **2** and **3** a detailed investigation using various experimental techniques will be presented. The self-assembly of both compounds is characterized in solution, as well as in the crystalline state. Furthermore, their supramolecular arrangement in polar media is revealed by microscopic techniques.

Part II contains the investigations on the bipyridine derivative **4**, its protonated species **4-H**$^+$ and the corresponding Pt(II) complex **5**. It focuses on the self-assembly mechanism of **4** in aqueous solution, as well as its responsiveness towards the addition of acid in organic medium. Furthermore, this section describes the intriguing change in the morphology of the supramolecular assemblies depending on the (*cis*-/*trans*-) conformation of the system.

Chapter 4 and *Chapter 5* give a summary of the presented work in English and in German.

Finally, in *Chapter 6* the experimental work to achieve the desired target ligands and complexes will be described.

Chapter 2

-

Literature survey[*]

2.1 Cooperativity in supramolecular polymers

Cooperative effects play a major role in numerous natural processes,[22] such as in the self-assembly of the tobacco mosaic virus into monodisperse, highly ordered structures.[23-25] Probably, the most widely studied example is the binding of oxygen to the carrier protein haemoglobin whose cooperative character was observed already at the beginning of the 20th century.[26,27] Haemoglobin fulfils the essential function of transporting oxygen from the lungs to the tissues and in return carbon dioxide from the tissues to the lungs.[26,28] In this regard, the binding of an oxygen molecule by the protein increases the affinity towards oxygen of the remaining binding sites. This behaviour perfectly illustrates the definition of G. Ercolani who stated in 2003 that "cooperativity takes place when the binding of one ligand influences the binding strength of a macromolecule toward a subsequent ligand (or ligands)".[29] Some years later, C. Hunter and H. L. Anderson redefined the original definition by Ercolani and explained that "cooperativity arises from the interplay of two or more interactions, so that the system as a whole behaves differently from expectations based on the properties of the individual interactions acting in isolation".[30]

---

[*] *Chapter 2* reproduced and adapted from C. Rest, R. Kandanelli, G. Fernández, *Chem. Soc. Rev.* **2015**, *44*, 2543-2572 with permission from The Royal Society of Chemistry.

2.2 Overview of various supramolecular polymerization mechanisms

Supramolecular polymers were broadly defined by A. Ciferri as “systems characterized by non-bonded interactions among repeating units”[31] These systems can be divided into three categories depending on the mechanism of their formation: isodesmic, cooperative and ring-chain polymerization. The mechanisms of supramolecular polymerization and their thermodynamic aspects have been extensively described in various reviews by the groups of Moore,[32] Würthner[33] and Meijer[34].

The ring-chain supramolecular polymerization is the least frequently found mechanism in artificial systems. This growth is characteristic for ditopic monomeric units in which equilibrium between linear and cyclic counterparts exists.[34] The isodesmic process is comparable to a step-growth polymerization in which all events of the self-assembly process are characterized by the same value of association constant K, regardless of the size of the aggregates.[32-36] On the other hand, the cooperative (or nucleation-elongation) mechanism is a two state process in which the formation of a thermodynamically unfavourable species, composed of a limited number of monomeric units (nucleation), is followed by a more favourable elongation step exhibiting a much larger value of the binding constant.[34] As a result, self-assembled structures with a high degree of internal order compared with the isodesmic counterparts are formed, which give rise to random-coil supramolecular polymers without internal order.[37] Since the temperature-dependent isodesmic model and two cooperative models (by van der Schoot and by ten Eikelder, Markvoort and Meijer) were applied in the present thesis to describe the investigated aggregation processes, a more detailed description and the corresponding equations of these models will be given in this chapter.

To assess whether a given molecule self-assembles in an isodesmic or cooperative fashion, a careful plan of representative studies is important.[35] First, the system under investigation should exhibit a property that changes with concentration, temperature or the solvent ratio. Usually this property is the UV/Vis light absorption, the Cotton effect or ^{1}H NMR chemical shifts, although other features of the system such as changes in viscosity, IR bands or fluorescence intensity among others have also been examined. An overview of the guidelines and different experimental and computational techniques that are used to investigate self-assembly mechanisms are covered in a concept article from the groups of Balasubramanian and George.[38] Ideally, it should be possible to monitor a complete transformation from monomeric to fully aggregated species in the course of temperature- or concentration-dependent studies. Should this be the case, the parameter α_{agg} (fraction of aggregated species) can be accurately derived, as depicted in Fig. 1. This parameter varies between 0 and 1 depending on whether all monomeric units are in a molecularly dissolved ($\alpha_{agg} = 0$) or an aggregated state ($\alpha_{agg} = 1$), respectively.

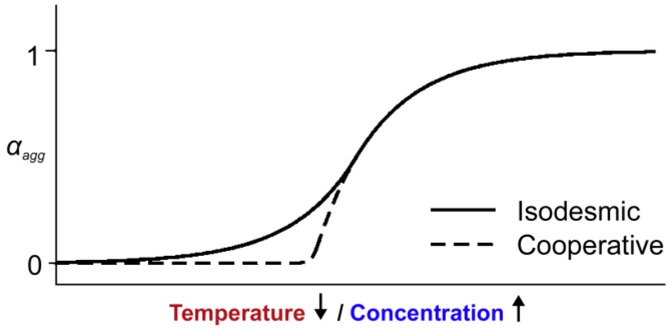

Fig. 1 Plot of the fraction of aggregated species (α_{agg}) against decreasing temperature and increasing concentration, respectively. The graph depicts the characteristic curves corresponding to an isodesmic or cooperative growth. Adapted with permission from ref. 35. Copyright (2010) Wiley-VCH Verlag GmbH & Co. KGaA, Weinheim.

The plot of α_{agg} against concentration or temperature defines a curve whose shape can be related to the self-assembly mechanism (Fig. 1). Sigmoidal curves are usually regarded as non-cooperative, as the transition from the monomeric to the aggregated state occurs in a gradual, stepwise fashion.[31-34] Highly cooperative systems, however, are characterized by much sharper and asymmetric curves showing an all-or-nothing behaviour.

2.3 Theoretical models to describe aggregation processes in thermodynamic equilibrium

As shown in the previous section, the plot of the α_{agg} values against temperature or concentration (Fig. 1) provides first indication whether the corresponding self-assembly follows an isodesmic or a cooperative pathway. Clear evidence for the aggregation mechanism can be gained upon fitting the data points to the appropriate model, yielding the characteristic thermodynamic parameters (enthalpy, entropy, binding constant…), as described below.

2.3.1 The isodesmic model

In case that the changes in a given property of the system against temperature or concentration yield a symmetric, sigmoidal curve, an isodesmic aggregation process is suggested. The isodesmic model[32-36] represents the simplest one to describe a one-dimensional supramolecular self-assembly. It assumes a single equilibrium constant K that is identical for all aggregation steps: $K = K_2 = K_3 = K_4 = \ldots = K_n = K$ (Fig. 2).

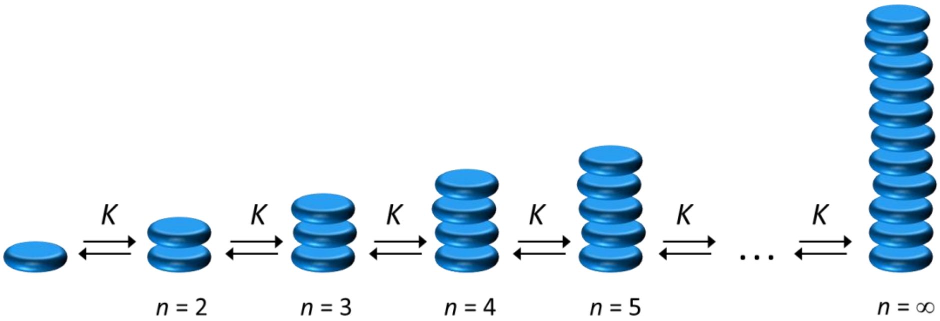

Fig. 2 Schematic representation of the isodesmic supramolecular polymerization. Adapted with permission from ref. 34. Copyright (2009) American Chemical Society.

The binding affinity of a molecule towards a self-assembled stack is equal for each association step, independent of the length of the supramolecular polymer.[32-36] Thus, the gradual growth is characterized by a constant decrease in the Gibbs free energy ΔG^0, as depicted in the energy diagram in Fig. 3.

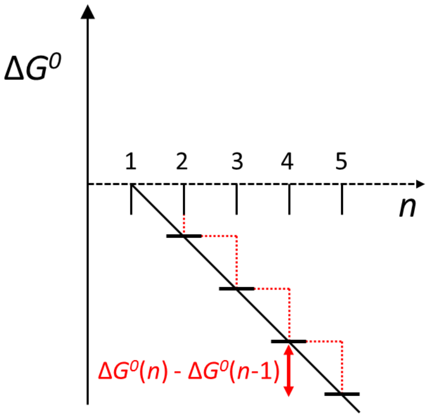

Fig. 3 Schematic energy diagram of an isodesmic process: changes in the Gibbs free energy (ΔG^0) as a function of the supramolecular chain length n. Adapted with permission from ref. 34. Copyright (2009) American Chemical Society.

For the temperature-dependent isodesmic model, a detailed derivation of the mathematical equations was presented by Meijer, Schenning and co-workers in 2010[35] and will be described below since this model is used to characterize the self-assembly of amphiphile **1** in this thesis.

By temperature-dependent absorption studies the fraction of aggregated species α_{agg} at different temperatures can be calculated according to eq. (1):

$$\alpha_{agg}(T) = 1 - \frac{\varepsilon(T) - \varepsilon_{agg}}{\varepsilon_{mon} - \varepsilon_{agg}} \qquad (1)$$

in which ε_{agg} corresponds to the (estimated) extinction coefficient of the fully aggregated species, ε_{mon} is the (estimated) extinction coefficient of the monomeric state and $\varepsilon(T)$ is the measured extinction coefficient at a certain temperature.

For an isodesmic aggregation pathway, the experimental α_{agg} values can be related to temperature by a sigmoidal relation, considering a two-state equilibrium.[35] The sigmoidal function for α_{agg} ($0 \leq \alpha_{agg} \leq 1$) can generally be expressed as:

$$\alpha_{agg}(T) \cong \frac{1}{1 + e^{\frac{T - T_m}{T^*}}} \qquad (2)$$

with the temperature T as variable and the melting temperature T_m as the temperature for $\alpha_{agg} = 0.5$.

The parameter T^* is related to the slope of the sigmoidal function at the temperature $T = T_m$. This slope can be expressed introducing the enthalpy release ΔH, as:

$$\left.\frac{\delta\alpha_{agg}(T)}{\delta T}\right|_{T=Tm} = \frac{-1}{4T^{*}} \approx \frac{\left(\frac{\sqrt{2}-1}{2\sqrt{2}-1}\right)\Delta H}{RT_m^2} \qquad (3)$$

with the universal gas constant R, defined as product of the Boltzmann constant k times Avogadro's number N_A.

Solving equation (3) for the temperature T^* gives the expression:

$$T^* = \frac{-RT_m^2}{0.908\,\Delta H} \qquad (4)$$

Subsequent combination of equations (2) and (4) provides the final function for α_{agg} that is related to the temperature T by:

$$\alpha_{agg}(T) = \frac{1}{1+e^{-0.908\,\Delta H\frac{T-T_m}{RT_m^2}}} \qquad (5)$$

Regarding different plots of the temperature-dependent α_{agg} values against the dimensionless temperature T/T_m (Fig. 4), one can obtain that the slope of the curves depends on the temperature-independent aggregation enthalpy ΔH.[34] Thus, the steepness of the curve changes with the corresponding ΔH value and does not signalize any degree of cooperativity.

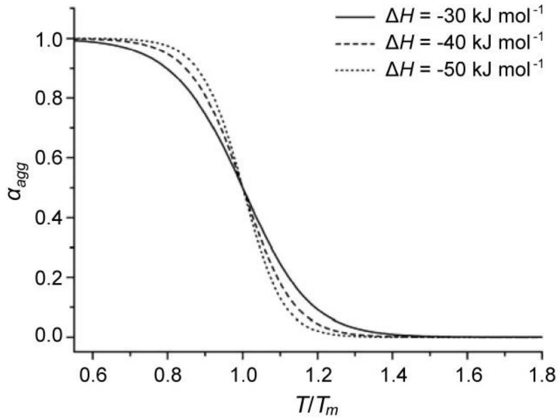

Fig. 4 Temperature-dependent isodesmic supramolecular polymerization: fraction of aggregated species α_{agg} as a function of the dimensionless temperature T/T_m for different values of ΔH. Adapted with permission from ref. 34. Copyright (2009) American Chemical Society.

2.3.2 Models describing the cooperative growth of supramolecular polymers

Various thermodynamic models have been used to describe a cooperative self-assembly process that is suggested by a non-sigmoidal aggregation curve.[35] From among several models developed by different authors, four of these are largely used to analyse self-assembly mechanisms depending on whether the data is based on temperature- or concentration-dependent experiments (Fig. 5).

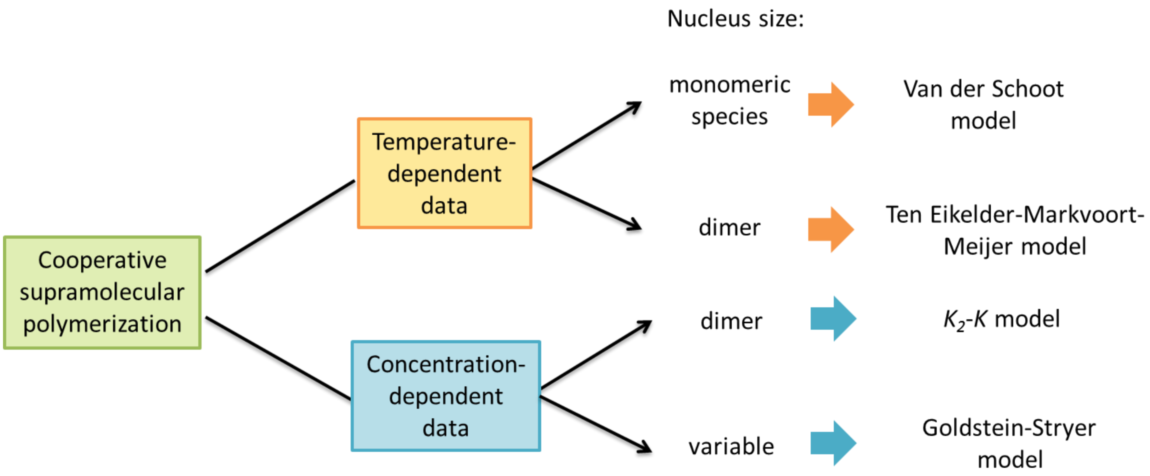

Fig. 5 Representation of the four most common models to describe a cooperative supramolecular polymerization.

All models have in common that they assume an initial, unfavourable nucleation step, characterized by a relatively low association constant. Once this step has been overcome, the elongation into extended supramolecular polymers occurs in a highly favourable fashion, as described by much greater binding constants.

2.3.2.1 Concentration-dependent cooperative models

For concentration-dependent cooperative processes the K_2-K and the more general *Goldstein-Stryer*-model, that differ in the assumed size of the nucleus, are the most applied models. The one reported by Goldstein and Stryer[34,39] considers in an initial process the formation of a nucleus of variable size s that is created in an isodesmic fashion with K_n. After this initial event the polymer further elongates, characterized by a different equilibrium constant K. These two parameters give the cooperativity factor $\sigma = K_n/K$, whose value is smaller than unity for a cooperative growth. Regarding the *Goldstein-Stryer*-model, however, the *cumulative cooperativity* ω ($\omega = \sigma^{s-1}$) is of importance since the polymerization depends not only on σ but also on the nucleus size s. Therefore, the fitting of the concentration-dependent data allows defining the *cumulative cooperativity* ω.

A more simplified model for concentration-dependent studies is represented by the K_2-K model,[34,40] in which the nucleus is assumed to comprise two units and its formation is characterized by a dimerization constant K_2. Except this dimerization step, all following binding events exhibit the same equilibrium constant K, representing an isodesmic elongation. Fitting of the measured data to the best match to this model allows the estimation of the cooperativity factor σ, the nucleation (dimerization) and elongation constant.

2.3.2.2 Temperature-dependent cooperative models

Different models exist to describe concentration- as well as temperature-dependent data. However, using variable-temperature measurements has a major benefit since this method provides a much larger number of data points.[35] For the investigation of a sample in the appropriate temperature range, it is thus possible to monitor the transition from a molecularly dissolved to an aggregated state in small, defined steps. Furthermore, in temperature-dependent studies potential dilution errors can be avoided that may occur in concentration-dependent experiments. The resulting detailed aggregation curve allows an accurate fitting and characterization of the self-assembly process of the system.[35] The cooperative *van der Schoot*-, as well as the recent *ten Eikelder-Markvoort-Meijer*-model is applied to temperature-dependent measurements of target molecules **2-4** in this work. For this reason, a more detailed presentation of these models will be given below.

a) The Nucleation-Elongation model by van der Schoot[34,41-43]

The model for *thermally activated equilibrium polymers* was described by van der Schoot and represents a modification of the *Oosawa-and-Kasai*-model. The model describes the aggregation of subunits into one-dimensional, linear aggregates. The corresponding elongation temperature T_e divides the self-assembly into the nucleation (above T_e) and the elongation process (below T_e). At T_e, the monomeric activation takes place that is characterized by a dimensionless equilibrium constant K_a. This parameter gives an indication of the degree of cooperativity for the system. The supramolecular polymerization can only proceed in the activated state, however this state is unfavourable and becomes obvious in a value for $K_a \rightarrow 0$. Consequently, a low K_a constant results in a very sharp transition from the monomeric to the aggregated state (highly cooperative process).

The mathematical equations of the *van der Schoot*-model are given below according to ref. 43, while their detailed derivation can be found in ref. 41. The elongation growth is characterized by the temperature-independent elongation enthalpy ΔH_e and the dimensionless equilibrium constant K_e that can be expressed by:

$$K_e = e^{\frac{-\Delta H_e}{RT_e^2}(T-T_e)} \qquad (6)$$

with T as the absolute temperature, T_e as the elongation temperature and R as the universal gas constant.

The equation for α_{agg} comprises the dimensionless equilibrium constants K_a and K_e, as well as the number-averaged degree of polymerization DP_N:

$$\alpha_{agg} = \frac{K_a}{K_e} DP_N \, (DP_N - 1) \qquad (7)$$

In the elongation regime ($T < T_e$), α_{agg} can be further described by expression (8):

$$\alpha_{agg} = 1 - e^{\frac{-\Delta H_e}{RT_e^2}(T-T_e)} \qquad (8)$$

Furthermore, for the nucleation regime ($T > T_e$) the values for α_{agg} are given by:

$$\alpha_{agg} = \sqrt[3]{K_a} \, e^{\left(\frac{2}{3\sqrt[3]{K_a}}-1\right)\frac{\Delta H_e}{RT_e^2}(T-T_e)} \qquad (9)$$

The number-averaged degree of polymerization (DP_N) in the elongation regime can be determined by:

$$DP_N = \frac{1}{\sqrt{K_a}} \frac{\alpha_{agg}}{1-\alpha_{agg}} = \frac{1}{\sqrt{K_a}} \frac{1-e^{\frac{-\Delta H_e}{RT_e^2}(T-T_e)}}{e^{\frac{-\Delta H_e}{RT_e^2}(T-T_e)}} \qquad (10)$$

To calculate the average stack length at the elongation temperature, i.e. DP_N at T_e, the relatively simple eq. (11) can be applied:

$$DP_N(T_e) = \frac{1}{\sqrt[3]{K_a}} \qquad (11)$$

This expression shows that the dimensionless constant K_a is directly related to the size of the stacks at T_e.

b) The Nucleation-Elongation Model by ten Eikelder, Markvoort and Meijer[44-46]

The more recent model developed by ten Eikelder, Markvoort and Meijer assumes the formation of a nucleus that consists of two units (a dimer). It describes a temperature-dependent cooperative (or isodesmic, $\Delta H^0_{nuc} = 0$) polymerization that allows a two-sided growth.

The model enables the characterization of a supramolecular process in which two types of monomers and aggregates are involved. Thus, it includes the supramolecular co-polymerization of enantiomeric species (*R*- and *S*-monomers) that can self-assemble into polymers with two types of helicity (*P*- or *M*-type). Besides the co-polymerization, this equilibrium model can also be applied to the more simplified case of a one-component supramolecular system (e.g. enantiomerically pure systems), as described below.

To analyse melting curves for a supramolecular polymerization, the temperature-dependence of the equilibrium constants is important. Eq. (12) describes the change in the standard Gibbs free energy ΔG^0, consisting of an enthalpy term ΔH^0 and an entropy term $T\Delta S^0$:

$$\Delta G^0 = \Delta H^0 - T\Delta S^0 \qquad (12)$$

This formula can be combined with eq. (13):

$$\Delta G^0 = -RT\, lnK \qquad (13)$$

with R as the universal gas constant, to the general expression for the equilibrium constant K:

$$K = e^{\frac{-(\Delta H^0 - T\Delta S^0)}{RT}} \qquad (14)$$

According to eq. (14) the binding constant for the unfavorable nucleation event (K_{nuc}) and the elongation steps (K_e), respectively, can be expressed as:

$$K_{nuc} = e^{\frac{-((\Delta H^0 - \Delta H^0_{nuc}) - T\Delta S^0)}{RT}} \quad (15)$$

$$K_e = e^{\frac{-(\Delta H^0 - T\Delta S^0)}{RT}} \quad (16)$$

with an elongation enthalpy ΔH^0, a nucleation penalty ΔH^0_{nuc} and the entropy ΔS^0.

The values for ΔH^0, ΔH^0_{nuc}, ΔS^0 and the elongation temperature T_e are obtained by fitting the changes in a certain property of the system (UV/Vis absorption or CD data) to the model. The entropy difference (ΔS^0) is assumed to be equal for the nucleation and elongation events. Furthermore, the nucleation penalty (ΔH^0_{nuc}) represents the difference between the enthalpy of nucleation and the enthalpy of elongation. With these parameters the binding constants K_{nuc} and K_e can be calculated according to eqs. (15) and (16). This, in turn, allows the determination of the cooperativity factor σ by:

$$\sigma = \frac{K_{nuc}}{K_e} \quad (17)$$

Including eq. (15) and (16), eq. (17) can further be expressed as:

$$\sigma = e^{\frac{\Delta H^0_{nuc}}{RT}} \quad (18)$$

For the elongation constant K_e at the elongation temperature T_e, the following relation is given:

$$K_e \cdot c_{total} = 1 \quad (19)$$

Combination of eq. (19) with the definition for the equilibrium constant (16) at T_e results in:

$$e^{\frac{-(\Delta H^0 - T_e\Delta S^0)}{RT_e}} c_{total} = 1 \quad (20)$$

that provides the definition of the elongation temperature T_e as:

$$T_e = \frac{\Delta H^0}{\Delta S^0 + R\ln(c_{total})} \quad (21)$$

2.4 Combinations of non-covalent interactions used to create cooperative systems

In accordance to the definition of cooperativity by Hunter and Anderson, supramolecular polymers are generally created by monomeric units that are held together by multiple (various kinds of) attractive, non-covalent forces,[30] while minimizing possible repulsive interactions that can restrict their supramolecular growth. These stabilizing forces depend on the investigated system and range from weak to relatively strong interactions.[47]

In the following literature survey a wide variety of supramolecular polymers will be presented that are classified on the cooperative interactions involved in their self-assembly, with particular emphasis on recent novel strategies introduced in the last half decade.

2.4.1 Hydrogen bonding (and π-π) interactions

By far, the most commonly used approach to construct highly ordered supramolecular polymers has been focused on examples that self-assemble through the combination of hydrogen bonding and π-π interactions, as described in various reviews.[34,38] However, also purely hydrogen bonding systems can on their own represent the driving force for the creation of supramolecular arrangements based on *cooperative hydrogen bonds*. The singularity of hydrogen bonds originates from their complex nature, whose characterization demands the contribution of different interaction types: electrostatics, polarization, van der Waals and covalency.[48-50] The principles of the cooperative effect in hydrogen bonded supramolecular systems have been reviewed by Meijer and coworkers[34] and its presence and origin described in several publications.[51-63] In those systems, cooperativity has been attributed to entropic reasons, due to a lower entropy demand for the association of a monomer to a polymeric structure as for the dimerization of two monomeric units, as well as enthalpic contribution, due to several electronic effects, namely long-range dipole-dipole interactions, polarization effects and resonance-assistance.[34]

In their seminal work from 2006, the group of Meijer reported on the hierarchical self-assembly of oligo(*p*-phenylene vinylene) (OPV) derivatives (**6**-**8**) into fibres by following a nucleation-growth mechanism.[42] The investigated molecules **6-8** feature a ureidotriazine moiety on one side and a peripheral trialkoxy group on the other edge of a central aromatic OPV unit (Chart 2). This molecular structure allows the formation of dimers by quadruple hydrogen bonding interactions between the complementary ureidotriazines.

Chart 2 Molecular structure of the oligo(*p*-phenylene vinylene) derivatives **6-8**.

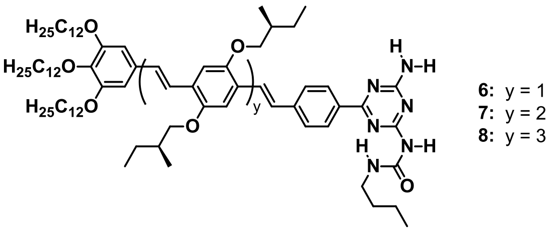

Earlier studies on these systems presented the formation of dimeric species in chloroform while in dodecane two different states were detected, namely monomeric species or dimers at high temperature that can further aggregate at low temperature into helical stacks, as observed by UV/Vis absorption, fluorescence and CD studies.[64,65] Regarding the aggregation process, dimerization of the monomers through hydrogen bonding most likely leads to a preorganization of the subunits and an extension of the π-surface. These effects facilitate the further growth of the system in apolar solvents. More detailed temperature-variable investigations in dodecane revealed a cooperative denaturation for the chiral stacks, whose stability depends on the length of the conjugated core since stronger π-π interactions result in higher melting temperatures.[65] The fibrillar arrangements could be further characterized by small-angle neutron scattering (SANS) and atomic force microscopy (AFM)[65] and the dimeric monolayers of OPVs by scanning tunnelling microscopy (STM)[66].

As shown in Fig. 6a, analysis of temperature-dependent CD measurements at different concentrations of **7** in dodecane reveals for all of them a clearly non-sigmoidal curve, whose detailed study allows a division of the helical aggregation process into hierarchical steps.[42] It is demonstrated that the self-assembly can be described by the model for *thermally activated equilibrium polymerization*, developed by Oosawa and Kasai and modified by van der Schoot.[41,67] Here, the pathway from isodesmic non-helical assembly to non-isodesmic helical assembly is characterized by an equilibrium between non-helical and helical structures of a critical size. Application of this model to the CD curves of **7** affords a perfect fitting for the lowest concentration and confirms that the helical aggregates do not exist until the temperature falls under the corresponding (concentration-dependent) elongation temperature T_e.[42]

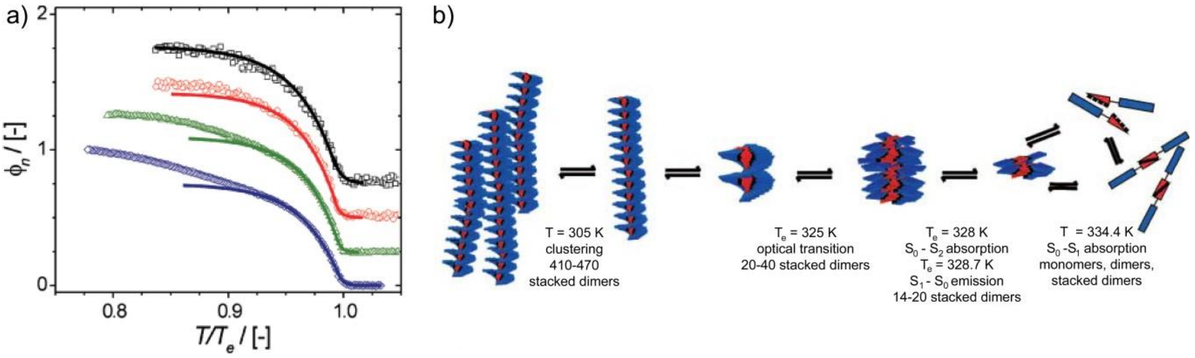

Fig. 6 a) Normalized CD intensities (ϕ_n) monitored at λ = 466 nm upon cooling for four concentrations of **7** in dodecane (symbols) and one-parameter fits to the data (lines). A vertical offset of the curves of 0.25 is applied for reasons of clarity. b) Schematic representation of the hierarchical self-assembly of **7** in solution. Adapted from ref. 42, with permission from AAAS.

However, for higher concentrated samples the data obtained at lower temperature cannot be described by the fitting curve for one-dimensional aggregation that is assigned to a clustering of the stacks.[42] This additional event could be characterized as an isodesmic process and AFM further revealed a more pronounced clustering effect at higher concentration. This process represents the last step of the aggregation cascade that consists of several stages (Fig. 6b): From high temperature, the monomeric species self-assembles into hydrogen-bonded dimers. Upon decreasing temperature, these subunits further aggregate in an isodesmic fashion into small stacks of around 15 dimeric units. Upon further cooling (T_e = 328 K), the molecules in the stack adopt a higher order that can be characterized as cooperative transition. Subsequently, a cooperative helical switching occurs in which the preaggregate transforms into an initial chiral species. The average degree of polymerization at this elongation temperature was determined for **7** to be 17 to 41 dimers, which fits well with the calculated number of 15 to 30 stacked dimeric units required for one helical pitch. Afterwards, the initial chiral stack can grow into extended helices following a cooperative mechanism.

The elongation temperature T_e depends on the length of the conjugated system of the molecules, with lower temperatures for smaller aromatic surfaces. Not only the conjugated π-surface but also solvent changes affect the T_e values, showing a dependence on the length of the hydrocarbon, as well as on the number of carbon atoms of the solvent, i.e. even-odd effect. This impact could also be observed for the binding constant and the number of dimers in the aggregates, indicating that the solvent molecules oriented at the periphery of the aggregates play an important role in the self-assembly process.

In a further example, the same group synthesized a related OPV host (**A-OPVUT 9**) with four aromatic rings bearing achiral linear substituents and a ureidotriazine end group (Chart 3).[68] Upon addition of (*R*)- or (*S*)-citronellic acid (**CA**) to **9** in methylcyclohexane (MCH), chirality could be introduced into the system. This process gives rise to mirror-image CD spectra depending on the chiral additive. The key role in generating chirality was attributed to hydrogen-bonded linking of the chiral **CA** guests to the ureidotriazine groups of the gelator **9** in a 1:1 stoichiometry (Chart 3). Interestingly, the self-assembly of the 1:1 (**A-OPVUT**:**CA**) complex also occurs in a cooperative fashion, similar to that of the individual OPV system.

Chart 3 Molecular structure of compound **9** and its 1:1 complex with (*R*)-citronellic acid (**CA**).

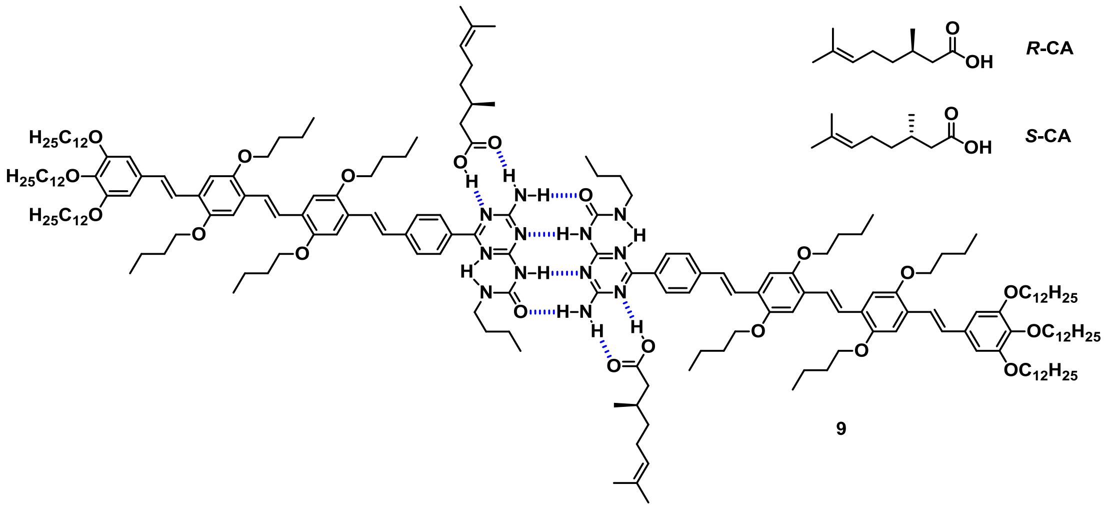

Benzene-1,3,5-tricarboxamides (BTAs) are a class of molecules that have been widely investigated by Meijer and co-workers.[69-73] In 2008, they investigated the cooperative self-assembly of two literature-known[74-76] C_3-symmetrical trialkyl-benzene-1,3,5-tricarboxamides with a chiral alkyl substituent for (*R*)-**10** and an achiral linear chain for **11** (Chart 4).[43]

Chart 4 Molecular structure of the trialkylbenzene-1,3,5-tricarboxamides (*R*)-**10** and **11**.

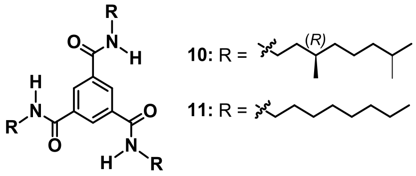

The chiral derivative (*R*)-**10** aggregates in a highly cooperative fashion in heptane, as observed by temperature-dependent CD measurements (Fig. 7).[43] This self-assembly gives rise to a right-handed columnar architecture that is based on triple hydrogen bonding interactions. The stacks at the elongation temperature (T_e) could be defined to consist of at least 100 discotic molecules that are extended to more than 10000 subunits upon cooling to room temperature.

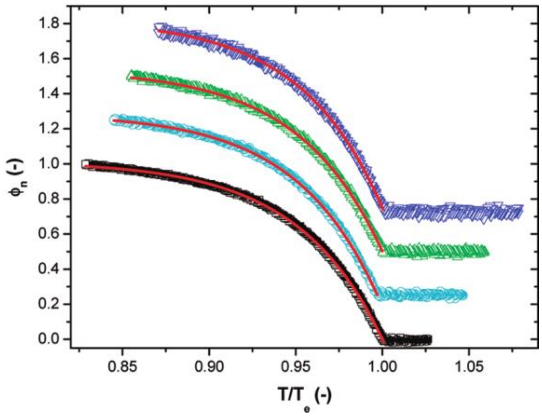

Fig. 7 Degree of aggregation with fitted (red line) elongation regime as a function of temperature for solutions of (*R*)-**10** in heptane, for different concentrations. The curves are shown with a 0.25 offset for each next concentration and as a function of the normalized temperature T/T_e. Reprinted with permission from ref. 43. Copyright (2008) American Chemical Society.

Similarly, an abrupt change in the degree of aggregation for (*R*)-**10** was also observed in temperature-dependent UV/Vis absorption studies.[43] Hence, it was possible to describe the spectral changes by the nucleation-elongation model of van der Schoot[41], showing that the CD studies of **10** are in good agreement with its UV/Vis absorption data. Likewise, the spectral changes for the achiral counterpart **11** revealed a cooperative aggregation mechanism and suggested that it also exists as helical stacks.[43] However, these assemblies do not exhibit a distinct helicity, resulting in a CD silent spectrum. The helical structures of **11** further interact laterally at lower temperature inducing a slight deviation from the one-dimensional fitting. A direct comparison shows that the thermodynamic parameters for the cooperative processes of (*R*)-**10** and **11** significantly differ, with a lower cooperative effect and a reduced aggregation tendency for **11**. Sergeant-and-soldiers studies show that the presence of only 4% of the chiral sergeant (*R*)-**10** in a heptane solution of **11** is enough to reach maximum handedness in CD experiments.

In 2011, the authors moved a step forward towards more complex systems by designing a ditopic BTA derivative **12**, whose cooperative self-assembly can be controlled by the addition of a N-methylated BTA **13** as monotopic chain stopper.[77] The investigated ditopic BTA **12** contains three amide groups stabilizing the supramolecular assemblies by hydrogen bonding interactions, while its monotopic counterpart **13** lacks the N-H moiety resulting in a monomeric state in MCH and acetonitrile (Chart 5).

Chart 5 Molecular structure of ditopic BTA **12** and N-methylated BTA derivative **13**.

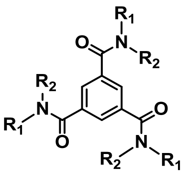

12: $R_1 =$ n-$C_{16}H_{33}$
$R_2 =$ H

13: $R_1 =$ n-$C_{12}H_{25}$
$R_2 =$ CH_3

Regarding the binary mixture of both BTA derivatives, the addition of **13** induces a drop in the relative viscosity of a MCH solution of **12** (Fig. 8a) that can be assigned to a shortening of the helical aggregates.[77] However, the affinity of **13** to link to the supramolecular polymers of **12** and thus acting as a chain stopper is relatively weak, as indicated by the low association constant for chain termination. This observation can be explained by considering the unfavourable conformation of monomeric **12** in solution that requires a reorganization of its amide functionalities before making contact with the stacks of **13** by hydrogen bonding. The studies on this BTA system enabled the development of a binary self-assembly model. This model generally describes cooperative supramolecular polymerizations in the presence of a second component that can interact with the monomers and/or polymers (Fig. 8b).

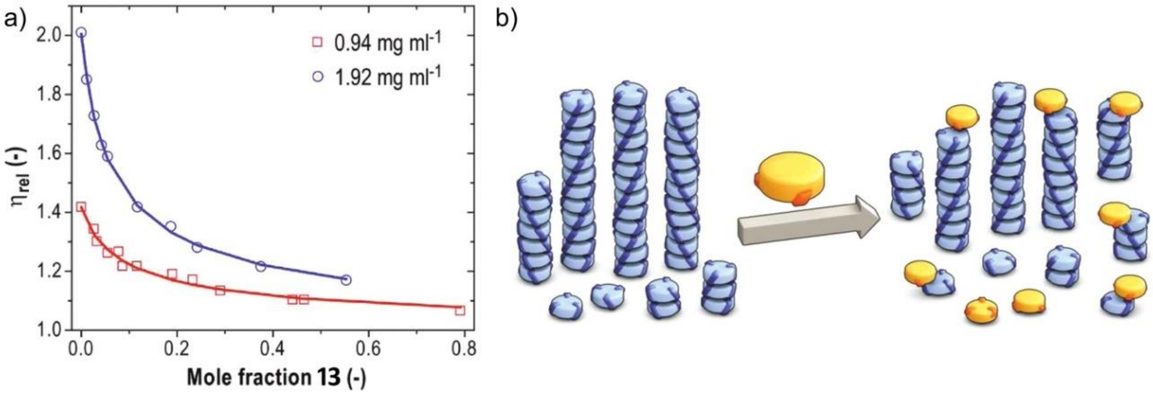

Fig. 8 a) Relative viscosity as a function of mole fraction **13** added for two concentrations of **12** in MCH. b) Schematic representation of the introduction of a monotopic monomer to a ditopic monomer that self-assembles into long 1-D assemblies via a cooperative mechanism (the monotopic monomer could interact with the end of the stacks, with monomers, with both, or with neither). Adapted with permission from ref. 77. Copyright (2011) American Chemical Society.

After these extensive investigations and characterizations of BTAs, Meijer, Palmans and co-workers questioned whether the substitution of the amide by thioamide groups would influence the supramolecular polymerization.[78] To that end, they synthesized new thioamide-based analogues (**14-16**) by treatment of the corresponding BTA precursors with P_2S_5 in hot toluene (Chart 6). The thioamide-based BTAs showed a similar behaviour and stability compared to the amide-based derivatives, even though differences could be observed concerning their self-assembly.

Chart 6 Molecular structure of compounds **14-16**.

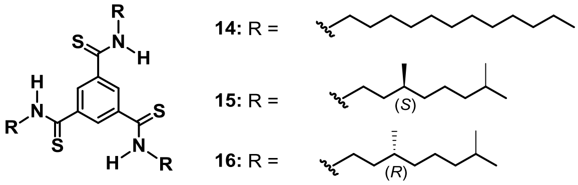

In hydrophobic solvents (MCH), the thio-BTAs self-assemble into one-dimensional helical structures that are stabilized by triple hydrogen bonding interactions, as detected by IR spectroscopy.[78] The melting curves of thio-BTAs extracted from CD studies showed a clearly non-sigmoidal shape, indicative of a cooperative behaviour. However, their cooperativity factor σ of 10^{-4} is around two orders of magnitude larger than that of their amide counterparts, revealing that the self-assembly of thio-BTAs is less cooperative. Since the aromatic unit is equivalent for both molecular classes, this significant difference in the cooperative effect has to be attributed to the hydrogen bonding interactions between the discotic units. The strength of hydrogen bondings between the thio-amides thus should be weaker than of those between the amide groups, as could also be identified in dimers of formamide and thio-formamide molecules in 2002.[79]

Sánchez and co-workers have devoted substantial efforts towards the creation of self-assembled oligo(phenylene ethynylenes) (OPEs).[80-85] In 2011, they reported the cooperative self-assembly of an achiral (**17**) and two chiral ((*S*)-**18** and (*R*)-**19**) C_3-symmetrical OPE-based trisamides (Chart 7) into helical structures.[86]

Chart 7 Molecular structure of OPE-based trisamides (**17-21**) and alkoxy-amides (**22-24**).

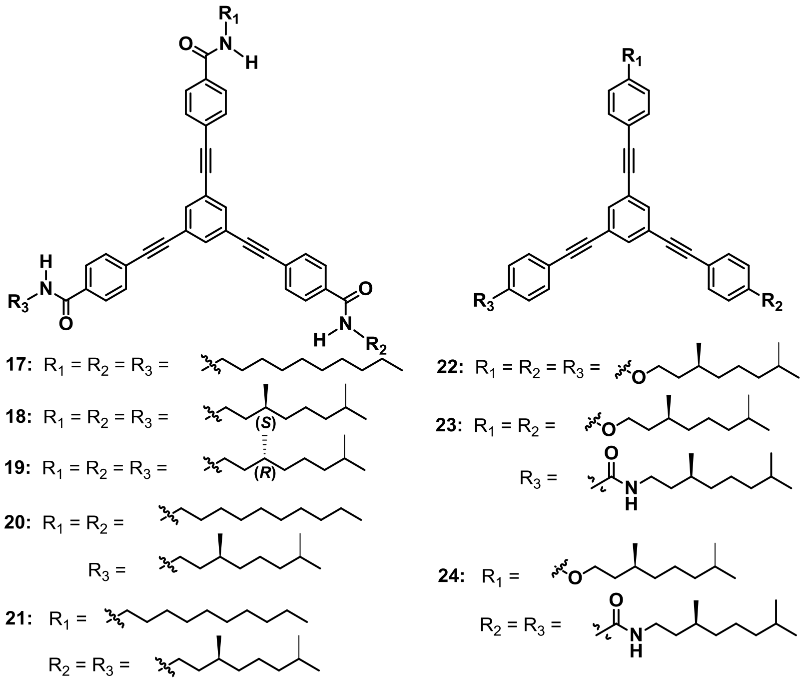

The helical nature of the assemblies of **17-19** in MCH could be identified by FTIR spectroscopy and further characterized as right-handed helix in case of (*S*)-**18** and an arrangement of opposite handedness for (*R*)-**19**.[86] Temperature-dependent CD studies reveal that these samples become CD inactive above 363 K, however upon cooling helicity is recovered and the CD signal abruptly grows in a non-sigmoidal fashion. The suggested cooperative pathway for the aggregation process can be confirmed by temperature-dependent UV/Vis absorption studies in MCH (Fig. 9).

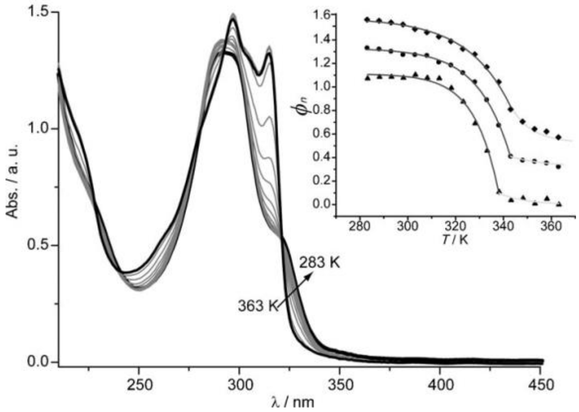

Fig. 9 Temperature-dependent UV/Vis absorption spectra of **17** (MCH, c = 1 x 10^{-5} M, 363 to 283 K, at intervals of 5 K). The inset shows plots of the molar fraction of aggregates versus temperature fitted within elongation (dark grey) and nucleation (light grey) regimes (squares = **17**, dots = (*S*)-**18**, triangles = (*R*)-**19**). Curves in the inset are depicted with a 0.3 offset. Reprinted with permission from ref. 86. Copyright (2011) Wiley-VCH Verlag GmbH & Co. KGaA, Weinheim.

The measurements shown in Fig. 9 reveal a transition from monomeric to aggregated species upon cooling (from 363 to 283 K) that fits perfectly to the nucleation-elongation model proposed by Meijer and co-workers.[42,43,87,88] The average size of the stacks at T_e could be defined to be around ten molecules.[86] This number perfectly matches the stabilization energy per subunit for a helical stack of **17** that saturates around 8-12 molecules, as suggested by DFT calculations. This aggregate size at the elongation temperature is around ten times smaller than that found for literature-known BTAs,[43,87,88] as *e.g.* previously described for molecule (*R*)-**10** that forms stacks of around 100 subunits at T_e.[43] This difference indicates that the extension of the π-framework from BTAs to the OPE-based trisamides favours the activation step and results in a reduction of the aggregate length at T_e.[86]

The thermodynamic parameters extracted from UV/Vis absorption studies are in good agreement with those of CD experiments offering a high cooperativity for (*S*)-**18** and (*R*)-**19** (K_a of 10^{-4}) and a slightly lower cooperative effect for the achiral substituted derivative **17** (K_a of 10^{-3}).[86] The origin of cooperativity in the helical architectures was attributed to the interplay of π-π interactions between the aromatic cores and triple hydrogen bonding between the amide groups, as identified by concentration-dependent ^{1}H NMR, FTIR studies and DFT calculations.

In a further work, the same authors extended their studies on OPE-based trisamides (**20**-**21**) as well as alkoxy-amides (**22-24**) (Chart 7).[89] For both classes, derivatives with only one kind of substituent as well as asymmetrical derivatives with different substituents in the molecular structure were synthesized and their ability to form chiral objects was investigated.

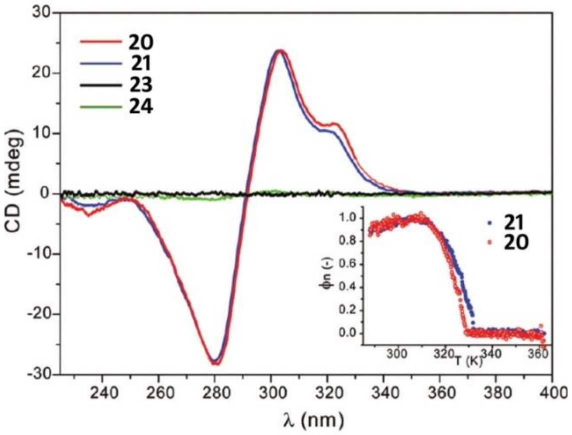

Fig. 10 CD spectra of **20** (red line), **21** (blue line), **23** (black line) and **24** (green line) (MCH, c = 1.5 x 10^{-5} M). Inset: Non-sigmoidal melting curves of **20** (red) and **21** (blue), from 363 to 288 K at intervals of 0.5 Kmin^{-1}. Adapted with permission from ref. 89. Copyright (2012) American Chemical Society.

Both unsymmetrical chiral compounds **20** and **21** show a very similar behaviour as previously reported for symmetrical systems **17** (achiral) and (*S*)-**18** (chiral).[86,89] The CD spectra of **20** and **21** reveal the presence of right-handed helical structures (Fig. 10) whose formation can be accurately described by the cooperative nucleation-elongation model by van der Schoot[42,43]. Remarkably, the helicity in aggregated **21** shows that the presence of only one stereogenic centre in the molecular design can dictate the handedness of the helical systems. However, the helical assemblies formed by asymmetrical monomers **20** and **21** are less stable than those of their symmetrical counterparts **17** and (*S*)-**18**, due to weaker stabilizing interactions generated between the dissimilar achiral and chiral side chains.

The important contribution of triple hydrogen bonding interactions to induce the aggregation into helical arrangements can be confirmed by investigating related OPE derivatives **22-24**, in which one to three amide functionalities are replaced by ether groups.[89] This structural variation precludes the stabilization by hydrogen bondings and thus the ability to form helical arrangements, as demonstrated by the absence of any CD signal. However, also for chiral but non-helical **24** the self-assembly into helical architectures can be induced by the addition of achiral but helical **17**. Upon cooling of the molecularly dissolved state in MCH, a cooperative 1:1 co-assembly takes place as determined by CD studies and Job's plot analysis. In the created assemblies both co-monomers benefit from this mixing process by a transfer of helicity and chirality, respectively.

In 2013, the enthalpy and entropy contribution in the self-assembly processes of OPE and BTA systems in MCH was compared.[90] In these studies, the thermodynamic parameters for the cooperative self-assembly of derivatives **17-19** (Chart 7) and an identically substituted BTA counterpart ((*S*)-enantiomer of molecule **10** (Chart 4)) exhibiting a reduced aromatic core were investigated. The direct comparison of the thermodynamic data revealed very similar values indicating that the created structures are based on similar attractive interactions. This result clearly shows that the main contribution to the formation of OPE and BTA assemblies derives from the directional hydrogen bonding interactions and that an enlargement of the *π*-surface does not account for an increased stability. Only the central rings (included both in BTAs and OPEs) can ideally overlap resulting in attractive aromatic interactions, as already illustrated in the calculated helical structure of **17**, reported in 2011.[86]

Chart 8 Molecular structure of compounds **25-28**.

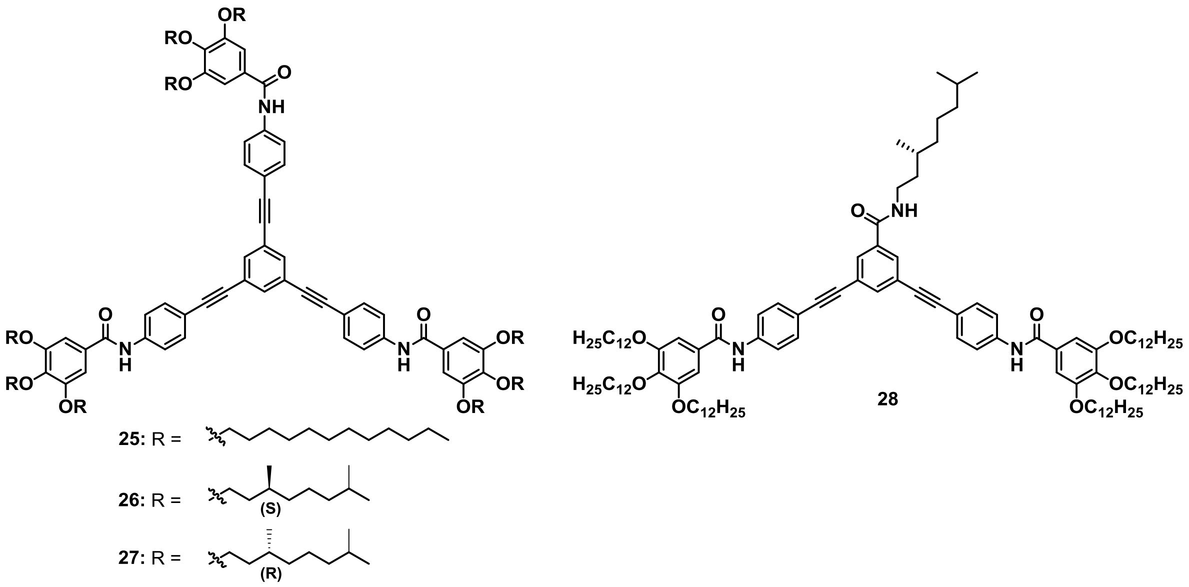

In a complementary work, Meijer and co-workers described the helical self-assembly of two structurally-related classes of OPE derivatives with C_3- (**25-27**) and C_2- (**28**) core symmetry, featuring three amide groups and two or three peripheral alkoxyphenyl substituents to enhance the solubility in apolar solvents (Chart 8).[91] The authors observed that the symmetry of the core has a significant impact on the aggregation process of the OPE derivatives. In this regard, the C_2-symmetrical discotics show a lower binding constant compared to the C_3-derivatives, as well as a tenfold higher σ value, indicating a lower degree of cooperativity.

In 2012, Sánchez and co-workers presented the cooperative aggregation of a chiral linear tetraamide **30** showing an amplification of chirality when the chiral derivative is mixed with a non-chiral counterpart **29** (Chart 9).[92]

Chart 9 Molecular structure of tetraamide derivatives **29** and **30** and the pharmaceutical ingredients aspirin (**ASP**), indomethacin (**IND**), caffeine (**CAF**) and carbamazepine (**CBZ**).

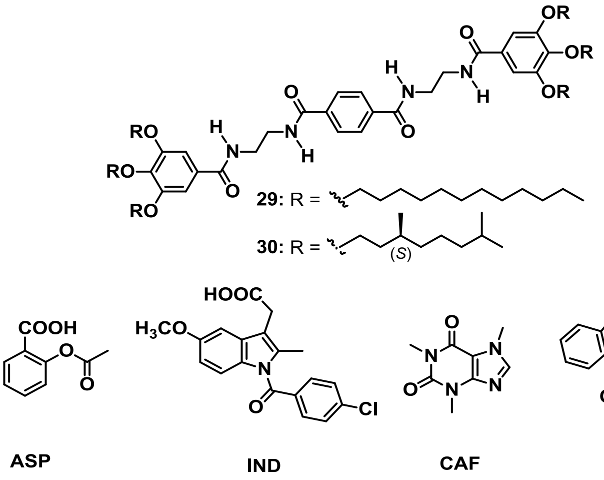

CD experiments of **30** in MCH show a bisignated Cotton effect that disappears at 363 K but shows a non-sigmoidal recurrence upon cooling, indicative of a cooperative behaviour (Fig. 11a).[92] The fitting of the extracted melting curve to the nucleation-elongation model[42,43] provides good results, demonstrating that the interplay of directional hydrogen bonding between the amides, aromatic contacts between the π-surfaces and van der Waals interactions between alkyl substituents results in the cooperative formation of helical structures. Similarly to **30**, the self-organization of **29** into helical columnar assemblies results in the formation of colourless gels in toluene. AFM images of these gels formed by **29** and **30** confirm the entanglement of one-dimensional, chiral aggregates into a dense network (Fig. 11b). This gelation ability can be ultimately exploited for the crystallization of pharmaceutical ingredients like aspirin (**ASP**), indomethacin (**IND**), caffeine (**CAF**) and carbamazepine (**CBZ**) (Chart 9). The crystals formed therein are easy to isolate and do not show differences in the polymorphic outcome compared to crystals gained in toluene. On the basis of these findings, related organogelators were synthesized by the same group to investigate how structural variations, affecting the number and type of non-covalent interactions in linear molecules, may modify their self-assembly.[93]

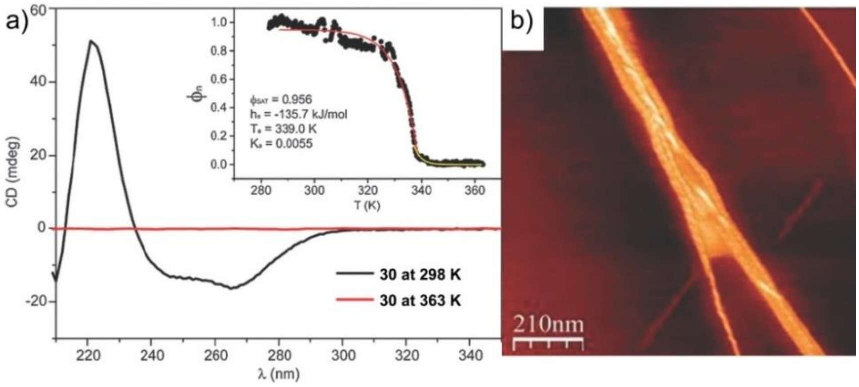

Fig. 11 a) CD spectra of **30** (MCH, 1 x 10^{-5} M). The inset depicts the melting curve from 363 to 283 K at intervals of 1 $Kmin^{-1}$. Red and yellow lines in the inset are the fits corresponding to the elongation and nucleation processes, respectively. b) AFM height image of the diluted (1 x 10^{-5} M, toluene) gel of **30** onto HOPG (z scale = 15 nm). Adapted from ref. 92 with permission of The Royal Society of Chemistry.

Würthner and co-workers have widely studied the self-assembly of perylene bisimides (PBIs).[33,94-97] In 2007, they reported a tetra-bay-substituted PBI **31** (Chart 10) that self-assembles in methylcyclohexane into J-aggregates exhibiting a fluorescence quantum yield near unity.[98] The novel, slipped aggregation pattern originates from the molecular design of this PBI. The sterically demanding bay substituents of **31** induce a twist of the aromatic PBI core assisted by terminal trialkoxyphenyl groups, while a linear arrangement of the dyes is accomplished by hydrogen bonding interactions. The result is the formation of helical fibres in non-polar solvents, as confirmed by UV/Vis absorption, FTIR and ^1H NMR measurements, as well as microscopic studies.

Besides PBI **31**, a second PBI reference compound (**36**) was synthesized that bears a *n*-butyl chain at the imide position (Chart 10). Based on that, this derivative was unable to stabilize self-assembled structures by hydrogen bonding interactions.[40,98]

Studies in MCH proved that **36** exists in its molecularly dissolved state at 10^{-5} M and forms only dimeric species upon increasing the concentration, instead of growing into extended aggregates.

Chart 10 Molecular structure of tetra-bay-substituted perylene bisimides **31**-**36**.

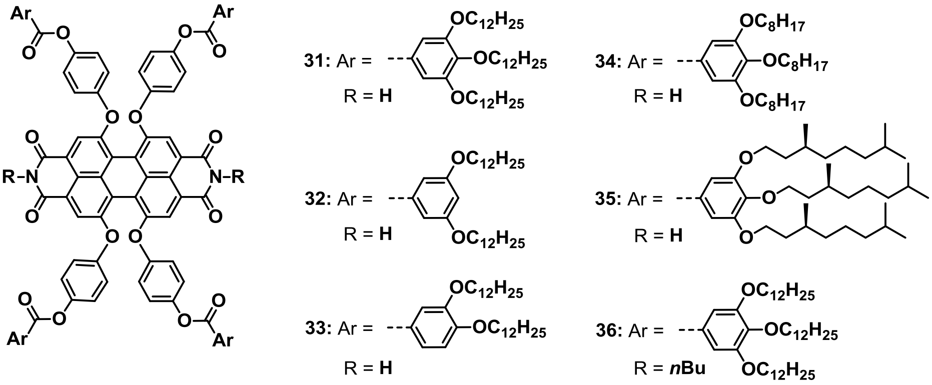

Furthermore, the investigations on the core-twisted PBI motif were extended by synthesizing four more derivatives (**32**-**35**) that differ in the number, length and nature (chiral and non-chiral) of the alkoxy bay substituents (Chart 10).[40] All investigated PBIs **32**-**35** show comparable spectroscopic characteristics with a strong J-aggregation tendency in MCH, similarly to the previously reported example of **31**. The aggregation strength for the self-assembly in MCH at 10^{-5} M was largely influenced by the side chains attached to the bay substituent. Unfortunately, stable aggregation down to a concentration of 10^{-8} M precludes further characterization of the self-assembly mechanism of **31**-**34** by concentration-dependent measurements. However, the branched alkyl chains of chiral **35** cause a reduced aggregation tendency enabling a further characterization of the system. Similarly to the temperature-dependent studies, the concentration range from 10^{-5} M to 10^{-7} M in MCH provided the complete transition from aggregated to monomeric species (Fig. 12). The plot of α_{agg} against Kc_T revealed a non-sigmoidal shape (Fig. 12, inset), characteristic of a cooperative process. Applying the K_2/K nucleation-elongation model to the spectral data enabled a manual fitting for the best match with σ values in the range of 10^{-5} to 10^{-6}, corroborating a highly cooperative process. The binding constant K_2 for the unfavourable dimerization step of **35** could be defined to be 13±11 M^{-1} while the subsequent elongation constant K has a remarkably higher value of $2.3\pm0.1 \times 10^{6}$ M^{-1}, due to the interplay of π-π and hydrogen bonding interactions between the cooperatively aggregating molecules. These attractive forces lead for chiral **35** to the creation of helical arrangements in MCH, as indicated by CD studies.

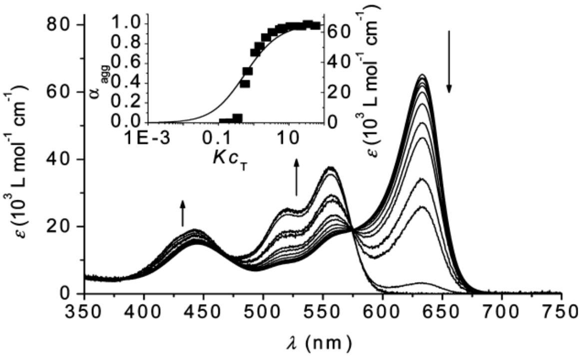

Fig. 12 Concentration-dependent absorption spectra of chiral **35** in MCH (c = 7.3 x 10^{-5} to 1.9 x 10^{-7} M). Arrows indicate the spectral changes with decreasing concentration. Inset: Change of absorption at λ = 633 nm (black squares) with decreasing concentration; the curve shows the resulting fit calculated according to the isodesmic model. Reprinted with permission from ref. 40. Copyright (2009) American Chemical Society.

Comparing the cooperative self-assembly of PBIs **31-35** with the dimerization of imide-substituted **36** that lacks contribution from hydrogen bonding, one can clearly recognize that the cooperativity in the aggregation process is induced by simultaneous participation of π-π and hydrogen bonding interactions in MCH.[40,98]

Recently, Würthner, Lochbrunner and co-workers investigated a structurally related core-twisted PBI **37** substituted with butylphenoxy substituents at the bay and bulky benzamide groups at the imide position (Chart 11).[99]

Chart 11 Molecular structure of tetra-bay-substituted PBI **37**.

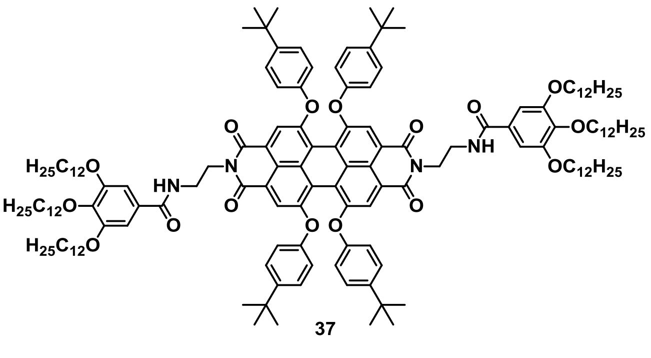

37

The amide spacers in **37** enable hydrogen bondings that support the aromatic attraction between the PBI cores, giving rise to a strong aggregation in MCH.[99] This self-assembly process shows a biphasic temperature dependence, as visualized by fluorescence studies of **37**, shown in Fig. 13a. Upon decreasing temperature from a fluorescent, molecularly dissolved state (90 °C) to 40 °C a simultaneous red-shift, decrease and broadening of the emission band can be detected that is accompanied by a drop of the fluorescence quantum yield by a factor of 2. However, upon further cooling to room temperature the emission is again blue-shifted and largely recovered with a significant increase of the quantum yield.

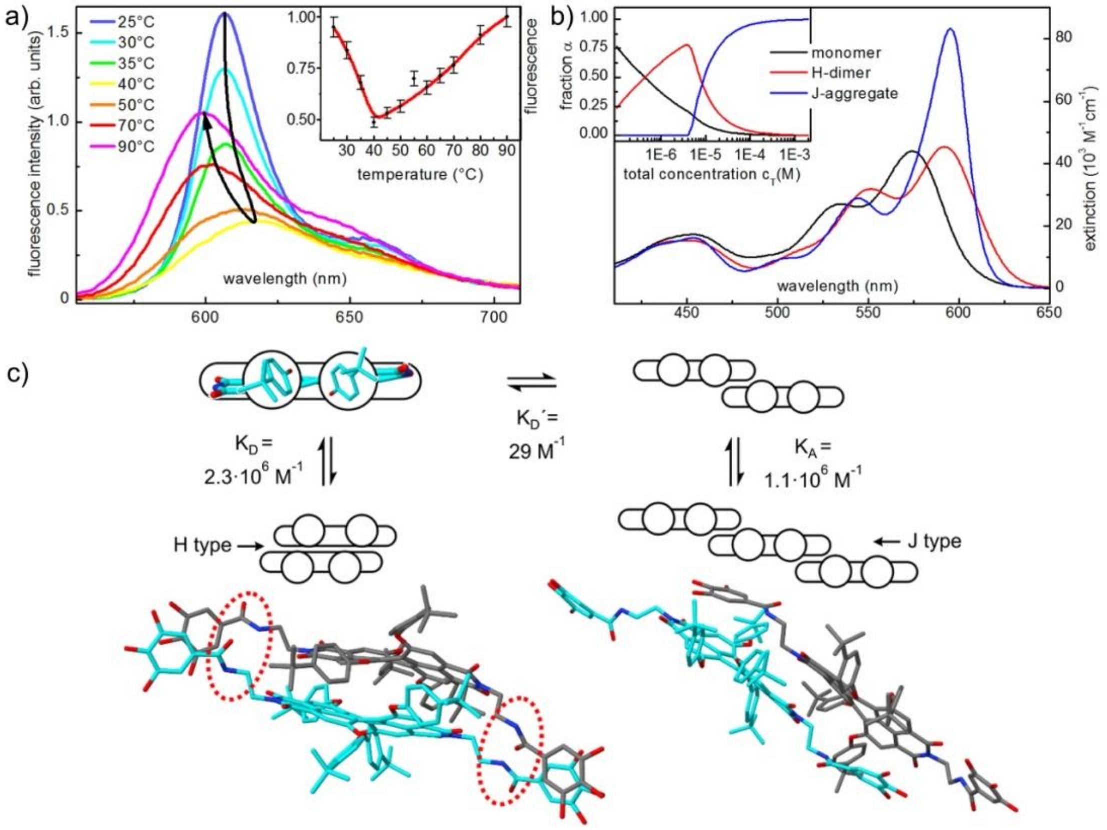

Fig. 13 a) Temperature-dependent fluorescence spectra and normalized integrated yield (inset) of PBI **37** in MCH at c = 0.02 mM. The red line serves as guide to the eye. b) Spectra of the monomer, favoured H-dimer and larger J-aggregates extracted from the aggregation model. The inset shows the fraction of monomers, molecules in the favoured H-dimer and molecules in J-aggregates as a function of the total dye concentration. c) Proposed aggregation model and calculated structures of the favoured dimer and the dimer acting as nucleus for the aggregates. Adapted with permission from ref. 99. Copyright (2013) American Chemical Society.

These changes, supported by quantum chemical calculations, could be attributed to the presence of two distinct self-assembled species, characterized by an initial "aggregation-induced quenching", followed by an "aggregation-induced emission" upon enlargement of the aggregated system.[99] A comparable, biphasic process could also be observed for variable-concentration studies in MCH. Combining all spectral features, the authors concluded that at intermediate temperature or concentration, hydrogen-bonded dimers with an H-type arrangement exist (suggested hydrogen bonds are highlighted as red circles in Fig. 13c). This stacked organization of the molecules makes the dimer formation energetically favourable, as evidenced by the high dimerization constant K_D (Fig. 13c), but simultaneously precludes a further growth of the structure. Consequently, at lower temperature or higher concentration a second, sterically less restricted J-type dimer is formed. This new, laterally-shifted organisation results in a reduced stabilization by hydrogen bonds and π-π contacts, as it becomes apparent in the low association constant K_D'. However, it facilitates a subsequent elongation of the system into J-type aggregates, as indicated by a binding constant $K_A >> K_D$'. Due to the biphasic behaviour, it is not possible to apply the data to a distinct aggregation model. However, regarding only the J-type aggregation pathway, the comparison of the equilibrium constants ($K_A >> K_D$'), as well as the plot of α against the total concentration (blue line in Fig. 13b), characterized by an abrupt increase in J-aggregated species upon reaching a certain concentration, is clearly indicative of a cooperative process.

Yagai and co-workers synthesized in 2011 monotopic melamines with two PBI chromophores attached via an alkyl spacer at the secondary amino groups and achiral (**40**) or chiral ((*S*)-**38** and (*R*)-**39**) substituents at the tertiary amino group (Chart 12).[100] The focus of their work was the investigation of a 3:1 mixture of the functionalized melamines and tritopic cyanuric acid (**CyA**). The monomeric complexes (**38_3*CyA** to **40_3*CyA**) are stabilized by multiple hydrogen bonding interactions between the central **CyA** unit and the melamine moieties of three linear molecules (**38-40**) (indicated by the arrows around **CyA** in Chart 12). This arrangement is supported by π-π interactions between the aromatic PBI surfaces, creating supramolecular disks (Fig. 14, left).

Chart 12 Molecular structure of the functionalized melamines **38-40** and the tritopic cyanuric acid.

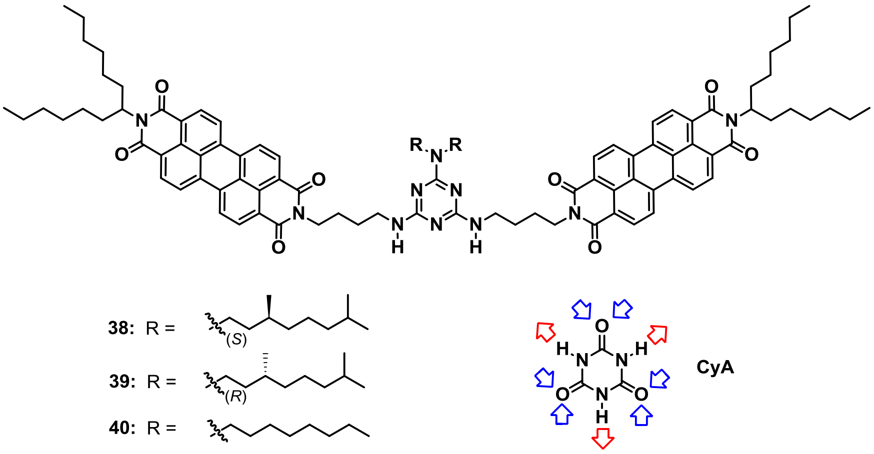

The self-assembly of these complexes in MCH was investigated by CD studies.[100] The titration of (*S*)-**38** with **CyA** revealed saturation in CD intensity at a 3:1 ratio of (*S*)-**38** : **CyA**. The same stoichiometry was observed for experiments with the enantiomer (*R*)-**39** giving rise to CD signals of opposite sign, indicative of helical structures of opposite handedness. Due to the discotic 3:1 geometry of one complex, it is suggested that the periphery of the helix consists of three rotating stacks of interacting PBI pairs while the **CyA** subunits constitute the central core, leading to an embedding of the chiral substituents in the inner part of the arrangement (Fig. 14).

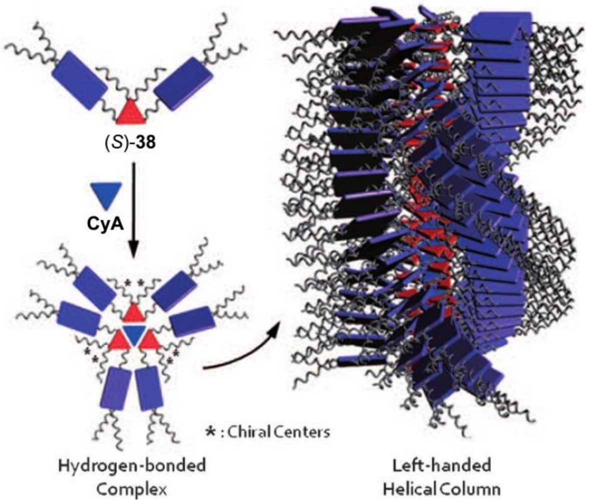

Fig. 14 Schematic representation of a proposed helical columnar structure formed from hydrogen-bonded complex **38$_3$*CyA**. Adapted with permission from ref. 100. Copyright (2011) Wiley-VCH Verlag GmbH & Co. KGaA, Weinheim.

The π-π interactions between the PBI units are confirmed by flash-photolysis time resolved microwave conductivity measurements affording mobility values indicative of extended π-stacks.[100] The dense helical architecture results for **38_3*CyA** (concentration of (*S*)-**38** > 20 mM) in the formation of a highly viscous solution in MCH that finally turns into gel after some weeks of aging. The gel morphology consists of fibres with a uniform width of 10 nm and a height of 2 nm that further organize into thicker bundles, as visualized by AFM and TEM imaging of a diluted sample. This behaviour differs from that of the individual ligand (*S*)-**38** that is not able to form gels in these aliphatic solvents.

Temperature-dependent CD studies of a diluted solution of **38_3*CyA** in MCH revealed a non-sigmoidal melting curve indicative of a cooperative aggregation that is driven by π-stacking and hydrogen bonding interactions.[100] Although the authors did not further focus on the cooperative nature of the self-assembly process, this exciting behaviour points out, along with recent examples from the groups of Würthner[40,101] and Meijer[102], that the self-assembly of PBIs is not exclusively limited to their usual, non-cooperative aggregation mechanism.[97,103,104]

These studies of Yagai and co-workers have been followed by other hydrogen bonded systems based on various classes of dyes.[105-108] In an interesting example, the creation of columnar structures by complex formation of a monochromophoric **CyA**-functionalized PBI derivative and melamine was explored.[109] Concentration-dependent absorption studies of a 1:1 mixture of these building blocks in chloroform revealed a cooperative process, when the data was fitted to a nucleation-elongation model[32].

The following example shows that also hydrogen bonding interactions as sole non-covalent forces can lead to cooperative phenomena, as previously illustrated in the introduction of this chapter. In this context, Bouteiller and co-workers have extensively focused on the self-assembly behaviour of bis-urea derivatives. Initial investigations of branched bis-urea derivative EHUT **45** (Chart 13) revealed its involvement in the formation of one-dimensional assemblies.[110,111] This self-assembly is driven by cooperative hydrogen bonding between two adjacent monomers resulting in viscous solutions in CCl_4 and toluene.

Due to the unique characteristics of bis-ureas, the studies were extended in 2003 by designing several bis-urea derivatives (**41**-**51**) with variations concerning the side groups and the position of the methyl group attached to the central phenylene ring (Chart 13).[112] Investigations on these molecules should reveal how slight structural changes may affect their self-assembly in organic media. Solvent-dependent studies show that the relative viscosity of EHUT (**45**) solutions increases upon lowering the polarity from chloroform to dodecane, as a result of stronger hydrogen bonding interactions within the assemblies. Monitoring free N-H vibrations by FTIR studies of EHUT (**45**) and its mono-urea counterparts (**52** and **53**) disclosed the formation of cooperative supramolecular structures in chloroform ($CDCl_3$) (Fig. 15), however, the cooperative effect for the mono-ureas is significantly weaker.

Chart 13 Molecular structure of the bis-urea derivatives **41-51** and the mono-urea derivatives **52-53**.

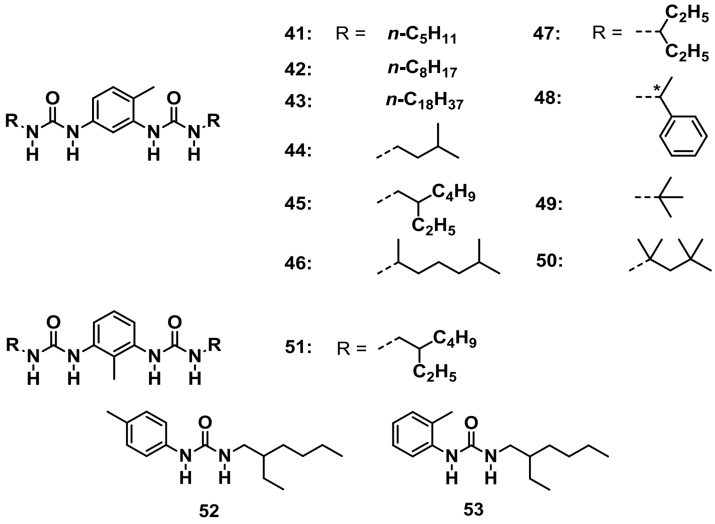

The cooperative character of EHUT (**45**) can be explained as follows: as can be observed in Fig. 15, the association of the two urea functions in one molecule does not occur independently, as for the mono-ureas a 100-fold higher concentration is needed to obtain the transition from monomeric to aggregated species (instead of a factor of 2).[112] Furthermore, the significant sharp curve for this transition of EHUT (**45**) could be successfully fitted to the non-isodemic two-constant model (K_2, K) giving rise to the thermodynamic K/K_2 value. This parameter also revealed slight cooperativity for the mono-ureas due to polarization effects upon dimer formation, but to a much lower extent. The cooperative behaviour of EHUT (**45**) can also be confirmed by comparing the calculated weight and number average degree of polymerization at given concentrations of **45** with an isodemic reference compound, that clearly reveals significant differences between the systems.

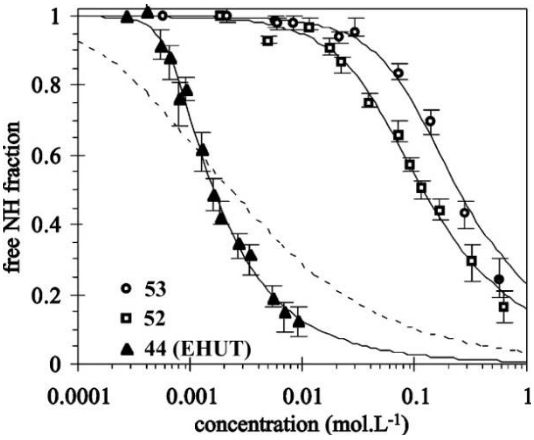

Fig. 15 Fraction of free NH groups of bis-urea EHUT (**45**) and model mono-ureas **52** and **53**, versus concentration in $CDCl_3$, at room temperature. The full curves are calculated with the non-isodesmic model. The dotted curve is the best fit of the EHUT (**45**) data to the isodesmic model. Adapted with permission from ref. 112. Copyright (2003) American Chemical Society.

In 2004, the class of bis-ureas was broadened by designing dissymmetrical systems based on 2,4-toluene diisocyanate, showing that the tendency to self-assemble decreases when the number of hydrogen bonding NH-groups is reduced.[113]

Following that, further inspection of EHUT (**45**) in toluene showed an unexpected viscosity behaviour with a sudden steep decrease around 40 °C, as depicted in Fig. 16.[114] FTIR measurements show hydrogen-bonded urea functions over the complete temperature range, ruling out a disassembly of the sample upon heating. However, slight changes in the N-H vibration band above 40 °C indicated a rearrangement of the urea moieties into less ordered assemblies. This structural change can also be monitored by small-angle-neutron scattering (SANS) studies revealing a morphology transition from thick into thinner and shorter filaments. All these changes are reversible and occur in a very narrow temperature range of 5 °C suggesting that this molecular rearrangement is highly cooperative. This can be supported by a perfect fitting of the FTIR data to the model for structural transitions in linear assemblies by van der Schoot *et al.*[115,116], providing a considerably high degree of cooperativity (very low σ value of ~3.9×10^{-5}). The structural transition can also be induced and tuned by dilution in toluene, solvent changes and by mixing of two bis-urea derivatives.[114]

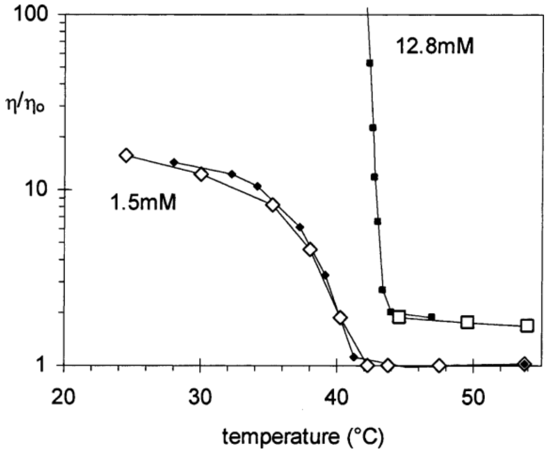

Fig. 16 Relative viscosity of EHUT (**45**) solutions in toluene against temperature. Heating run (open symbols); cooling run (full symbols). Reprinted with permission from ref. 114. Copyright (2005) American Chemical Society.

After the application of EHUT (**45**) as racemic mixture in various reports, the same authors compared its self-assembly with the behaviour of the enantiopure monomers (**54** and **55**, Chart 14).[117]

Chart 14 Molecular structure of the bis-urea derivatives EHUT-*SS* **54** and EHUT-*RR* **55**.

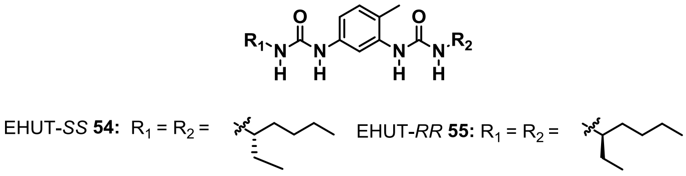

As can be observed in Fig. 17, CD spectroscopy in cyclohexane showed a significant Cotton effect for EHUT-*SS* (**54**) that represents the mirror image to the EHUT-*RR* (**55**) spectrum.[117] The opposite sign of the signal clearly indicates that the chirality of the side-chains dictates the handedness of the self-assembled structures. Majority-rules experiments showed that a distinct handedness, which was absent for individual EHUT-*rac* (**45**) solutions, can be induced upon addition of a chiral counterpart in a slight enantiomeric excess without influencing the cooperativity of the system. Moreover, the dissolution of EHUT-*rac* (**45**) in chiral solvents (*S*)- and (*R*)-limonene also showed the corresponding Cotton effect indicating that the solvent molecules can act as chiral regulator for the helical assemblies.

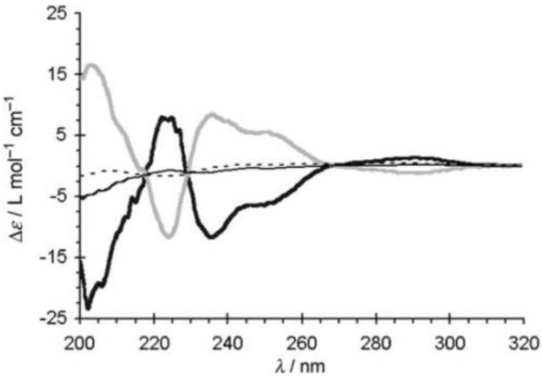

Fig. 17 CD spectra of 1 mM solutions in cyclohexane of: EHUT-*SS* (**54**) at 20°C (bold black line); EHUT-*RR* (**55**) at 20°C (bold grey line); EHUT-*SS* (**54**) at 60°C (black line) and EHUT-*rac* (**45**) at 20°C (dashed black line). Reproduced with permission from ref. 117. Copyright (2010) Wiley-VCH Verlag GmbH & Co. KGaA, Weinheim.

2.4.2 *π-π* and metal-metal interactions

The unique properties of metal complexes have been exploited in different research fields, with particular emphasis on supramolecular chemistry. The ability of metal complexes to form self-assembled structures by various non-covalent interactions, often supported by metal-metal interactions, leads to materials with remarkable optical, electrochemical, redox and other fascinating properties.[8,11,12,118-121] Strong interactions among closed-shell metal ions have been extensively utilized by several research groups to create 1D crystalline or soft materials.[10,122-124] For instance, trinuclear Au(I) pyrazolate complexes have been reported by Aida and co-workers to form stable organogels that show a luminescence colour switch from red to blue to green upon simple addition of silver cations and heating.[125] Interestingly, a structurally related Cu(I) pyrazolate complex was investigated that can be applied in security technology for rewritable media.[126] This complex exhibits a dichroic luminescence character that can be controlled by kinetic or thermodynamic self-assembly. The groups of Yam, Che, De Cola and Strassert, among others, have exhaustively investigated Pt(II) complexes due to their ideal square-planar geometry and intriguing properties, as also described in recent exciting examples.[18,127-135]
Although extensive efforts have been devoted to the characterization of supramolecular systems based on metal-metal interactions in the last decade, it was not until 2013 when the quantitative contribution of these weak forces to supramolecular polymerization processes was examined.[136]

Chart 15 Molecular structure of the Pd(II) complex **56** and the counterpart without metal centre **57**.

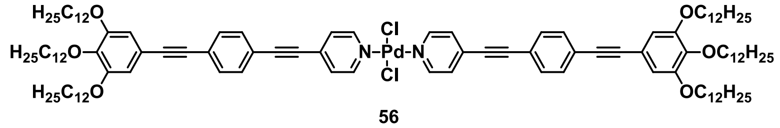

56

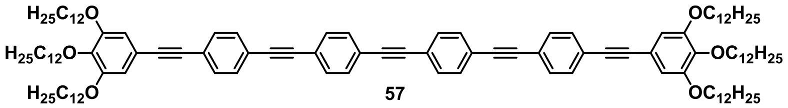

57

In this regard, our group reported an OPE-based Pd(II) pyridyl complex **56** (Chart 15) that shows a significant colour change in MCH from colourless to greenish yellow upon cooling down from a molecularly dissolved (50 °C) to an aggregated state (room temperature) (Fig. 18a, photographs).[136] Detailed investigations of the aggregation process by temperature-dependent UV/Vis absorption studies revealed the appearance of a red-shifted band at room temperature, covering the spectrum up to 470 nm (Fig. 18a). This band can be ascribed to cooperative metallophilic interactions involving the Pd(II) centres and π-π interactions between the OPE cores. The cooling curve of **56** at 415 nm possesses a non-sigmoidal shape indicative of a cooperative aggregation phenomenon (Fig. 18b). Fitting these data points to the nucleation-elongation model developed by ten Eikelder, Markvoort, Meijer and co-workers[44,45] gave a perfect match with a significant degree of cooperativity (σ = 3.5 x 10^{-5}). Similar results were obtained by concentration-dependent studies of **56** in MCH. Successful application of the cooperative *Goldstein-Stryer*-model[34,39] to the self-assembly process confirmed its highly cooperative character.

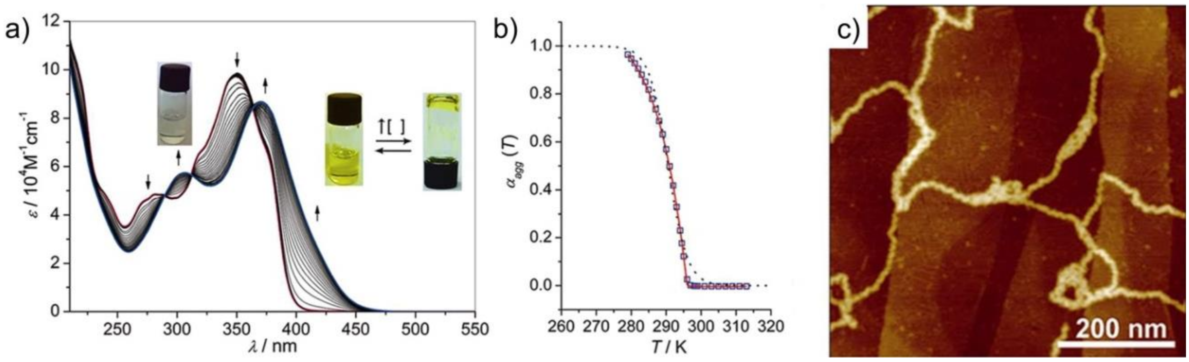

Fig. 18 a) Temperature-dependent UV/Vis absorption experiments of **56** (MCH, 1.6 x 10^{-4} M, 343 to 278 K). Arrows indicate the spectral changes upon decreasing temperature. b) Fitting of α_{agg} at 415 nm to the *ten Eikelder-Markvoort-Meijer*-model. c) Height AFM image obtained upon spin-coating a solution of **56** (MCH, c = 8 x 10^{-4} M) on HOPG. Adapted with permission from ref. 136. Copyright (2013) American Chemical Society.

To get closer insight into the quantitative influence of Pd···Pd interactions on the cooperative self-assembly, an OPE derivative **57** exhibiting same size and shape as complex **56** was synthesized, but the metal centre was replaced by an alkyne function.[136] Variable-temperature UV/Vis absorption studies show a comparatively slight bathochromic shift of the absorption maximum upon aggregation, clearly indicating that the red-shifted band in case of Pd(II) complex **56** stems from the participation of the Cl-Pd(II)-Cl units in intermolecular bonding. Moreover, the aggregation mechanism of **57** could be characterized as isodesmic, further suggesting that cooperativity in the Pd(II) system **56** arises from metallophilic Pd···Pd interactions, most likely reinforced by *π-π* stacking. This assumption was supported by density functional theory (DFT). These calculations revealed a simultaneous *σ*-bond between the Pd centres and two Pd-Cl interactions that involve different monomeric units. As shown in Fig. 18, the increased stability based on these interactions also becomes visible in microscopic studies (AFM) revealing extended associates for **56**. In contrast to these assemblies, the metal-free counterpart **57** aggregates into considerably smaller and lower-ordered rod-like structures.

Recently, the group of Wang reported the self-assembly of rod-like platinum(II) acetylide complexes into extended supramolecular aggregates.[137] These molecules contain two amide groups and terminal linear achiral (**58**) or chiral (**59**) alkyl chains (Chart 16).

Chart 16 Molecular structure of Pt(II) acetylide complexes **58** and **59**.

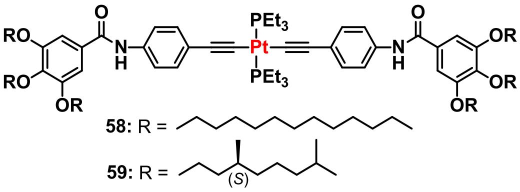

The assemblies of **58** are able to form gels in non-polar solvents accompanied by a gelation-induced emission enhancement.[137] Detailed ^{1}H NMR studies show that the polymerization is originated from simultaneous intermolecular hydrogen bonding and *π-π* interactions between the subunits. Furthermore, the self-assembly of **59** into helical structures was identified as cooperative growth, as the successful fitting to the *van der Schoot*-model[42,43] with a K_a value of 4×10^{-4} shows. However, the contribution of metal-metal interactions in the self-assembly of the complexes is not discussed. Although it is known that bulky groups attached to the Pt centres hinder the realization of the metal-metal interactions,[138] it cannot be ruled out that the $Pt(PEt_3)_2$ centres can come close enough to participate in non-covalent interactions.

2.4.3 Metal-ligand and *π*-*π* interactions

In the following section, a special kind of cooperative process will be described, which stems from the interplay of metal-ligand and intramolecular *π*-*π* interactions and can thus be characterized as "supramolecular chelation based on folding".[139,140]

In this regard, Moore and co-workers investigated the coordination of five mono-functionalized *m*-phenylene ethynylene (*m*PE) oligomers **60**-**64** (Chart 17) to a palladium centre and the tendency of the resulting complexes to organize in a folded conformation.[139] The authors based their studies on previous investigations by Nelson *et al.* on the affinity of elongated phenylacetylene oligomers to cooperatively adopt a stable helical conformation by interstrand contacts.[141] Nelson *et al.* were also able to determine the critical chain length for *m*PE derivatives required for helical stability, which were at least 7-8 aromatic units per molecule. The oligomer folding was confirmed by the group of Moore in 1999.[142] They presented the fitting to the helix-coil equilibrium model[143] supporting the cooperative conformational transition by intramolecular aromatic stacking and solvophobic effects.

The *m*PE derivatives **60**-**64** published in 2005 by Moore and co-workers consist of aromatic scaffolds of 1 to 9 rings, terminated at one end with a pyridine group as metal ligating moiety (Chart 17).[139]

Chart 17 Molecular structure of the *m*PE derivatives **60-64**.

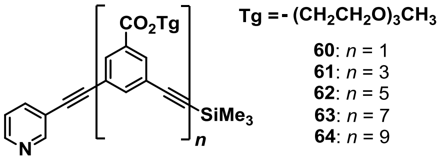

The coordination of the *m*PE derivatives to palladium dichloride results in the formation of 2:1 *trans*-complexes of square-planar geometry.[139] As monitored by ^{1}H NMR studies, the complexation of the monomer **60** and the pentamer **62** with *trans*-Pd(MeCN)$_2$Cl$_2$ shows distinct differences. The 2:1 complex formed by ligand **60** exists in a still unfolded state, while for the complex of **62** a tremendous broadening of the ^{1}H NMR signals in the aromatic region clearly indicates a folded conformation (Fig. 19a).

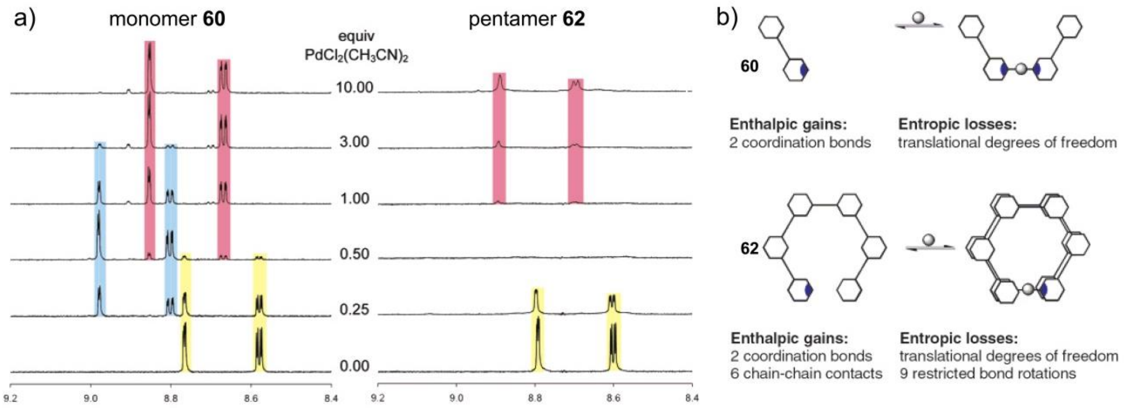

Fig. 19 a) ^{1}H NMR spectra of monomer **60** and pentamer **62** (c = 1 mM) with varying equiv. of $PdCl_2(CH_3CN)_2$ in CD_3CN. Resonances coloured as follows: free ligand (yellow), 2:1 complex (blue), and 1:1 complex (red). b) Simplified model of the thermodynamics of complexation. Adapted with permission from ref. 139. Copyright (2005) American Chemical Society.

These distinct characteristics are consistent with former findings of a critical chain length, indicating that the elongation of the meta-linked aromatic backbone upon coordination of **62** to Pd(II) activates the self-assembly of the 2:1 complex into helices with six repeat units per turn[144].[139] This folding can be partially rescinded by the addition of an excess of Pd(II), resulting in a reorganization of the ligands into 1:1 complexes. These complexes do not reach the required critical length for **60** just as for **62**. Upon closer inspection of the ^{1}H NMR data, a significant difference in the behaviour of **60** and **62** becomes noticeable that indicates positive cooperativity for the pentamer. While after addition of 0.5 equiv. of Pd(II), the monomeric species, 2:1 and 1:1 complexes coexist for **60**, in the case of **62** the exclusive formation of the folded 2:1 assembly occurs. Furthermore, in the presence of an excess of Pd(II) the 1:1 complex dominates for **60**, while the majority of **62** persists in the 2:1 assemblies indicating an increased stability of this species. This evidence for cooperativity of **62** was further proven by isothermal titration calorimetry (ITC). This technique enables the calculation of the thermodynamic parameters, as well as the association constants for the coordination of the first (K_1) and second (K_2) ligand to the metal centre. In contrast to the short oligomers **60** and **61**, a K_2 value greater than K_1 can be defined for the folding species **62-64**. This indicates a cooperative process, similarly to a chelating effect[145,146] as suggested by the authors. Regarding the coordination of the second ligand to a Pd(II) centre, the enthalpic and entropic contributions revealed significant differences between the oligomers of different length that did not occur for the first step (Fig. 19b). This can be explained by considering that the first coordination step only represents the formation of a new metal-nitrogen bond. This process is equal for all *m*PEs, while the second step includes the second metal-ligand bond formation and the folding of the 2:1 assemblies of different length.

Shortly after these studies, Moore and co-workers investigated similar bis-functionalized *m*PE molecules (**65-67**) with two terminal pyridyl groups per molecule (Chart 18).[140]

Chart 18 Molecular structure of the bis-functionalized *m*PE derivatives **65-67** and the linear reference compound **68**.

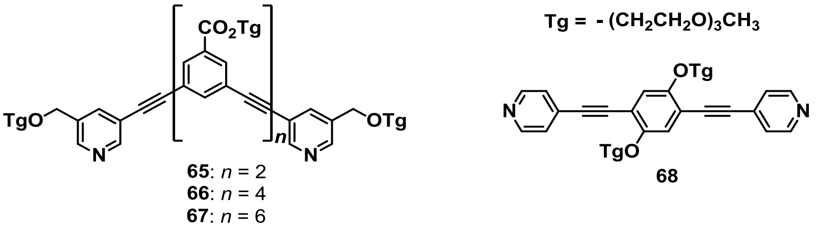

65: *n* = 2
66: *n* = 4
67: *n* = 6

68

Similarly to the previous example, the addition of Pd(II) to **65-67** results in the creation of different supramolecular structures.[140] For the hexameric derivative **66** columnar assemblies were formed. This architecture originates from the isodesmic stacking of 2:2 (**66**:Pd(II)) macrocycles, as a result of a perfect fit of the hexamer length into such unstrained cyclic structures (Fig. 20). However, the addition of Pd(II) to the tetramer (**65**) or octamer (**67**) induces polymerization into helical arrangements. The formation of these assemblies can be described by a nucleation-elongation mechanism involving cooperative ligand-Pd(II) and interstrand π-π interactions, as illustrated in Fig. 20.

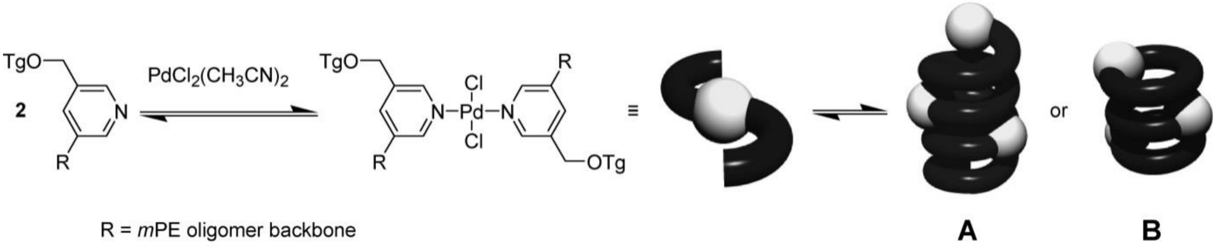

Fig. 20 Palladium-pyridine binding to form a metal-ligand complex followed by subsequent “monomer” additions to form a supramolecular foldamer (A) or a π-stacked columnar polymer (B). Reprinted with permission from ref. 140. Copyright (2006) American Chemical Society.

Regarding this process, the essential number of coordination steps to reach the suitable nucleus size depends on the oligomer length, since the elongation does not start until the folding of the chain occurs.[140] Similar experiments for a reference compound **68** show that changing the linkage of the oligomer scaffold from *meta* to *para* results in the formation of linear assemblies, now following a non-cooperative growth.

These diverse polymerization mechanisms highlight that the self-assembly of these coordinating oligomers can be controlled by the length, as well as the geometry of their aromatic backbone.

2.4.4 Dipole-dipole/zwitterionic interactions and other contributions

Dipole-dipole interactions arise from electrostatic interactions of polar molecules due to their ground state dipole moment μ_g. These highly attractive interactions lead to preferred antiparallel arrangements in a dimer species in a so called “sandwich-type” orientation.

A great deal of effort was dedicated by Würthner and co-workers to study the properties and the self-assembly of dipolar merocyanine (MC) dyes.[147-154] In their seminal work of 2003, they described the first example of a hierarchical supramolecular polymer based on MC dyes by synthesizing a bis(MC) derivative **70** (Chart 19).[155] This molecule contains a tridodecyloxybenzyl unit that allows its dissolution in a large variety of organic solvents. The behaviour of **70** was compared with a reference compound **69** that features a single MC chromophore, likewise decorated with this solubilizing substituent.

Chart 19 Molecular structure of the MC derivative **69** and the bis(MC) molecule **70**.

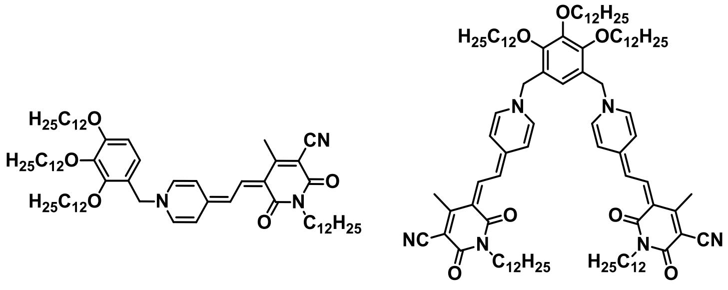

69 **70**

Whereas reference mono-MC **69** self-assembles into dimeric aggregates in nonpolar media, a more complex solvent-dependent behaviour was observed for the bis(MC) **70**.[155] For this target compound different assemblies (dimers and extended H-type species) appear, as characterized by distinct absorption bands (Fig. 21a). While at 10^{-5} M for a dichloromethane solution of **70** a monomer spectrum with λ_{max} = 570 nm (M band) can be observed, in trichloroethylene the band is hypsochromically shifted to λ_{max} = 480 nm. These characteristics in trichloroethylene can be assigned to a dimerization of MC units (D band) that results for the bis(MC) in an extended polymer chain. However, upon further decreasing the polarity to tetrachloromethane or methylcyclohexane, a sharper and further hypsochromically shifted H-band appears (λ_{max} = 447 nm) indicating an extended aggregation of the self-assembled strands.

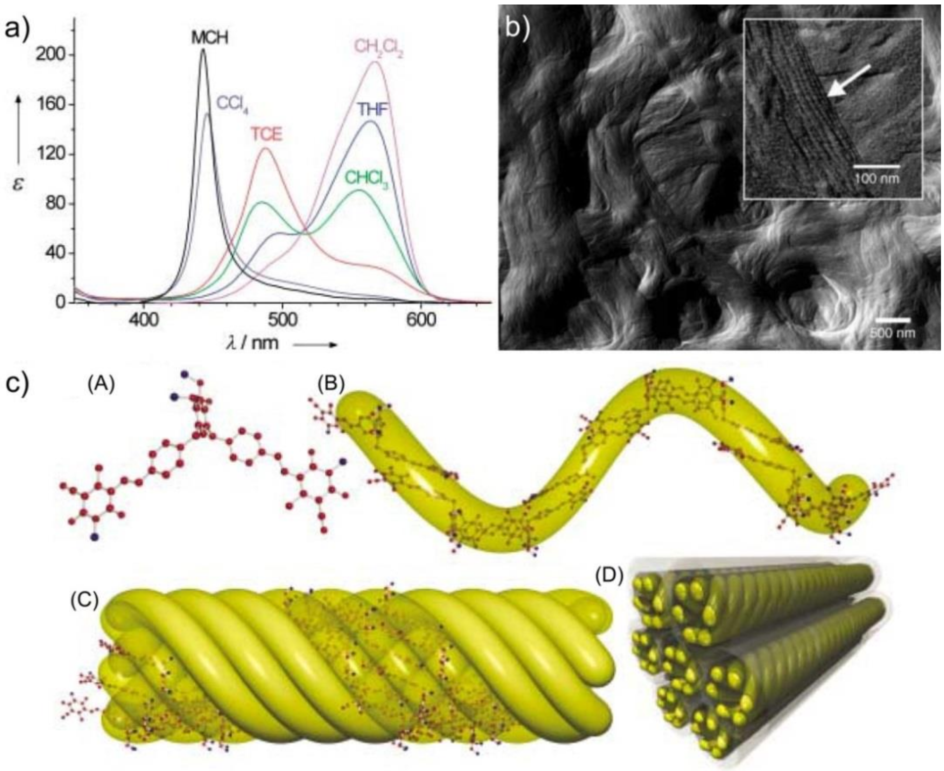

Fig. 21 a) Solvent-dependent UV/Vis absorption spectra (ε in 10^3 $M^{-1}cm^{-1}$, c = 10^{-5} M) of **70** at 293 K. b) Cryo-TEM picture of a gel of **70** in *n*-hexane (c = 6.5 x 10^{-3} M). The inset shows a magnification of the rod aggregates. c) Model for the hierarchical growth of the assemblies of **70**: (A) force-field-optimized molecular structure of **70**; (B) helical supramolecular polymer of **70** formed by dipolar aggregation of the MC units; C) rod-type H-aggregate formed from six helical polymeric strands; D) hexagonal arrangement of the columns. For clarity and ease of calculation, all dodecyl chains have been replaced by methyl groups. Adapted with permission from ref. 155. Copyright (2003) Wiley-VCH Verlag GmbH & Co. KGaA, Weinheim.

The distinct stages of self-assembly are depicted in Fig. 21c: the monomeric bis(MC) **70** initially self-assembles into a one-dimensional strand due to dipolar aggregation of the MC units of one molecule with neighbouring dyes.[155] These polymeric assemblies adopt a helical conformation and can further bundle into thicker fibres consisting of six filaments. The subunits in these sophisticated aggregates show an H-type packing in an antiparallel orientation. Further entanglement of these fibres is responsible for the gelation of MCH at high concentrations of **70** and the formation of highly ordered supramolecular structures (Fig. 21b).

To analyse the contribution of dipole-dipole interactions to the supramolecular growth, the same group reported the self-assembly of a related bis(MC) dye series in which the substitution pattern was changed from *meta* to *para* (Fig. 22c).[156] These bis(MC) compounds exhibit a linear (**71**, **72**) or branched alkyl chain (**73**) on the terminal rings. For **73** the monomeric form dominates over a large concentration range as a result of high solubility and steric effect, introduced by the branched chains. In contrast, molecules with linear substituents were identified as the first example of MC dyes to show a cooperative supramolecular polymerization based on dipole-dipole and van der Waals interactions. The temperature-dependent UV/Vis absorption studies for **71** and **72** in chloroform reveal an almost identical behaviour of the dyes. The spectra show a blue-shift of the absorption maximum from 589 to 462 nm when the temperature is decreased (as depicted in Fig. 22a for **72**) or the concentration is increased. These spectral changes are characteristic for an antiparallel arrangement of the MC chromophores with H-type excitonic coupling.

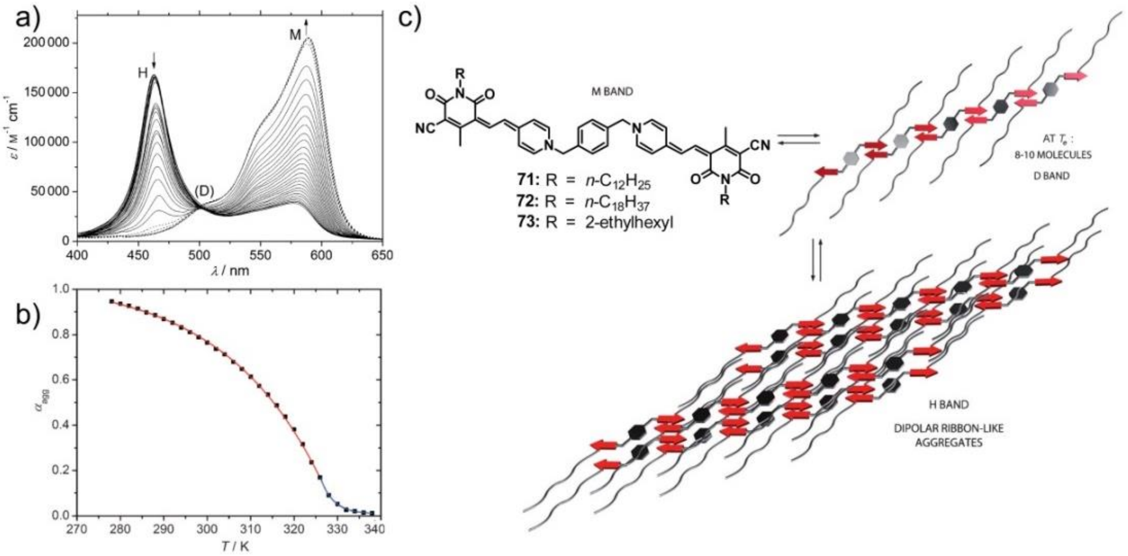

Fig. 22 a) Temperature-dependent UV/Vis absorption spectra of **72** ($CHCl_3$, c = 3.1 x 10^{-6} M) from 278 to 338 K. Arrows indicate the spectral changes upon increasing temperature. M and H denote the monomeric and H-aggregated species, respectively, whereas D corresponds to the intermediate (thermodynamically disfavoured) antiparallel dimeric aggregate species. b) Fitting of α_{agg} against T in the framework of the nucleation-elongation model by van der Schoot. Black squares represent the experimental data of **72** obtained in temperature-dependent experiments at λ = 589 nm. The blue line corresponds to the nucleation and the red line to the elongation regime. c) Proposed self-assembly model for bis(MC) dyes **71** and **72**. Adapted with permission from ref. 156. Copyright (2013) Wiley-VCH Verlag GmbH & Co. KGaA, Weinheim.

Detailed inspection of the spectral features associated to the self-assembly of **71** and **72**, respectively, discloses abrupt changes upon reaching a certain temperature or concentration (Fig. 22a,b).[156] Remarkably, the successful application of the cooperative nucleation-elongation model by van der Schoot[35,41] to the temperature-dependent data, as well as the fitting of concentration-dependent studies to the *Goldstein-Stryer*-model[39] yields comparable results. The size of the aggregates at the elongation temperature could be defined to be around 8-10 monomeric units that are stabilized by dipole-dipole forces (Fig. 22c). These one-dimensional stacks further grow into 2D lamellae by the interplay of dipole-dipole interactions between the MCs and lateral van der Waals forces between the alkyl substituents.

In a separate work, the same group designed a more sophisticated system based on a Hamilton receptor-tethered bis(MC) **74** (Fig. 23).[157] This molecule shows a biphasic solvent-induced self-assembly into two distinct species, by a sequence of isodesmic and cooperative self-assembly events. The aggregation was thoroughly investigated by means of UV/Vis absorption studies in THF/MCH mixtures of various ratios (Fig. 23a). In pure THF the monomeric species **A** dominates, while the addition of MCH clearly induces aggregation in two steps (species **B** and **C**), as characterized by two distinguishable isosbestic points. These two self-assembly processes were also observed in capillary viscosity measurements shown in Fig. 23a (inset). Initially, the expected enhancement in the reduced viscosity can be noticed upon increasing concentration, followed by a sudden drop-off above a certain concentration, suggesting the appearance of a second species of smaller size.

The UV/Vis absorption spectra at 10^{-5} M from 0 to 70% MCH in THF feature an isosbestic point at 517 nm and correspond to the first transition towards species **B**. The studies show a decrease of the monomer band along with the emergence of a hypsochromically shifted band, indicating the formation of extended H-type aggregates. The data points extracted at a particular wavelength from concentration-dependent UV/Vis absorption studies in THF/MCH = 30:70 perfectly follow a sigmoidal curve that enables a successful fitting to the isodesmic model (Fig. 23b). This fitting gives the value for the single binding constant $K \approx 3.9 \times 10^5$ M^{-1}. Microscopic imaging of species **B** reveals long fibres that can further interact creating extended networks. The model based on these findings shows an antiparallel aggregation of the highly dipolar MC moieties, resulting in a flexible polymer with the aliphatic units pointing towards the surrounding medium (Fig. 23d).

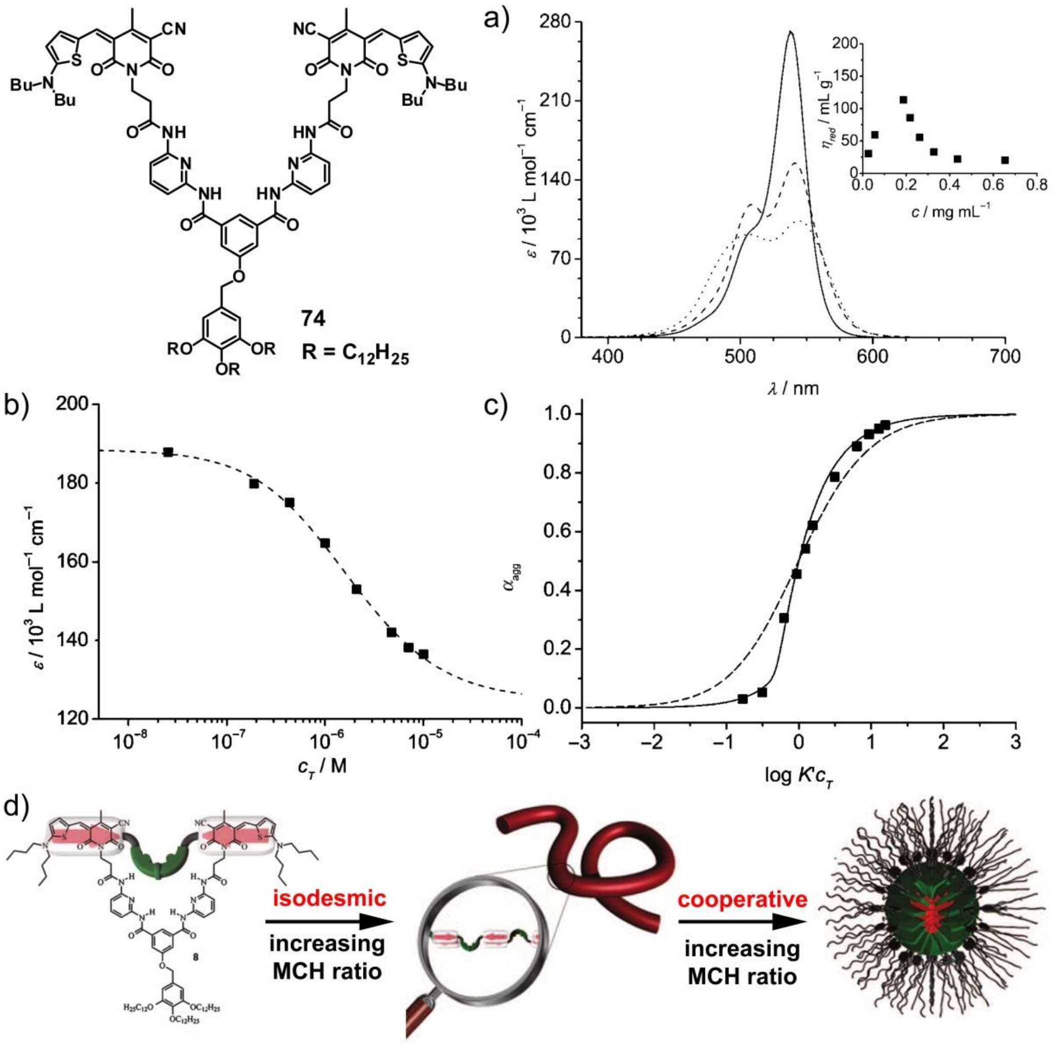

Fig. 23 a) UV/Vis absorption spectra of **74** (c = 1.0 x 10^{-4} M) in THF/MCH mixtures at 298 K. The spectra correspond to the monomers **A** (THF/MCH = 100:0vol%, solid line), and self-assembled species **B** (THF/MCH = 40:60vol%, dashed line) and **C** (THF/MCH = 10:90vol%, dotted line). The inset shows the reduced viscosity η_{red} of **74** in THF/MCH = 40:60vol% at different concentrations. b) Concentration-dependent UV/Vis studies of **74** in THF/MCH = 30:70vol%: Apparent absorption coefficient at 533 nm plotted against c_T and the result of the non-linear regression analysis based on the isodesmic model for the formation of **B**. c) Concentration-dependent UV/Vis studies of **74** in THF/MCH = 20:80vol%: α_{agg} plotted as a function of log$K'c_T$ according to the isodesmic model (dashed curve) and to the self-assembly of a closed oligomer (solid curve) and plot of the experimental data at 507 nm for the formation of **C** after manual fit of the line shape. d) Schematic representation of the solvent-dependent self-assembly of bis(MC) **74**. Adapted with permission from ref. 157. Copyright (2010) Wiley-VCH Verlag GmbH & Co. KGaA, Weinheim.

The second transition (towards **C**) at higher MCH content (above 70% at 10^{-5} M) shows an isosbestic point at 496 nm and a broadening of the spectra, resembling a less ordered state.[157] When this transition is monitored by concentration-dependent studies in THF/MCH = 20:80, a distinctly different, non-sigmoidal curve is found (Fig. 23c). Characterization of the created assemblies **C** by AFM and dynamic light scattering (DLS) revealed a spherical morphology with a diameter of ~9.0 nm. The suggested arrangements are inverted micelles, whereby the dipolar MC units are shielded inside the core, while the alkyl chains are exposed towards the non-polar solvent (Fig. 23d). These findings prompted the authors to apply a cooperative fitting model[30] that includes the formation of closed systems. Indeed, satisfactory fitting supports the presence of closed species that consist of around 20 molecules. These structures are formed by the cooperative interplay of dipolar and hydrogen bonding interactions and are further driven by solvophobic effects as the content of apolar solvent increases.

Schmuck and co-workers have exploited the properties of guanidiniocarbonyl pyrrole carboxylate zwitterions in terms of ion binding, receptor ability and self-assembly.[158-165] In 1999, they reported the formation of highly stable dimers of 5-(guanidiniocarbonyl)-1*H*-pyrrole-2-carboxylate zwitterions in DMSO by multiple weak interactions between the self-complementary binding groups, that was evident from NMR and molecular modelling.[158] This dimerization was also observed for a similar derivative bearing flexible triethyleneglycol chains at the pyrrole center.[161] In 2001, the authors designed a related 2-(guanidiniocarbonyl)-pyrrole-4-carboxylate zwitterion that self-assembles into larger (oligomeric) structures in DMSO.[160] This arrangement originates from ion pairing between the carboxylate function and the guanidinium group of neighbouring monomers, resulting in one-dimensional assemblies.

More recently, the authors extended their studies to a series of novel 2-(guanidiniocarbonyl)-pyrrole-5-carboxylate derivatives (**75-81**) with different substituents on the pyrrole ring (Chart 20) that similarly show an initial dimerization, followed by a further self-association step into different types of arrangements.[166] The molecular structure of the zwitterions is structurally related to the initial molecule studied in 1999,[158] however amide substituents on the central pyrrole facilitate the additional assembly of the dimers into larger aggregates. Microscopic studies of **77** and **78** show extended bundles of laterally interacting fibres with a length of several hundred nanometres and heights that correspond to the formed dimers.

Chart 20 Molecular structure of the 2-(guanidiniocarbonyl)-pyrrole-5-carboxylate derivatives **75-81**.

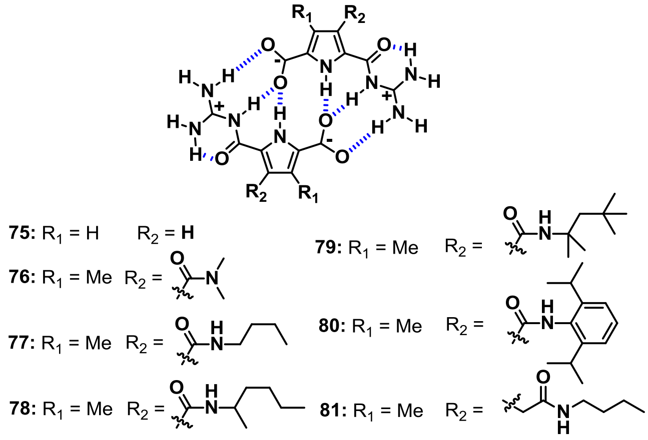

The hierarchical organisation by initial dimerization, followed by π-stacking of the dimerized zwitterions was corroborated by molecular modelling.[166] The calculations show that the H-bonding stabilized dimers are planar and thus can further grow in one direction, driven by aromatic contacts and hydrogen bonding between the peripheral amide groups. This model also explains why microscopic imaging did not reveal any discrete structures for derivative **76** lacking the amide proton in the substituent. UV/Vis absorption studies of **77** in DMSO at various concentrations (10^{-4} to 10^{-9} M) show an isosbestic point at 312 nm and a bathochromic shift of the maximum from ~300 to ~320 nm upon decreasing concentration. These spectral changes can be assigned to the organization of the dimers into one-dimensional rods and do not include the dimerization itself, since this initial process has already taken place at nanomolar concentration, as indicated by the high dimerization constant ($K > 10^{10}$ M^{-1} in DMSO).[158,161]

To examine the mechanism of self-assembly, the degree of aggregation was plotted against the concentration, giving rise to a non-sigmoidal curve with a dramatic increase of α_{agg} upon reaching 10^{-5} M (Fig. 24a).[166] Fitting of the data points to the nucleation-elongation model confirmed a cooperative process with a σ value of 0.09, indicating that the aggregation is split into a nucleation and an elongation event. For the nucleation, two dimers have to come into close contact, inducing a planarization of the molecules (Fig. 24b). This goes along with the rotation of the peripheral amide groups out of plane to enable perpendicular hydrogen bonding with neighbouring molecules, causing a notable energy penalty. While for the nucleus formation this conformational change has to be accomplished four times, each subsequent stacking requires only two rotation events. Accordingly, the initial dimerization step represents an unfavourable process, while the further stacking can proceed in a cooperative fashion. This orientational change of the amide groups also causes the ~20 nm bathochromic shift of the absorption spectra, as shown by DFT calculations. Similar to **77**, all other investigated derivatives with an amide NH group self-assemble in a cooperative fashion, for the same interactions as mentioned above. The peripheral substituents can further be involved in attractive aromatic or van der Waals interactions, directly affecting the degree of cooperativity and the binding constant, as well as the morphology of the aggregates visualized by microscopic studies.

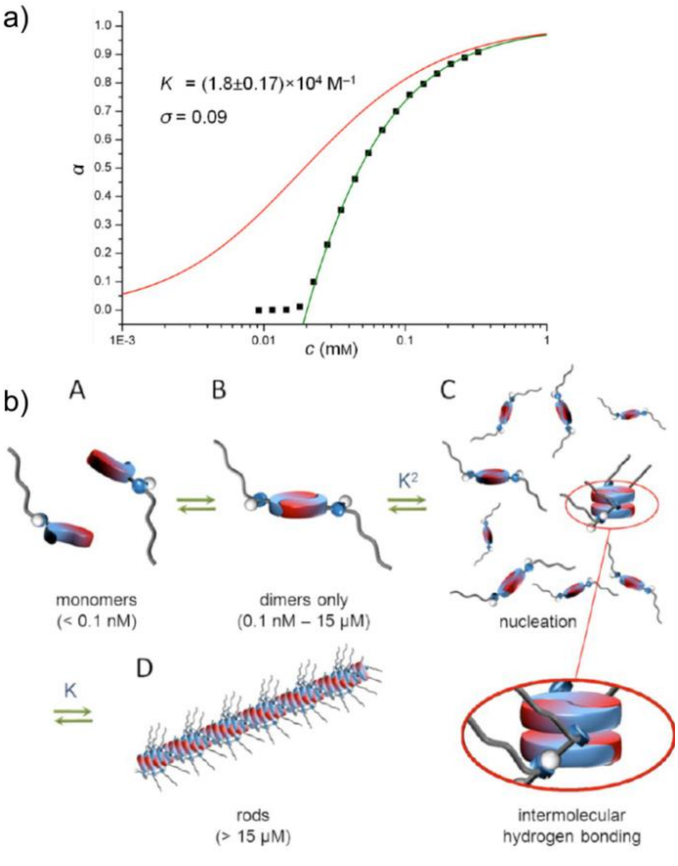

Fig. 24 a) Plot of α_{agg} of **77** against the concentration (black squares). The data can only be fitted to a strongly cooperative aggregation model (green) but clearly not to an isodesmic growth model (red). b) Schematic self-assembly of **77** starting at infinite diluted solution (**A**), via dimerization (**B**) and nucleation (**C**) to the formation of one-dimensional rod-like structures (**D**). Adapted with permission from ref. 166. Copyright (2013) American Chemical Society.

Due to the sensitivity of the zwitterions to changes in the pH value, protonation of the molecules by addition of HCl leads to a complete structural change, as *e.g.* from the extended rod-like arrangements to small vesicles for **77**.[166] These self-assembled structures of the cationic species **77-H**$^+$ can be retransformed into the initial one-dimensional fibres by a systematic deprotonation to the zwitterionic state.

In 2012, Meijer and co-workers investigated in detail the self-assembly of two series of partially fluorinated BTAs that unexpectedly revealed a two-step aggregation for one series, resulting in the formation of helical assemblies.[167] All investigated molecules contain one fluorinated side chain that is decorated with a terminal hydrogen for series **A** (derivatives **82**, **83**), whereas series **B** (derivatives **84-86**) bears a terminal fluorine atom (Chart 21).

Chart 21 Molecular structure of the partially fluorinated BTAs of class **A** (**82-83**) and class **B** (**84-86**).

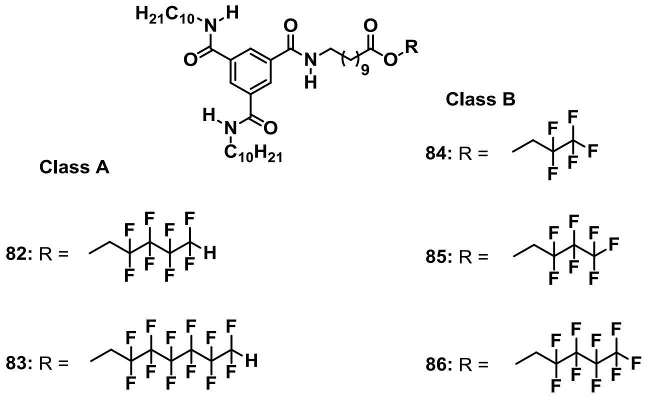

According to temperature-dependent UV/Vis absorption measurements in MCH, the self-assembly of class **B** into one-dimensional structures occurs in a highly cooperative fashion (black data in Fig. 25a), mainly driven by hydrogen bonding interactions.[167] Due to the achiral character of the molecules, no CD signal appears upon aggregation, clearly indicative of equal ratios of P-type and M-type helices (grey data in Fig. 25a). In contrast, the fibre-like structures formed by achiral class **A** derivatives generate a CD effect, as observed in temperature-dependent CD studies below room temperature (grey data in Fig. 25b). This unexpected behaviour was further investigated by temperature-dependent UV/Vis absorption experiments (black data in Fig. 25b). Upon cooling down the monomeric state from high temperature, the molecules initially show a comparable behaviour to series **B**. Consequently, the spectral features of class **A** molecules were similarly assigned to the aggregation into P- and M-type helical strands, lacking any CD effect and following a cooperative aggregation pathway. However, unlike studies of class **B** derivatives, the absorption measurements reveal a second abrupt change at room temperature that is in agreement with the appearance of a Cotton effect in the corresponding CD spectra. This indicates that the self-assembly of class **A** features a further (second) aggregation step. This process could be characterized as bundling of the initially formed (optically non-active) helices into significantly larger (optically-active) assemblies, as confirmed by AFM. While the first cooperative step is driven by hydrogen bonding interactions, the second step must be related to a secondary nucleation with minute amounts of chiral impurities, driven by dipole-dipole forces.

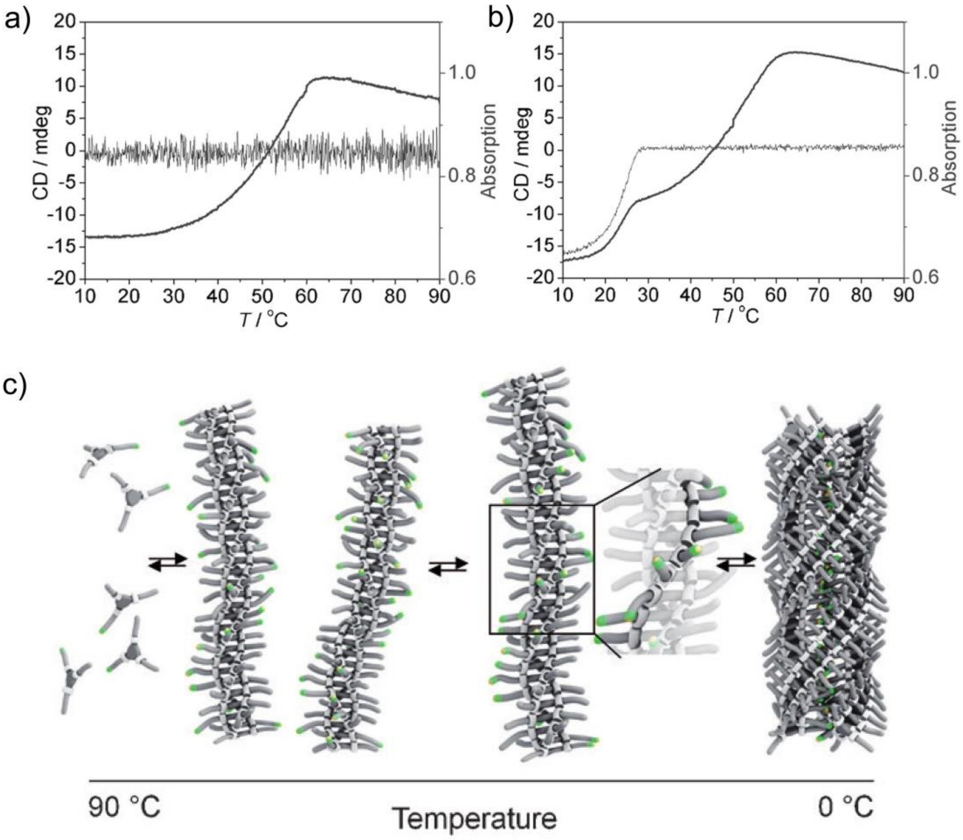

Fig. 25 a,b) Temperature-dependent UV (black) and CD measurements (grey) in MCH of a) BTA-F$_9$ **86** and b) BTA-F$_8$H **82** (c = 30 μM, at λ = 223 nm, l = 1 cm). c) Proposed self-assembly mechanism for partially fluorinated BTAs of class **A**. Adapted with permission from ref. 167. Copyright (2012) Wiley-VCH Verlag GmbH & Co. KGaA, Weinheim.

The suggested model for this two-step mechanism of class **A** is shown in Fig. 25c.[167] It considers that a rearrangement of the molecules in the initially formed helical fibres occurs that leads to a fluorine-enriched patch on the fibre surface. This subsequently induces a further bundling of the fibres that is supported by weak attractive interactions between the fluorine atoms of one helix and terminal electron-deficient hydrogen atoms of a neighbouring stack. The appearance of a preferred handedness might be attributed to the presence of chiral impurities. The effect of chiral additives was investigated upon adding a small amount of chiral guests to the class **A** solutions in MCH resulting in a significant increase in the CD signals.

2.4.5 *π-π* interactions supported by other weak non-covalent or conformational contributions

The previous examples describe in detail that cooperative systems can be originated from cooperative hydrogen bonding interactions or, as most examples show, arise when two or more specific non-covalent interactions act simultaneously. However, a handful of examples of unexpected, slightly cooperative systems can be found in literature that are mainly based on *π-π* interactions, supported by important contributions of other weak non-covalent forces or conformational changes.

An illustrative example in this regard was reported by Sánchez and co-workers in 2011.[168] The authors investigated the self-assembly of four triangular-shaped OPEs (**87**-**90**) on surfaces and in solution, three of them featuring chiral aliphatic chains (**87**-**89**) and one literature-known[169,170] achiral OPE bearing a non-branched alkyl substituent (**90**) (Chart 22).

Chart 22 Molecular structure of the triangular-shaped OPEs **87-90**.

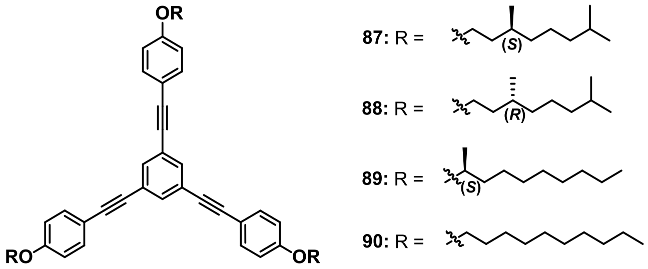

AFM images of the two enantiomers (*S*)-**87** and (*R*)-**88**, exhibiting a stereogenic centre in the 3-position of the alkyl substituent, displayed rope-like aggregates in MCH with lengths of several micrometres and a height that corresponds to a single-molecule length.[168] The structures show opposed handedness originated from the opposite chirality in the molecular design. These left- and right-handed fibres for (*S*)-**87** and (*R*)-**88**, respectively, are formed by *π-π* stacking interactions between the aromatic cores with a different mutual rotation of the discs. Similarly, helical stacks were also created by the chiral derivative (*S*)-**89**, as shown in Fig. 26a,b. However, these right-handed helices unexpectedly exhibit an opposite handedness to the assemblies formed by (*S*)-**87** with the same stereoconfiguration. Furthermore, the helical pitch for the (*S*)-**89** helix is smaller than that for the (*S*)-**87** aggregates indicating that the position of the chiral methyl group and the (branched) nature of the aliphatic substituents have a significant influence on the direction and magnitude of rotation of the subunits within the stack. The aggregation of achiral **90** also results in helical arrangements, even though the amount of P- and M-type columnar assemblies is equal.

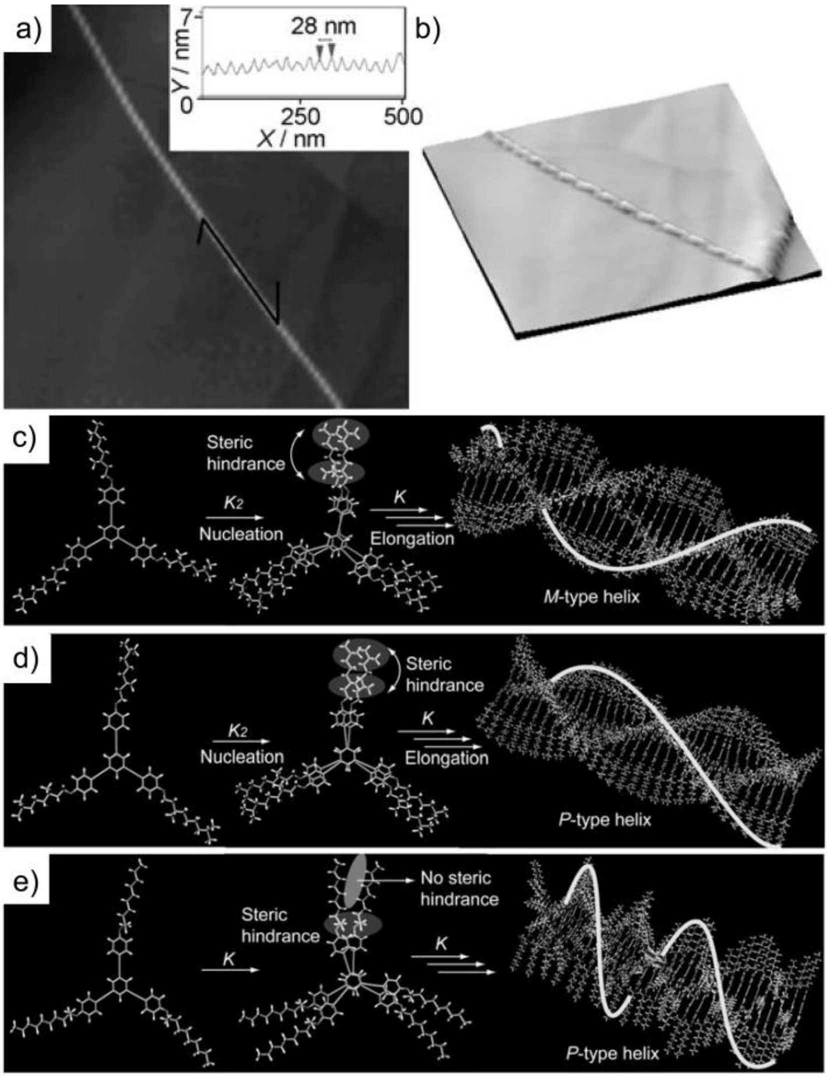

Fig. 26 a) Tapping-mode and b) 3D AFM images (air, 298 K) of a spin-cast MCH solution of (*S*)-**89** (~10^{-4} M, HOPG) showing a P-type helix (Z scale = 10 nm). The inset depicts the corresponding height profile and the helical pitch along the black line in a). c-e) Schematic illustration of the self-assembly of c) (*S*)-**87**, d) (*R*)-**88** and e) (*S*)-**89**. The line depicts the helicity of the aggregates. The ellipsoids indicate the steric hindrance between the peripheral substituents or the lack of such steric interaction. Adapted with permission from ref. 168. Copyright (2011) Wiley-VCH Verlag GmbH & Co. KGaA, Weinheim.

The self-assembly behaviour of (*S*)-**89** in MCH was investigated by concentration-dependent UV/Vis absorption experiments.[168] These studies show significant changes upon increasing concentration owing to π-stacking interactions. Plotting α_{agg} against the concentration gives rise to a sigmoidal curve, revealing that (*S*)-**89** self-assembles in an isodesmic fashion. Similar results were obtained for the self-assembly of achiral **90**.[170] In contrast, fitting of the concentration-dependent α_{agg} values to the isodemic model failed for the chiral counterparts (*S*)-**87** and (*R*)-**88**, clearly indicating that the monomer-to-aggregate transition follows a cooperative pathway.[168] Application of the cooperative K_2-K nucleation-elongation model[32,33,36,40] yielded satisfactory fits for a cooperativity factor $\sigma = 0.2$, giving comparable thermodynamic parameters for the aggregation of (*S*)-**87** and (*R*)-**88**.

Although the degree of cooperativity is relatively low (σ value of 0.2), it is somewhat unexpected in these systems because the aggregation affinity is mainly based on π-π interactions.[168] Comparing the molecular design of (*S*)-**87** and (*R*)-**88** with (*S*)-**89**, the only structural variation, most likely responsible for the slight cooperativity in the aggregation process, lies in the position of the stereogenic centre and the branched nature of the peripheral substituent in (*S*)-**87** and (*R*)-**88** (Fig. 26c-e). Thus, when initially two monomeric molecules come into close contact by π-π interactions, conformational changes are necessary to reduce the steric demand of the bulky substituents. This process represents the unfavourable step, characterized by a relatively low binding constant of $2.6 \times 10^4\ M^{-1}$ and can thus be regarded as the nucleation. The subsequent association of a third or fourth molecule requires less pronounced conformational changes. This results in a twenty-fold higher binding constant of these steps that can thus be defined as the elongation event.

Recently, Würthner and co-workers reported two pieces of work regarding the self-assembly of perylene bisimide (PBI) dyads **91** and **92** (Chart 23).[101,171] They could show that a variation in the backbone length induces a change in the self-assembly from dimerization to cooperative elongated π-stacking.

In their initial work they synthesized dyad **91**, constructed of two PBI chromophores both capped with branched alkyl chains and connected by a diphenylacetylene (DPA) unit as backbone.[171] This molecule aggregates into stable interlocked dimers due to the perfect matching of the PBI distance to stable π-π interactions.

Chart 23 Molecular structure of perylene bisimide (PBI) dyads **91-92** and the PBI precursor **93**.

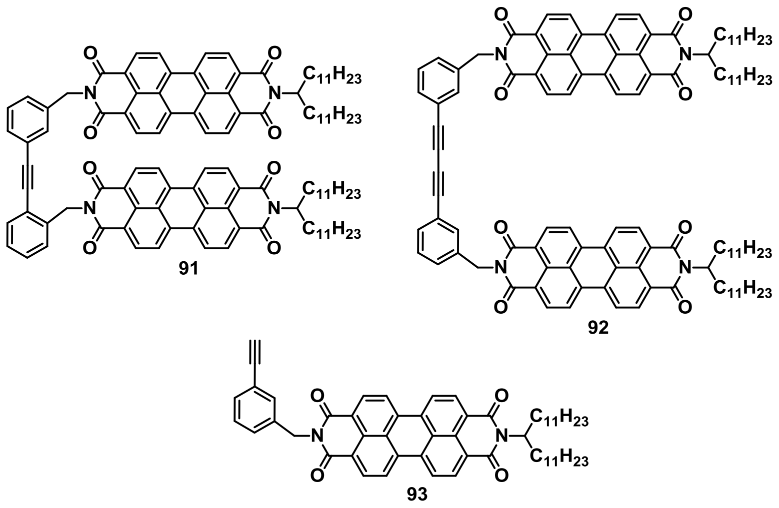

In the following studies the structural motif was maintained but the connecting unit elongated to a diphenylbutadiyne (DPB) spacer (derivative **92**), leading to a PBI-PBI distance that is three times the expected distance for aromatic PBI stacking.[101] MALDI-TOF spectra of a MCH solution revealed the presence of extended aggregates of up to 21 dyads of **92** that could be confirmed by DOSY measurements. Concentration-dependent UV/Vis absorption studies in $CHCl_3$/MCH = 30:70 monitored the transition from aggregated to monomeric species with the plot of α_{agg} against Kc_T being non-sigmoidal. At first glance, this behaviour is rather unexpected since π-π interactions constitute the sole intermolecular force between the PBI surfaces. This attraction thus results in a value of $\sigma = 0.1$ for the fitting to the cooperative K_2-K model, revealing that the aggregation pathway for **92** is slightly cooperative. This behaviour is contrary to the PBI precursor **93** that represents only half of the investigated dyad. The molecule **93** aggregates in a non-cooperative fashion, resulting in much less stable aggregates. The cooperative character of **92** was further confirmed by kinetic studies, regarding the time-dependent deaggregation upon dilution of a highly aggregated sample. The spectral changes upon disassembly exhibit several isosbestic points that reveal the existence of only two defined states (monomeric **92** and aggregated **92**). Furthermore, the changes over time follow a first order kinetics, also indicating that the oligomers of **92** disassemble cooperatively.

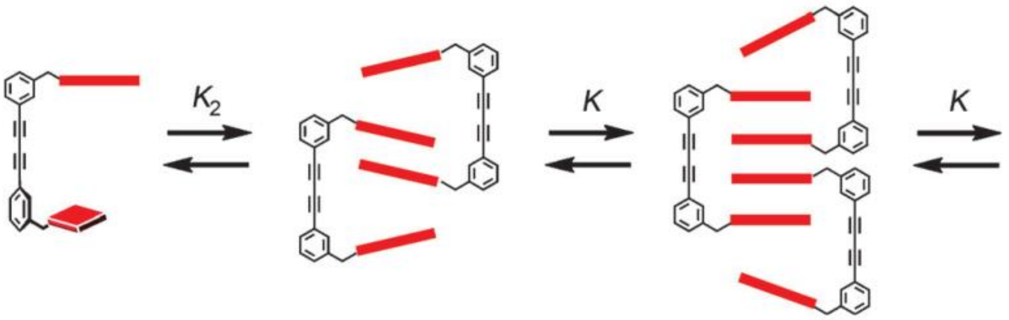

Fig. 27 Model of the backbone-directed “arm-in-arm” aggregation of PBI **92** into extended oligomeric π-stacks. Reprinted with permission from ref. 101. Copyright (2013) Wiley-VCH Verlag GmbH & Co. KGaA, Weinheim.

The described results indicate that the dyad assembly is divided into an unfavourable dimerization that is followed by an elongation step, characterized by a tenfold higher binding constant.[101] Due to the presence of only π-π interactions as interactive forces, the second important driving force contributing to the cooperative mechanism should come from the arrangement of the chromophores in the stack. As already mentioned, the molecular design of **92** includes a PBI distance that is three times the ideal value for π-π interactions (3.3-3.4 Å), thus enabling an “arm-in-arm” aggregation (Fig. 27). Regarding the nucleation step, only one PBI surface enters this space, resulting in a comparatively weak π-interaction. However, in the elongation process these dimers can interdigitate to perfectly fill this intramolecular space, resulting in a more stable association of dense elongated π-stacks.

Similarly to the previous example of triangular-shaped OPEs from Sánchez and co-workers,[168] this example points out that π-π interactions as single attractive interaction can, if at all, only result in a weak cooperative strength.

In 2007, the groups of de Feyter, Meijer and Schenning studied the self-assembly of an oligo(*p*-phenylene vinylene) (OPV)-substituted hexaarylbenzene by various techniques in solution and on surface.[172] Star-shaped molecule **94** features a hexaarylbenzene centre that is connected to six OPV segments. These units are decorated with branched chiral (*S*)-side chains resulting in a propeller-like structure (Chart 24). Thermogravimetric analysis (TGA) of **94** shows that this molecule is stable up to 300 °C. Upon slow cooling of the molten sample a crystalline phase can be visualized by means of polarized optical microscopy (POM), revealing a fan-shaped texture (Fig. 28a). This high degree of order in the plastic crystalline phase can also be detected in 2D WAXS studies that indicated a perfect columnar stacking of the molecules, whose OPV-propeller arms are not completely planar but slightly rotated.

Chart 24 Molecular structure of the oligo(*p*-phenylene vinylene) (OPV)-substituted hexaarylbenzene **94**.

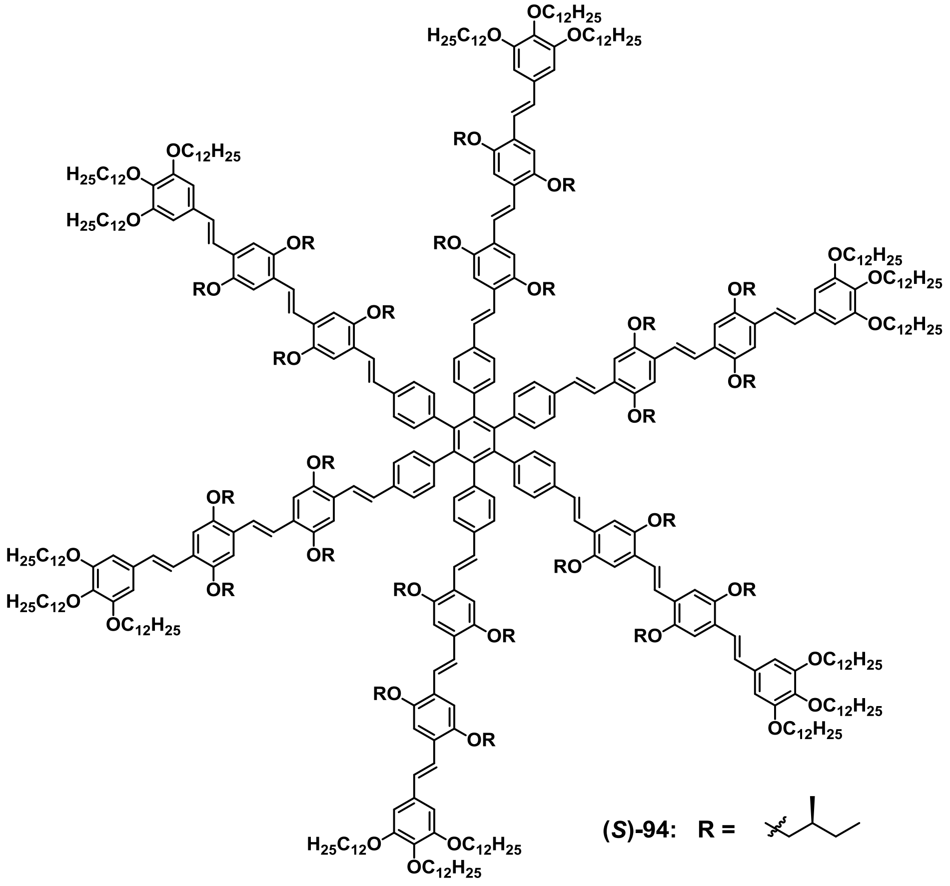

UV/Vis absorption measurements showed that OPV **94** exists in an aggregated state in heptane solution that could be further characterized by CD studies as helical stacks.[172] These arrangements were stable up to 90 °C, also for a highly diluted sample of 10^{-7} M. In contrast, switching to MCH allowed the disassembly of the helical species upon heating, as observed in UV/Vis absorption and CD experiments. The cooling curves associated to this transition are clearly non-sigmoidal with a significant onset of aggregation at the elongation temperature T_e = 331 K (Fig. 28b). Fitting the UV/Vis absorption data to the nucleation-growth model[42,43] determined an average size of the assemblies at T_e of around 32 molecules that grow into π-stacked arrangements of more than 10000 subunits at room temperature, as confirmed by AFM imaging.

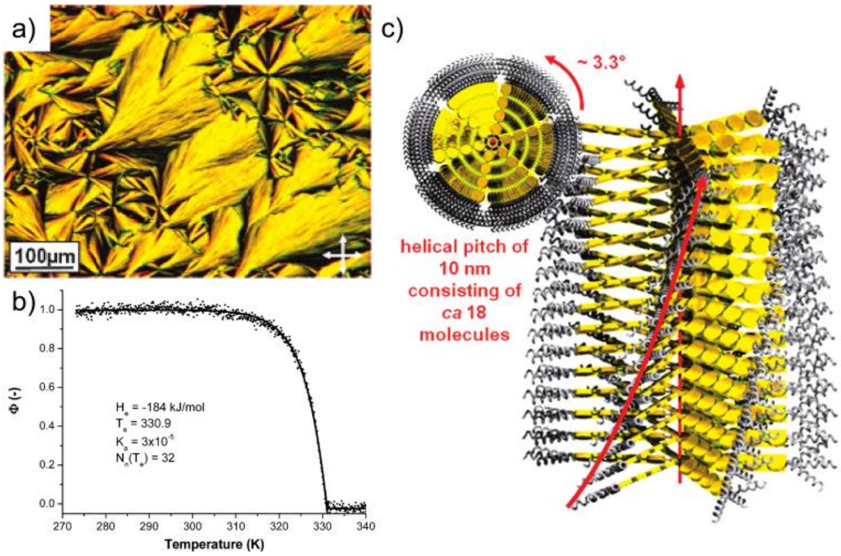

Fig. 28 a) Image from polarized optical microscopy of the star-shaped OPV **94** obtained by cooling from the isotropic phase. b) Fit of the normalized CD melting curve using the nucleation-growth model. c) Schematic illustration of the helical columnar packing of **94** based on X-ray, CD and AFM data. Adapted with permission from ref. 172. Copyright (2007) American Chemical Society.

A close-up shot of an aggregate sample on silicon wafer revealed the formation of chiral arrangements that consist of around 18 molecules within one helical pitch, as illustrated in the model in Fig. 28c.[172] This observation confirms a dense packing of the OPV units by efficient π-π stacking, provided by the pronounced overlap of the aromatic surfaces of the slightly rotated propeller arms. As the detailed investigation shows, the arrangement into chiral stacks follows a highly cooperative mechanism, although π-π interactions represent the chief attractive forces in the system. The cooperative nature of the self-assembly becomes noticeable in a remarkably low value of the dimensionless activation constant K_a (3 x 10^{-5}), that gives an indication of the strength of cooperativity in the system (as the cooperativity factor σ does in other models)[34]. One possible explanation can be seen in the conformational changes that are necessary to start the effective interactions with adjacent subunits. While in non-aggregating solution the propeller arms of the OPVs are independent and can freely rotate, the activation of the monomer affords conformational changes. To enable effective π-interactions, the six arms of the molecule have to adopt a more ordered conformation that is accomplished in an unfavourable rearrangement of the molecular scaffold. Once this is overcome, the system can elongate by favourable association of further molecules into extended helical structures.

Although this explanation is similar to the triangular-shaped OPEs reported by Sánchez and co-workers,[168] the cooperative character of star-shaped OPV **94**[172] is much more pronounced than of this system and also than of PBI dyad **92** of Würthner and co-workers[101]. The reason for this might be related to flexibility and conformation aspects of the chromophores. Due to the six substituents attached to the central benzene ring, the centre of the molecule **94** is sterically crowded. This sterical overload induces a conformational adaption of the propeller arms out of plane that can occur unrestrictedly around the single bond in the OPV system, unlike more rigid OPEs **87**-**88** and PBI dyad **92** in which this motion is restricted. Furthermore, in comparison to the presented OPEs[168] and the PBI system[101], the extended OPV arms are much more flexible which might facilitate conformational changes and closer packing of the subunits that are essential for the stable growth of the system.

2.4.6 Cooperative systems in water

Due to the unique properties of water, the self-assembly in this medium is highly influenced by the well-known *hydrophobic effect*.[173-177] The origin of this unique effect lies in the fact that the interactions of water molecules among each other are much more favourable than the interactions of water molecules with non-polar groups (hydrophobic surfaces). Solvation of a non-polar solute leads to a cleavage of hydrogen bonding interactions when its size is not fitting within the cavities of the water network. To minimize this loss of highly attractive interactions, the added molecules are forced to aggregate into larger clusters, thus the hydrogen bonding network can be maintained to the greatest possible extent. This generates a strong supporting driving force for the self-assembly of amphiphilic molecules in aqueous medium,[8,37,96,178-187] compared to an organic solvent environment, that can additionally contribute to induce cooperative phenomena.

In the following, some remarkable examples of cooperative supramolecular polymerisation in water are classified that are driven, besides the hydrophobic effect, by other non-covalent interactions.

2.4.6.1 Encapsulation/co-assembly

In 2012, our working group showed an intriguing example of a water-soluble linear oligo(phenylene ethynylene) (OPE) amphiphile **95** whose aggregate morphology and self(co)-assembly mechanism (isodesmic or cooperative) can be controlled by the addition of a related hydrophobic OPE **96** with similar shape.[188] Furthermore, the self-assembly of an equimolar mixture of **95** and **96** into independent (narcissistic) or co-assembled (social) aggregates was observed to strongly depend on the investigated concentration.

The molecules consist of three linear OPE units equipped with three triethyleneglycol (**95**) and alkyl chains (**96**) on each side, respectively (Chart 25). The water-soluble derivative **95** shows a propensity to aggregate in water by aromatic interactions, as evidenced by a significant quenching of the emission upon increasing concentration.

Chart 25 Molecular structure of the oligo(phenylene ethynylene) (OPE) amphiphile **95** and its non-amphiphilic counterpart **96**.

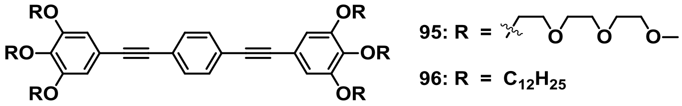

The spectral changes during variable-temperature UV/Vis absorption studies in water are characterized by a defined isosbestic point indicating equilibrium between well-defined species.[188] Switching to the less polar solvent mixture THF/water (1:1) revealed a similar self-assembly behaviour. The cooling curves at certain wavelength showed a sigmoidal shape for both samples (water and THF/water). This behaviour is indicative of an isodesmic process that could be confirmed by good fitting to the non-cooperative model. Atomic force microscopy (AFM) and scanning electron microscopy (SEM), as well as DLS studies of the arrangements of **95** in both media revealed spherical objects of 3-10 nm in size. This self-assembly is driven by π-π stacking between the OPE cores with the triethyleneglycol chains exposed towards the surrounding solvent, acting as hydrophilic micelle shell. On the other hand, the non-amphiphilic derivative **96** shows a strong aggregation tendency in THF (10^{-5} M) when 30% water is added, while at a concentration of 10^{-3} M the compound directly precipitates due to its remarkable hydrophobicity. Microscopic and DLS studies of **96** in THF/water (1:1) revealed similar results as for the amphiphilic counterpart **95** showing discrete spherical objects. These assemblies of **96** can further conglomerate due to the hydrophobic effect giving rise to particles of up to 50 nm.

The self-sorting behaviour upon mixing these two aggregating species **95** and **96** showed a pronounced concentration-dependence. In THF/water (1:1) at 10^{-5} M, a clear narcissistic self-sorting occurs, as evidenced by the UV/Vis absorption spectra representing an overlay of the absorption of the two distinct compounds. This characteristic is supported by the appearance of only spherical aggregates in SEM studies (Fig. 29a and model in Fig. 29c, top). However, when the concentration is increased to 1 mM, a clear co-assembly process can be observed, driven by the hydrophobic effect and facilitated by the identical sizes of the aromatic OPE cores. This social self-sorting behaviour results in the appearance of a red-shifted transition (400-500 nm) in the UV/Vis absorption spectra upon addition of water to a 1:1 mixture of **95** and **96**, that was absent at lower concentration.

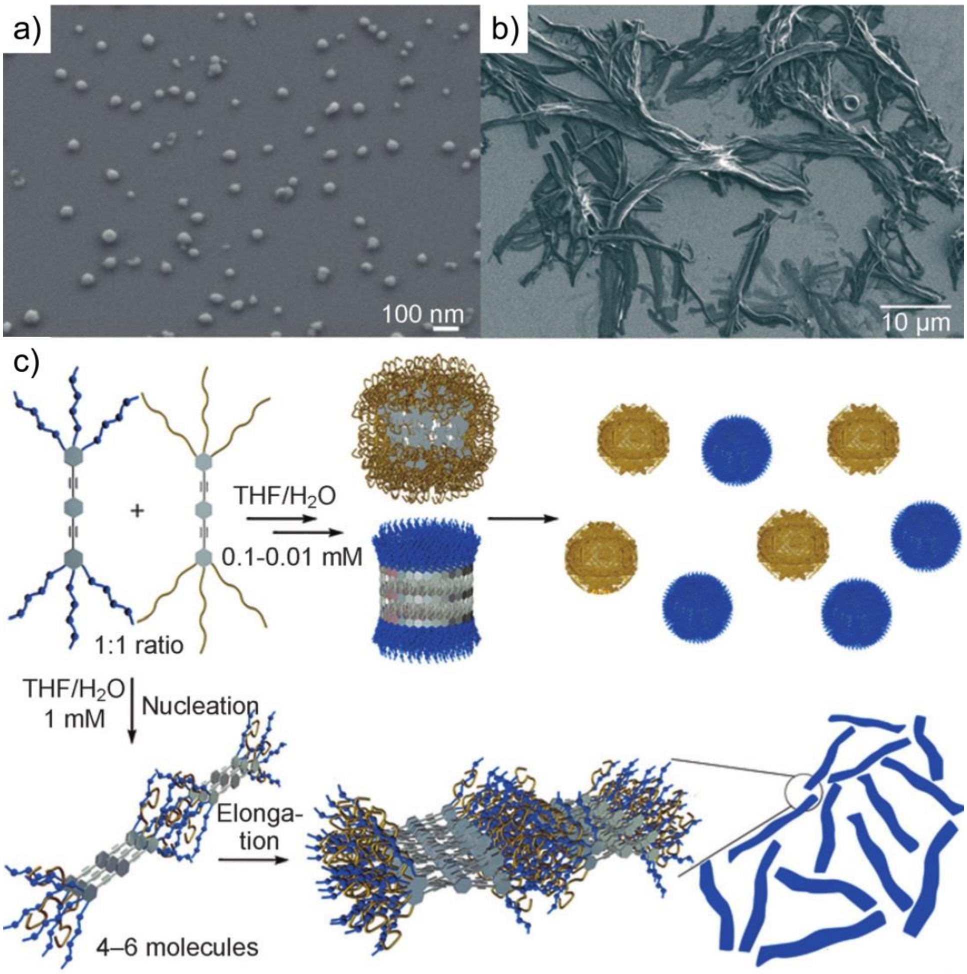

Fig. 29 SEM images obtained by spin-coating a 1:1 mixture of **95** and **96** in THF/water at a) c = 0.1 mM and b) c = 1 mM on a silicon wafer. c) Cartoon representation of the concentration-dependent self-sorting behaviour of a 1:1 mixture of **95** and **96** in THF/water (1:1). Narcissistic self-sorting between c = 0.01 mM and c = 0.1 mM (top) and social self-sorting at c = 1 mM (bottom). Reprinted with permission from ref. 188. Copyright (2012) Wiley-VCH Verlag GmbH & Co. KGaA, Weinheim.

Analysis of temperature-dependent UV/Vis absorption studies of a 1:1 (**95**:**96**) mixture in THF/water (6:4) reveals a cooperative co-aggregation pathway.[188] This behaviour can be described by the nucleation-elongation model developed by Schenning, Meijer and van der Schoot[42,43], determining an aggregate size at the elongation temperature (T_e) of 6 molecules. The co-assembly process is accompanied by notable structural changes, as could be visualized by SEM. While the isodesmic self-assembly of the individual compounds **95** or **96** gave rise to spherical particles, their co-assembly results in the cooperative formation of extended ribbons with a length of up to several micrometres (Fig. 29b and model in Fig. 29c, bottom).

Recently, our group extended the studies on co-assembly processes in aqueous medium and investigated the self-assembly of an OPE-4,4-difluoro-4-bora-3a,4a-diaza-*s*-indacene (BODIPY) bolaamphiphile **97** (Chart 26) in water and its size-dependent co-assembly phenomena with small aromatic molecules such as tetracene and anthracene.[189]

Chart 26 Molecular structure of the amphiphilic BODIPY derivative **97**.

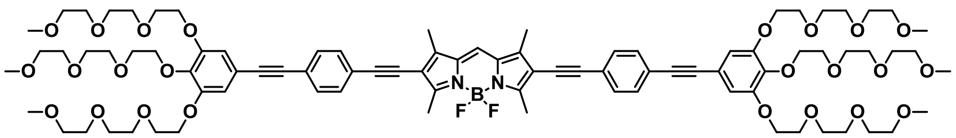

97

UV/Vis absorption and fluorescence experiments suggest that **97** self-assembles in water into H-type aggregates that are stabilized by π-π interactions and characterized by a twisted conformation of the subunits in the assemblies.[189] Temperature-dependent investigations showed a reversible transition between the monomeric and aggregated state that is defined by a sigmoidal cooling curve. Applying the isodesmic model to the data confirmed the non-cooperative pathway with binding constants around 1 x 10^6 M^{-1}.

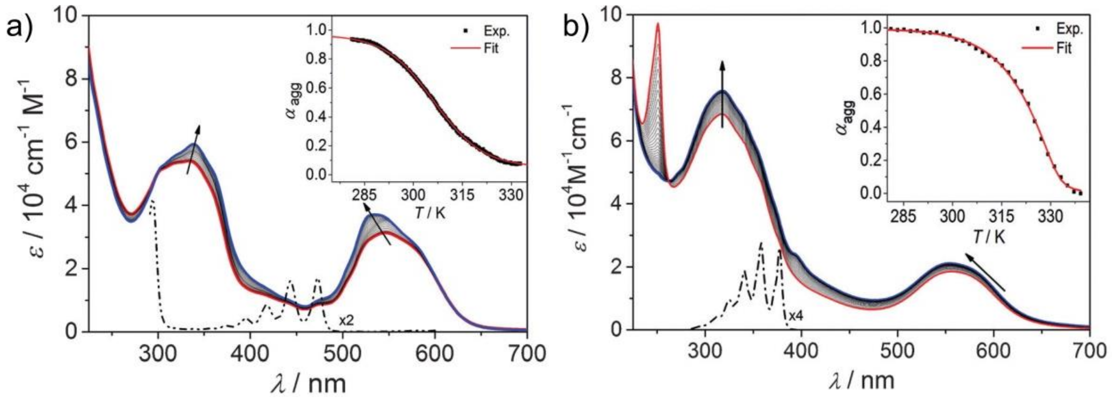

Fig. 30 Temperature-dependent UV/Vis absorption studies of **97** in aqueous solution (10^{-5} M) containing one equivalent of a) tetracene and b) anthracene. Arrows indicate spectral changes upon temperature decrease. Dash-dotted line: UV/Vis spectra of a) tetracene and b) anthracene in THF. Inset in a): Fitting of α_{agg} at 510 nm to the isodesmic model. Inset in b): Fitting of α_{agg} at 555 nm to the *ten Eikelder-Markvoort-Meijer*-model. Adapted with permission from ref. 189. Copyright (2014) Wiley-VCH Verlag GmbH & Co. KGaA, Weinheim.

The hydrophobic interior of the fibrils was further tested for the embedding of hydrophobic guest chromophores such as tetracene and anthracene that are both insoluble in water and precipitate out rapidly.[189] Thus, the absence of precipitation is a clear indication of the successful uptake within the self-assembled systems. Indeed, the addition of either 1 equiv. of tetracene or anthracene to an aggregate solution of BODIPY **97** in water results in a clear solution, suggesting the encapsulation of the insoluble dye molecules. This co-assembly can also be detected in the UV/Vis absorption spectra, exhibiting a new, albeit weak maximum corresponding to the dyes. Although Job’s plot analysis reveals an identical host:guest binding stoichiometry of 1:1 for both dyes, their co-assembly occurs in a distinct fashion, as shown by temperature-dependent encapsulation studies in Fig. 30.

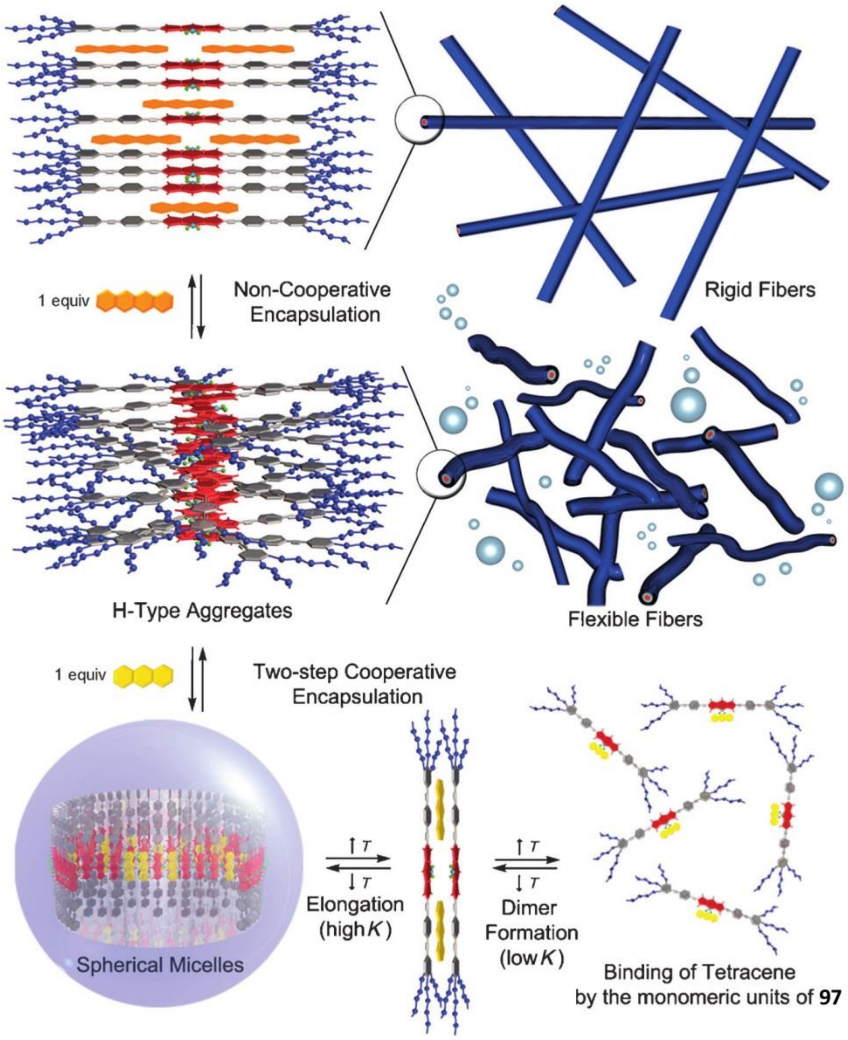

Fig. 31 Cartoon representation of the self-assembly of **97** into H-type aggregates and its reversible guest-dependent encapsulation processes. Reprinted with permission from ref. 189. Copyright (2014) Wiley-VCH Verlag GmbH & Co. KGaA, Weinheim.

By monitoring the cooling curve of the mixture of **97** with tetracene (Fig. 30a, inset), a sigmoidal curve is obtained, indicating that the co-assembly proceeds in an isodesmic manner.[189] This non-cooperative co-aggregation induces a stiffening and elongation of the fibres, while the internal order is not increased (model in Fig. 31, top). In contrast, the cooling curve associated to the co-assembly with the smaller dye anthracene (Fig. 30b, inset) can be clearly described as cooperative process, accompanied by a change in the morphology of the aggregates to highly ordered spherical micelles (model in Fig. 31, bottom).

These results indicate not only that slight structural changes in the guest molecule induce a fascinating switch in the aggregation pathway, but also that hydrophobic interactions can become strong enough to induce cooperative effects.

2.4.6.2 *π-π*, hydrogen bonding interactions and the hydrophobic effect

In 2014, Rybtchinski and co-workers have investigated two unsymmetrically bay-substituted PBI amphiphiles.[190] These molecules bear a solubilizing glycol group on one side and either a linear alkyl substituent (**98**) or a perfluorinated chain (**99**) on the opposite side that is attached to the aromatic core via a spacer unit (Chart 27). Comparing these structurally similar derivatives, the authors delivered insight into the influence of the highly hydrophobic fluorocarbon group on the self-assembly behaviour.

Chart 27 Molecular structure of the bay-substituted PBIs bearing a linear alkyl chain (**98**) or a perfluorinated end group (**99**).

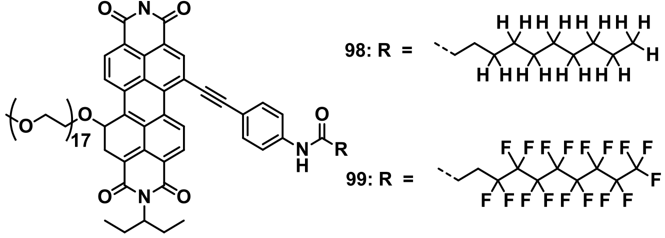

Regarding the absorption studies in THF/water mixtures of varying ratio, both compounds **98** and **99** show similar spectral changes upon increasing water content that are characteristic for an H-type stacking with a slight rotation of the subunits.[190]

Cryo-TEM studies in water/THF (65:35) showed fibre-like structures for both derivatives (Fig. 32a, left), with smaller assemblies formed by **98**. The dimensions match well with linearly *π*-stacked PBIs that fill the inner fibre compartment, surrounded in the case of **99** by the (fluoro)alkyl substituents exposed towards the surrounding medium (Fig. 32a, right). Due to the more flexible character of the H-chains in **98** they are in close contact with the inner PBI units, while the F-chains in **99** are rigid and have an extended conformation resulting in a larger diameter for the F-derivative. These assemblies are further stabilized by hydrogen bonding interactions that are possible even in the aqueous medium, due to the hydrophobic environment of the hydrogen bonding units in the molecular structure.

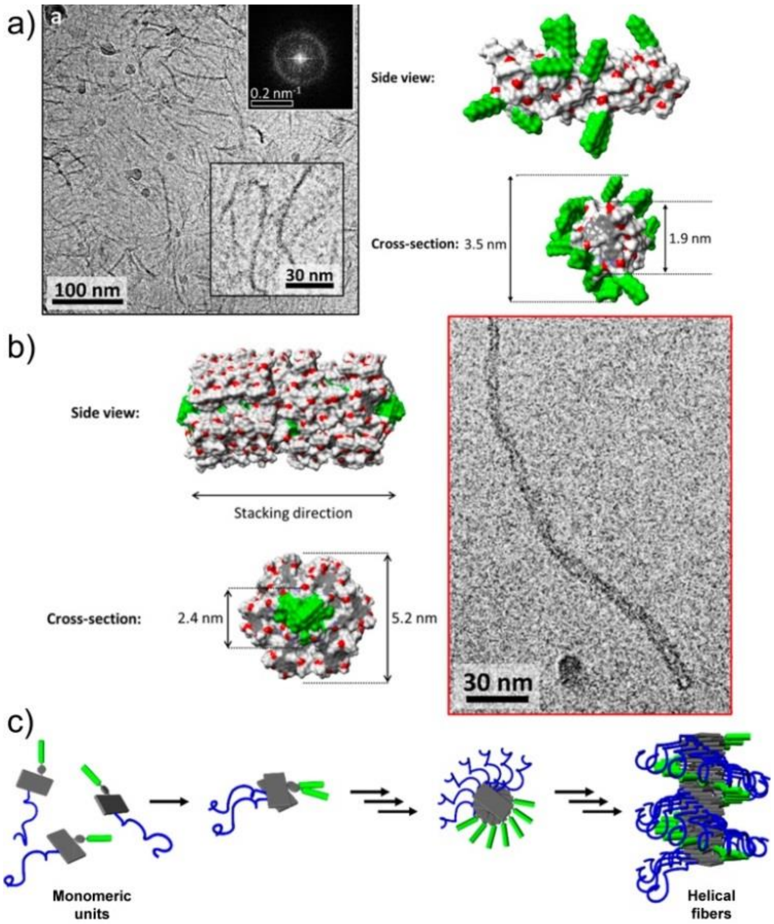

Fig. 32 a, left) Cryo-TEM image of **99** (10^{-4} M) in water/THF = 65:35 (v/v). Inset: FFT of the image, revealing a periodicity of ∼8.2 nm, which corresponds to the average fibre-fibre spacing. a, right) Proposed molecular model of the supramolecular fibres of **99**. b, right) High-magnification cryo-TEM image of tube-like fibres of **99** (10^{-4} M) in water/THF = 80:20 (v/v). b, left) Proposed molecular model. c) Schematic illustration of the proposed mechanism of the cooperative aggregation of **99**. Adapted with permission from ref. 190. Copyright (2014) American Chemical Society.

Upon increasing the water content to 80%, the assemblies of **98** are barely influenced while assemblies of **99** undergo a morphological transformation (Fig. 32b).[190] Still, fibre-like structures are present but of larger diameter (5-6 nm). Closer inspection of cryo-TEM images indicated that the perfluorooctyl chains are embedded in the fibre core due to increased hydrophobic interactions, while the outer layer consists of densely π-stacked PBI chromophores (Fig. 32b, left).

Temperature-dependent UV/Vis absorption studies show that the structural reorganization of **99**, observed in cryo-TEM upon increasing water content, is accompanied by unexpected spectral changes. The measurements for a water content of 65% show monomeric species at 65 °C that self-assemble upon decreasing temperature, characterized by the appearance of a defined isosbestic point. The cooling curves feature a steep slope, indicative of a cooperative mechanism that was perfectly described by the nucleation-elongation model.[35,41-43] In contrast, the aggregation into reversed fibres at higher water content clearly follows an isodesmic pathway.[190] This difference indicates that the water content directly dictates the molecular organization within the stacks and in this regard the corresponding aggregation mechanism. Those changes do not occur for the derivative **98**, characterized by an isodesmic aggregation mechanism independent of the water content.

The cooperative formation of the thinner fibres of **99** can be rationalized by considering the helical arrangement of the molecules and the remarkable hydrophobicity of the rigid F-chains. As illustrated in the model in Fig. 32c, in this molecular organization the bulky F-chains, just as the triethyleneglycol groups, point towards the aqueous environment. The contact of the F-chains with this medium is clearly unfavourable. However, the unattractive contact surface can be reduced once the stacks reach a certain length. At this point, the F-chains can be surrounded by the flexible hydrophilic PEG chains of interacting subunits, resulting in a shielding from the polar solvent molecules. In the first association steps, this stabilization is not yet possible since the chains are oriented at opposite sides of the stack. However, once the stack finishes a half-helical turn, each further associated molecule contributes to the stabilization of the system, thus turning these steps into a favourable elongation of the system. This helicity explanation also includes the non-cooperativity of the tube-like structures of **99** formed at higher water content, due to the lack of helicity in these one-dimensional structures.

2.4.6.3 Ionic/electrostatic interactions and the hydrophobic effect

Meijer and co-workers studied in detail the fine balance between attractive and repulsive interactions in supramolecular systems and their influence on the morphology and aggregation mechanism of the self-assembled structures.[191] Furthermore, they could show that the ionic strength of the aqueous environment can dramatically influence the aggregation process.

Chart 28 Molecular structure of the discotic BTA derivatives **100-102**.

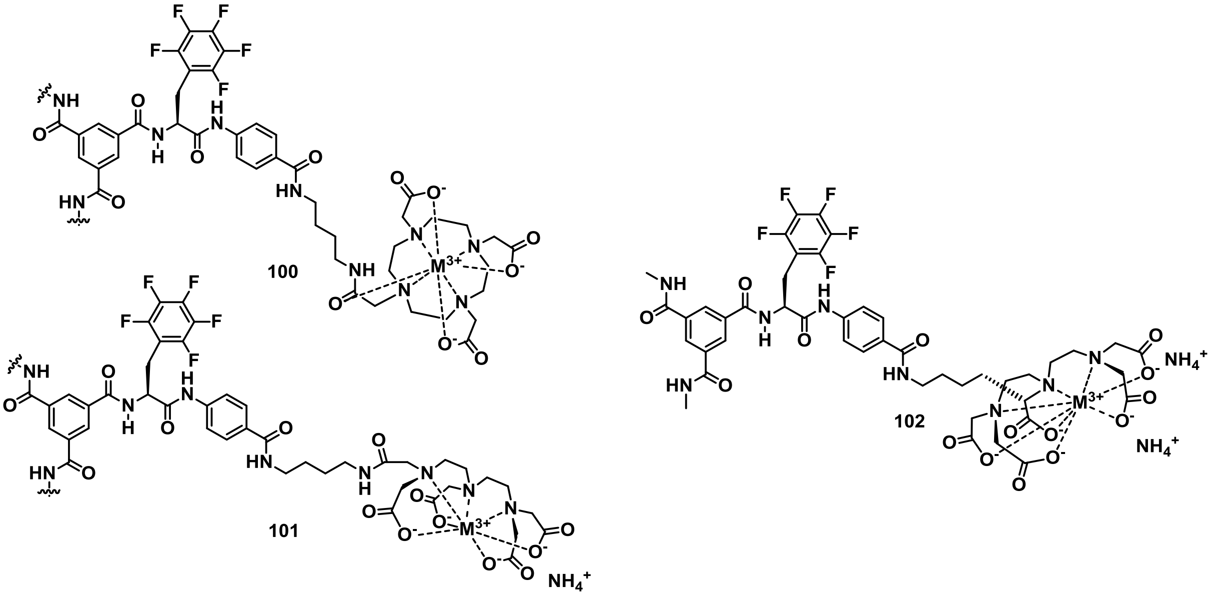

They synthesized three discotic BTA derivatives (**100-102**), all sharing a fluorinated phenylalanine substituent and an aminobenzoate function as connecting unit to a hydrophilic metal complex (Chart 28).[191] The molecular design of **100-102** enables a self-assembly of the molecules by hydrogen bonding and π-π interactions (Fig. 33a). The three derivatives differ in the nature of the metal complex, varying from charge-neutral (**100**) to negative complexes with one (**101**) or two (**102**) charges per terminal unit. The dissimilar nature of the systems in terms of repulsive electrostatic forces induce significant changes in the aggregate morphology of **100-102**, as suggested by small angle X-Ray scattering (SAXS) and cryo-TEM studies.

For **100** in citrate buffer, rod-like structures of single-molecule diameter could be observed whose length depends on the concentration of the sample. In contrast, the six-fold negatively-charged BTA **102** self-assembles into spherical objects of around 5 nm in size at 1 mM. Not only do repulsive Coulombic interactions control the morphology of the helical aggregates, but also the mechanism of self-assembly under buffered conditions. Cooling curves extracted from temperature-dependent CD and UV/Vis absorption studies show that both neutral BTA **100** as well as singly-charged complex **101** self-assembles in a cooperative fashion. The application of a nucleation-elongation model[35,41] to the non-sigmoidal curve gives the thermodynamic parameters with the activation constant K_a of 10^{-4} for **100** and 10^{-3} for **101** and elongation temperatures T_e that increase with increasing concentration. However, the organisation of **102** into spherical structures is characterized by a sigmoidal curve indicating that this derivative aggregates in a non-cooperative fashion. Combining these results, the authors concluded that the cooperative supramolecular polymerization no longer exists when the repulsive ionic character of the molecules dramatically increases, resulting in the formation of discrete objects with reduced degree of polymerization.

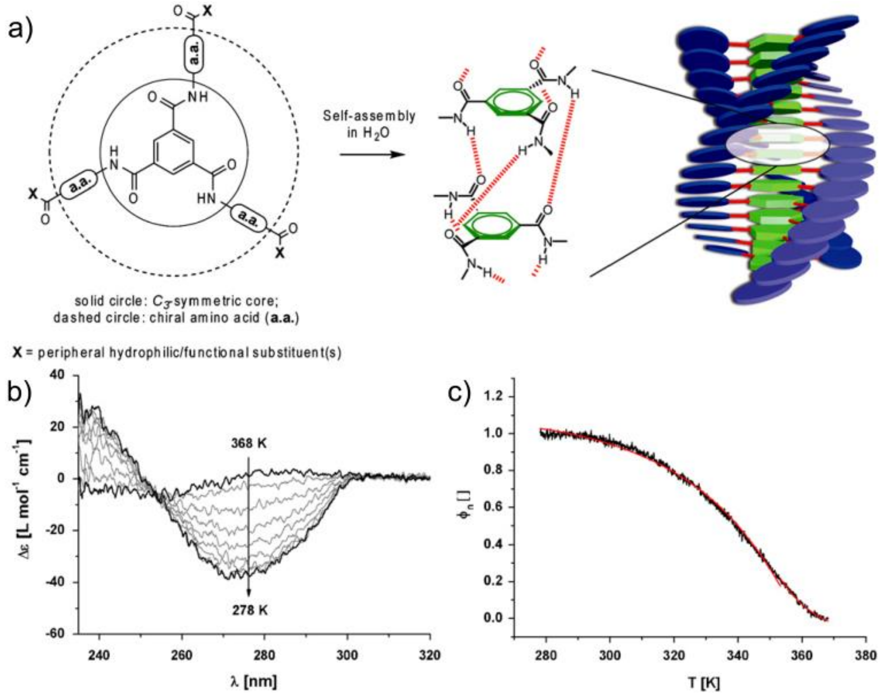

Fig. 33 a) Schematic representation of the self-assembly of discotic amphiphiles: the hydrophobic BTA core (solid circle) directs the self-assembly into a helical architecture; the hydrophobic, chiral amino acid substituents (dashed line) in the second layer determine the handedness and stability of the helix; the peripheral hydrophilic groups introduce an amphiphilic character to the design. b) Temperature-dependent CD spectra of discotic **100** (c = 7 x 10^{-6} M) in a c = 100 mM citrate buffer (pH 6) and overall NaCl concentration of 0.5 M. c) Corresponding normalized and fitted CD cooling curves, monitored at λ = 276 nm. Adapted with permission from ref. 191.

However, one has to note that the self-assembly process of **102** can also be controlled by changing the buffered environment.[191] An increase in the ionic strength of the aqueous solution by adding NaCl (0.5 M), instead of taking the pure citrate buffer, results in a change of the aggregation mechanism. As depicted in Fig. 33b,c the non-cooperative aggregation of **102** can thus be turned into a cooperative growth. This cooperative process results in the formation of extended rod-like structures, similarly to the assemblies formed by the less-charged BTA derivatives in citrate buffer.

Later on, the same group synthesized three further amphiphilic BTAs **103-105**, similarly decorated with a peripheral Gd^{III}-DTPA complex that is attached to the hydrophobic BTA core by different linking units (Chart 29).[192] Extensive studies show that the length of these hydrophobic spacer units directly dictates the self-assembly of the molecules. For the smallest discotic **103**, no self-assembled structures could be observed over the whole investigated concentration range, indicating that the molecule exists in its monomeric state. Upon elongation of the hydrophobic spacer, the aggregation ability of **104** shows a clear concentration-dependence while the largest discotics **105** directly aggregate into helical stacks in a non- or anti-cooperative manner.

Chart 29 Molecular structure of compounds **103-105**.

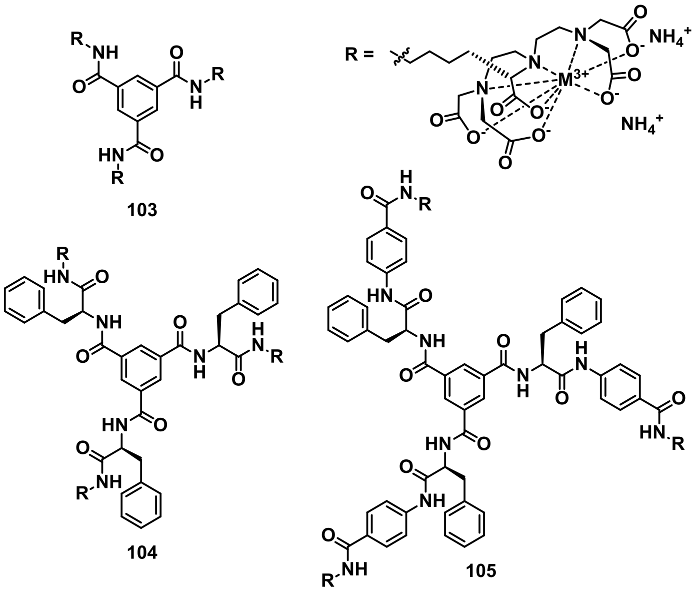

These significant differences between the derivatives indicate that the ability to form stable aggregates clearly depends on the size of the hydrophobic spacer unit.[192] Once the spacer reaches a certain length, it enables an efficient hydrophobic shielding of the triple hydrogen bonding amide functions of the BTA core through solvophobic effects that results in the formation of stable, helical aggregates.

Recently, Besenius and co-workers studied the individual self-assembly and co-assembly of two complementary supramolecular monomers in water (**106** and **107**).[193] They consist of a C_3-symmetrical core bearing pentapeptide sidearms (Chart 30). Those are decorated with either positively or negatively charged groups that are complementary to each other by hydrogen bonding interactions.

Chart 30 Molecular structure of the co-monomers **106** and **107**.

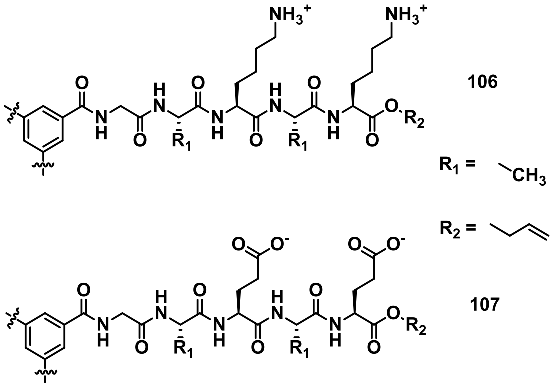

The investigation of **106** or **107** in isolation under buffered conditions revealed a CD spectrum that is indicative of a lack of secondary structure.[193] Although the monomeric units are expected to self-assemble by multiple hydrogen bondings between the amide groups, these attractive forces are outbalanced by strong repulsive electrostatic interactions between the anionic side chains in **107** and the cationic substituents in **106**, respectively. As a result, the monomers are unable to self-assemble separately and exist in their monomeric state in buffered solution.

However, if the oppositely charged monomers **106** and **107** are mixed in a 1:1 ratio an efficient supramolecular co-polymerization, driven by multiple hydrogen bonding and electrostatic interactions occurs (Fig. 34). As visualized by HRTEM, long one-dimensional nanorods with a uniform diameter of 4 nm are formed. The CD spectrum is characteristic for a hydrogen-bonded parallel β-sheet architecture that is formed in a cooperative fashion. The term “cooperative” was used by the authors to describe the aggregation by multiple non-covalent interactions, although the aggregation mechanism could not be elucidated due to a lack of required statistical theory for the linear co-polymerization. On the basis of the overall findings, it seems rational to argue that a cooperative co-polymerization would most likely occur, since for the co-aggregation attractive electrostatic and directional hydrogen bonding interactions support each other resulting in one-dimensional structures of high aspect ratio. Theoretical calculations confirmed the contribution of these attractive forces and revealed that water molecules are present between the central aromatic rings precluding further stabilization by π-π stacking of the aromatic cores.

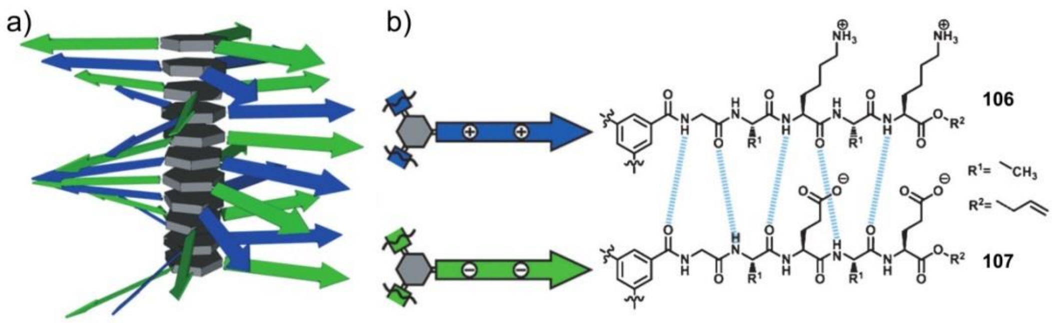

Fig. 34 a) Schematic representation of the supramolecular co-polymer and b) the anionic/cationic β-sheet-encoded dendritic co-monomers **106**/**107**. Reproduced with permission from ref. 193. Copyright (2013) Wiley-VCH Verlag GmbH & Co. KGaA, Weinheim.

Interestingly, as a result of the acidic and basic nature of the side chains of the monomers, the co-polymers are responsive towards pH changes.[193] Due to their ampholytic character a shift in the pH value of the aqueous medium directly results in a change of the ionic character of the molecules and of the self-assembled structures. Monitored by CD studies, the characteristics of parallel β-sheets at neutral pH remain intact in the range of 3.7 to 8.6, however the signal decreases upon leaving neutral conditions due to a weakening of the assemblies. Finally, at pH 3.6 and 8.9 the co-polymers completely disassemble due to the loss of salt bridges between the oppositely-charged subunits, indicated by CD characteristics corresponding to monomeric **106** and **107**. This disassembly was observed to be a reversible process since the co-aggregates can be recovered upon going back to neutral pH range.

Chapter 3

-

Results and discussion

Part I:

Pyridine-based OPE amphiphiles and their Pt(II) and Pd(II) complexes

3.1 Introduction

3.1.1 Supramolecular architectures formed by amphiphilic molecules

Compounds of amphiphilic nature are unique species since they combine both hydrophilic and hydrophobic moieties in their molecular structure.[7,179,194-196] Due to this special characteristic, amphiphiles are prone to self-assemble into different supramolecular architectures in polar media. During this process, the hydrophobic moieties pack tightly by non-covalent interactions to minimize the energetically unfavourable contact to the polar solvent molecules, while the hydrophilic moieties are oriented towards the surrounding polar medium creating a hydrophilic shell.[7,179,194-196]

The morphology of the assemblies formed by amphiphilic molecules with a hydrophobic chain and hydrophilic head in aqueous solution can be predicted by the dimensionless molecular packing parameter *P*.[197-201] This simple model, first described by Israelachvili,[199] defines the value *P* by the optimal polar head group area a_0, the volume of the hydrocarbon unit v and its critical chain length l_c to:

$$P = \frac{v}{a_o l_c} \qquad (22)$$

Thus, with the knowledge of the individual parameters a_0, v and l_c it is possible to calculate *P* for the corresponding amphiphile by eq. (22). This value gives information about the predicted geometry of the self-assembled structures according to Fig. 35.

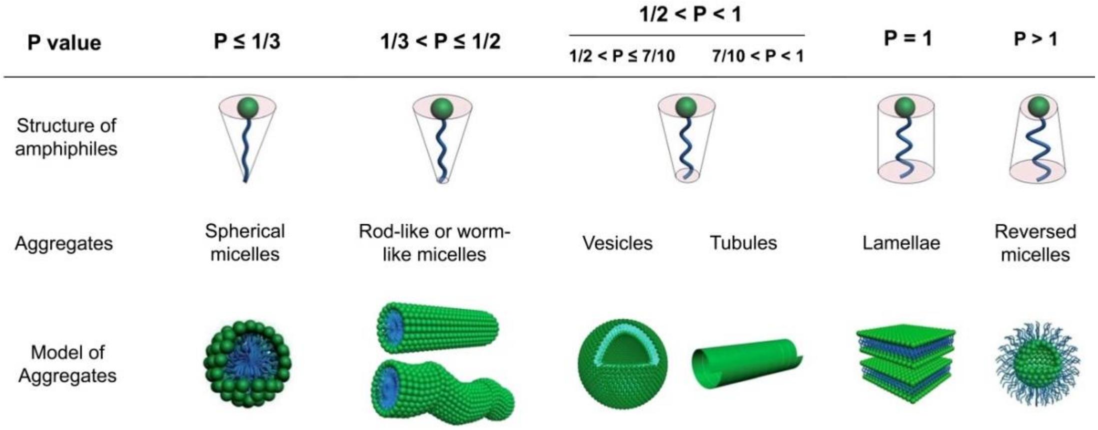

Fig. 35 Architecture of the self-assembled structures predicted by the critical packing parameter *P*. Adapted from ref. 201 with permission of The Royal Society of Chemistry.

For low P values ($P \leq 1/3$) a self-assembly into spherical micelles is predicted, while a slight increase in P ($1/3 < P \leq 1/2$) leads to the formation of rod- or worm-like micelles.[197-201] For values $1/2 < P \leq 1$ the formation of vesicles or tubules will most likely be obtained, whereas for $P = 1$ the reduced curvature results in the creation of lamellar structures. Finally, for a packing parameter above unity reversed micelles are expected.

Due to the non-covalent character of the interactions that stabilize the supramolecular nanostructures, the assemblies are responsive to various changes in the environmental conditions.[198] Changes concerning the pH, ionic strength, temperature, (UV) light as well as redox reactions or the addition of additives can act as external stimuli on the assemblies,[201-208] resulting in changes in the supramolecular system, i.e. disassembly or morphological transition.

In particular, the appropriate design of an amphiphilic molecule that can act as a ligand allows the creation of water-soluble metal complexes. The amphiphilic system benefits from novel properties upon coordination to a metal ion, such as the structural gain with different geometries around the metal centre,[9] interesting photophysical properties[10-14] and the possibility of metal-metal interactions.[18-20]

3.1.2 The importance of Pt(II) and Pd(II) complexes in different fields of research

Platinum(II) complexes have found application in numerous fields of research.[20,122] Since the first application of *cis*-diammine dichloroplatinum(II) (termed “*cis*-Platin”) in 1971, Pt(II) complexes play a crucial role in the antitumor therapy and still represent an active field of research.[209-216] Besides this important medical application, Pt(II) complexes are also in the focus of interest in supramolecular chemistry, which benefits from the square-planar geometry around the Pt(II) centre. In this way, a great number of Pt(II) complexes has been reported in literature that show well-defined supramolecular structures endowed with tunable photophysical properties.[10,11,14-20,122,217] In the abundance of different ligands, also Pt(II) complexes with pyridine-based ligands were investigated in the field of chemistry and medicine since several decades.[218-223]

Besides Pt(II) complexes, also Pd(II) complexes play an important role in different research areas, however they are much less established than their Pt(II) counterparts. The main focus of Pd(II) complexes is on their use concerning catalysis for different types of reactions,[224] however they are also considered as anti-tumour agents.[225-227] Furthermore, in the field of supramolecular chemistry Pd(II) coordination compounds are highly promising in the creation of new supramolecular structures that originates from their square-planar coordination geometry. In this regard, the Pd(II) nanocages of the Fujita group should be noted as a milestone in supramolecular chemistry, with application e.g. in host-guest chemistry or for the formation of TiO_2 nanoparticles of controlled size.[228-233]

On this basis, the use of amphiphilic ligands for the creation of metal complexes opens up new avenues towards a promising variety of supramolecular architectures in organic and aqueous media with fascinating properties.

3.2 Studies on pyridine-based ligand 1[*]

3.2.1 Synthesis of 1

The design of ligand **1** was motivated by the beneficial characteristics known for amphiphilic systems (see previous section), combined with the prospect of creating novel water-soluble complexes by subsequent coordination to different metal centres. Amphiphile **1** consists of a linear oligo(phenylene ethynylene) (OPE) core, a terminal pyridine ring and solubilizing hydrophilic glycol chains.

The synthetic pathway to achieve the target molecule **1** was first reported in the bachelor thesis of A. Martin under the supervision of C. Rest, Prof. Dr. G. Fernández and Prof. Dr. F. Würthner.[234] The first part of the synthetic route (Chart 31) towards the desired intermediates ((4-bromophenyl)ethynyl)trimethylsilane **109**,[235] triisopropyl((4-((tri-methylsilyl)ethynyl)phenyl)ethynyl)silane **110**,[235] ((4-ethynylphenyl)ethynyl)triiso-propylsilane **111**,[236] 5-bromobenzene-1,2,3-triol **113**,[237] 2-(2-(2-methoxyethoxy)-ethoxy)ethyl 4-methylbenzenesulfonate **116**[238] and 5-bromo-1,2,3-tris(2-(2-(2-methoxyethoxy)ethoxy)ethoxy)benzene **117**[239] was performed following reported procedures (unlike reported in ref. 238, the reaction towards **116** was not stirred under an argon atmosphere). As initial step, commercially available 1-bromo-4-iodobenzene (**108**) was reacted with trimethylsilyl (TMS) acetylene through a Sonogashira cross coupling reaction in the presence of the catalyst bis(triphenylphosphine)palladium(II) dichloride and copper(I) iodide in triethylamine. This reaction was carried out under argon at room temperature to selectively functionalize the iodine atom leading to **109** in 95% yield. By increasing the temperature to 100 °C in the next step, the bromine could be substituted by triisopropylsilyl (TIPS) acetylene via a further Sonogashira cross coupling reaction affording intermediate **110** in 85% yield. Subsequent selective deprotection of the TMS group by use of potassium carbonate gave intermediate **111** in a yield of 81%.

---

[*] Reproduced and adapted with permission from C. Rest, M. J. Mayoral, K. Fucke, J. Schellheimer, V. Stepanenko, G. Fernández, *Angew. Chem. Int. Ed.* **2014**, *53*, 700 - 705. Copyright (2014) Wiley-VCH Verlag GmbH & Co. KGaA, Weinheim.

Synthetic procedure towards **1** (section 3.2.1) and basic studies concerning the optical properties of **1** (section 3.2.2) have been initially elaborated and described in the bachelor thesis of A. Martin[234] under supervision of C. Rest, Prof. Dr. G. Fernández and Prof. Dr. F. Würthner, Julius-Maximilians-Universität Würzburg, **2012**.

Chart 31 Synthetic route to achieve the intermediates **111** and **117**.

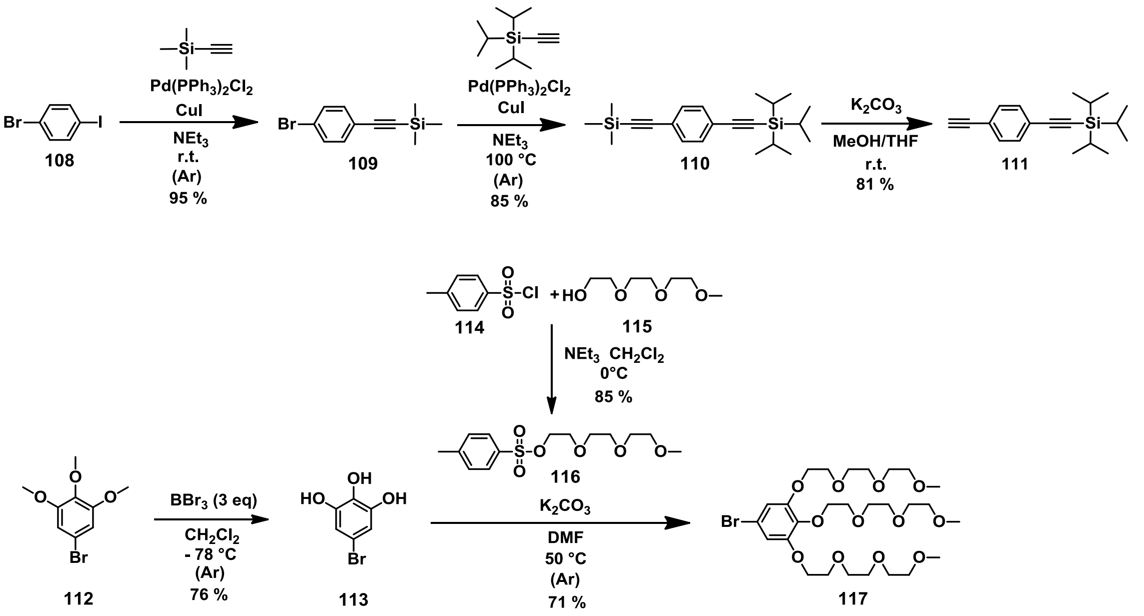

On the other hand, derivative **117** was synthesized starting from commercially available 5-bromo-1,2,3-trimethoxybenzene (**112**). The first step is the cleavage of the ether group, which was accomplished in 76% yield by treatment of **112** with boron tribromide at -78 °C under argon. Subsequent nucleophilic substitution reaction of **113** with synthesized intermediate **116** under basic conditions at 50 °C gave **117** in a yield of 71%. Compound **116** was previously realized through a nucleophilic substitution reaction of *p*-toluenesulfonyl chloride (**114**) with triethylene glycol monomethyl ether (**115**) in 85% yield.

The following steps (Chart 32) were performed following the reaction conditions presented in ref. 234. Derivatives **111** and **117** of the two reaction cascades were combined via a Sonogashira cross coupling protocol in the presence of a Pd(0) catalyst and copper(I) iodide in trimethylamine, isolating **118** in 73% yield. Removal of the TIPS protecting group by tetrabutylammonium fluoride gave the alkyne **119** in 83% yield. This compound was finally combined with 4-iodopyridine (**120**) in a further Sonogashira cross coupling reaction at 80 °C in the presence of a Pd(0) catalyst and copper(I) iodide to obtain the target amphiphile **1** in 84% yield. Changes in the eluents for column chromatography (silica gel) of the crude product (from (1) MeOH/toluene = 15:85, (2) MeOH/diethyl ether = 10:90 and (3) MeOH/CH_2Cl_2 = 5:95[234] to (1) MeOH/CH_2Cl_2 = 5:95 and (2) MeOH/diethyl ether = 10:90) reduced the required steps of purification. In this way, the yield of **1** could be improved from

62%[234] to 84%. Compound **1** was characterized by ^{1}H NMR, ^{13}C NMR, MALDI-TOF-MS and HRMS (ESI).

Chart 32 Synthetic steps to obtain the target molecule **1**.

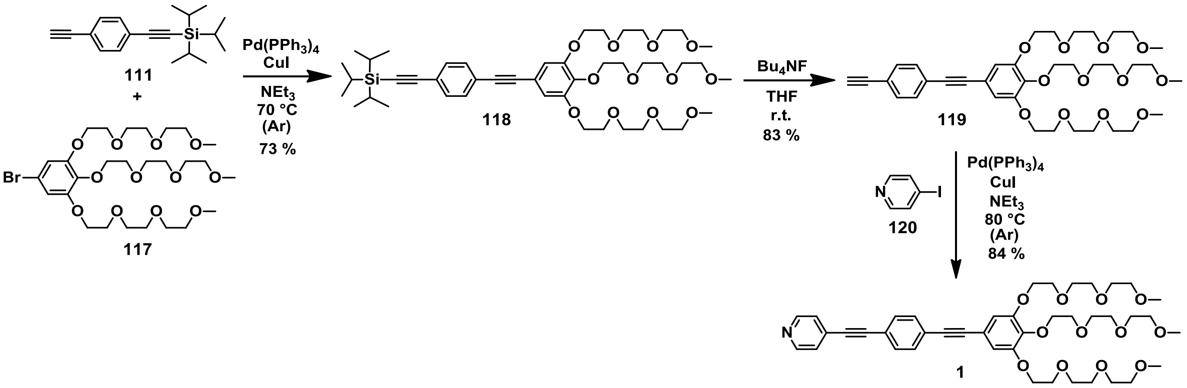

3.2.2 Optical properties of 1

3.2.2.1 Solvent-dependent characteristics of 1

The optical properties of OPE-based pyridine-substituted ligand **1** were investigated by UV/Vis absorption studies in different solvents. As depicted in Fig. 36, the samples show similar band shapes in the investigated organic solvents and water, with a maximum located at 329-332 nm.

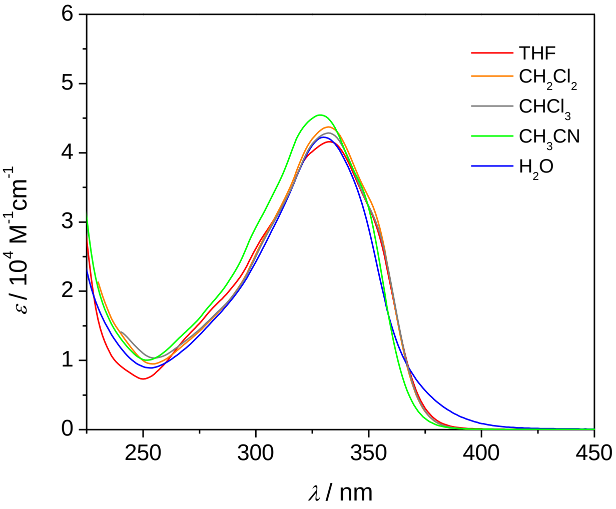

Fig. 36 Solvent-dependent UV/Vis absorption studies of **1** (1.6 - 1.8 x 10^{-5} M) at 295 K.

However, the absorption spectrum in water exhibits an additional red-shifted shoulder at ~380 nm that does not appear in organic media (Fig. 36). Regarding the emission spectra (λ_{ex} = 330 nm) of **1** in THF and water, the aqueous solution shows a significant decrease in the fluorescence intensity that comes along with a ~60 nm red-shift of the emission maximum (Fig. 37). These optical characteristics in absorption and fluorescence are distinctive of the stacking of the OPE units of **1** driven by π-π and hydrophobic interactions in water.[240]

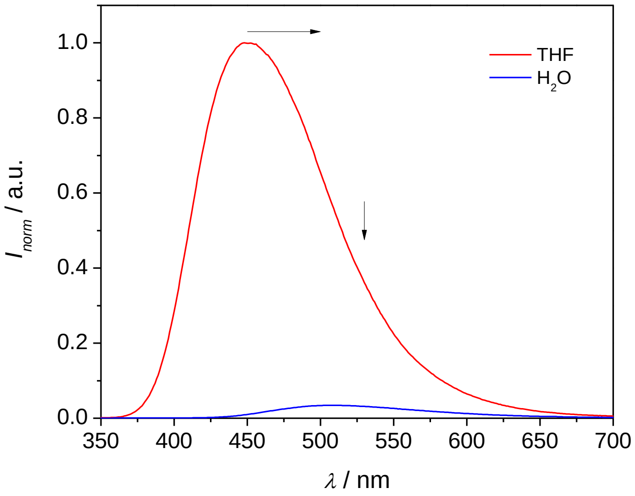

Fig. 37 Normalized fluorescence spectra of ligand **1** in THF and water (3.5 x 10^{-5} M) at room temperature (excitation wavelength λ_{ex} = 330 nm). Arrows indicate the spectral differences between the emission bands of **1** in THF and water.

3.2.2.2 Temperature-dependent self-assembly of 1

Since the solvent-dependent absorption (Fig. 36) and emission measurements (Fig. 37) suggest an aggregation process of **1** in water, this solvent was chosen to gain a closer insight into the self-assembly mechanism. In this regard, a sample of **1** in water (3.5 x 10^{-5} M) was investigated by temperature-dependent absorption studies. To ensure the formation of monomeric species, the solution was initially heated up to 363 K, upon which a slow cooling process (1 Kmin^{-1}) was applied in order to favour the formation of self-assembled species. The spectral changes between 327 and 279 K are depicted in Fig. 38a and show a bathochromic shift of the absorption maximum from 326 nm to 335 nm upon cooling, which is accompanied by the growth of a shoulder around 380 nm.

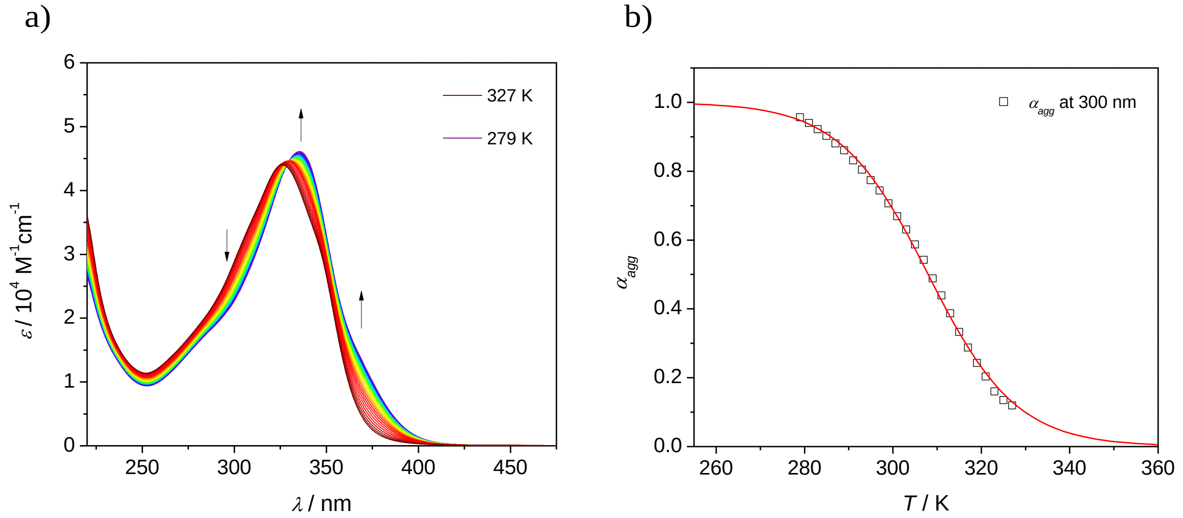

Fig. 38 Temperature-dependent UV/Vis absorption experiments of **1** in water (3.5 x 10^{-5} M) upon cooling with a rate of 1 Kmin^{-1}. a) Absorption spectra between 327 and 279 K. Arrows indicate the spectral changes upon decreasing temperature. b) Corresponding fraction of aggregated species (α_{agg}) at λ = 300 nm (black squares) against temperature and fitting of the spectral changes to the Boltzmann equation (red line, R^2 = 0.9984).

From these measurements the corresponding cooling curve was extracted by plotting the α_{agg} values at 300 nm as a function of temperature (Fig. 38b). The α_{agg} values were calculated according to eq. (1), which was already described in section 2.3.1. The spectral changes in Fig. 38b show a sigmoidal curve indicating that the aggregation of ligand **1** in water follows a non-cooperative pathway. The non-cooperative character could be confirmed by successful fitting of the data points to the Boltzmann model (R^2 = 0.9984), as shown by the red line in Fig. 38b. From this fit, the melting temperature (T_m), which is defined as the temperature value at α_{agg} = 0.5,[35] can be determined to be 308 K.

Furthermore, the temperature dependence for the number-average degree of polymerization (DP_N) and the equilibrium constant (K) can be obtained, according to the following equations. The value of DP_N at different temperatures was calculated from the degree of aggregation following equation (23)[35]:

$$DP_N(T) = \frac{1}{\sqrt{1-\alpha_{agg}(T)}} \qquad (23)$$

The DP_N value is further defined as:

$$DP_N(T) = \frac{1+\sqrt{4\,K(T)c_T+1}}{2} \qquad (24)$$

with c_T as the total concentration and K as the equilibrium constant.[35]

Herein, only the most important equations for the further analysis are given, according to ref. 35. A detailed derivation of those, with regard to the concentration-dependent isodesmic model can be found in the review of Würthner and co-workers published in 2009.[33]

Solving eq. (24) for the association constant K gives eq. (25):

$$K(T) = \frac{[2\left(DP_N(T)-\frac{1}{2}\right)]^2-1}{4\,c_T} \qquad (25)$$

By using eqs. (23) and (25), the values for DP_N and K at different temperatures for ligand **1** were calculated. In Fig. 39a the changes in DP_N against temperature are monitored. The data points in Fig. 39b represent the van't Hoff plot with the values of *ln K* as a function of T^{-1},[170] showing a linear behaviour.

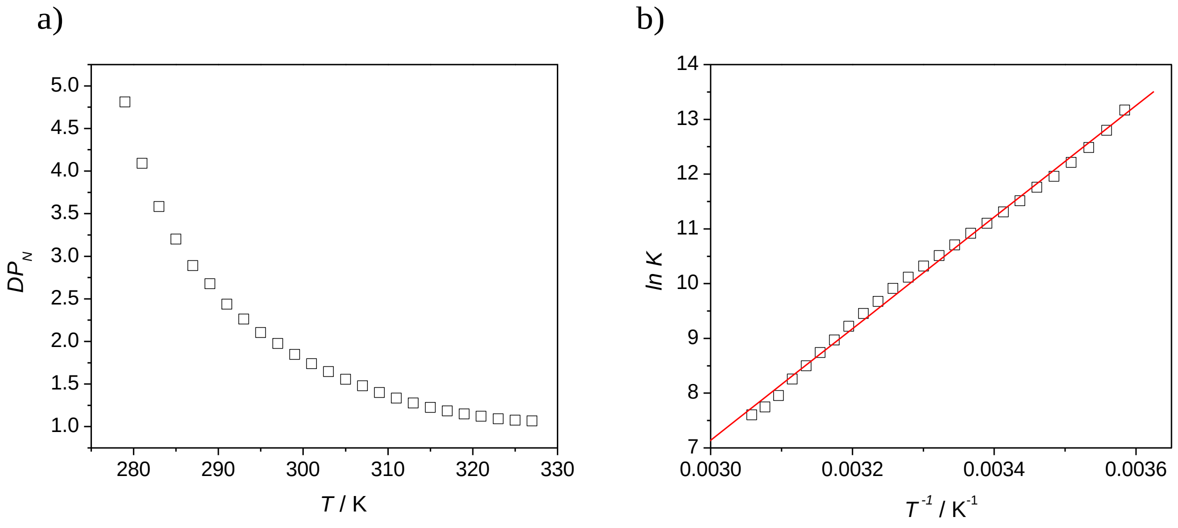

Fig. 39 Temperature-dependent UV/Vis absorption data of **1** in water (3.5 x 10^{-5} M) corresponding to the measurement shown in Fig. 38. a) Number-averaged degree of polymerization (DP_N) of **1** at different temperatures. b) Van't Hoff plot showing the values for *ln K* against T^{-1} (R^2 = 0.9961).

With these plots the standard values for the thermodynamic parameters can be determined. From Fig. 39a the number average degree of polymerization DP_N at 298 K can be defined to 1.9. The red line in Fig. 39b represents the regression line to the data points ($R^2 = 0.9961$) that enables the determination of the association constant K at 298 K to 5×10^4 M^{-1}. The corresponding standard enthalpy (ΔH^0) and entropy (ΔS^0) can be defined in terms of the linear form of the van't Hoff equation (26) with R as the universal gas constant:

$$\ln K = -\frac{\Delta H^0}{RT} + \frac{\Delta S^0}{R} \qquad (26)$$

Finally, the standard Gibbs free energy (ΔG^0) can be calculated according to equation (12) whose value is given in Table 1 together with all defined parameters at 298 K.

Table 1 Thermodynamic parameters associated to the self-assembly process of **1** in water (3.5×10^{-5} M) at a temperature of 298 K.

T_m [K]	DP_N	K [M^{-1}]	ΔH^0 [kJmol^{-1}]	ΔS^0 [Jmol^{-1}K^{-1}]	ΔG^0 [kJmol^{-1}]
308	1.9	5×10^4	-84.7±1.1	-194.7±3.6	-26.7±0.01

3.2.3 Microscopic studies and molecular modelling of 1

To visualize the architecture of the self-assembled species in water onto surfaces, an aqueous solution of **1** was investigated by transmission electron microscopy (TEM). Fig. 40 shows the TEM micrographs of a highly concentrated sample of **1** (1.6×10^{-3} M) after an aging time of 16 weeks onto a carbon-coated copper grid.

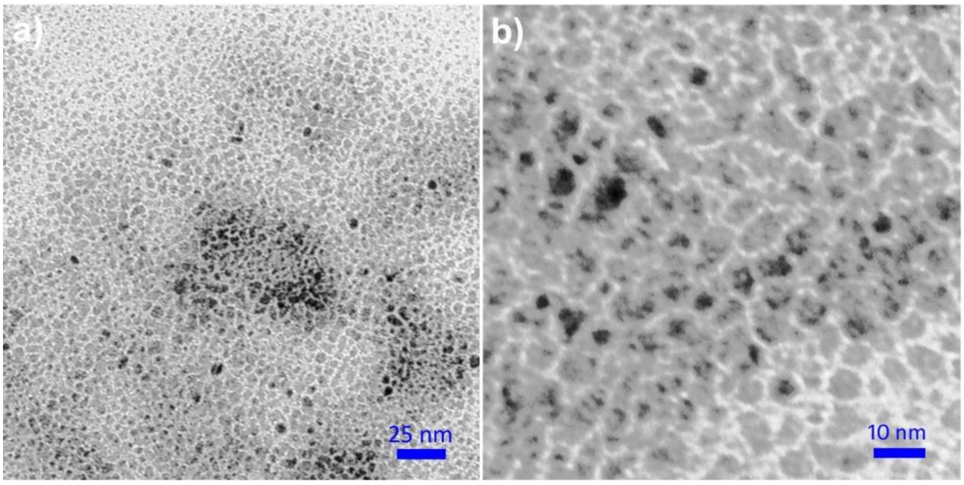

Fig. 40 TEM images of self-assembled ligand **1** in water (1.6×10^{-3} M) onto a carbon-coated copper grid. The studies were performed after an aging time of the sample of 16 weeks.

The images in Fig. 40 reveal an extended network constituted by small worm-like structures. The aggregates exhibit a regular width of 1.8±0.2 nm while the length can be estimated to several tens of nanometres.

Theoretical calculations have been performed to establish a correlation between the molecular structure and the aggregates observed by TEM. Fig. 41 shows the energy minimized structure of **1** calculated by the semi-empirical AM1 method.[241] The geometry optimization provides a planar OPE scaffold, as depicted in Fig. 41b. The glycol chains are not completely outstretched but show a bent arrangement that originates from their flexible character. To gain some insight into the dimension of a monomeric unit, the distance from the nitrogen atom of the pyridine unit to the first methylene group of the middle glycol chain (the atoms are highlighted in blue in Fig. 41a) was measured. With a length of 2.00 nm this value is in agreement with the diameter of the rods determined from TEM imaging (1.8±0.2 nm).

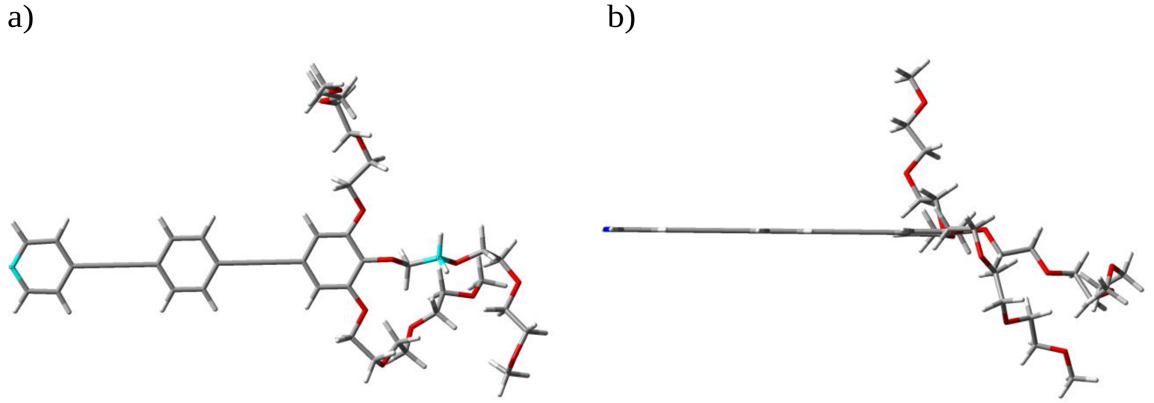

Fig. 41 Geometry optimized molecular structure of **1** by the semi-empirical approach AM1.[241] Top view (a) and side view (b).

The one-dimensional structures show a single-molecule diameter, as revealed by combined TEM imaging and geometry optimization. This leads to the suggested model shown in Fig. 42. The linear aggregates are most likely created by π-stacked OPE units that exhibit a small rotation angle to minimize the steric repulsion between the glycol chains. The inner part contains the aromatic OPE scaffolds while the glycol chains are directed to the surrounding medium. Due to the flexible character of the terminal chains, these can form a hydrophilic shell around the inner aromatic block to minimize the unfavourable contact of the π-surfaces with water. The attractive aromatic contacts between the OPE units are most likely supported by strong hydrophobic interactions in aqueous medium, resulting in a relatively high association constant (5 x 10^4 M^{-1}).

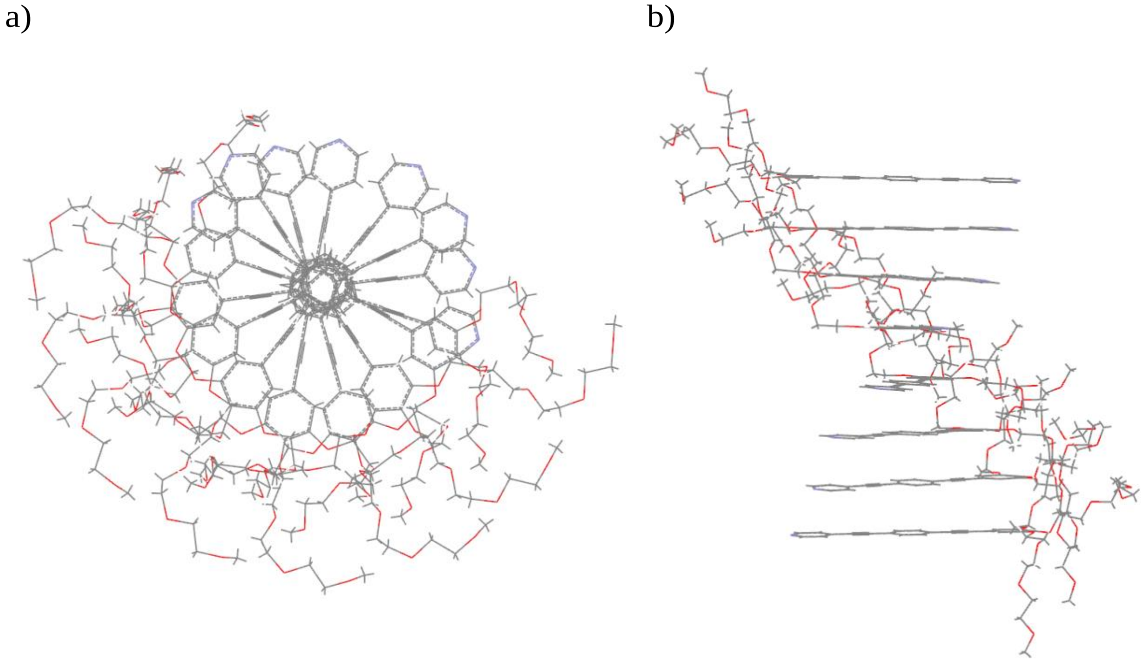

Fig. 42 Cartoon representation of the suggested self-assembly of **1** resulting in linear *π*-stacks with a slight mutual rotation (distance between central OPE units ≤3.5 Å).

Close contact between the formed *π*-stacks results in a porous network, as visualized by the microscopic images in Fig. 40. As already mentioned, the driving force for the stacking of **1** can be seen in attractive aromatic interactions between the planar OPE cores that are supported by the hydrophobic effect in water. However, the absence of additional intermolecular forces appears to be responsible for the non-cooperative fashion of the self-assembly that results in the formation of relatively small, linear aggregates.

3.3 Studies on the pyridine-based Pt(II) complex 2[*]

3.3.1 Synthesis of 2

The metal-ligating ability of the previously described ligand **1** was exploited for the creation of amphiphilic metal complexes.

For the synthesis of Pt(II) complex **2** (Chart 33), two equivalents of freshly purified **1** were combined with bis(benzonitrile)dichloroplatinum(II) in degassed benzene. The mixture under argon was heated to 87 °C for six days until the reaction control by ^{1}H NMR revealed almost complete consumption of the free ligand **1** (Fig. 43). Upon complexation to the Pt(II) centre, the ^{1}H NMR spectrum shows a significant downfield shift of the signal corresponding to the alpha protons of the pyridine units. Initially, two new signals appear around 8.75-8.9 ppm (one of them very small, ratio 1:0.06 after a reaction time of two days) that might be assigned to the formation of the *trans*- and, to a much smaller extent, the *cis*-isomer of the desired complex (see red spectrum in Fig. 43). The undesired, supposed *cis*-signal diminishes up to a ratio of 1:0.02 after six days. Purification of the reaction mixture by column chromatography (silica gel, CH_2Cl_2/MeOH = 95.5:4.5) provided the pure *trans*-Pt(II) complex **2** in a yield of 69%. Compound **2** was characterized by ^{1}H NMR, ^{13}C NMR, HRMS (ESI) and elemental analysis.

Chart 33 Synthetic procedure to synthesize the target Pt(II) complex **2**.

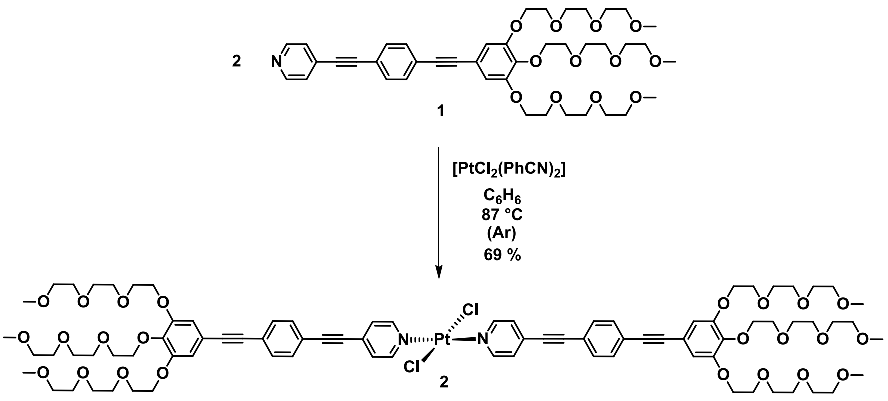

---

[*] Reproduced and adapted with permission from C. Rest, M. J. Mayoral, K. Fucke, J. Schellheimer, V. Stepanenko, G. Fernández, *Angew. Chem. Int. Ed.* **2014**, *53*, 700 - 705. Copyright (2014) Wiley-VCH Verlag GmbH & Co. KGaA, Weinheim.

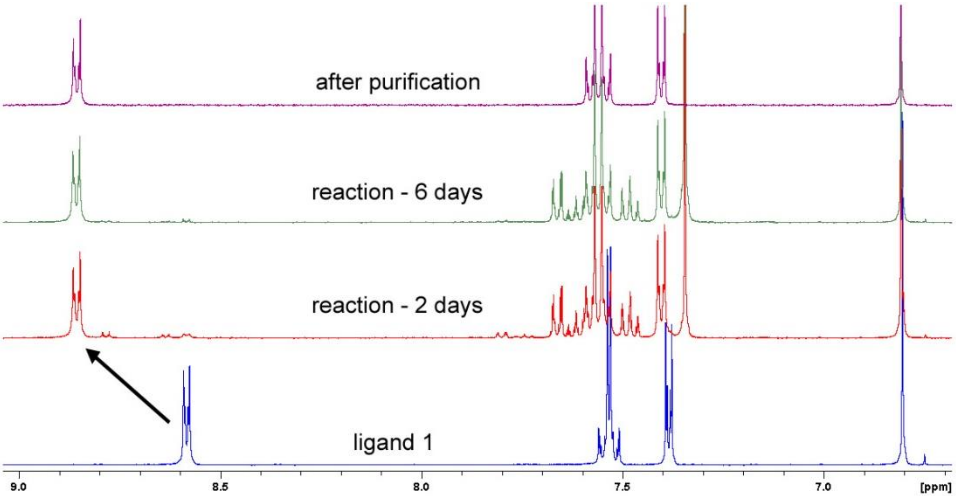

Fig. 43 ^{1}H NMR spectra (CD_2Cl_2, 400 MHz, 300 K) of the reaction shown in Chart 33 to achieve the target Pt(II) complex **2**.

3.3.2 Optical properties of 2

3.3.2.1 Solvent-dependent characteristics of 2 in solution and temperature-dependent behaviour in water

The optical properties of **2** were investigated by solvent-dependent UV/Vis absorption studies in organic solvents of different polarity and water (Fig. 44).

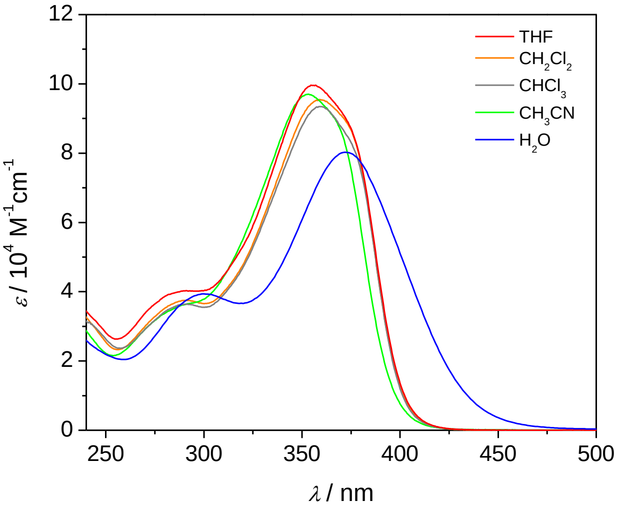

Fig. 44 Solvent-dependent UV/Vis absorption experiments for complex **2** (1.1 - 1.2 x 10^{-5} M).

The band shape of **2** in solution is similar for all investigated organic media with a maximum around 355 nm. However, in water the absorption intensity is reduced and the maximum significantly red-shifted (372 nm) compared to the organic solvents. The spectral features of **2** in organic media can be attributed to a molecularly dissolved state, while the red-shift and decrease of the absorption band strongly suggest a self-assembly process of **2** in aqueous solution.

Thus, water was the first solvent of choice to further study the aggregation of **2** by temperature-dependent measurements. Fig. 45 shows the UV/Vis absorption experiment of an aqueous solution of **2** (1.0 x 10^{-5} M) upon heating between 283 and 363 K. As the absorption spectra in Fig. 45 reveal, only minor spectral changes are observed upon increasing the temperature from 283 to 363 K, indicating that the aggregates of **2** do not disassemble upon heating under these conditions.

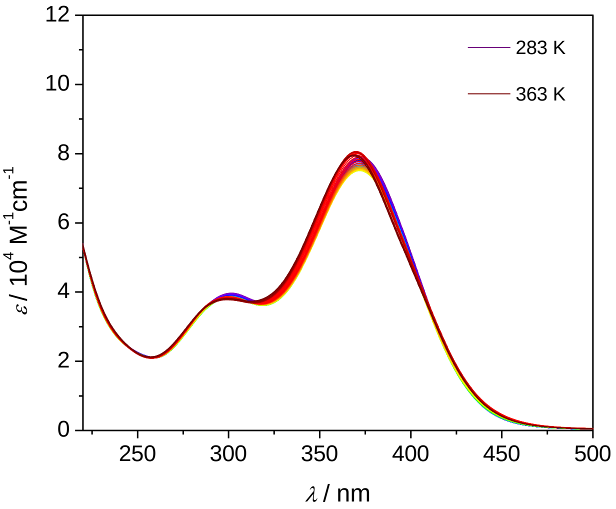

Fig. 45 Temperature-dependent UV/Vis absorption experiment of Pt(II) complex **2** in water (1.0 x 10^{-5} M) upon heating the solution from 283 to 363 K with 1 $Kmin^{-1}$.

The presented behaviour is in clear contrast to that of ligand **1** in water (3.5 x 10^{-5} M), in which a clear transition from monomeric to aggregated species could be followed by decreasing temperature (Fig. 38). The remarkable difference between **1** and **2** suggests a significantly increased aggregation strength of the complex **2**. The stronger self-assembly can be most likely assigned to an extension of the aromatic surface upon coordination of the ligand to the Pt(II) centre that may also be supported by the involvement of the Cl-Pt(II)-Cl fragment in intermolecular interactions.

3.3.2.2 Temperature-dependent self-assembly of 2 in methanol/water mixtures

It has been previously observed, that **2** is strongly bound in pure water even at an elevated temperature of 363 K (Fig. 45). To enable a deaggregation of the species upon heating, the effect of methanol (MeOH) as co-solvent was investigated. In this regard, temperature-dependent absorption measurements of the Pt(II) complex **2** in MeOH/water mixtures of varying ratio were performed.

For the preparation of all investigated solutions of **2** in MeOH/water, the samples of **2** in the required solvent mixture were briefly heated to facilitate the dissolution of the compound.

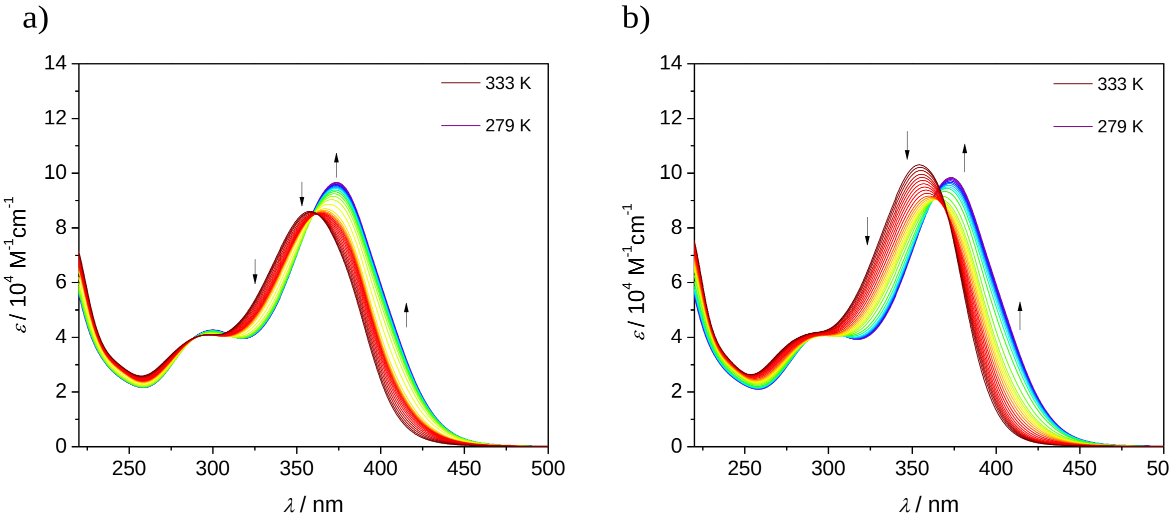

Fig. 46 Temperature-dependent UV/Vis absorption experiments of Pt(II) complex **2** in MeOH/water mixtures upon cooling the solution from 333 to 279 K with 1 $Kmin^{-1}$. a) MeOH/water = 50:50 (1.3 x 10^{-4} M). b) MeOH/water = 60:40 (1.2 x 10^{-4} M). Arrows indicate the spectral changes upon cooling.

With a MeOH content below 50%, the temperature-dependent UV/Vis absorption experiment (between 333 and 279 K) does not show a transition of **2** to fully monomeric species at high temperature, due to strong hydrophobic interactions between the molecules in this solvent composition. Consequently, the MeOH content was further increased to reduce the solvophobic effect. Fig. 46 shows the temperature-dependent experiments of **2** in aqueous solution with a MeOH content of 50% and 60%, respectively. The studies in MeOH/water = 50:50 (Fig. 46a) reveal a hypsochromic shift of the absorption band for high temperatures that is centred at

358 nm for 333 K. With a MeOH content of 60% (Fig. 46b) this effect is even more pronounced with a displacement of the absorption maximum to 354 nm upon heating. However, closer inspection reveals that the deaggregation at 333 K is not complete since still at high temperature spectral changes occur. Upon further increase of the MeOH content to 70% (Fig. 47a) the entire transition from monomeric species at high temperature to an aggregated state at low temperature can be visualized. The compound is completely disassembled at high temperature with an absorption maximum at 353 nm. This pronounced band decreases upon cooling at the expense of a red-shifted aggregate band centred at 370 nm for 279 K. If the MeOH content is increased to 80% (Fig. 47b) the monomeric form dominates over the entire temperature range and complex **2** only becomes partially aggregated upon cooling, as evident by a slight red-shift of the maximum to 361 nm.

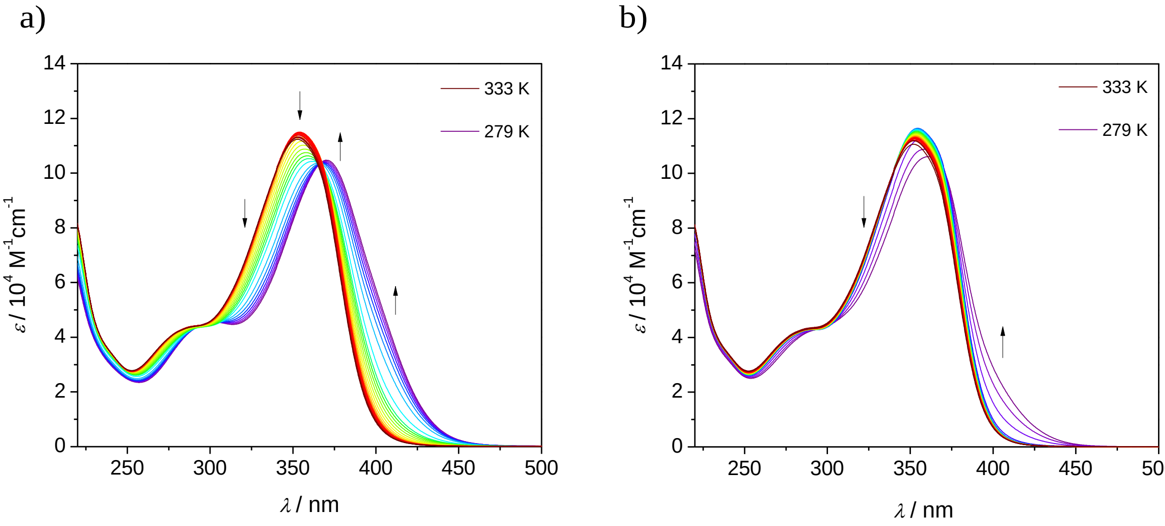

Fig. 47 Temperature-dependent UV/Vis absorption experiments of Pt(II) complex **2** in MeOH/water mixtures upon cooling the solution from 333 to 279 K with 1 Kmin^{-1}. a) MeOH/water = 70:30 (1.3 x 10^{-4} M). b) MeOH/water = 80:20 (1.2 x 10^{-4} M). Arrows indicate the spectral changes upon cooling.

Consequently, the mixture of MeOH/water = 70:30 was optimal to perform the temperature-dependent studies. Fig. 48 shows the analogous temperature-dependent UV/Vis measurement in MeOH/water = 70:30 to Fig. 47a at a higher concentration of 2.3 x 10^{-4} M. Since both samples are appropriate to monitor the aggregation process, this concentration range was chosen to record the corresponding curves.

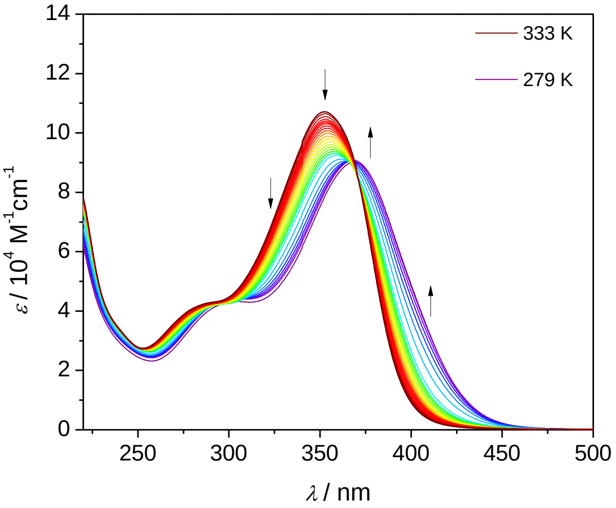

Fig. 48 Temperature-dependent UV/Vis absorption experiments of Pt(II) complex **2** in MeOH/water = 70:30 (2.3×10^{-4} M) upon cooling the solution from 333 to 279 K with 1 Kmin^{-1}. Arrows indicate the spectral changes upon cooling.

The temperature-dependent curves were recorded at a detection wavelength λ = 420 nm by heating the samples of **2** in a rate of 0.2 Kmin^{-1}. The values for α_{agg} against temperature, calculated according to equation (1), are depicted in Fig. 49. The resulting curves monitor the transition from an almost aggregated state at ~279 K to the monomeric species upon heating and are clearly non-sigmoidal in shape. This behaviour indicates that the self-assembly process follows a cooperative pathway. Accordingly, the nucleation-elongation model of ten Eikelder, Markvoort and Meijer[44,45] was used to describe the spectral changes.

The successful fitting of the experimental data to the *ten Eikelder-Markvoort-Meijer*-model (coloured lines in Fig. 49) confirmed the cooperative character of the supramolecular polymerization. As described previously (Chapter 2), this implies that the process is divided into a nucleation (dimerization) and an elongation event. The fitting gave the enthalpy for the elongation process ($\Delta H°$), the nucleation penalty ($\Delta H°_{nuc}$), the entropy ($\Delta S°$) and the elongation temperature T_e (Table 2). The enthalpy of elongation lies in the range of -108 to -120 kJmol^{-1}. The entropy change is assumed by the cooperative model to be equal for the nucleation and elongation step and corresponds to ~-0.33 kJmol^{-1}K^{-1}.

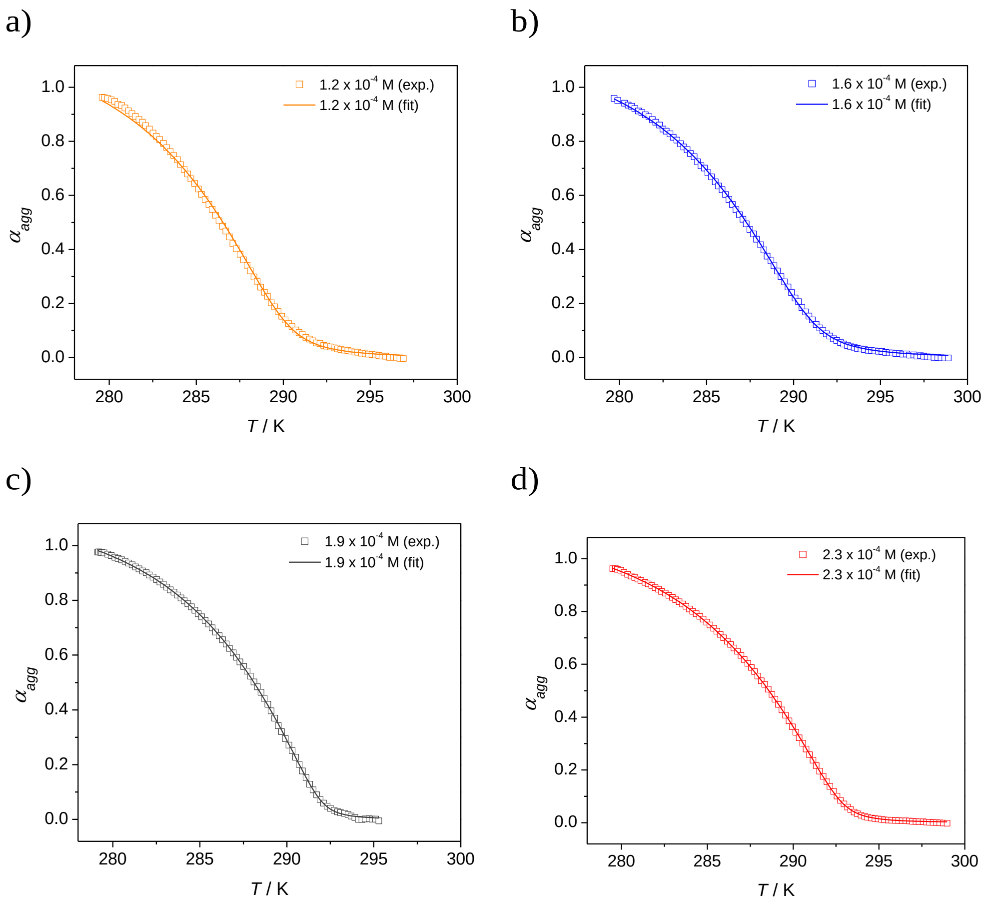

Fig. 49 Plot of α_{agg} against temperature for **2** (λ = 420 nm) at different concentrations from 1.2 - 2.3 x 10^{-4} M in MeOH/water = 70:30. The temperature was increased from 279 K with a rate of 0.2 Kmin^{-1}. The coloured lines represent the fitting of the spectral changes to the *ten Eikelder-Markvoort-Meijer*-model[44,45].

The binding constants K_{nuc} and K_e at the corresponding elongation temperatures T_e can be calculated according to equations (15) and (16), respectively (Table 2). For the nucleation constant, values from 7 - 64 M^{-1} could be calculated, while the elongation constants are significantly higher ranging from 4 - 8 x 10^3 M^{-1}. This relationship between K_{nuc} and K_e can also be expressed by the cooperativity factor σ (eq. (17)) yielding values between 1 x 10^{-3} and 10 x 10^{-3}. Those low σ values indicate a highly cooperative behaviour of the Pt(II) complex **2**.

The obtained elongation temperatures T_e and the corresponding binding constants K_e at T_e can be combined in the van't Hoff analysis upon plotting the values for $\ln K_e$ as a function of T_e^{-1} (Fig. 50).

Table 2 Thermodynamic parameters characterizing the temperature-dependent UV/Vis absorption experiments of **2** in MeOH/water (70:30) at different concentrations. Values for $\Delta H°$, $\Delta H°_{nuc}$, $\Delta S°$ and T_e were extracted from the fitting to the *ten Eikelder-Markvoort-Meijer*-model[44,45] and K_{nuc}, K_e and σ were calculated at the corresponding elongation temperature T_e.

conc. [M]	**$\Delta H°$** [$kJmol^{-1}$]	**$\Delta H°_{nuc}$** [$kJmol^{-1}$]	**$\Delta S°$** [$kJmol^{-1}K^{-1}$]	**T_e** [K]	**K_{nuc}** [M^{-1}]	**K_e** [M^{-1}]	**σ**
1.2×10^{-4}	-120.0±7.1	-11.6±0.6	-0.3402±0.0246	289.2±0.1	63.8	8.0×10^{3}	7.9×10^{-3}
1.6×10^{-4}	-119.7±2.9	-11.1±0.2	-0.3399±0.0100	290.0±0.1	64.3	6.4×10^{3}	1.0×10^{-2}
1.9×10^{-4}	-116.9±1.1	-16.2±0.2	-0.3298±0.0037	291.4±0.03	6.6	5.3×10^{3}	1.3×10^{-3}
2.3×10^{-4}	-107.5±0.7	-15.3±0.1	-0.2983±0.0023	292.2±0.02	8.0	4.3×10^{3}	1.8×10^{-3}

The regression line (red line in Fig. 50) can be described by the linear form of the van't Hoff equation (eq. (26)) that allows the calculation of ΔH^0 and ΔS^0 (Table 3). Finally, the standard Gibbs free energy ΔG^0 is defined using eq. (12) (Table 3).

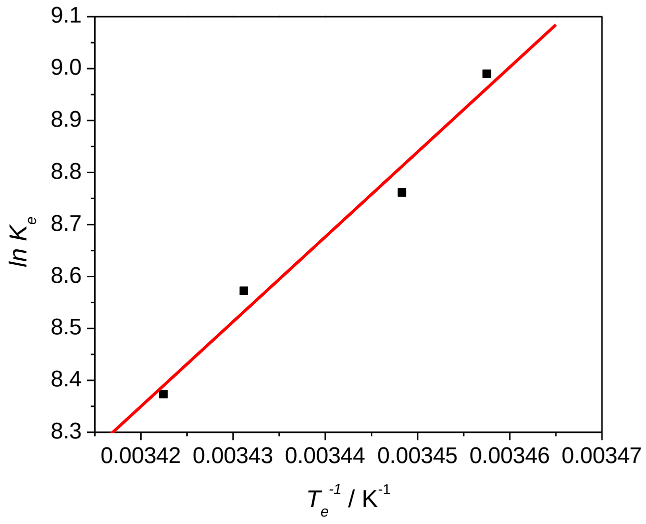

Fig. 50 Van't Hoff plot of the $ln\,K_e$ values of **2** in MeOH/water (70:30) against T_e^{-1} (R^2 = 0.9626). T_e and the corresponding K_e values at T_e were determined by temperature-dependent UV/Vis experiments at different concentrations (Table 2).

Table 3 Thermodynamic parameters associated to the self-assembly process of **2** in MeOH/water = 70:30 at 298 K.

$\Delta H°$ [$kJmol^{-1}$]	**$\Delta S°$** [$kJmol^{-1}K^{-1}$]	**$\Delta G°$** [$kJmol^{-1}$]
-135.7±15.3	-0.3946±0.0527	-18.1±0.4

3.3.3 Gelation and microscopic studies of 2

To further characterize the self-assembled structures of **2**, their gelation ability in solvents of different polarity was tested. Previous measurements revealed that the self-assembly of **2** is accompanied by a red-shift of the absorption band (Fig. 44 - Fig. 48). This colour change becomes apparent by the naked eye showing an intensification from pale to deep yellow upon aggregation. Above a certain concentration, complex **2** showed gelation of different alcohols and water. The samples shown in Fig. 51 were prepared by briefly heating the sample to facilitate dissolution of the compound. The gelation ability was tested by the "stable-to-inversion of the test tube" method when the samples had cooled down to room temperature. While the gels in alcohols form immediately, complete dissolution of **2** in water takes some hours at r.t. and gelation occurs after several days due to slow kinetics in this medium[183] (some-days aged sample depicted in Fig. 51).

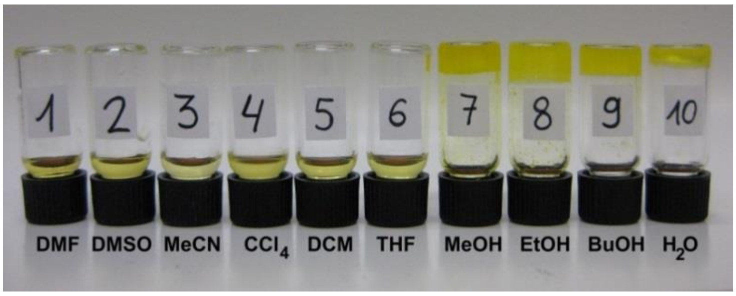

Fig. 51 Gelation studies of **2** showing the monomeric and self-assembled state (gel) of **2** in different solvents. The samples demonstrate the yellow colour intensification upon aggregation.

Table 4 Critical gelation concentration (*cgc*) for the gels of **2** in methanol, ethanol and butanol.

	MeOH (fridge)	**EtOH (at r.t.)**	**BuOH (at r.t.)**
***cgc* [mg/ml]**	16.2	12.0	7.9

Regarding the aggregation in alcohols, the stability of the gels significantly increases when moving from methanol (MeOH) over ethanol (EtOH) to butanol (BuOH). This behaviour also becomes noticeable upon comparing the critical gelation concentration (*cgc*) for EtOH and BuOH that could be determined at room temperature to 12 mg/ml and 8 mg/ml, respectively (Table 4). Due to the reduced stability of the gel in methanol, the value was defined at lower temperature to be 16 mg/ml.

The gels in ethanol and butanol show a remarkable temperature-responsiveness that is concomitant with a colour change (Fig. 52). Upon heating the sample, the yellow gel at room temperature converts into a pale yellow solution. However, the gel is reformed after the sample has cooled down to room temperature again.

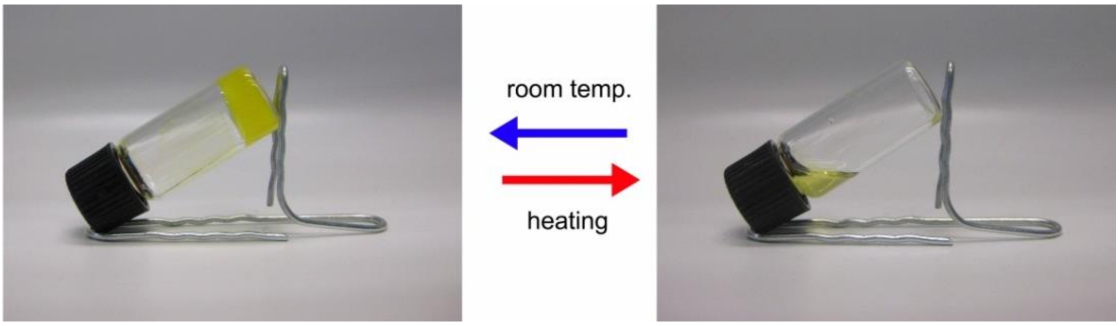

Fig. 52 Gelation studies showing the reversible gel-sol transition of a highly concentrated sample of **2** in ethanol (10 mM).

Fig. 53 depicts the normalized absorption spectra of thin films of the gels compared to the red-shifted band of the highly aggregated solution of **2** in water (1.2 x 10^{-5} M, from Fig. 44). The band shape of the gel material is identical to the spectrum of the species in aqueous solution that further confirms the strongly bound state of the molecules in the gels.

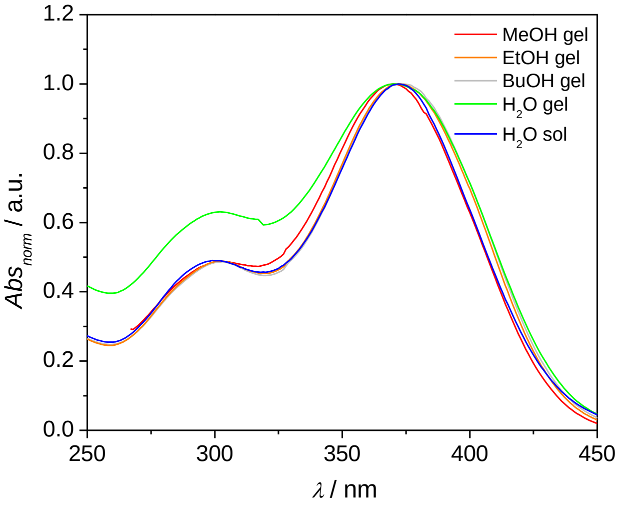

Fig. 53 UV/Vis absorption experiments of thin-films of gels of **2** in MeOH, EtOH, BuOH and water compared to the 1.2 x 10^{-5} M solution of **2** in water. Each spectrum was normalized in the corresponding absorption maximum.

To visualize the morphology of the highly self-assembled material, gels in water and ethanol were investigated by AFM (diluted samples) and SEM, as depicted in Fig. 54 and Fig. 55.

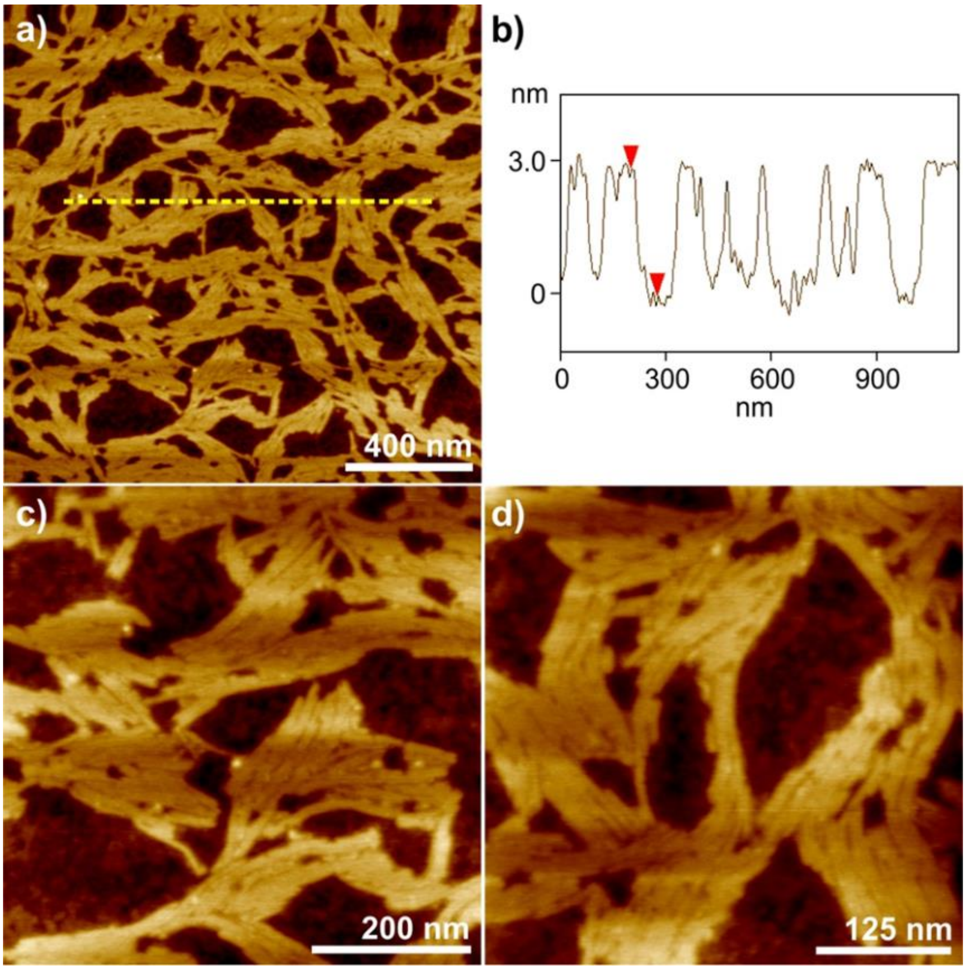

Fig. 54 Tapping-mode height (a, c, d) AFM images of a diluted gel solution of **2** (2.2 x 10^{-3} M) in water. The samples were prepared by drop-casting of gel solutions in water onto mica. (b) depicts the cross-section analysis along of the yellow line 1-1’ in image (a). *Z* scale is 6 nm.

In Fig. 54 the AFM images of a diluted gel of **2** (2.2 x 10^{-3} M) in water onto mica are presented. These show a network of elongate, thin fibres with a height and diameter of 3.0±0.2 nm and 5.8±0.3 nm, respectively, while the length of the aggregates corresponds to up to 500 nm. SEM studies of a non-diluted gel of **2** in water similarly show entangled fibres that create a dense network, as depicted in Fig. 55.

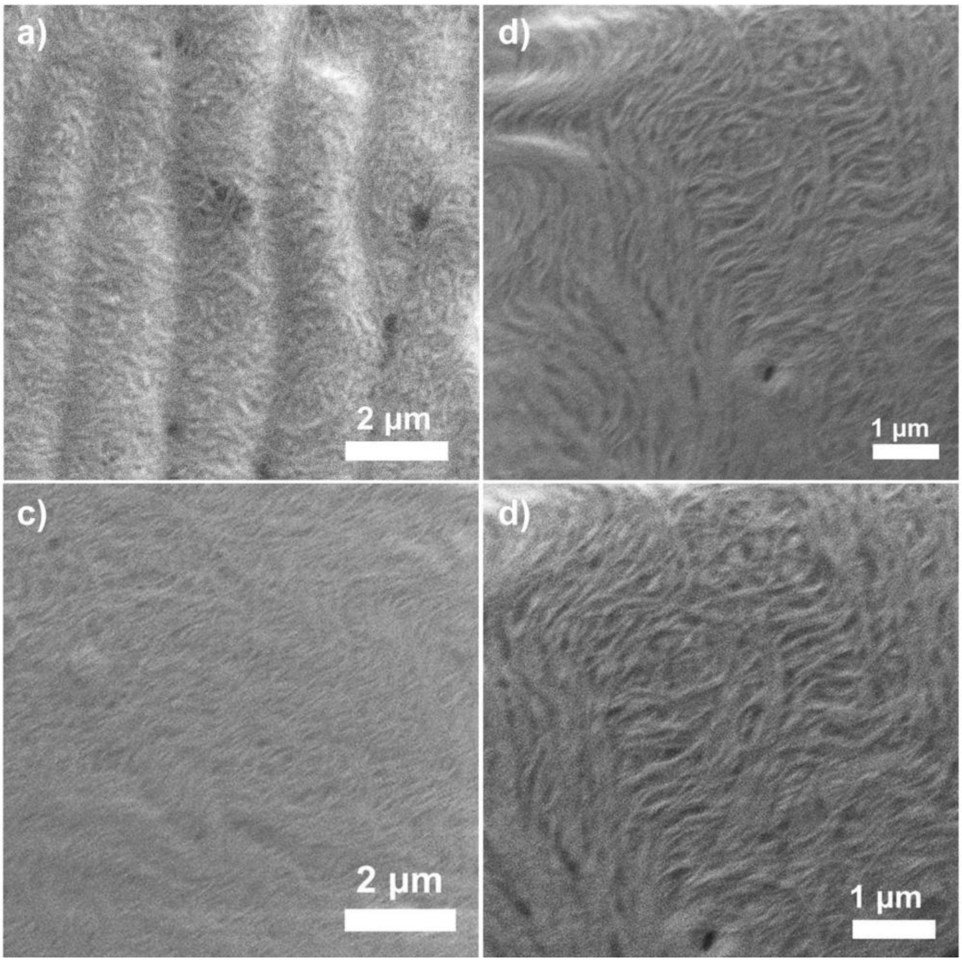

Fig. 55 SEM images of a gel of **2** in water (~9.0 x 10^{-3} M). The samples were prepared by drop-casting a gel in water onto coverslip.

Next, DLS measurements were performed in order to gain insight into the particle size in solution.[242,243] To allow a further investigation of the fibrillar aggregates of **2**, the dense hydrogel was sufficiently diluted (~10 times) with water and the filtered solution investigated at different detection angles from 11.1° to 90.0°. As depicted in Fig. 56b, the autocorrelation functions exhibit a sigmoidal shape. The corresponding unimodal size distributions at different angles (Fig. 56a) reveal aggregates of different dimensions with maxima centred between ~80 nm and ~320 nm. Furthermore, the angular dependence of the detected sizes indicates that the formed assemblies are of non-spherical geometry.[244] These findings are in accordance with the morphology of the gel material visualized by different imaging techniques that revealed long, one-dimensional structures with a length of up to 500 nm.

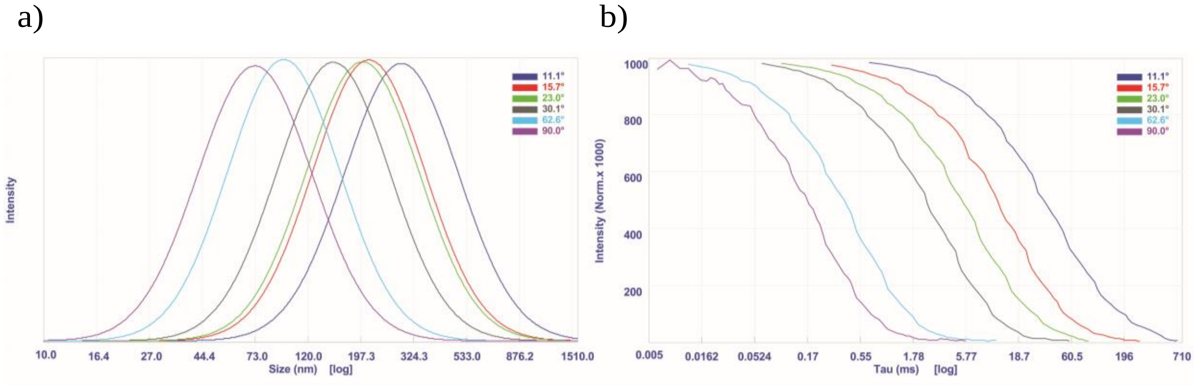

Fig. 56 Unimodal size distributions (a) from CONTIN analysis of the autocorrelation function (b) of a diluted gel of **2** in water (298 K).

For the gel in ethanol microscopic investigations (Fig. 57 and Fig. 58) reveal comparable results to the hydrogel. SEM studies of the original gel show a dense network of thin fibrillar assemblies, as depicted in Fig. 57. These structures are consistent with the morphology observed by AFM (Fig. 58) for the diluted sample (4.9 x 10^{-3} M). AFM imaging allows defining a regular diameter of 6.0±0.5 nm for the one-dimensional aggregates.

Comparison of the recorded microscopic images in alcohols and water reveals very similar structures for both media, which is in full agreement with the UV/Vis absorption spectra of the gels (Fig. 53). On the basis of these results, the subunits of **2** show an identical arrangement in both media upon formation of the gel.

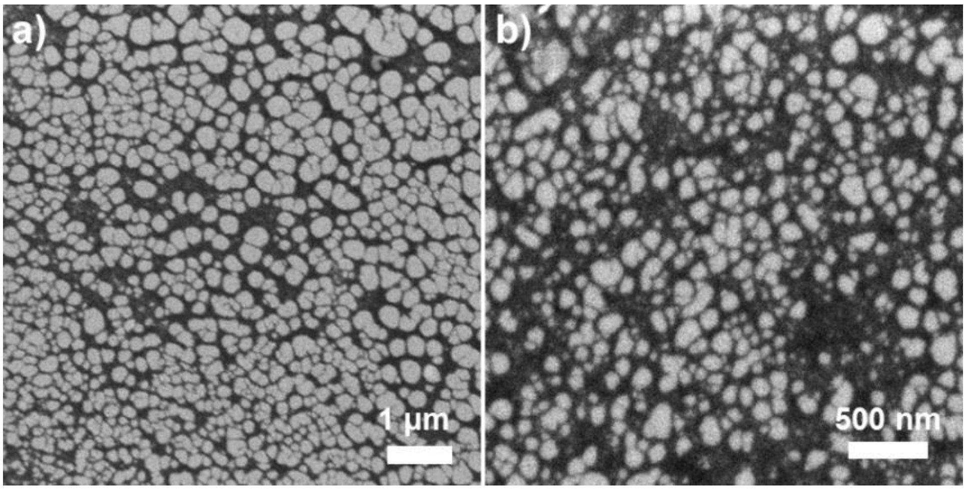

Fig. 57 SEM images of a gel of **2** in ethanol (9.7 x 10^{-3} M). Sample was prepared by drop-casting of gel solution in ethanol onto silicon wafer.

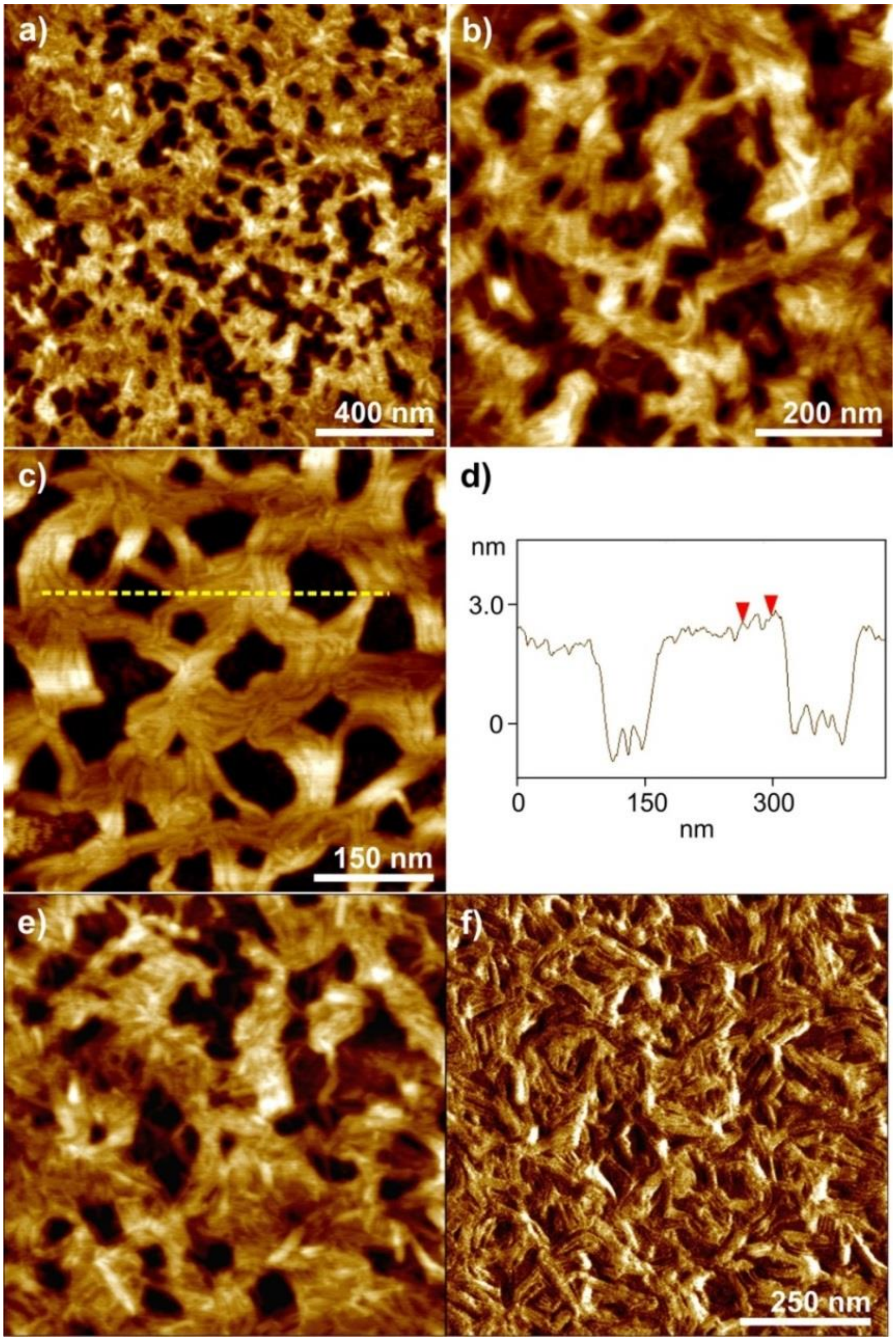

Fig. 58 AFM height (a, b, c, e) and phase (f) images of a diluted gel solution of **2** in ethanol (4.9 x 10^{-3} M). The samples were prepared by drop-casting a diluted gel solution in ethanol onto mica. Image (d) shows the cross section analysis along the yellow line in image (c). Z scale is 6 nm.

3.3.4 ^{1}H NMR analysis of 2

3.3.4.1 Concentration-dependent ^{1}H NMR studies of 2

The microscopic studies in the previous section provided an insight into the morphology of the highly aggregated gel material onto surfaces. These studies have been complemented by 1D and 2D ^{1}H NMR experiments, which can be exploited to propose a molecular packing within the self-assembled structures in solution. Initially, concentration-dependent studies of complex **2** in polar solution were performed. To this end, all samples of **2** in these media were prepared by briefly heating to facilitate the dissolution of the compound.

The first series was recorded in a methanol/dichloromethane (90:10) mixture between 1.1 x 10^{-2} M and 1.5 x 10^{-4} M. Dichloromethane was chosen as co-solvent to slightly decrease the aggregation tendency of the complex and thus increase the stability of the samples. All samples of **2** were prepared in advance and measured after an aging time of around one day. For the series of spectra in Fig. 59 a simultaneous shielding and broadening of the signals upon increasing concentration can be obtained.

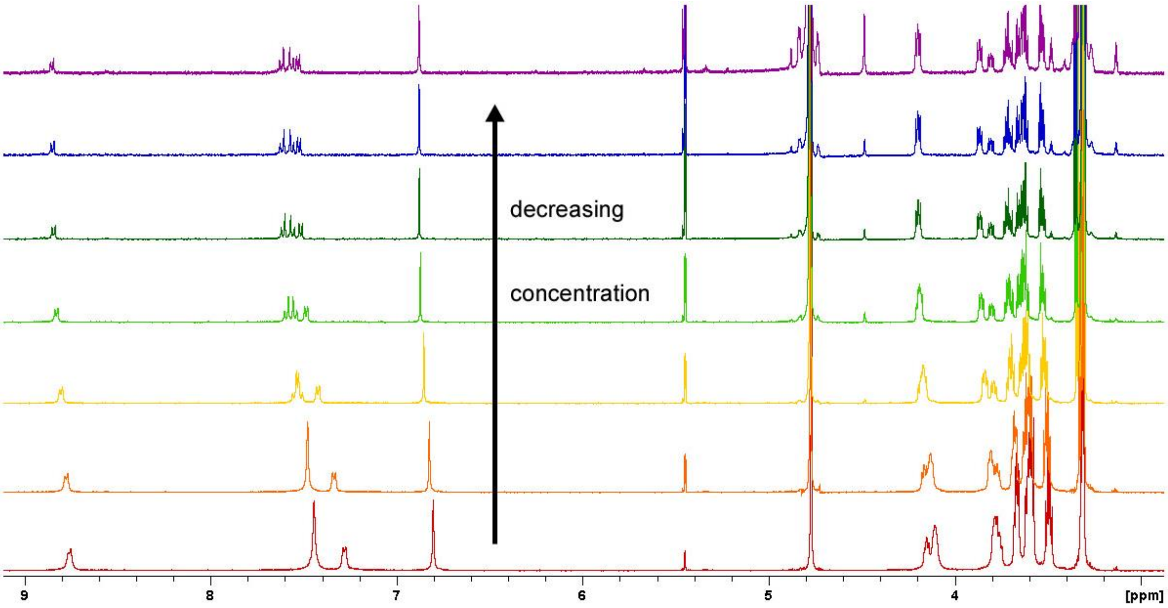

Fig. 59 Concentration-dependent ^{1}H NMR spectra (400 MHz, 300 K) of complex **2** in MeOD/CD_2Cl_2 = 90:10 one day after preparation. Investigated concentrations: 1.5 x 10^{-4} M (purple), 3.3 x 10^{-4} M (blue), 6.3 x 10^{-4} M (green), 1.3 x 10^{-3} M (light-green), 2.5 x 10^{-3} M (yellow), 5.2 x 10^{-3} M (orange) and 1.1 x 10^{-2} M (red).

The spectral changes can better be distinguished by enlarging the two relevant regions covering the protons of the aromatic rings (Fig. 60a) and those corresponding to the glycol chains (Fig. 60b).

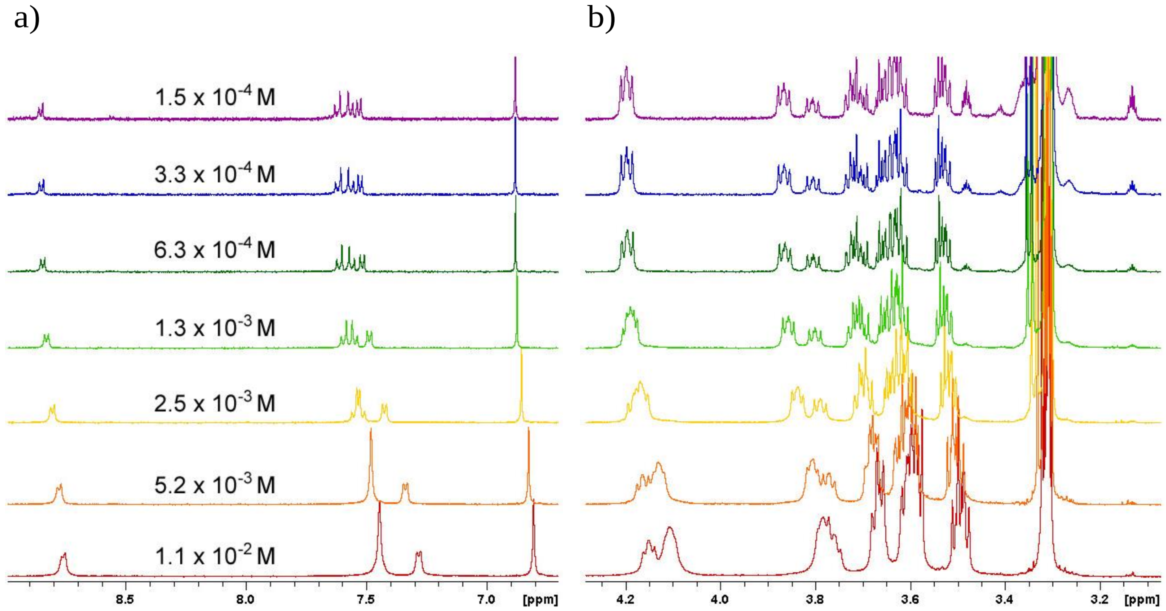

Fig. 60 Partial concentration-dependent ^{1}H NMR spectra (400 MHz, 300 K) of complex **2** in MeOD/CD_2Cl_2 = 90:10 from 1.5 x 10^{-4} M (purple) to 1.1 x 10^{-2} M (red). Zoom into selected regions corresponding to the protons of the pyridine and OPE units (a) and those of the glycol chains (b) of Fig. 59.

The subsequent broadening of the signals is indicative for non-covalent interactions between the subunits that drive the self-assembly in MeOD/CD_2Cl_2 (90:10). The fact that the aromatic resonances as well as the signals of the terminal chains are affected by the concentration changes clearly suggests that both aromatic and glycol units are involved in the aggregation process of **2**.

Subsequently, the solvent was changed from MeOD/CD_2Cl_2 to pure MeOD to achieve an even higher aggregation strength. As shown in Fig. 61, the ^{1}H NMR studies in pure deuterated methanol show sufficiently sharp signals in the investigated concentration range. The series started with the highest concentration (1.3 x 10^{-2} M) and all samples were investigated immediately after preparation to ensure their stability during measurement time. Dilution of the sample was performed by adding the corresponding volume of MeOD, so the final concentration of **2** is always half of the previous mother solution.

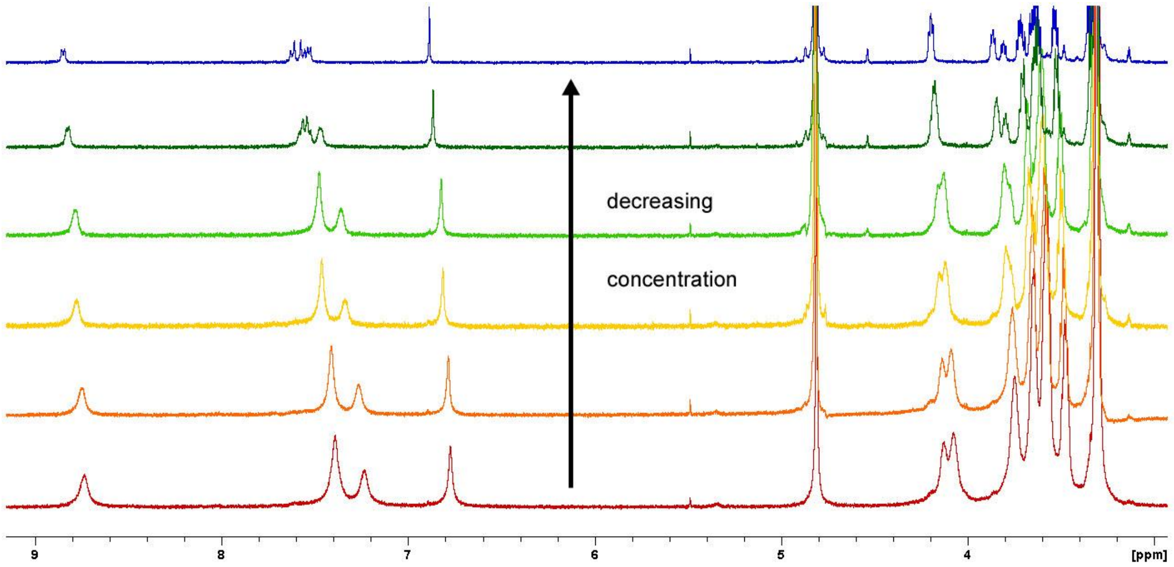

Fig. 61 Concentration-dependent ^{1}H NMR spectra (400 MHz, 300 K) of complex **2** in MeOD. Investigated concentrations: 4.0 x 10^{-4} M (blue), 8.1 x 10^{-4} M (green), 1.6 x 10^{-3} M (light-green), 3.2 x 10^{-3} M (yellow), 6.5 x 10^{-3} M (orange) and 1.3 x 10^{-2} M (red).

As can be seen in the ^{1}H NMR spectra (Fig. 61 and zoom-in in Fig. 62), the behaviour of **2** in deuterated methanol is similar to that in the solvent mixture with 10% of CD_2Cl_2, which indicates a similar aggregation fashion in both media.

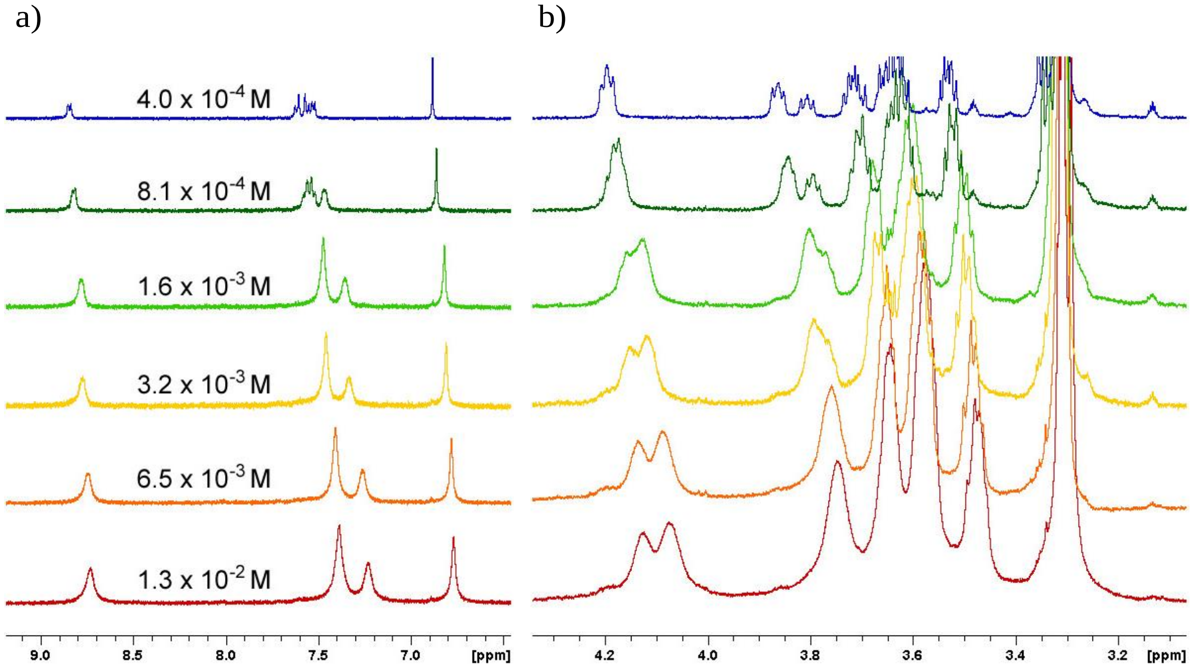

Fig. 62 Partial concentration-dependent ^{1}H NMR spectra (400 MHz, 300 K) of complex **2** in MeOD from 4.0 x 10^{-4} M (blue) to 1.3 x 10^{-2} M (red). Zoom into selected regions corresponding to the protons of the pyridine and OPE units (a) and those of the glycol chains (b) of Fig. 61.

However and as expected, the broadening of the signals in pure methanol is even more pronounced at comparable concentration as a result of the stronger aggregation tendency of **2** in the former medium. As can better be observed in Fig. 62 this significant broadening concerns all signals, indicating that all protons of **2** are involved in intermolecular interactions.

3.3.4.2 Two-dimensional ^{1}H NMR studies of 2

2D ^{1}H NMR measurements were performed to derive an aggregate structure for **2** in solution. Initially, the ROESY (rotating-frame Overhauser effect spectroscopy) experiment in pure dichloromethane is depicted (Fig. 63), a solvent in which **2** exists in its monomeric state (see absorption studies in Fig. 44). As expected, the ^{1}H NMR spectrum shows sharp signals and in the 2D plot no cross-peaks for intermolecular interactions appear. This clearly confirms the assumption that complex **2** is molecularly dissolved in this medium.

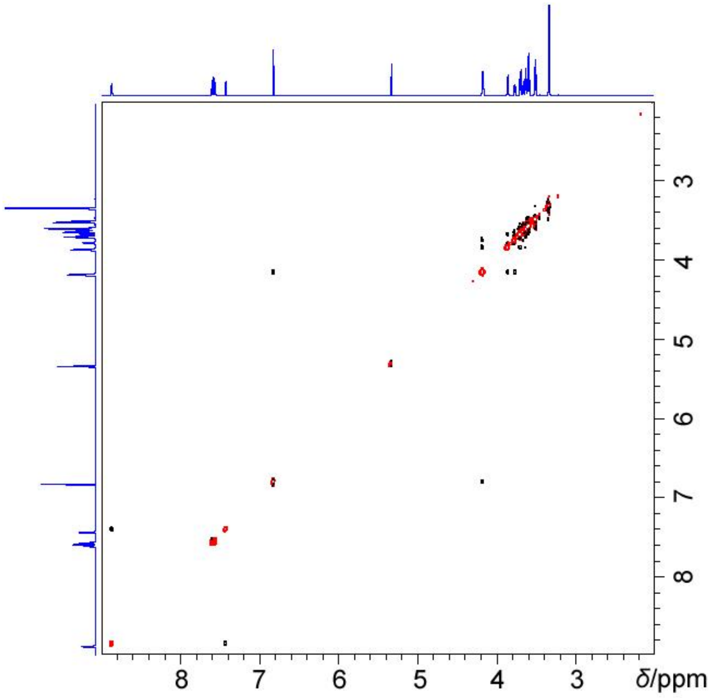

Fig. 63 600 MHz ROESY NMR spectrum of **2** in CD_2Cl_2 at 7.9 x 10^{-3} M (293 K).

To allow a comparison between the monomeric and aggregated state, ROESY studies of **2** in MeOD solution (1.4 x 10^{-2} M) were performed. To achieve an aggregate solution in MeOD that is stable during the time required for the 2D ^{1}H NMR measurement and furthermore shows sufficiently sharp signals to assign them to the individual protons, for the preparation a minimal amount of CD_2Cl_2 was added followed by briefly heating of the sample. In contrast to CD_2Cl_2, the aggregate spectrum (Fig. 64) reveals several through-space coupling signals for protons that come into spatial proximity.

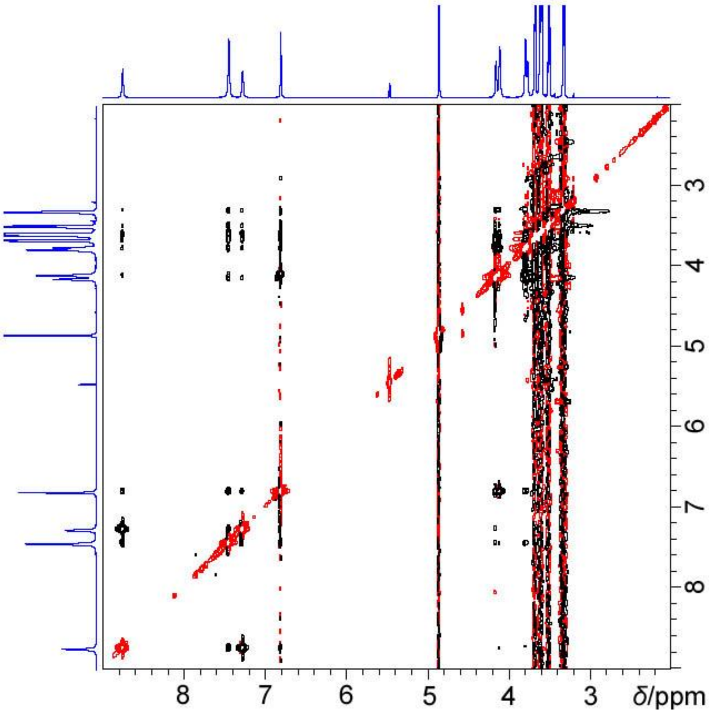

Fig. 64 600 MHz ROESY NMR spectrum of **2** in MeOD solution at 1.4 x 10^{-2} M (293 K).

To facilitate the assignment of the cross-peaks to the corresponding signals, a zoom-in of the regions of interest is shown in Fig. 65. The spectrum in Fig. 65a presents coupling signals between the aromatic OPE protons with orange and green circles highlighting the intramolecular and intermolecular contacts, respectively.

In Fig. 65a clear cross-peaks between the proton H_d belonging to the outer phenylene rings and protons H_a and H_b of the pyridine units can be identified, indicating a non-symmetric aggregate structure. Furthermore, Fig. 65b reveals proximity of the glycol chains to all protons of the aromatic OPE units (see green circles in Fig. 65b).

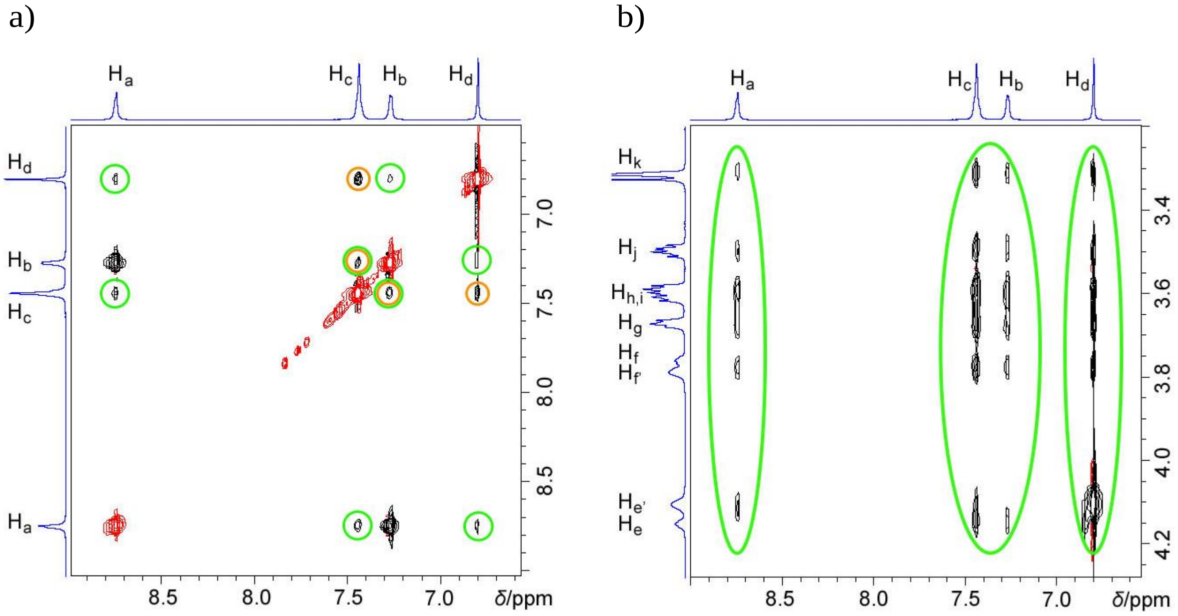

Fig. 65 Zoom into the ROESY NMR spectrum (600 MHz, 293 K) of **2** at 1.4 x 10^{-2} M shown in Fig. 64. The orange and green circles highlight intra- and intermolecular through-space coupling signals, respectively.

Taking into consideration all coupling signals, a model with a slipped arrangement of the molecules is proposed, as shown in Fig. 66. The Pt(II) centres are highlighted in purple, the chlorine atoms in green, the nitrogen atoms in blue and the oxygen in red colour.

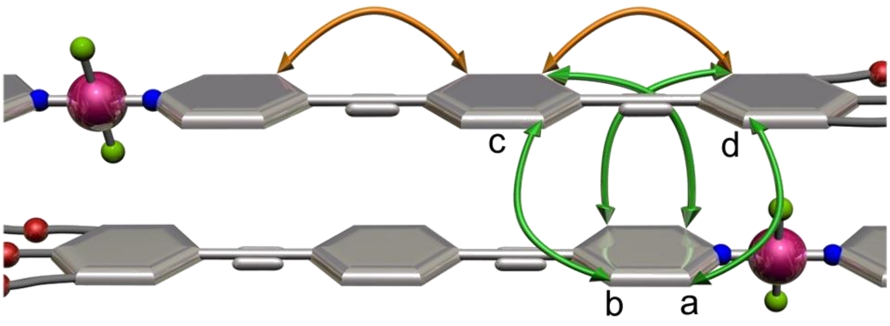

Fig. 66 Representation of the molecular organization of **2** in the self-assembled structures on the basis of ROESY studies.

The orange arrows depict the intramolecular contacts between the neighbouring protons $H_c \cdots H_d$ and $H_b \cdots H_c$, while the green ones stand for the intermolecular couplings, as observed in ROESY studies (Fig. 65a). To realize all of the through-space coupling signals, the Cl-Pt(II)-Cl centre has to be located on top of the outer aromatic ring of the neighbouring molecule in the stack (Fig. 66). This molecular organization also satisfies the intermolecular cross-peaks between H_c of one unit with H_a and H_b of another molecule. Further stabilization most likely results from attractive π-π contacts between the aromatic surfaces and $Cl\cdots\pi$ interactions in solution. The additional cross-peaks in Fig. 65b between protons of the glycol chains ($H_{e\text{-}k}$) and the aromatic protons $H_{a\text{–}d}$ suggest that the glycol chains of one molecule are in close contact with the π-surface of an adjacent unit within the self-assembled structure.

3.3.5 X-Ray characterization of 2

Needle-shaped, yellow single crystals suitable for X-ray diffraction measurements could be obtained from a concentrated methanol solution of **2**. The crystal structure was solved and refined in the triclinic space group $P\bar{1}$ with half a molecule in the asymmetric unit.

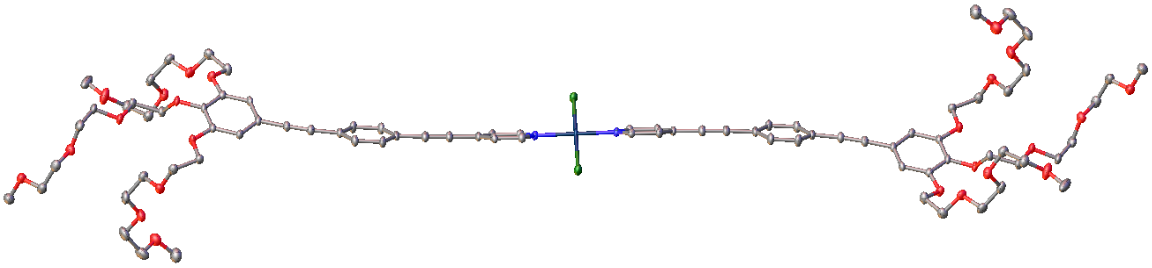

Fig. 67 Molecular structure of **2**. Element (colour): carbon (grey), oxygen (red), nitrogen (blue), platinum (dark blue), chlorine (green). Hydrogen atoms are omitted for clarity, atomic displacement ellipsoids are drawn at 50% probability.

In Fig. 67 the arrangement of one molecule in the crystalline packing is depicted. The molecule adopts a symmetrical structure with regard to the metal centre (inversion centre) that shows a N-Pt(II)-N angle of 180.0°. The OPE surfaces adopt a relatively planar arrangement with a slight twist between the phenylene rings.

With regard to the aromatic surface of the pyridyl groups, the chlorine atoms (green) are twisted out of the plane (Fig. 67 and Fig. 68). Upon closer examination, an angle of 47° can be identified considering the orientation of the plane defined by the pyridyl groups (highlighted in blue in Fig. 68) towards the plane defined by the chlorine, nitrogen atoms and the Pt(II) centre (highlighted in red in Fig. 68). The Cl-Pt(II)-Cl arrangement is perfectly linear with an angle of 180° while the N-Pt(II)-Cl angle corresponds to 90.1°. This organization results in a perfect square-planar geometry around the metal centre. Furthermore, the chlorine atoms are located 1.63 Å above/below the plane defined by the pyridyl rings (Fig. 68).

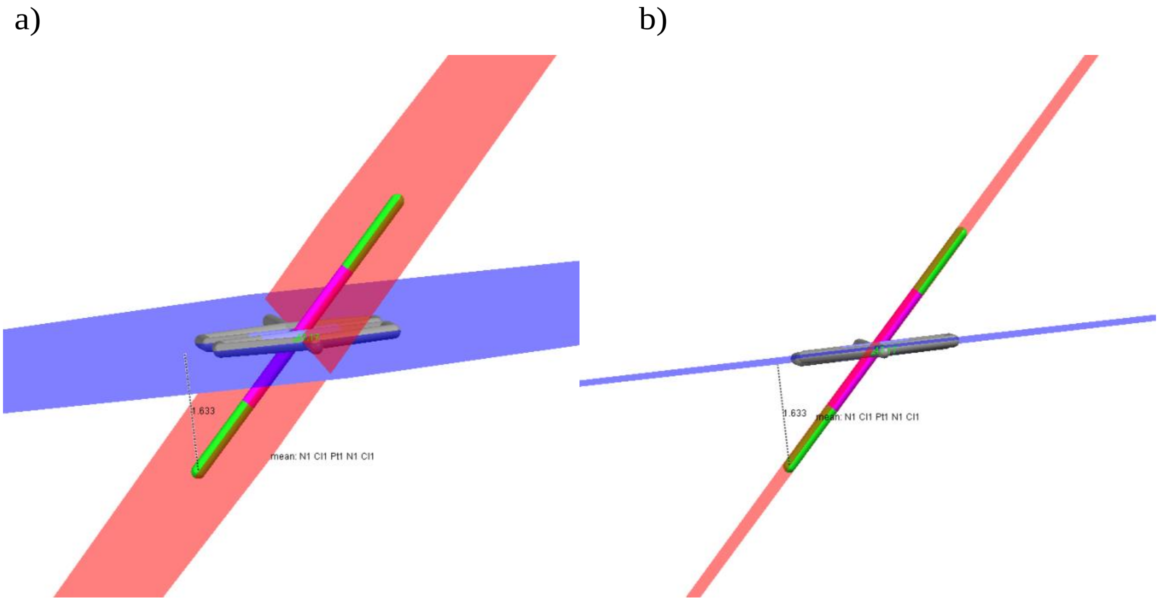

Fig. 68 Angle between the plane defined by the pyridyl groups (blue) and the plane defined by the two nitrogen, two chlorine and the platinum atoms (red) in the crystal structure of **2**.

Regarding the spatial organization within the crystal, one can observe a slipped organization of the molecules that originates from the bulkiness of the terminal glycol chains and the central Cl-Pt(II)-Cl moiety. This arrangement is stabilized by C-H···π contacts, as well as several C-H···Cl and C-H···O hydrogen bonding interactions.

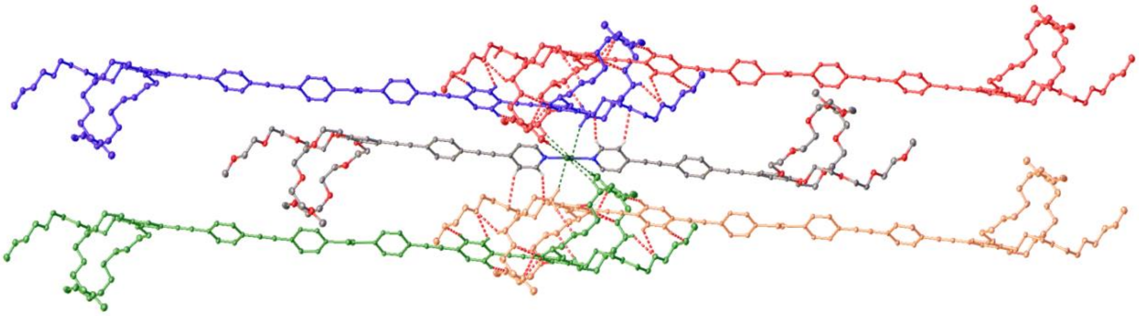

Fig. 69 Crystal structure of **2**, representing the C-H···Cl contacts (green dotted lines) of one Cl-Pt(II)-Cl centre with the glycol chains of four neighbouring molecules and the C-H···O hydrogen bondings (red dotted lines) between glycol chains. Elements of the central unit (colour): C (grey), O (red), N (blue), Pt (dark blue), Cl (green), H (white).

With respect to the contribution of the Cl-Pt(II)-Cl centres, each of them is involved in hydrogen bonding interactions with glycol chains of four neighbouring molecules. These interactions are depicted in Fig. 69 for the central molecule whose chlorine-hydrogen contacts with glycol units are highlighted by green dotted lines. Upon closer inspection, the two C-H···Cl (A-H···D) contacts for one chlorine atom reveal to be slightly different with donor-acceptor distances (black dotted lines in Fig. 70a) of 3.796 Å and 3.895 Å, respectively. This pattern is symmetrical relating to the Pt(II) centre.

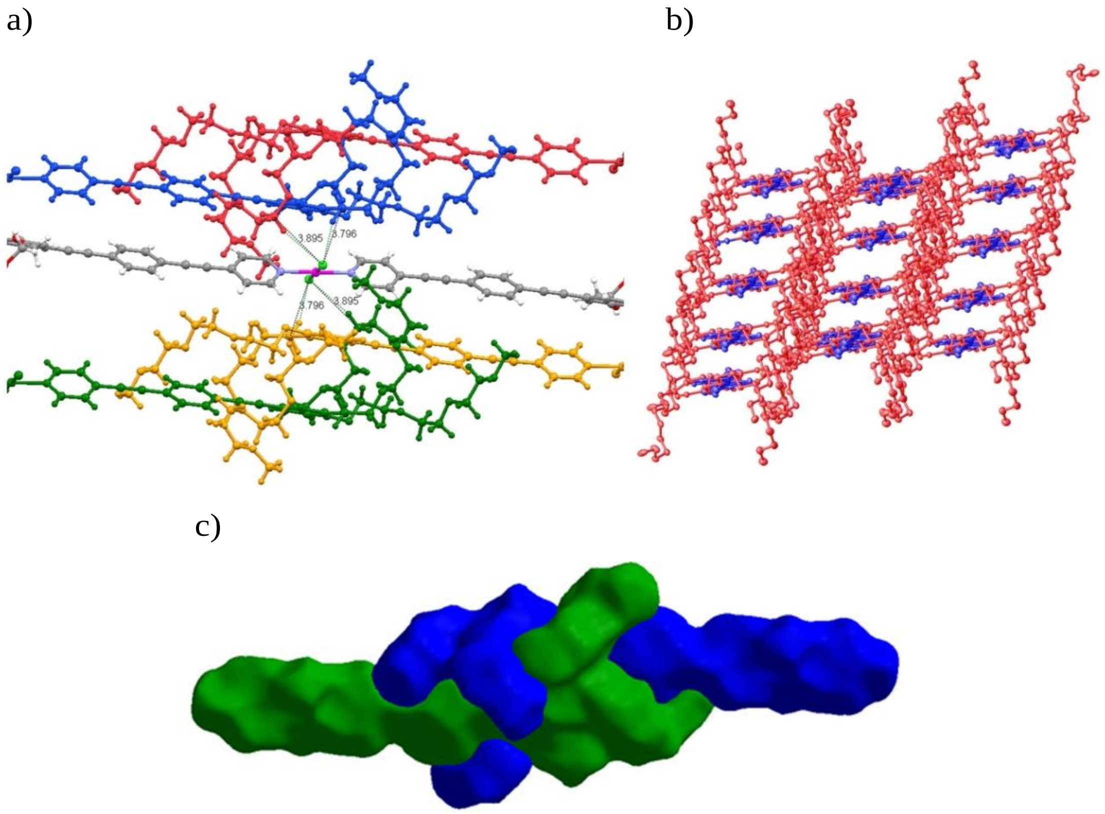

Fig. 70 Crystal structure of **2**. a) Short contacts of one Cl-Pt(II)-Cl centre with the glycol chains of four neighbouring molecules, values give the donor-acceptor distances for the C-H···Cl (D-H···A) interactions. b) Overall packing of the crystal structure seen along the OPE units, with OPEs highlighted in blue and TEG chains in red. c) Interlocking of the molecules visualized by the Hirshfeld surface representing the “molecular handshake”.

Further stabilization of the arrangement is gained by multiple C-H···O hydrogen bonding interactions between the glycol chains of two neighbouring molecules, which are highlighted in red in Fig. 69 and also become apparent for the projection along the OPE units in Fig. 70b. The interplay between these attractive forces, in part involving aromatic C-H groups, leads to a fascinating packing mode of the glycol units that can be termed as molecular “hand-shake” (Fig. 70c).

The observed crystalline packing is in good agreement with the molecular arrangement of **2** in solution (Fig. 64 - Fig. 66). The slipped aggregation fashion of the molecules explains all cross-peaks between most of the protons of the glycol chains (H_e - H_k) and protons H_a - H_d that appeared for the ROESY measurement of the self-assembled solution of **2**.

To provide a picture of the volume occupied by a molecular subunit in a crystal, the Hirshfeld surface can be defined by partitioning of space in the crystal.[245-248] Hereby, the molecule itself and the proximity of neighbouring units are taken into account. A weight function $w_A(r)$ has to be considered, given by the ratio between promolecule and procrystal electron densities:

$$w_A(r) = \frac{\sum_{i\,\epsilon\, molecule} \rho_i(r)}{\sum_{i\,\epsilon\, crystal} \rho_i(r)} = \frac{\rho_{promolecule}(r)}{\rho_{procrystal}(r)} \qquad (27)$$

with the individual $\rho_i(r)$ as spherical atomic electron distribution centred at the *i*-th nucleus.

The weight function takes a value $0 < w_A(r) < 1$, while the Hirshfeld surface of a molecule is defined by $w_A(r)$ = 0.5. Thus, the isosurface describes the crystalline volume where the promolecule electron density exceeds that of all other molecules. This partitioning gives smooth surfaces for the molecular volumes that are in close contact but never overlap.[245-248]

The Hirshfeld surface of **2** (Fig. 71) depicts a colour code to characterize the normalized distance to the neighbouring molecule. The normalized distance d_{norm} is defined by the parameters d_e, d_i and the van der Waals radii of the atoms r^{vdW} by eq. (28):[247,248]

$$d_{norm} = \frac{d_i - r_i^{vdW}}{r_i^{vdW}} + \frac{d_e - r_e^{vdW}}{r_e^{vdW}} \qquad (28)$$

The parameter d_e defines the distance from a point on the surface to the nearest nucleus outside the surface, while d_i shows this distance to the nearest atom inside the surface.[247-249] The colour scheme for d_{norm} highlights distances being longer than the sum of the van der Waals radii in blue, contacts being approximately the van der Waals separation in white, while red represents shorter contacts. In this regard, the red regions are the most important ones and close intermolecular contacts can be identified by two identical red spots.

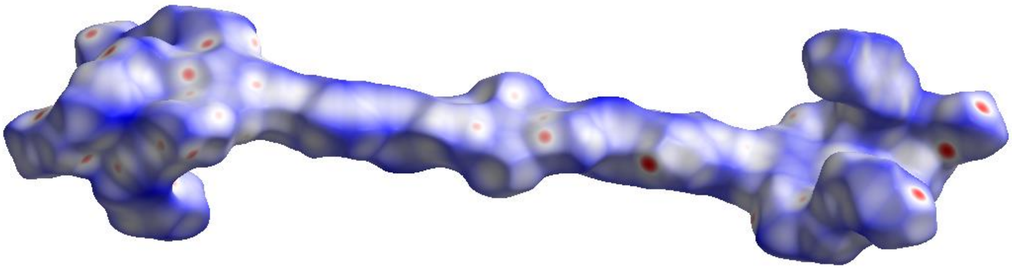

Fig. 71 Hirshfeld surface of the crystal structure of **2** with the colour scheme representing the normalized distance (d_{norm}) to the neighbouring molecule (blue being longer than the sum of the van der Waals radii, white being approximately the sum and red being shorter than the sum).

The corresponding 2 D fingerprint plots (Fig. 72) are generated by combination of d_e and d_i data for the entire Hirshfeld surface.[246-249] The plot results from binning (d_e, d_i) pairs in intervals of 0.01 Å. The colouring of the diagram signalizes the frequency of a specific interaction (d_e, d_i pair) and thus allows a visualization of the intermolecular forces stabilizing the packing.

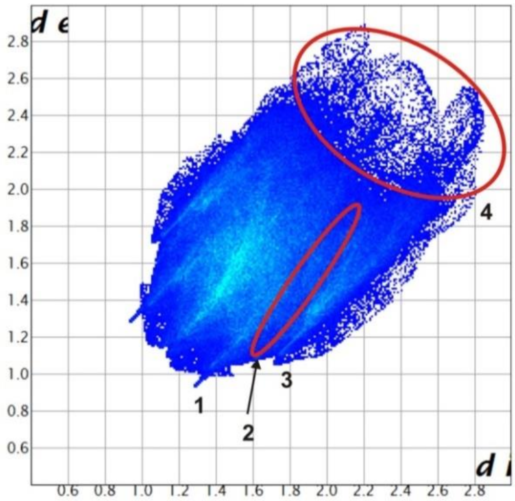

Fig. 72 Hirshfeld surface fingerprint plot of **2**. Colours describe the frequency of a specific distance with blue being less frequent and light green being most common.

In Fig. 72 the fingerprint plot of **2** is shown including different interaction types, with regions in blue colour representing less frequent distances while light green describes the most common. While region 1 depicts C-H···O hydrogen bonds, region 2 represents C-H···C and C-H···π short contacts. Region 3 corresponds to C-H···Cl interactions whereas region 4 clearly signifies that the crystalline packing includes relatively large voids.

The C-H···O hydrogen bonds (region 1) cover a total of 16.6% of the surface indicating their prominent contribution to the packing of **2**. These contacts are also the shortest and can thus be assumed as the strongest interactions. C-H···C and C-H···π interactions (region 2) are longer in distance and thus not as strong as the C-H···O hydrogen bonding interactions. However, with a remarkable percentage of 22.3% they also play an important role. Finally, C-H···Cl interactions are depicted in region 3. They exhibit a distance comparable to the C-H···C contacts, however with only 4.5% of the surface they represent a minor contribution to the overall structure of **2**. The 2D fingerprint plot also visualizes relatively large voids in the crystalline space (region 4) that can be attributed to the high degree of flexibility that inheres in the monomeric structure.

3.4 Studies on the pyridine-based Pd(II) complex 3[*]

3.4.1 Synthesis of 3

The synthesis of target compound **3** was realized by the complexation reaction of freshly purified ligand **1** with dichlorobis(benzonitrile)palladium(II) in a 2:1 ratio at room temperature under argon (Chart 34). The complex **3** was synthesized for the first time by A. Martin during the laboratory work of the bachelor thesis.[234] The reaction towards **3** was performed according to this reference, however the conditions were modified insofar as the complexation was performed under argon atmosphere. In this way, the yield could be remarkably improved from 17%[234] to 80%. The target complex **3** was characterized by ^{1}H NMR, ^{13}C NMR, HRMS (ESI) and elemental analysis.

Chart 34 Synthetic route to achieve the target Pd(II) complex **3**.

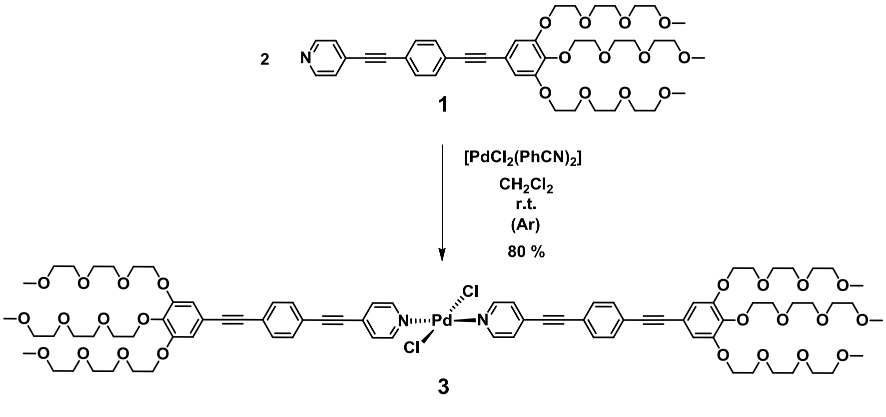

The reaction was controlled by ^{1}H NMR measurements that indicated complete consumption of the ligand **1** after one day. The disappearance of this ligand signal occurs at the expense of a new downfield shifted signal that can be assigned to complex formation (Fig. 73). The target molecule **3** could be purified in a yield of 80% by repeated precipitation of the solid using dichloromethane and hexane.

---

[*] Reproduced and adapted with permission from C. Rest, A. Martin, V. Stepanenko, N. K. Allampally, D. Schmidt, G. Fernández, *Chem. Commun.*, **2014**, *50*, 13366.

Synthetic Procedure (3.4.1.) has been initially elaborated and described in the bachelor thesis of A. Martin[234] under the supervision of C. Rest, Prof. Dr. G. Fernández and Prof. Dr. F. Würthner, Julius-Maximilians-Universität Würzburg, 2012. Some investigations are based on preliminary studies on **3** presented therein.[234]

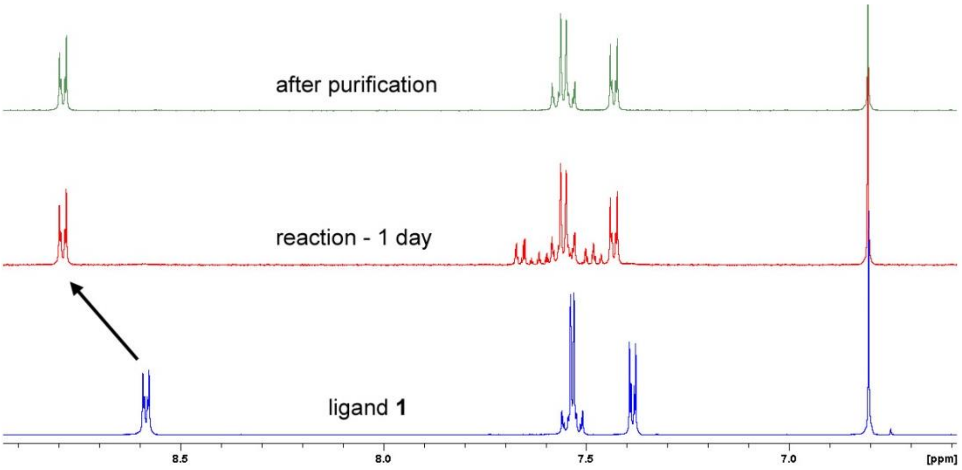

Fig. 73 ^{1}H NMR spectra (CD_2Cl_2, 400 MHz, 300 K) of the reaction shown in Chart 34 to achieve the target Pd(II) complex **3**.

3.4.2 Optical properties of 3 in solution

3.4.2.1 Solvent-dependent characteristics of 3

Solvent-dependent absorption studies were performed to examine the behaviour of complex **3** in different media (Fig. 74). The yellow solid is highly soluble in THF, dichloromethane and chloroform, while its solubility is limited in pure alcohols and water. Consequently, for the samples of **3** in alcohols and aqueous medium the solid was dissolved in 2% of dichloromethane and THF (thin film in solution), respectively, before the poor solvent was added.

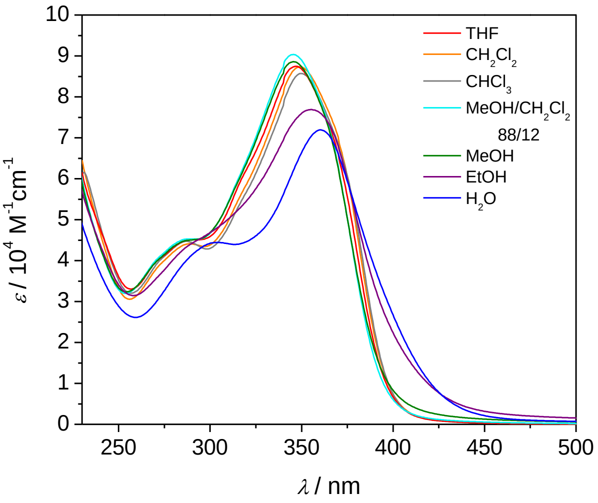

Fig. 74 Solvent-dependent UV/Vis absorption experiments for complex **3** (3.1 - 3.2 x 10^{-4} M).

In most organic solvents the maximum is centred at 346 - 350 nm, while a bathochromic shift to 355 nm in ethanol and to 360 nm in water appears. This indicates that complex **3** is present as monomeric species in most organic media of different polarity. However, the significant red-shift of the maximum along with the broadened absorption band around 420 nm suggests an aggregation process in ethanol and water.

3.4.2.2 Temperature-dependent behaviour of 3 in methanol and methanol/ dichloromethane mixtures

Similar to the related Pt(II) complex **2**, temperature-dependent studies have been employed to gain information about the aggregation mode of **3**. Water revealed to be unsuited for these studies since the molecules of **3** are too strongly aggregated to reach the completely monomeric state, even at low concentration (10^{-6} M) and high temperature (~363 K). Thus, methanol was tested for these experiments due to the lower aggregation tendency of the complex in this solvent. Although the solvent-dependent studies for **3** at room temperature did not indicate any aggregation in methanol, the similarity of this solvent to ethanol suggested potential aggregation upon cooling or increasing concentration. For the preparation of all samples in methanol solution (8.0×10^{-4} M to 3.6×10^{-4} M), the compound was first dissolved in 2% of dichloromethane to form a thin film in solution, before the poor solvent (MeOH) was added. The samples were then cooled from 312 to 270 K with 1 Kmin^{-1} and each 0.4 K a data point at 425 nm was recorded.

For the plot of α_{agg} (eq. (1)) against temperature, the range from 312 to 270 K (for the 8.0 and 6.7×10^{-4} M samples) and from 305 to 270 K (for the 5.0 and 3.6×10^{-4} M samples), respectively, was considered. The corresponding curves in Fig. 75 exhibit for all concentrations a steep and clearly non-sigmoidal shape. Thus, the cooperative model of ten Eikelder, Markvoort and Meijer was applied to fit the spectral changes.[44,45] This model yielded satisfactory fits (coloured lines in Fig. 75) confirming the cooperative character of the aggregation process. The fitting provided the values for the elongation enthalpy ($\Delta H°$), the nucleation penalty ($\Delta H°_{nuc}$), the entropy ($\Delta S°$) and the elongation temperature T_e (Table 5).

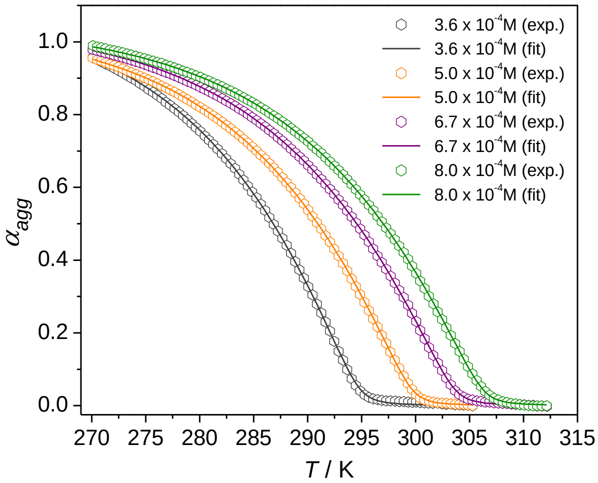

Fig. 75 Temperature-dependent UV/Vis absorption experiments of **3** in methanol solution: Cooling curves (λ = 425 nm) at different concentrations from 8.0 - 3.6 x 10^{-4} M. The temperature was decreased from 312 to 270 K with a rate of 1 Kmin^{-1}. The coloured lines represent the fitting of the spectral changes to the cooperative *ten Eikelder-Markvoort-Meijer*-model.[44,45]

As directly becomes apparent in Fig. 75, the activation of the self-assembly does not start until the temperature reaches a certain point. This critical temperature obviously increases with concentration. The elongation enthalpy for the different samples shows very similar values from -57 to -56 kJmol^{-1}. With the defined parameters $\Delta H°$, $\Delta H°_{nuc}$, $\Delta S°$ and T_e (Table 5) the binding constants K_{nuc} and K_e at the corresponding elongation temperature can be calculated according to eqs. (15) and (16).

Table 5 Thermodynamic parameters characterizing the temperature-dependent UV/Vis absorption experiments of **3** in methanol solution at different concentrations. Values for $\Delta H°$, $\Delta H°_{nuc}$, $\Delta S°$ and T_e were extracted from the fitting to the *ten Eikelder-Markvoort-Meijer*-model[44,45] and K_{nuc}, K_e and σ were calculated at the corresponding elongation temperature T_e.

conc. [M]	**$\Delta H°$ [kJmol^{-1}]**	**$\Delta H°_{nuc}$ [kJmol^{-1}]**	**$\Delta S°$ [kJmol^{-1}K^{-1}]**	**T_e [K]**	**K_{nuc} [M^{-1}]**	**K_e [M^{-1}]**	**σ**
3.6 x 10^{-4}	-57.2±0.5	-19.1±0.3	-0.1287±0.0017	294.1±0.05	1.14	2.8 x 10^{3}	4.1 x 10^{-4}
5.0 x 10^{-4}	-56.7±0.2	-20.0±0.2	-0.1262±0.0007	299.1±0.03	0.66	2.0 x 10^{3}	3.3 x 10^{-4}
6.7 x 10^{-4}	-55.8±0.2	-20.0±0.1	-0.1236±0.0006	302.9±0.02	0.53	1.5 x 10^{3}	3.6 x 10^{-4}
8.0 x 10^{-4}	-55.6±0.2	-20.4±0.1	-0.1228±0.0005	305.6±0.02	0.40	1.3 x 10^{3}	3.2 x 10^{-4}

The dimerization constant K_{nuc} that characterizes the unfavourable nucleation process has very low values from 0.4 to 1.1 M^{-1} while the elongation constant K_e at T_e is in the range of 1.3 to 2.8 x 10^3 M^{-1}. This significant difference also becomes noticeable in the degree of cooperativity σ (eq. (17)) whose low values of 10^{-4} characterize a highly cooperative process.

In the same way as shown for the Pt(II) complex **2** (section 3.3.2.2), the defined parameters (Table 5) could be combined in the van't Hoff analysis. The $ln\ K_e$ values at the corresponding elongation temperature were plotted against T_e^{-1} and reveal a linear dependence. Consequently, the linear regression of the data, described by the linear form of the van't Hoff equation (eq. (26)) provides a good fitting with $R^2 = 0.9957$.

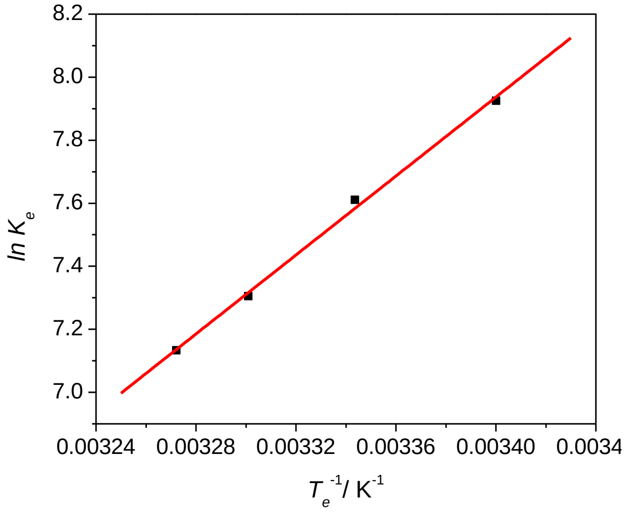

Fig. 76 Van't Hoff plot of the $ln\ K_e$ values of **3** in MeOH against T_e^{-1} ($R^2 = 0.9957$). T_e and the corresponding K_e values at T_e were determined by temperature-dependent UV/Vis experiments at different concentrations (Table 5).

With the slope and the y-axis intercept of the regression line (Fig. 76), the values of ΔH^0 and ΔS^0 can be calculated (eq. (26)), which finally allows the determination of the standard Gibbs free energy ΔG^0 according to eq. (12) (Table 6).

Table 6 Thermodynamic parameters associated to the self-assembly process of **3** in methanol solution at 298 K.

Δ*H*° [kJmol^{-1}]	**Δ*S*°** [kJmol^{-1}K^{-1}]	**Δ*G*°** [kJmol^{-1}]
-52.1±2.0	-0.1111±0.0065	-19.0±0.02

Despite that the self-assembly of **3** can be effectively described by the nucleation-elongation model by ten Eikelder, Markvoort and Meijer, it was observed that the sample is not completely stable in MeOH solution and a small fraction (~15%) of **3** disassembles during the time required to record the cooling curve, as detected by ^{1}H NMR studies (Fig. 77). The blue spectrum corresponds to the sample in deuterated solvent that was prepared identically (dissolution in 2% of CD_2Cl_2 prior to the addition of MeOD) and treated under the same cooling conditions as the previous samples presented in Fig. 75.

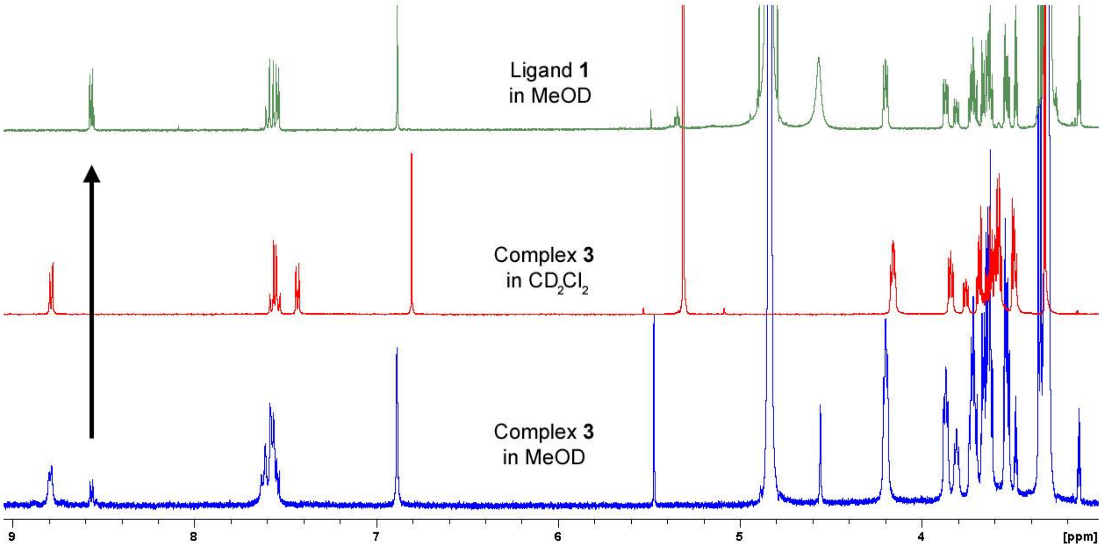

Fig. 77 ^{1}H NMR spectra (400 MHz, 300 K) showing the partial disassembly of **3** in MeOD solution (3.6×10^{-4} M, blue spectrum) after measurement of the melting curve from 312 - 270 K. For comparison, the spectrum in red corresponds to the original complex **3** in dichloromethane, while the green spectrum shows the ligand **1** in MeOD.

Since the fitting to the non-sigmoidal model worked properly, it is assumed that the small percentage of dissociated complex **3** negligibly influences the self-assembly process. Nevertheless, a better solvent mixture was chosen to enable reliable temperature-dependent investigations without dissociation. In this regard, the presence of different amounts of dichloromethane (DCM) in methanol was tested in order to find out whether an increased solubility might improve the stability of **3**. Indeed, the absorption spectrum of **3** in a mixture of 12% DCM and 88% methanol did not reveal any changes comparing the UV/Vis absorption measurements before and after the temperature-dependent studies (Fig. 78b). This mixture of MeOH/DCM = 88:12 appeared to be the best compromise in terms of solubility at high concentration and strong aggregation at low temperature. However, a tenfold higher concentration was required compared to pure methanol to monitor the complete aggregation process. This clearly demonstrates the reduced tendency of the system to self-assemble due to the better solvation of **3** resulting from the presence of dichloromethane as good solvent.

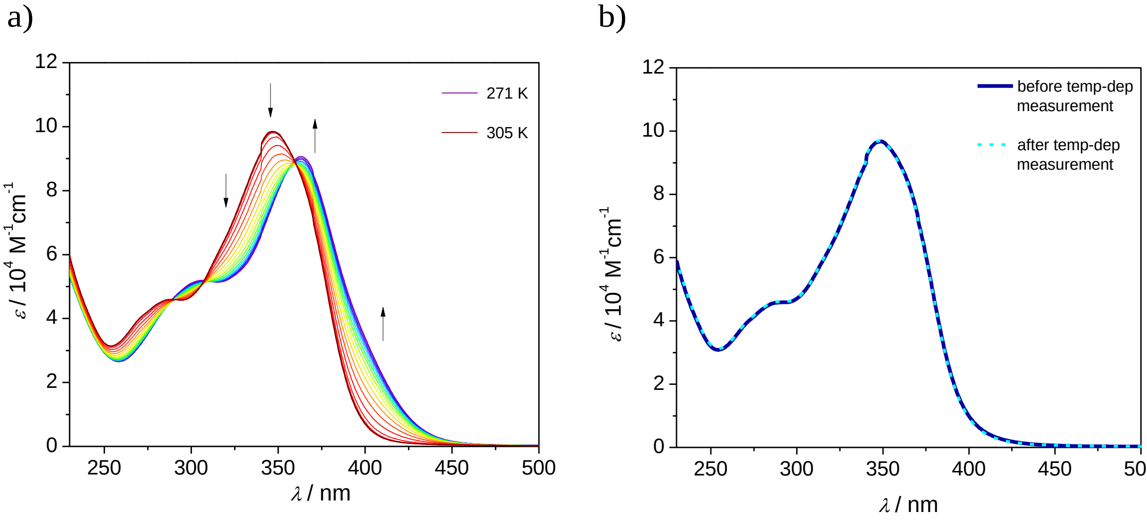

Fig. 78 a) Temperature-dependent UV/Vis absorption experiments of **3** in MeOH/DCM = 88:12 (3.5 x 10^{-3} M) upon decreasing temperature from 305 to 271 K with 1 Kmin^{-1}. Arrows indicate the spectral changes upon cooling. b) Corresponding UV/Vis absorption spectra at 298 K before and after the temperature-dependent UV/Vis experiments (305 to 271 K) shown in a).

Fig. 78a illustrates the temperature-dependent absorption studies of **3** in MeOH/DCM = 88:12 (3.5 x 10^{-3} M) upon decreasing temperature from 305 to 271 K. Upon cooling, a significant red-shift of the absorption maximum from 347 nm to 363 nm is observed. Simultaneously, an increase in absorption in the region of ~420 nm can be noticed, which is indicative of the transition from monomeric to aggregated species upon temperature decrease. Cooling curves at 425 nm for four concentrations, ranging from 3.5 x 10^{-3} M to 1.6 x 10^{-3} M, were recorded (Fig. 79). To this end, the sample was heated to 305 K and cooled down to 270 K with 1 Kmin^{-1}. Similarly to the methanol samples of **3** described previously, the plot of α_{agg} (temperature range from 305 to 270 K for all concentrations) revealed steep, non-sigmoidal curves that could be satisfactorily fitted to the cooperative model.[44,45] The values for $\Delta H°$, $\Delta H°_{nuc}$, $\Delta S°$ and T_e are directly extracted from the cooperative fitting and given in Table 7. By analogy to the previous measurement in methanol solution, the remaining parameters at T_e were calculated upon applying eqs. (15) and (16).

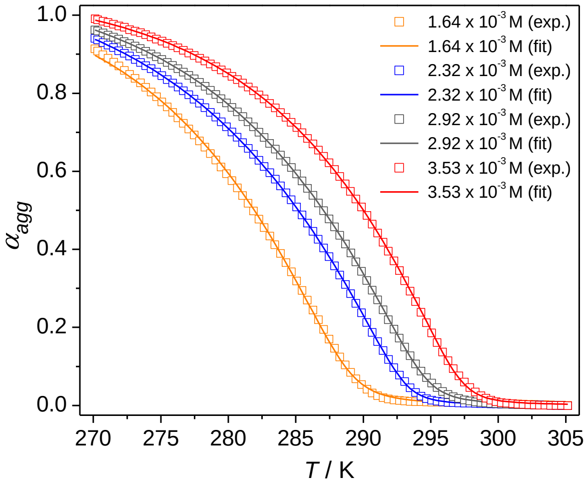

Fig. 79 Temperature-dependent UV/Vis absorption experiments of **3** in methanol/ dichloromethane (88:12) mixture: Cooling curves (λ = 425 nm) at different concentrations from 3.5 - 1.6 x 10^{-3} M. The temperature was decreased from 305 - 270 K with a rate of 1 Kmin^{-1}. The coloured lines represent the fitting of the spectral changes to the cooperative *ten Eikelder-Markvoort-Meijer*-model.[44,45]

For the elongation temperature T_e, the values range from 288.0 to 296.5 K and increase with increasing concentration. The binding constants at the corresponding T_e show values from 0.3 - 1.4 M^{-1} for K_{nuc} and 3 - 6 x 10^2 M^{-1} for K_e, respectively. Accordingly, the cooperativity factor σ (eq. (17)) lies in the order of 10^{-3}.

Table 7 Thermodynamic parameters characterizing the temperature-dependent UV/Vis absorption experiments of **3** in MeOH/DCM = 88:12 at different concentrations. Values for $\Delta H°$, $\Delta H°_{nuc}$, $\Delta S°$ and T_e were extracted from the fitting to the *ten Eikelder-Markvoort-Meijer*-model[44,45] and K_2, K and σ were calculated at the corresponding elongation temperature T_e.

conc. [M]	**$\Delta H°$ [kJmol^{-1}]**	**$\Delta H°_{nuc}$ [kJmol^{-1}]**	**$\Delta S°$ [kJmol^{-1}K^{-1}]**	**T_e [K]**	**K_{nuc} [M^{-1}]**	**K_e [M^{-1}]**	**σ**
1.6 x 10^{-3}	-64.2±1.5	-14.6±0.3	-0.1696±0.0052	288.0±0.10	1.37	6.1 x 10^2	2.3 x 10^{-3}
2.3 x 10^{-3}	-55.8±0.3	-18.2±0.1	-0.1405±0.0009	292.4±0.02	0.24	4.3 x 10^2	0.6 x 10^{-3}
2.9 x 10^{-3}	-61.1±0.3	-16.5±0.1	-0.1594±0.0012	293.8±0.03	0.40	3.4 x 10^2	1.2 x 10^{-3}
3.5 x 10^{-3}	-67.2±0.4	-17.1±0.2	-0.1796±0.0014	296.5±0.04	0.28	2.8 x 10^2	1.0 x 10^{-3}

These σ values of 10^{-3} (Table 7) are slightly higher, suggesting lower cooperativity than in methanol solution (Table 5). While the dimerization constants do not show great differences between methanol and methanol/dichloromethane, the lower σ value in the mixture originates from the elongation constants K_e that are almost five times higher in methanol. These lower values for the solvent mixture are most likely due to the addition of the good solvent dichloromethane that provides a better solvation of the molecular surfaces and reduces the solvophobic effect of the medium.

The reliability of the model was further proven by van't Hoff analysis that already provided satisfactory results for the previous measurements of **3** (Fig. 76). For the MeOH/DCM (88:12) samples, the data points for the $ln\ K_e$ values as a function of the corresponding elongation temperature T_e^{-1} are depicted in Fig. 80.

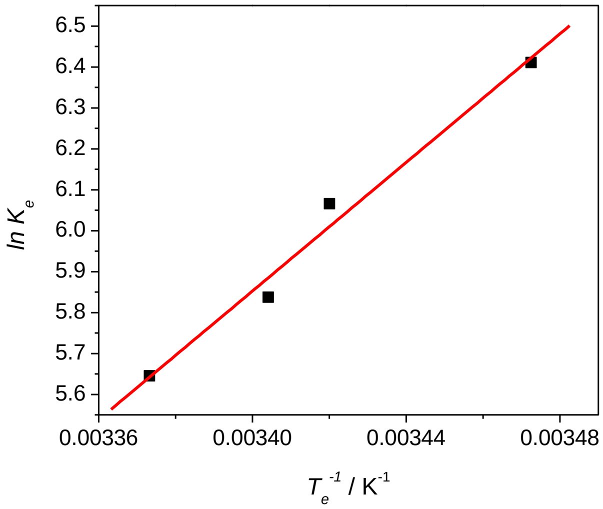

Fig. 80 Van't Hoff plot of the $ln\ K$ values of **3** in MeOH/DCM = 88:12 against T_e^{-1} (R^2 = 0.9746). T_e and the corresponding K_e values at T_e were determined by temperature-dependent UV/Vis experiments at different concentrations (Table 7).

The values for ΔH^0 and ΔS^0 were calculated from the regression line (red line in Fig. 80) according to eq. (26). These parameters can subsequently be applied to define the standard Gibbs free energy ΔG^0 by means of the Gibbs-Helmholtz equation (12). These values at 298 K are given in Table 8.

Table 8 Thermodynamic parameters associated to the self-assembly process of **3** in MeOH/DCM = 88:12 at 298 K.

$\Delta H°$ [$kJmol^{-1}$]	$\Delta S°$ [$kJmol^{-1}K^{-1}$]	$\Delta G°$ [$kJmol^{-1}$]
-65.3±6.1	-0.1734±0.0207	-13.6±0.11

3.4.3 Gelation and microscopic studies of 3

The high tendency of **3** to aggregate in alcohols and water results in the formation of stable gels. To investigate the gelation behaviour in organic solvents, the compound was initially dissolved by heating of the samples. When the samples had cooled to room temperature again, an immediate gelation in ethanol and butanol could be observed (Fig. 81).

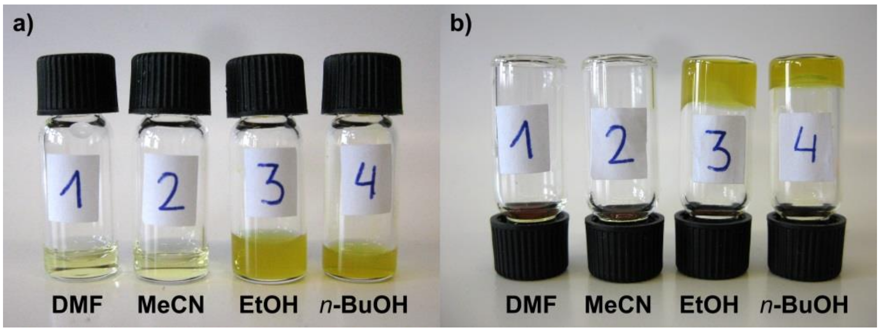

Fig. 81 Gelation studies of **3** showing the monomeric and self-assembled state (gel) of **3** in different solvents (0.9 - 1.0 x 10^{-2} M). b) depicts the “stable-to-inversion of the test tube” method.

The critical gelation concentrations of **3** at room temperature could be determined to be ~7 mg/ml in ethanol and ~6 mg/ml in butanol, as listed in Table 9. In analogy to the Pt(II) complex **2**, the gel samples give a clear solution upon heating.

Table 9 Critical gelation concentration (*cgc*) for the gels of **3** in the alcohols ethanol and *n*-butanol.

	EtOH (at r.t.)	***n*-BuOH (at r.t.)**
***cgc*. [mg/ml]**	6.7	6.2

To visualize the morphology of the self-assembled species, a gel in ethanol was investigated by microscopic techniques. Fig. 82 shows the AFM studies of a diluted gel of **3** onto mica with its cross-section analysis being depicted in image c). The studies disclose long, one-dimensional fibres that form an intertwined network. The height and diameter of fibres was measured to be 2.4±0.5 nm and 6.2±0.6 nm, respectively.

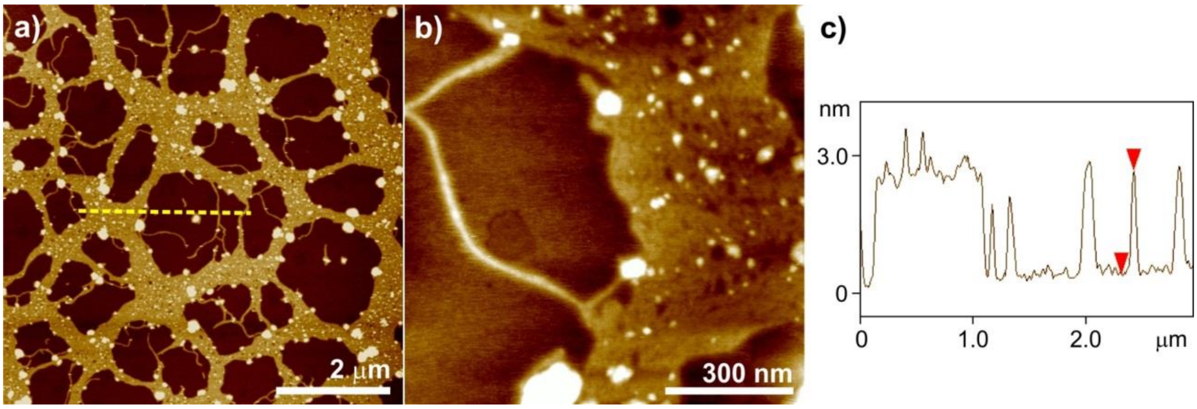

Fig. 82 AFM height images (a, b) of a diluted gel of **3** in ethanol. The samples were prepared by drop casting a diluted gel solution in ethanol onto mica. Image (c) depicts the cross-section analysis along of the yellow line 1-1' in image (a). Z scale is 5 nm.

A similar morphology could be visualized by Scanning Electron Microscopy. The image of a two times diluted gel, shown in Fig. 83, also illustrates a two-dimensional network that consists of extended, flexible fibres.

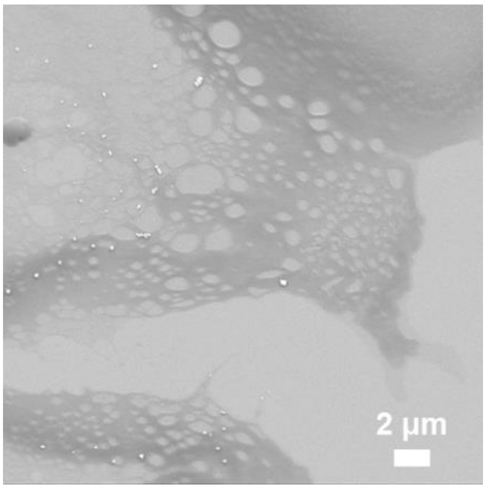

Fig. 83 SEM images of a diluted gel solution of **3** in ethanol (5.1 x 10^{-3} M) on silicon wafer.

Besides the diluted samples to elucidate the “fine-structure” of the gel, also the original gel was investigated by microscopic imaging as a bead dried in air. The images in Fig. 84 identify the gel as a densely packed material that is created by close contact of fibrous structures (marked by the yellow arrow).

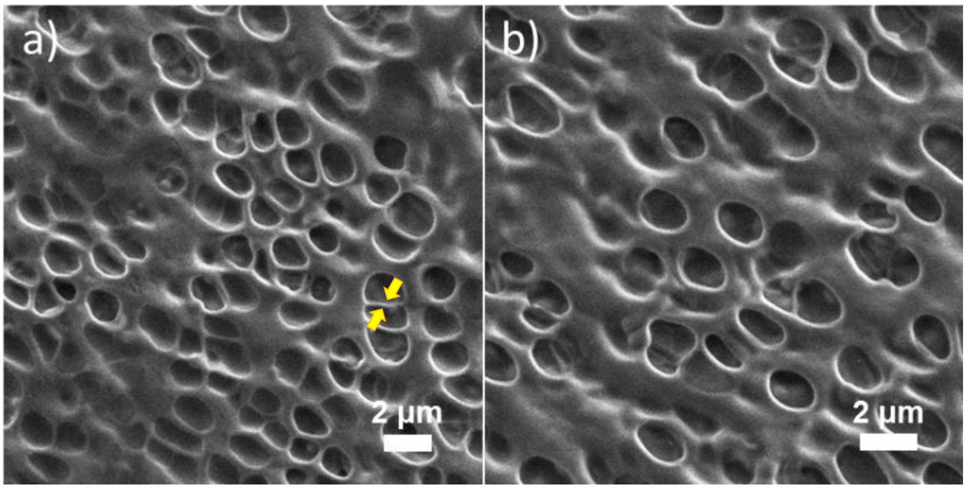

Fig. 84 SEM images of the gel of **3** in ethanol (1.0 x 10^{-2} M) on silicon wafer. The images show the surface of the gel bead dried in air.

Similarly to ethanol, also for **3** in aqueous medium a gel could be obtained that was investigated by TEM and AFM. However, in contrast to the sample in EtOH the hydrogel does not form immediately after preparation. For **3** in aqueous solution it could be observed after a time course of around 2.5 month at room temperature that the sample finally transformed from a yellow solution into a stable hydrogel. This is illustrated by the “stable-to-inversion of the test tube” method in Fig. 85.

Fig. 85 Photograph showing the “stable-to-inversion of the test tube” method of the hydrogel of **3** in water.

The gel in water was investigated by TEM (Fig. 86) and AFM imaging (Fig. 87) that both reveal comparable structures.

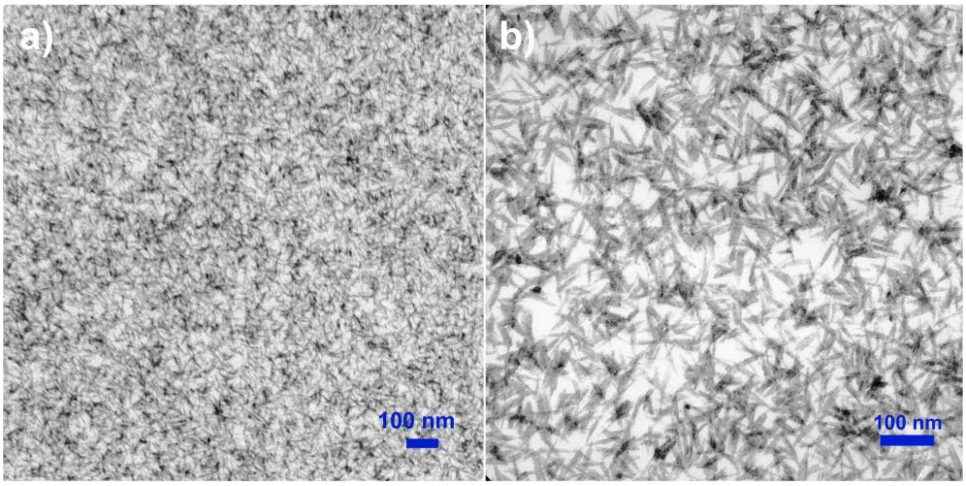

Fig. 86 TEM images of a gel of **3** in water onto a carbon-coated copper grid.

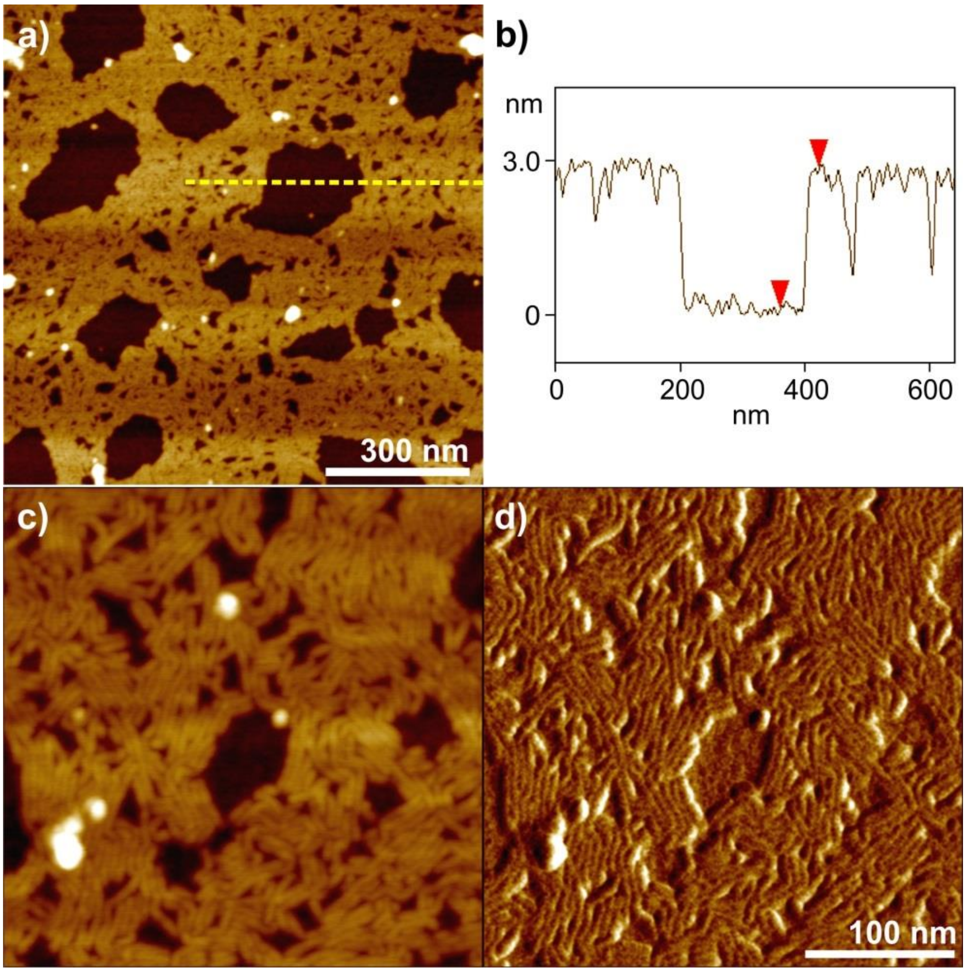

Fig. 87 AFM height (a, c) and phase (d) images of a gel of **3** in water. The samples were prepared by spin-coating a drop of the hydrogel onto mica with 5000 rpm. Image (b) shows the cross section analysis along of the yellow line in image (a).

TEM shows that the hydrogel originates from a dense, three-dimensional interlocking of self-assembled fibres. The visualized morphology bears close resemblance to the

AFM studies of the hydrogel (Fig. 87) that present an adsorption layer with a height of 3.0±0.2 nm. This film is composed of flexible worm-like aggregates with a diameter of 5.7±0.3 nm and a length of up to 120 nm.

3.4.4 Two-dimensional ^{1}H NMR analysis of 3

Besides the structures on surface, the molecular organization was also investigated in solution. In this regard, a highly concentrated solution (3.4×10^{-3} M) of **3** in MeOD/CD_2Cl_2 = 80:20 was prepared for ^{1}H NMR ROESY studies. Similarly to previous studies of **2** in methanol/dichloromethane mixtures, the yellow solid was initially dissolved in CD_2Cl_2 prior to the addition of MeOD to the solution.

As depicted in Fig. 88, the MeOD/CD_2Cl_2 mixture (80:20) shows relatively sharp signals, yet a sufficiently high degree of aggregation to enable 2D ^{1}H NMR investigations. The ROESY spectrum shows multiple cross coupling signals. To focus on the protons in close proximity, a zoom-in into the regions of interest is shown in Fig. 89.

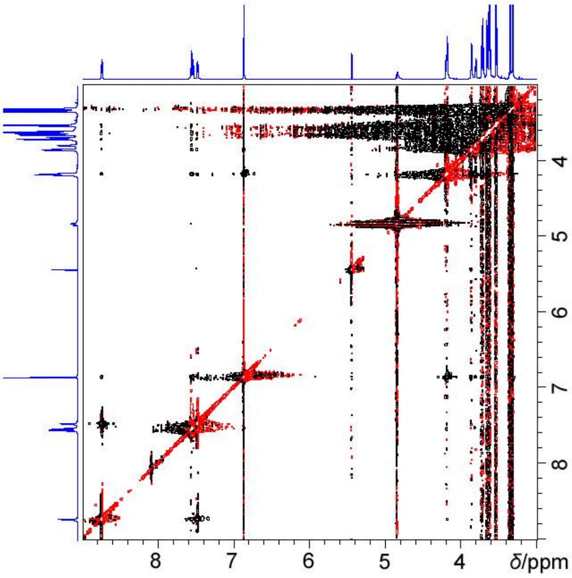

Fig. 88 600 MHz ROESY spectrum of **3** in MeOD/DCM = 80:20 at 3.4×10^{-3} M (293 K).

The spectrum in Fig. 89a shows the signals involving the protons of the pyridine and OPE rings of two neighbouring molecules, while Fig. 89b reveals contacts between the protons of the aromatic scaffold of one unit with the protons of the glycol chains of an adjacent one. The coupling between protons H_a and H_b of one molecule and protons H_c and H_d of another unit clearly suggests a slipped arrangement. This organization of the molecules is further confirmed by the proximity of protons of the aromatic unit and the protons of the glycol chains of a neighbouring molecule, similarly to Pt(II) complex **2** described in section 3.3.4.2

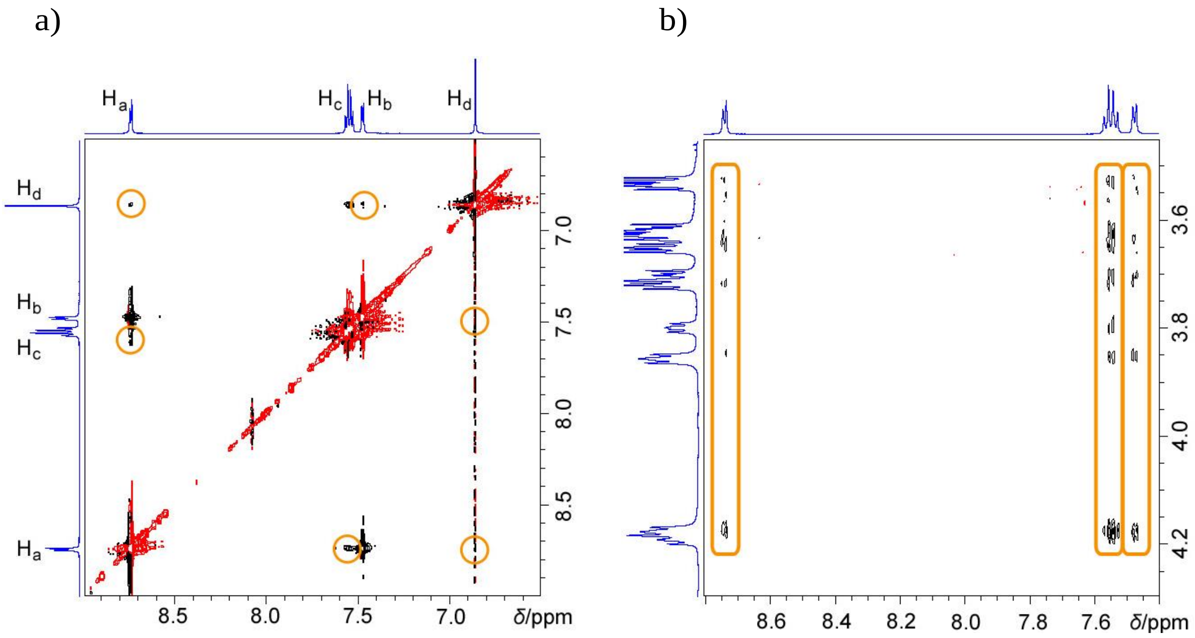

Fig. 89 600 MHz ROESY spectrum of **3** in MeOD/DCM = 80:20 at 3.4 x 10^{-3} M (293 K). The spectra represent the intermolecular through-space coupling signals between the protons of the pyridine and OPE units (in a) and between those and protons of the glycol chains (in b).

In Fig. 90 a tentative model for the self-assembly of **3** is presented that takes into account all coupling signals observed in ROESY studies, in analogy to the packing of the Pt(II) complex **2** (Fig. 66).

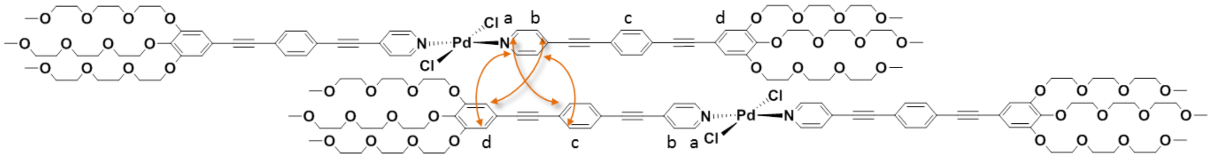

Fig. 90 Model of the slipped arrangement of **3** in a solution of MeOD/CD_2Cl_2 = 80:20. The organization is based on the cross peaks observed in ROESY ^{1}H NMR measurements presented in Fig. 88 and Fig. 89.

3.4.5 X-ray diffraction studies of 3

Suitable crystals for X-ray diffraction measurements were grown upon slow diffusion of diethyl ether (overlay) into a solution of **3** in ethanol. The crystal structure was solved as triclinic lattice with the $P\overline{1}$ space group. Fig. 91 shows the molecular structure of **3** in the crystalline packing.

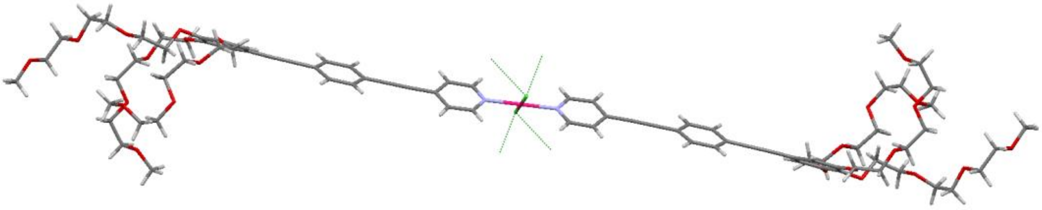

Fig. 91 Molecular structure of **3** in the solid state. The green dotted lines show the nearest chlorine-hydrogen contacts to neighbouring molecules. Element (colour): carbon (grey), oxygen (red), nitrogen (blue), platinum (magenta), chlorine (green), hydrogen (white).

Similarly to the aggregation pattern of the related complexes **2** and **3** in solution extracted from ROESY measurements, also the crystal structure for the Pd(II) complex **3** is highly reminiscent of the crystalline packing of its Pt(II) counterpart **2**. The green dotted lines in Fig. 91 represent the contacts of the chlorine atoms to the nearest hydrogen atoms. In this regard and as already observed for the crystal structure of **2**, each Cl-Pd(II)-Cl centre participates in Cl···H hydrogen bonding interactions with the glycol chains of four different molecules (Fig. 92).

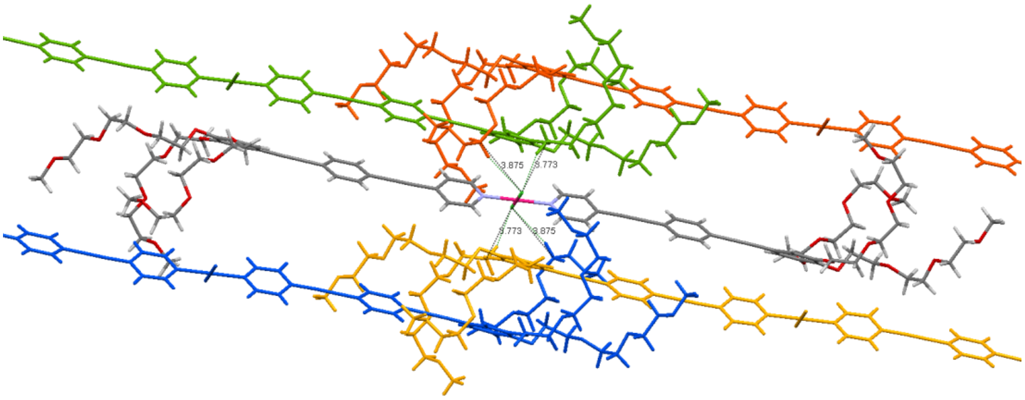

Fig. 92 Crystal structure of **3**, representing the C-H···Cl contacts of one Cl-Pt(II)-Cl centre with the glycol chains of four neighbouring molecules.

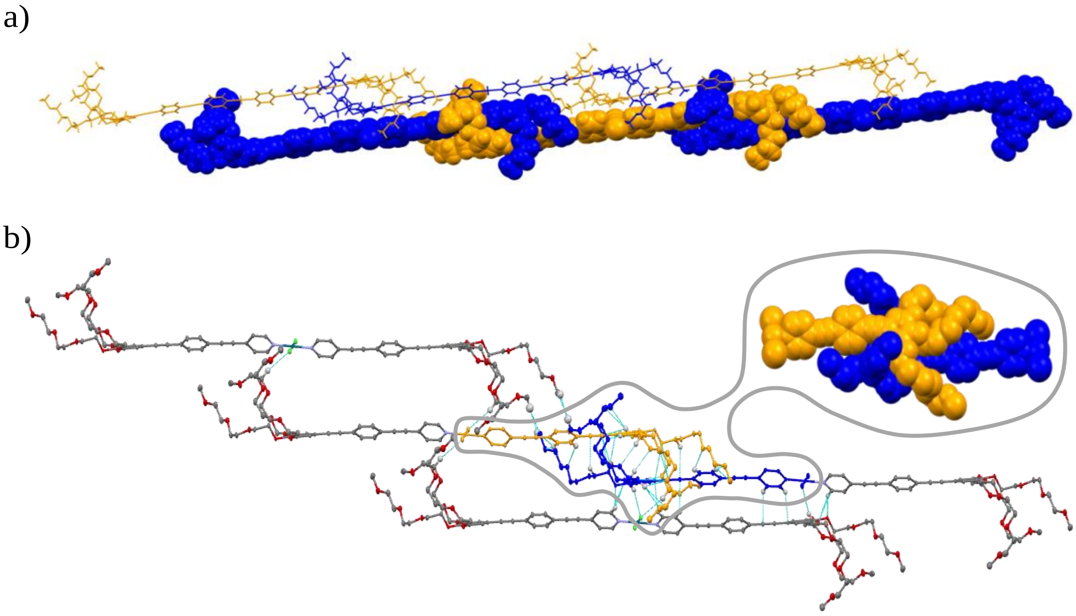

Fig. 93 Crystal structure of Pd(II) complex **3**: a) One-dimensional double-strands of **3** arranged in a parallel fashion. b) Packing following CH···Cl contacts. Hydrogen atoms have been omitted for clarity, except those integrated in the network of weak intermolecular interactions. Atomic displacement ellipsoids are drawn at 50% probability. Magnification of the “handshake-like” intertwining (coloured in blue and orange) represented as space fill model.

As depicted in Fig. 92, the C-H···Cl (D-H···A) interactions are asymmetric with one donor-acceptor distance of 3.773 Å and one of 3.875 Å per chlorine atom. In addition to C-H···Cl interactions, the crystalline arrangement is further stabilized by numerous short C-H···O contacts. These intermolecular interactions result in the creation of what has been previously termed as “molecular handshake” (Fig. 93), originally observed for the Pt(II) complex **2** (Fig. 69). This exciting molecular intertwining of the adjacent units is further supported by the involvement of aromatic C-H bonds. The interplay of these attractive forces results in a slipped, parallel arrangement of the molecules with a translationally displacement along the long axis of the molecule that further enables stabilizing C-H···π interactions.

On the basis of these findings, it can be concluded that cooperative C-H···O, C-H···Cl, C-H···π and π···π interactions are the driving force for the formation of self-assembled structures for complexes **2** and **3**, whereas the nature of the metal ions represents only a minor contribution in these systems.

Part II:

Amphiphilic bipyridine-based OPE systems and their responsiveness towards pH changes and metal ions

3.5 Introduction:

Bipyridine as popular ligand in supramolecular chemistry

Bipyridine derivatives have awakened the interest of chemists for many years.[250-255] The multiplicity of bipyridine-based molecules originates from the different isomers that can be modified by simple variation of the attached substituents. Regarding these isomers, 2,2'-bipyridine-based derivatives are most widely used. The 2,2'-bipyridine unit can act as a bidentate ligand to coordinate to metal ions. In this way, manifold stable metal complexes are created whose geometry depends mainly on the nature of the metal centre. Square-planar or tetrahedral geometries appear for a four-fold coordinated metal centre, while a complex with six ligands mainly adopts an octahedral arrangement around the metal center.[9] Besides the metal ion, also other aspects may influence the coordination geometry, as e.g. the ligand structure.[256] In this regard steric effects (size, shape) as well as multidentate ligands can have a relevant influence on the organisation around the metal centre.

The most representative candidates of 2,2'-bipyridine-based complexes are the coordination compounds with ruthenium that found application in the field of artificial photosynthesis.[257-261] Besides this area of research, bipyridine derivatives and their complexes could establish also as structural units of optical chemosensors,[262-267] in the field of non-linear optics,[268-270] optoelectronic materials[271-274] and supramolecular chemistry[275-283]. The complexation ability of 2,2'-bipyridine is not limited to metal ions but also results in a pronounced pH-responsiveness of the systems. In acidic media, the mono-protonated H^+-adduct is created, whose formation can be followed by absorption and ^{1}H NMR titration studies.[284-287]

The presented properties turn the 2,2'-bipyridine-based derivatives into promising molecules for supramolecular chemistry that can be exploited as multi-stimuli-responsive systems.

3.6 Self-assembly studies on bipyridine-based ligand 4

3.6.1 Synthesis of 4

The previously described beneficial aspects of 2,2’-bipyridine-based derivatives can be exploited to create a stimuli-responsive system in water. For this purpose, an amphiphilic bipyridine derivative **4** with potential solubility and aggregation propensity in polar solvents was designed. This supramolecular system is expected (anticipated) to provide responsiveness towards multiple changes in its environment, concerning the pH and the addition of metal ions. The molecular structure of target amphiphile **4** (Chart 35) exhibits an extended oligo(phenylene ethynylene) (OPE) scaffold that is prone to aggregation in aqueous media, a bipyridine ligand as pH-responsive and metal coordinating moiety and flexible triethylene glycol chains as solubilizing groups in polar media.

For the synthesis of the bipyridine ligand **4**, a previously synthesized intermediate **117** (see section 3.2.1.) was required. The reaction of commercially available 4,4’-dibromo-2,2’-bipyridine **121** with **117** under nitrogen atmosphere in a triethylamine/THF mixture at elevated temperature yields the amphiphilic target molecule **4** in 20% yield (Chart 35).

Chart 35 Final step of the synthetic route to achieve the target compound **4**.

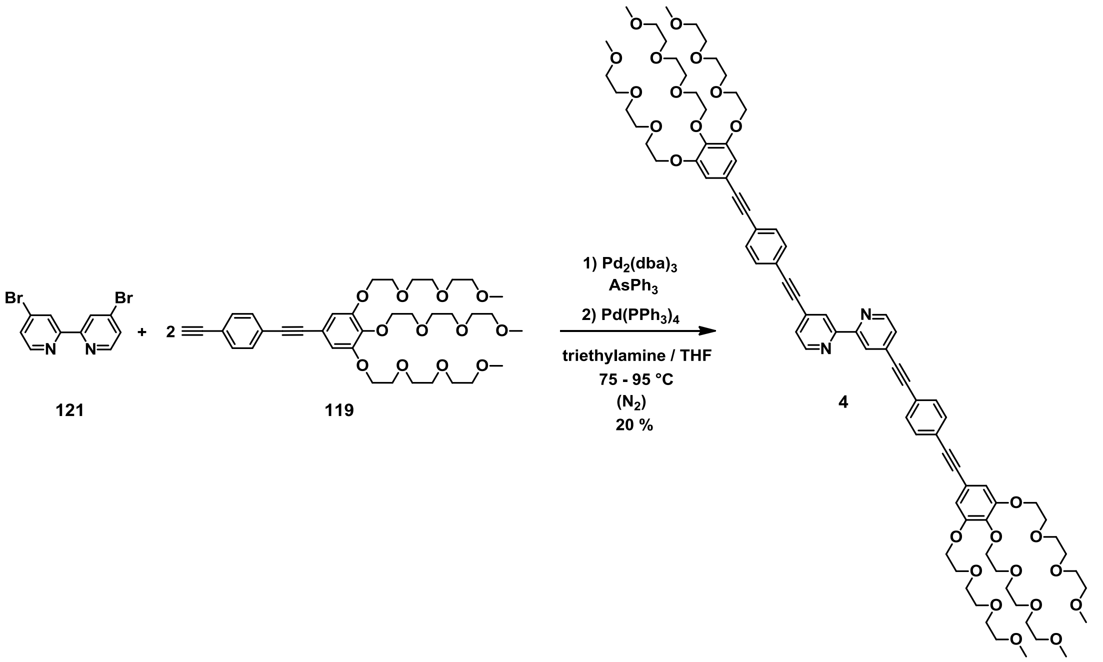

For an appropriate progress of the synthesis, monitoring of the reaction by thin-layer chromatography (TLC) was necessary. Thus, the mixture was initially stirred at 75 °C in the presence of triphenyl arsine and tris(dibenzylideneacetone)dipalladium(0) for two hours. After the progress seemed to pause, the Pd(0) catalyst tetrakis(triphenylphosphine)palladium(0) was added to the reaction mixture and the temperature increased to 85 °C for 1.5 hours. Finally, the addition of further glycol reactant **119** and an additional reaction time of around one hour at 95 °C provided a significant spot of the target product **4** on TLC. The purification was carried out by column chromatography (silica gel) with CH_2Cl_2/MeOH = 96:4 as eluent to achieve **4** in a yield of 20%. The moderate yield of the reaction can be explained by the formation of an undesired side product that appeared close to the target product **4** on TLC/column and thus complicated the purification of **4**. This spot indicates the homocoupling side reaction of alkyne **117**, whose product exhibits similar molecular weight and amphiphilicity to the target bipyridine derivative **4** and thus can hardly be separated. The target molecule **4** was characterized by ^{1}H NMR, ^{13}C NMR, MALDI-TOF-MS, HRMS (ESI) and elemental analysis.

3.6.2 Optical properties of 4

3.6.2.1 Solvent-dependent characteristics of 4

The new OPE-based amphiphilic derivative containing a central bipyridine unit was characterized by solvent-dependent absorption studies (Fig. 94). Compound **4** is readily soluble in THF, dichloromethane and chloroform while in more polar solvents such as acetonitrile, methanol and water its solubility is decreased. To facilitate the sample preparation in these solvents, the compound is initially dissolved in 1% of THF, followed by removal of the THF until a thin film of **4** is formed and subsequent addition of the respective solvent. The bands for the organic solvents present a similar shape with a maximum centred at 334 - 338 nm (Fig. 94). However, the absorption maximum in aqueous solution undergoes a red-shift to 345 nm and the spectrum broadens up to 425 nm. This spectral feature in water, along with a decrease in absorption intensity can be assigned to the self-assembled state of **4** that originates from its high aggregation tendency in this medium.

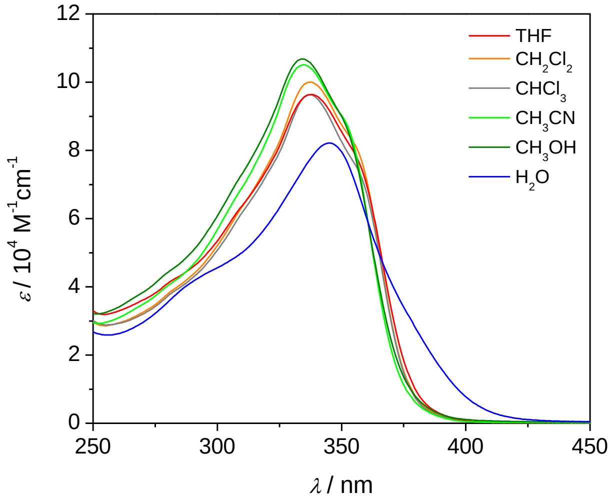

Fig. 94 Solvent-dependent UV/Vis absorption measurements of bipyridine derivative **4** (0.9 - 1.2 x 10^{-5} M).

As depicted in Chart 35, the transoid conformation of the central unit is the energetically most stable conformation for bipyridine derivatives in neutral media.[281,286-288] On this basis, it is expected that OPE scaffolds of **4** can interact by intermolecular aromatic contacts that are reinforced in water by the hydrophobic effect.[96,179,180,181,183,187]

Emission studies of **4** were performed to complement previous UV/Vis absorption experiments. First indication of the emission behaviour was provided by a photograph of solutions of **4** in different solvents under UV light (Fig. 95).

Fig. 95 Photograph illustrating the luminescence of compound **4** in different solvents (0.9 - 1.2 x 10^{-5} M) under UV light (wavelength of the UV lamp: 350 nm).

The photograph in Fig. 95 clearly reveals a strong luminescence in chloroform, THF and dichloromethane, while a significant quenching in acetonitrile and particularly in methanol and water is observed. The solution of **4** in chloroform shows a clear blue fluorescence while it slightly changes to greenish in THF and dichloromethane. This greenish character intensifies for the acetonitrile sample, however the emission intensity decreases.

The colour impression by the naked eye originates from the shift of the emission maxima of the investigated samples, as depicted in Fig. 96a. All spectra were normalized by division of the data with the intensity value of the maximum in chloroform. While the emission band in chloroform is centred at 448 nm, it shifts to 465 nm and 468 nm for THF and dichloromethane, respectively. Regarding the spectrum in acetonitrile, the intensity is significantly reduced and the maximum shifts to lower energy (503 nm), which is responsible for the green emission colour of the solution. In methanol and water the emission intensity is dramatically quenched, to the point that their maxima have to be enlarged to distinguish their intensity (Fig. 96b). For the methanol solution the emission is centred at ~469 nm while in water it is further displaced to ~505 nm.

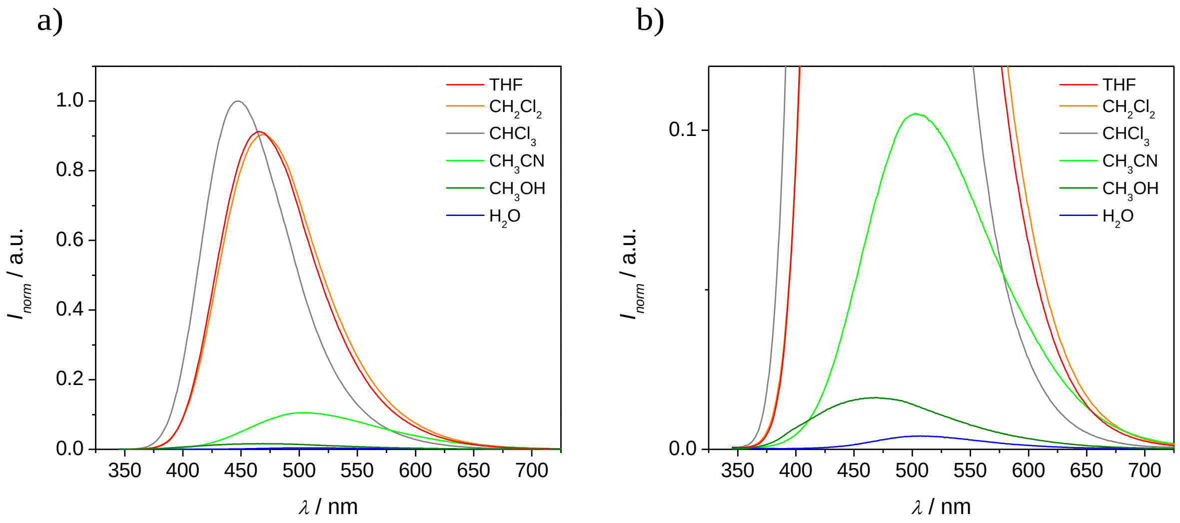

Fig. 96 Normalized solvent-dependent fluorescence spectra of bipyridine derivative **4** (0.9 - 1.2 x 10^{-5} M), (excitation wavelength λ_{ex} = 335 nm). To distinguish their emission maxima, a zoom-in into the spectra of low intensity is depicted in b).

The optical characteristics of **4** were also investigated at a higher concentration (10^{-4} M) in order to investigate possible aggregation phenomena. Due to the limited solubility of **4** in some organic solvents and water, the spectra were recorded in those solvents (THF, dichloromethane and chloroform) in which a good solubility is present. The absorption bands look similar to the lower concentrated solution, exhibiting a maximum at 337 - 338 nm (Fig. 97).

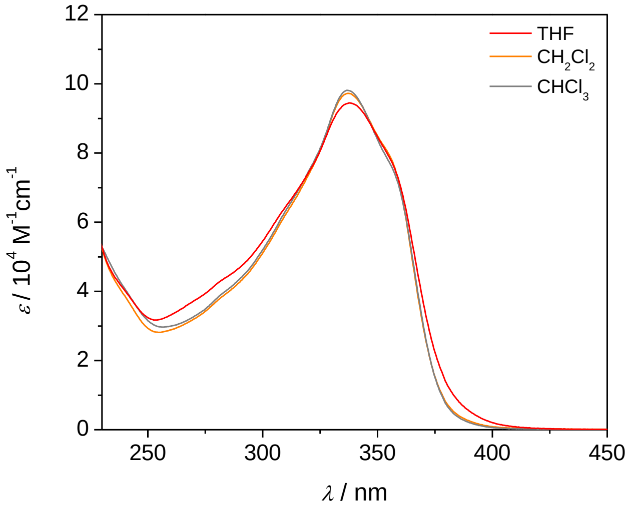

Fig. 97 Solvent-dependent UV/Vis absorption measurements of bipyridine derivative **4** (0.9 - 1.0 x 10^{-4} M).

Likewise, the emission spectra (normalized by division with the intensity value of the maximum in chloroform) of the 10^{-4} M solutions (Fig. 98) show no obvious differences compared to the lower concentrated samples, which suggests a comparable behaviour. Regarding the absorption band shape and the relatively high fluorescence intensity, it is suggested that the molecules exist in their molecularly dissolved state.

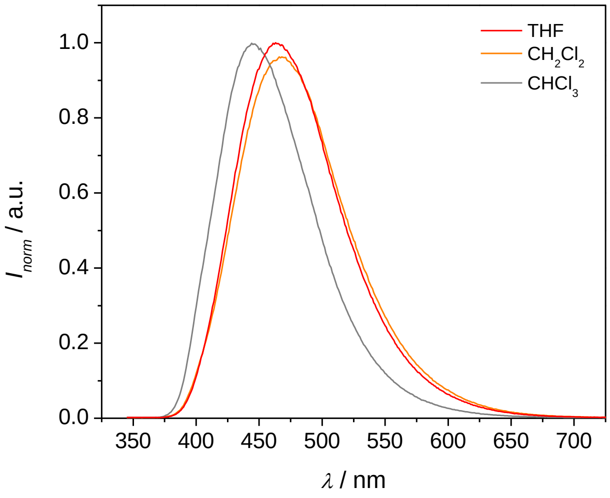

Fig. 98 Normalized, solvent-dependent fluorescence spectra of bipyridine derivative **4** (0.9 - 1.0 x 10^{-4} M), (excitation wavelength λ_{ex} = 335 nm).

To quantify the emission of **4** in different solvents, the fluorescence quantum yield was determined (Table 10). As reference compound, quinine sulphate in 0.05 M H_2SO_4 (refractive index η = 1.33) was chosen whose quantum yield is defined as 0.52.[289,290] To yield an absorption value <0.05 a concentration of 4.0 - 5.0 x 10^{-7} M was used.

Table 10 Fluorescence quantum yield ϕ_{FL} for **4** in different solvents at 4.0 - 5.0 x 10^{-7} M.

	$CHCl_3$	**THF**	**CH_2Cl_2**	**CH_3CN**	**MeOH**	**H_2O**
ϕ_{FL}	0.52±0.05	0.52±0.04	0.50±0.04	0.08±0.005	0.01±0.001	0.01±0.002

The low-concentrated solutions of **4** in chloroform, tetrahydrofuran and dichloromethane exhibit very similar fluorescence quantum yields of 0.52 - 0.50. In the more polar solvent acetonitrile the value is reduced to 0.08, while the fluorescence is almost completely quenched in methanol and water (ϕ_{FL} ~0.01).

3.6.2.2 Temperature-dependent self-assembly of 4

As demonstrated by previous UV/Vis absorption and emission studies, the bipyridine derivative **4** shows a high tendency to aggregate in aqueous medium. Thus, water was chosen as solvent to investigate the aggregation behaviour by temperature-dependent studies.

The first measurements were recorded in pure water. Due to the limited solubility of **4**, the compound is initially dissolved in 0.5% of THF, followed by removal of the THF until a thin film of **4** is formed and subsequent addition of water. Fig. 99 depicts the temperature-dependent studies of a 2.9 x 10^{-5} M solution of **4** upon cooling from 359 to 275 K with a rate of 1 $\mathrm{Kmin^{-1}}$. Regarding the state at high temperature, the initial absorption spectrum at 359 K is centred at 335 nm. Upon cooling, the red-shift of the maximum to 348 nm at 275 K is accompanied by the appearance of two shoulders at ~290 nm and ~385 nm, respectively. Additionally, the absorption bands show a broadening of the whole spectrum upon decreasing temperature.

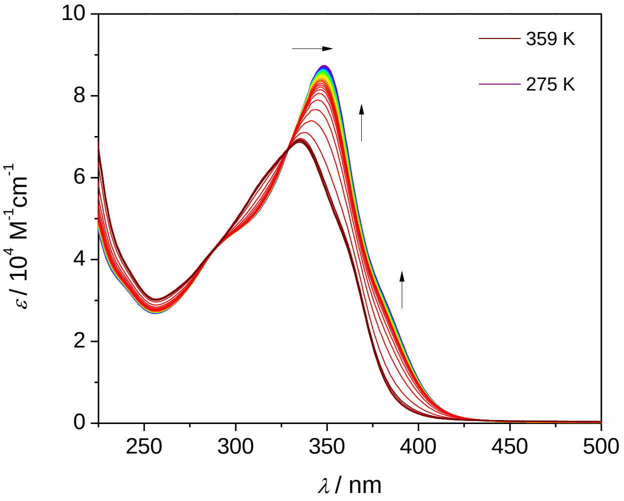

Fig. 99 Temperature-dependent UV/Vis absorption experiment of **4** in water (2.9 x 10^{-5} M) upon decreasing temperature from 359 to 275 K with 1 Kmin^{-1}. Arrows indicate the spectral changes upon decreasing temperature.

To facilitate the sample preparation for further studies on **4** in aqueous media, the effect of adding a small amount of THF was investigated. Thus, the same experiment as shown in Fig. 99 was performed at 2.4 x 10^{-5} M but in the presence of 1% of THF. Similarly to the previous experiment the compound was dissolved in THF (1%), however water was added without removal of the good solvent (initial thin film in THF solution).

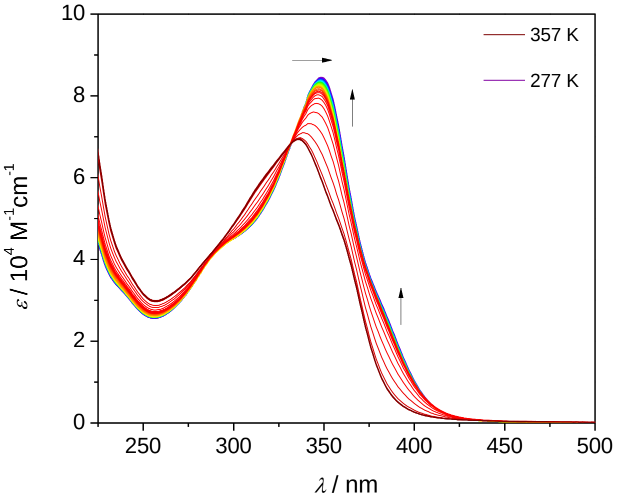

Fig. 100 Temperature-dependent UV/Vis absorption experiment of **4** in water/THF = 99:1 (2.4 x 10^{-5} M) upon decreasing temperature from 359 K with 1 Kmin^{-1}. Arrows indicate the spectral changes upon decreasing temperature.

The measurement was performed upon cooling the aqueous solution of **4** from its molecularly dissolved state (359 K), using identical conditions as chosen for the studies shown in Fig. 99. The spectral changes of the sample between 357 and 277 K are depicted in Fig. 100. The comparison of Fig. 99 and Fig. 100 reveals no distinct changes, indicating that the small amount of THF has no influence on the self-assembly of the molecules. Thus, due to a higher stability, the solvent mixture of water/THF = 99:1 was used to inspect the underlying aggregation mechanism. In this regard, a solution of 1.5 x 10^{-5} M was heated to a molecularly dissolved state at 359 K and gradually cooled down by only 0.1 Kmin^{-1} to ensure that the aggregation in aqueous medium occurs under thermodynamic control. The cooling process causes a progressive shift of the absorption maximum from 334 nm at 359 K to 346 nm at 319 K (Fig. 101a). The corresponding cooling curve (plot of ε at λ = 353 nm against temperature) was extracted manually from the experimental data (Fig. 101b).

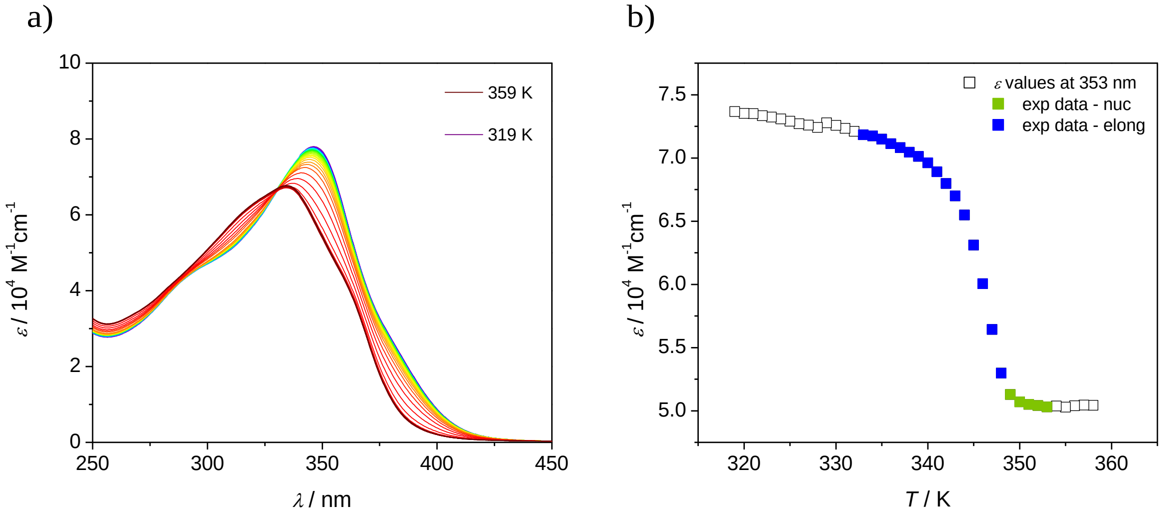

Fig. 101 a) Temperature-dependent UV/Vis absorption experiments of **4** in water/THF = 99:1 (1.5 x 10^{-5} M) upon decreasing temperature from 359 to 319 K with a cooling rate of 0.1 Kmin^{-1}. b) Corresponding cooling curve (ε values) extracted from the spectra in a) at λ = 353 nm.

As can be seen in Fig. 101b the plot of the ε values at 353 nm as a function of temperature is non-sigmoidal in shape with a sharp onset of aggregation at a defined temperature. The fact that the band shape and the maximum of the aggregate spectrum remain unchanged below 329 K (light blue to purple spectra) indicates that the aggregation process is complete. However, upon closer inspection it becomes noticeable that the intensity of the low temperature transition slightly, but continuously increases upon cooling (Fig. 101a). This trend becomes obvious for both cooling rates of 1 and 0.1 Kmin^{-1} (Fig. 100 and Fig. 101), as well as with and without addition of 1% of THF (Fig. 99 and Fig. 100). This special feature causes a continuous, slight rise of the α_{agg} values when saturation should have come to an end (~329 K). This behaviour of **4** resembles that observed in hydrogen-bonded OPVs described by van der Schoot, Meijer and co-workers (see derivatives **6**-**8** in section 2.4.1).[42] During their work, they observed that the experimental data shows deviations from the cooperative fitting below a certain temperature, as shown in Fig. 6a. In their case and as it can also be assumed for the system of bipyridine **4** in aqueous solution, this continuous increase of the cooling curve indicates the presence of a second process that occurs additionally to the formation of one-dimensional aggregates. It is suggested that the molecules first self-assemble into fibre-like structures, which subsequently interact laterally with neighbouring fibres into thicker bundles (so called "clusters")[42]. Due to this unusual self-assembly behaviour of **4**, the cooling curve in Fig. 101b was separated into several steps to allow the fitting of the data points. The data points highlighted in green were considered for the nucleation process while the blue data points represent the elongation process into individual fibres. As already mentioned, the spectral changes upon further cooling (shown as open squares) suggest further aggregation on a higher level and thus were not included in the fitting range.

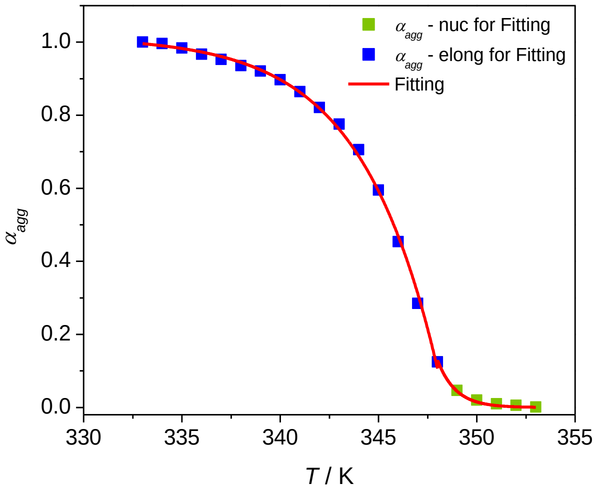

Fig. 102 Temperature-dependent UV/Vis absorption experiment of **4** in water/THF = 99:1: Plot of the α_{agg} values at 353 nm for the self-assembly of **4** as a function of temperature from 353 to 333 K. The cooling curve was extracted from the temperature-dependent series shown in Fig. 101a.

Consequently, for the fitting of the data to a cooperative aggregation model the range from 353 K to 333 K is of relevance, as depicted for the corresponding α_{agg} values in Fig. 102. For the temperature of 333 K an almost completed (first) self-assembly process is assumed, with a α_{agg} value close to unity.

Further analysis of the nucleation and elongation data was performed using the model for *thermally activated equilibrium polymers* by van der Schoot[34,41-43] (see section 2.3.2.2). Application of this model revealed suitable fitting for both the nucleation (R^2 = 0.9915) and elongation (R^2 = 0.9979) regimes, as represented by the red lines in Fig. 102. As previously explained, the model assumes a nucleus of monomeric size whose activation is characterized by a dimensionless equilibrium constant K_a. Regarding the investigated bipyridine system **4**, this activation most probably includes a decrease in flexibility of the freely rotatable bipyridine centre accompanied by a planarization of the OPE cores. This preorganization of the molecular surface facilitates initial interactions with another monomer and thus starts the aggregation process. The fits to the nucleation-elongation model by van der Schoot yielded a value for T_e of 348 K, an elongation enthalpy of -257 kJmol^{-1} and a dimensionless equilibrium constant K_a with a value of 2.1 x 10^{-3} M.

The number-average stack length at the elongation temperature $DP_N\,(T_e)$ can be calculated according to eq. (11) (see section 2.3.2.2.) to around eight molecules. Furthermore, in the elongation regime the averaged degree of polymerization at different temperatures ($DP_N\,(T)$) can be calculated according to eq. (29)[43]:

$$DP_N\,(T) = \frac{1}{\sqrt{K_a}}\,\frac{\alpha_{agg}}{\alpha_{SAT} - \alpha_{agg}} \qquad (29)$$

with α_{SAT} as a parameter to ensure that $\alpha_{agg}/\alpha_{SAT}$ does not exceed unity.[43]

Using the K_a value of 2.1 x 10^{-3} M and α_{SAT} of 1.016, it is thus possible to suggest the length of the individual one-dimensional stacks of **4** in the completely aggregated state (≤ 333 K). For a α_{agg} value of 1 an average stack size of ~1370 molecules can be calculated by (**29**) for this temperature range. Assuming a π-π distance of 0.35 nm between the subunits of **4** an average length of the fibres of ~480 nm can be proposed.

3.6.3 Microscopic characterization of 4

To reveal the architecture of the self-assembled aggregates of **4** on surfaces, samples of relatively high concentration were investigated by TEM. To this end, aqueous solutions of 5.7 and 8.0 x 10^{-4} M were prepared.

As depicted in Fig. 103 for the 5.7 x 10^{-4} M sample, already after few days of aging one-dimensional structures with a uniform diameter of 4 - 5 nm could be visualized. Due to their flexible character and the close contact between the individual fibres a dense layer is formed. Thus, the length cannot be accurately determined but rather estimated to some tens of nanometres.

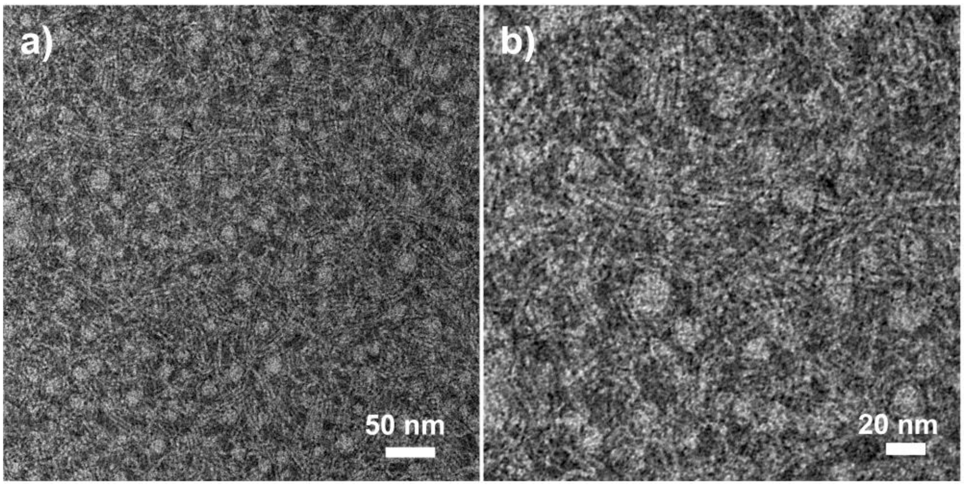

Fig. 103 TEM images of a two-days aged solution of **4** in water (5.7 x 10^{-4} M) onto a carbon-coated copper grid.

The influence of the concentration on the self-assembled fibres of **4** was investigated by keeping the aging time constant. Even though the concentration is not tremendously higher (8.0 x 10^{-4} M), a clear trend of the sample to grow into longer aggregates can be observed (Fig. 104). The shape of the structures is identical to the lower concentration with flexible, well-defined nanofibers of 4 - 5 nm in diameter. However, the assemblies formed by the higher-concentrated sample are much longer. Due to the close contact between the fibres their lengths cannot be precisely defined but estimated to be some hundreds of nanometres.

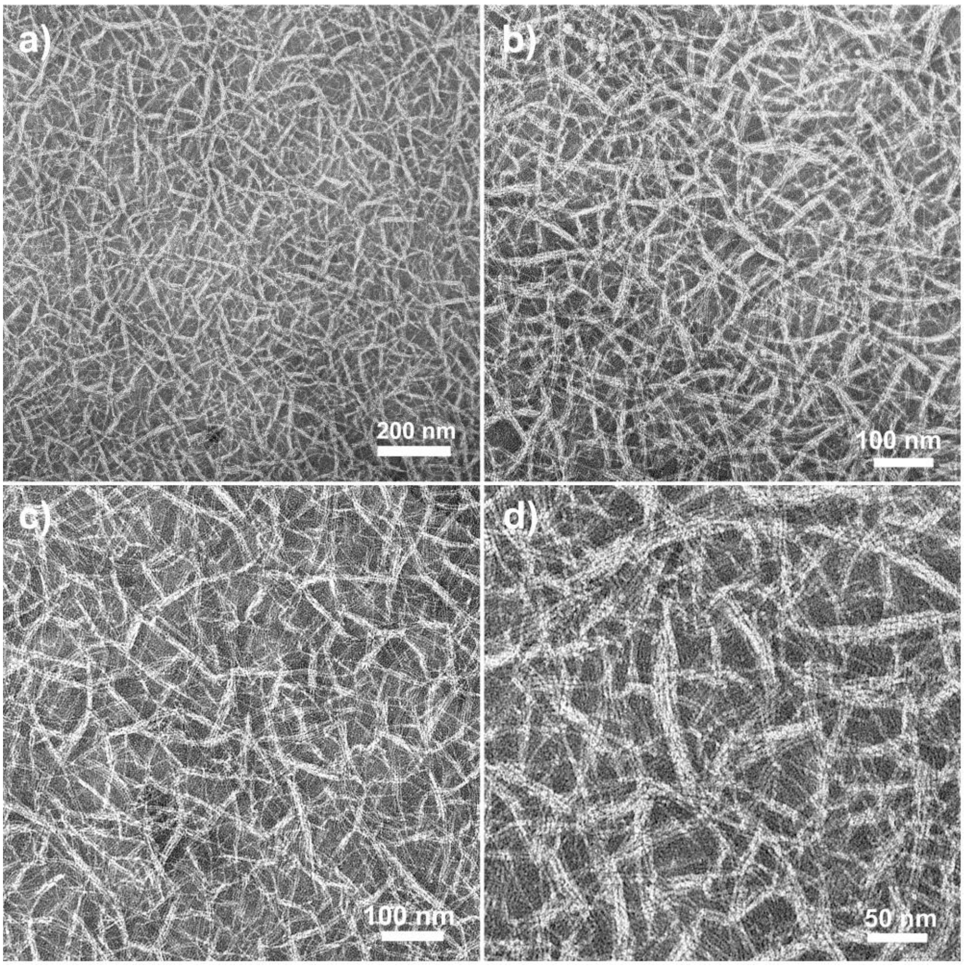

Fig. 104 TEM images of a two-days aged solution of **4** in water (8.0 x 10^{-4} M) onto a carbon-coated copper grid.

To compare the results from TEM with the dimension of molecule **4**, its energetically minimized structure in the *trans*-conformation was calculated by molecular modelling (AM1).[241] Fig. 105 shows that the geometry optimized structure for a monomeric *trans*-unit does not exhibit a completely planar aromatic surface but shows a slight twist around the C2-C2' bond. An interplanar angle for bipyridine units can also be found in literature that was determined to around 20° in carbon tetrachloride.[291] For this most stable *trans*-conformation of **4** the distance between the carbon atoms highlighted in blue in Fig. 105 was determined according to molecular modelling to be 4.37 nm. This is in agreement with the diameter of 4 - 5 nm measured in TEM for the self-assembled structures at both investigated concentrations (Fig. 103 and Fig. 104). However, it is notable to mention that the non-planar aromatic surface caused by the twist in the centre will certainly adopt a further planarization upon aggregation to maximize the overlap of the OPE scaffolds of neighbouring molecules.

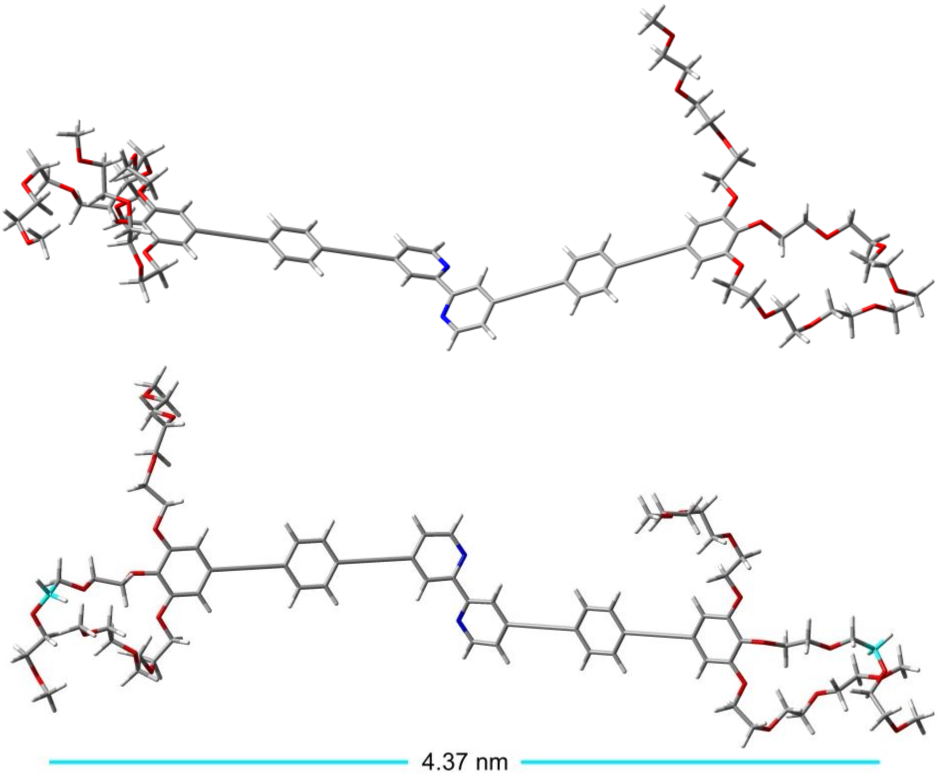

Fig. 105 Geometry-optimized molecular structure of **4** by the semi-empirical approach AM1.[241]

The microscopic imaging in Fig. 103 and Fig. 104 revealed that the supramolecular polymers are densely packed on the copper grid. These lateral interactions between the flexible fibres are in agreement with the suggested two-step aggregation mechanism extracted from temperature-dependent UV/Vis absorption studies (see previous chapter). However, upon comparison of the fibre length it becomes obvious that the dimensions observed by TEM are smaller than the average stack length of around 480 nm suggested by the UV/Vis absorption data. Concerning this difference in length several reasons might be considered, as e.g. the different sample preparation methods. While the solution prepared for UV/Vis studies contains 1% of THF, the TEM samples initially contain ~15% of THF that evaporates over time. Upon this reduction of the good solvent in the aqueous TEM solution, the aggregation strength between the molecular subunits increases. In contrast, the structures formed during UV/Vis studies result from very slow cooling (0.1 Kmin^{-1}) of the initially monomeric state in water/THF (99:1) to ensure the creation of thermodynamically stable assemblies. Moreover, the cooperative model proposes the average length of the fibres in solution, while in TEM the dried structures on the hydrophobic copper grid are investigated. Considering these aspects the differences in length are comprehensible, however both investigation methods similarly indicate the formation of extended, one-dimensional stacks that finally cluster. In general, further insight into the aggregate structure in solution can be yielded by DLS measurements. However, this spectroscopic method revealed not to be suitable for the investigated system of **4** in aqueous medium that might be attributed to the proposed clustering of the individual aggregates at ambient temperature.

3.6.4 Model for the aggregation process of 4

Combination of the findings by UV/Vis absorption experiments, microscopic studies and molecular modelling allows proposing a model of hierarchical aggregation, as depicted in Fig. 106.

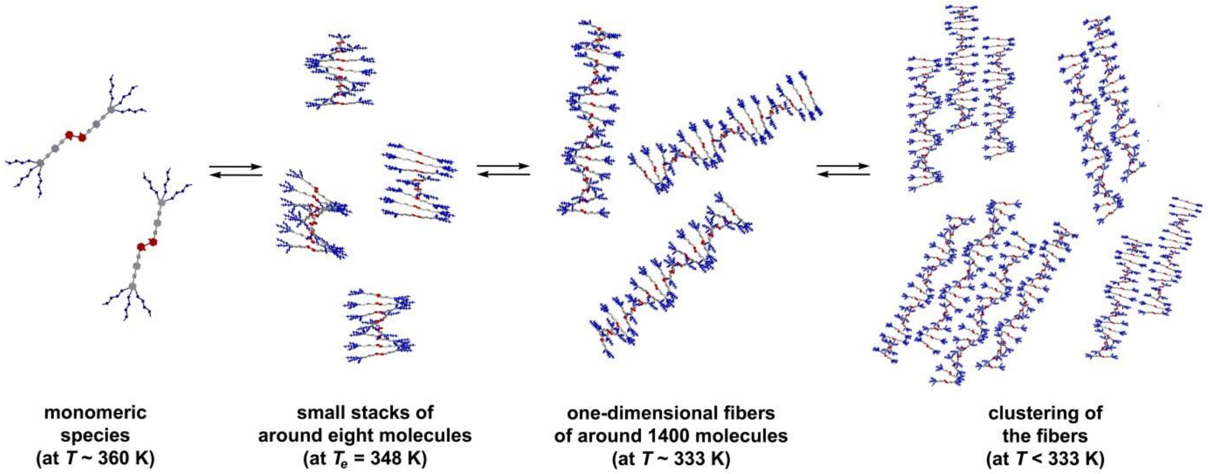

Fig. 106 Cartoon representation of the proposed hierarchical aggregation pathway of **4** in aqueous solution.

Starting at high temperature (~360 K), the molecules are molecularly dissolved in solution and exist in their energetically favoured *trans*-conformation, as reported for several 2,2'-bipyridine derivatives in literature.[281,286-288] During the slow cooling process to ~333 K, the subunits self-assemble by aromatic interactions into one-dimensional π-stacks that most likely come along with a planarization of the aromatic core. Within the stacks, the molecules have to adopt a slight rotational displacement due to the sterical hindrance of the bulky glycol chains, as shown in the suggested model (Fig. 106). The diameter of these assemblies can be determined by TEM to 4 - 5 nm (Fig. 103 and Fig. 104), which is in agreement with the AM1 calculation (Fig. 105). The average size of the stacks at the elongation temperature (T_e = 348 K) could be defined by the successful cooperative fitting to around eight molecules (solution of 1.5 x 10^{-5} M). Upon further cooling, the cooperative aggregation results in a further growth of the one-dimensional stacks into elongated, helical fibres. The suggested average degree of polymerization for the completely aggregated species ($\alpha_{agg} = 1$, $T \leq 333$ K) can be calculated to around 1370 molecules within one fibrillar structure. Their relatively flexible nature allows a further lateral contact into bundles of fibres, as indicated by the slight but constant increase of the absorption band upon cooling and visualized by TEM imaging (Fig. 103 and Fig. 104).

To explain the origin of the hierarchical character, the following self-assembly model is suggested: the molecules in the fibres most likely exhibit a rotational displacement resulting in helical structures of different handedness (see fibres in Fig. 106). This aggregation pattern is induced by π-stacking interactions between the aromatic OPE cores that are significantly supported by hydrophobic interactions. Due to the flexible glycol chains that can create a hydrophilic shell, the hydrophobic OPE and bipyridine units are shielded from the aqueous environment. However, it is likely that not all aromatic OPE surfaces are efficiently shielded from the surrounding medium. Thus, to minimize these unfavourable contacts, the fibres further self-assemble laterally into dense clusters to additionally protect the hydrophobic regions from the solvent molecules. The close contact between the one-dimensional fibres of **4** might be further stabilized by an interdigitation of the glycol chains of neighbouring aggregates by hydrogen bonding interactions, as previously shown for the investigated complexes **2** and **3** in section 3.3. and 3.4, respectively. This behaviour is similar to a recently reported example by Würthner and co-workers focusing on hierarchical self-assembly of an amphiphilic PBI derivative.[187] In the first step, they observed the aggregation of the PBI monomers in water into helical assemblies that subsequently undergo a morphology transition (fusion) into densely packed nanoribbons. Comparably to the presented case of **4**, the reported *sequential growth* in water from nanorods to nanoribbons avoids the unfavourable exposure of the hydrophobic PBI cores in the initially formed rods to the aqueous medium.

The question comes up, how the presented self-assembly fashion of **4** can be cooperative. The reason for this appears to lie in the interplay of conformational changes of the monomeric species and *π*-*π* and hydrophobic interactions between the OPE surfaces upon aggregation. As assumed in the cooperative model by van der Schoot, the nucleus is represented by a monomeric unit that initially has to overcome an activation step. To answer the question how the activation for species **4** can proceed, the peculiarities of the molecular building block have to be inspected. As known from literature and revealed by molecular modelling (Fig. 105), the rings of the 2,2'-bipyridine unit in the *trans*-conformation are not completely planar. With regards to possible conformational changes of the aromatic OPE segment of **4**, it is widely established that OPE derivatives adopt various random orientations from twisted to coplanar[21,292-294] due to the very low rotational-energy barrier that allows an almost unrestricted torsion of the phenylene units. For instance, for an OPE derivative exhibiting three aromatic units a rotational potential for the central ring of only 0.5 kcalmol^{-1} could be defined comparing the fully planar and perpendicular arrangement, upon keeping the outer phenylenes coplanar.[21] These aspects express the high conformational flexibility of **4** that may play a crucial role regarding the cooperative aggregation. While the free monomers profit from the presented structural flexibilities, the monomeric activation step might predominantly constitute a preorganization of the nucleus into a more ordered, planar structure. This is essential to start the aggregation but is accompanied by a loss of conformational freedom, turning this activation into an unfavourable step.

3.7 pH-responsiveness of 4

3.7.1 Absorption studies upon protonation of 4

As discussed in the previous section, bipyridine derivatives readily undergo protonation in acidic media.[284-287] In the case of 2,2'-bipyridine, the addition of acid results in the formation of the mono-protonated species leading to an interconversion from the more elongate *trans*- to the V-shaped *cis*-conformation. This *cis*-locked structure benefits from stabilization by N-H···N interactions, as depicted in Chart 36.[286,288] The mono-protonated species is in this regard the favoured or even single, charged species.[286,287]

Chart 36 Interconversion of the bipyridine unit from *trans*- to *cis*-conformation upon protonation and conformational locking of the protonated form due to N-H···N interactions.

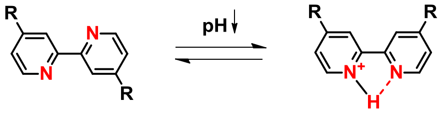

The first solvent of choice to investigate the pH-responsiveness of **4** by absorption studies was an aqueous solution (water/THF = 99:1) at a concentration of 1.5 x10^{-5} M. The solution was prepared similarly to that investigated by temperature-dependent studies (section 3.6.2.2). Subsequently, a diluted solution of trifluoroacetic acid (TFA) (water/TFA = 3:1, c = 3.3 M) was added up to pH ~2.2, while afterwards concentrated TFA was used.

In analogy to the previous studies of bipyridine derivative **4** in aqueous media, the absorption band with its maximum at ~346 nm (Fig. 107) clearly indicates that **4** exists in a highly aggregated state at room temperature. Upon addition of acid, a decrease in intensity of the absorption can be detected. However, the band shape remains completely unaffected even down to highly acidic conditions at pH ~1. This behaviour is at first glance surprising, since the bipyridine units are known to undergo protonation in acidic solution. The explanation for the negligible responsiveness of **4** depicted in Fig. 107 is most likely ascribed to its highly aggregated state under the present conditions. The temperature-dependent studies in aqueous solution (section

3.6.2.2.) suggested that already around 333 K the molecules of **4** are highly aggregated into one-dimensional structures (α_{agg} ~1) that further bundle at lower temperature. This dense packing most likely hinders the access of the central bipyridine to the surrounding protons in acidic medium and consequently the protonation of these functional units.

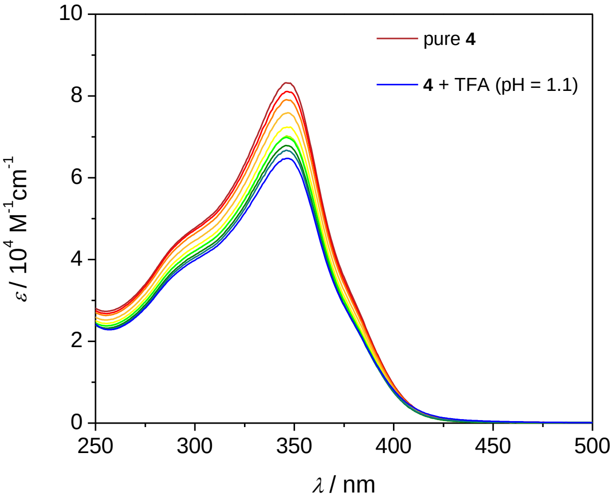

Fig. 107 Protonation studies of **4** in water/THF = 99:1 (1.5 x 10^{-5} M) upon addition of TFA down to pH = 1.1.

However, the decrease in absorption intensity upon lowering the pH (Fig. 107) indicates some changes in solution. This effect most likely results from slight precipitation of the aggregates in strong acidic medium, although these are not visible by the naked eye. Precipitation can be explained by changes in the hydrogen bond structure between the outer hydrophilic shell of the clusters/fibres and surrounding water molecules at low pH.[295] The high amount of protons present in the medium can influence the stabilizing hydrogen bonding between the solvent molecules and the hydrophilic part of the bipyridine derivative[295] and thus reduce the solubility of the aggregated species.

To prove whether time has an impact on the protonation of the bipyridine units, the solution at pH = 1.1, representing the end point of the titration studies in Fig. 107, was further controlled over time. To this end, the solution was kept at room temperature and each 30 minutes an absorption spectrum was recorded over 20.5 hours. As can be observed in Fig. 108, the band shape remains unchanged and only negligible changes in intensity occur over this period of time.

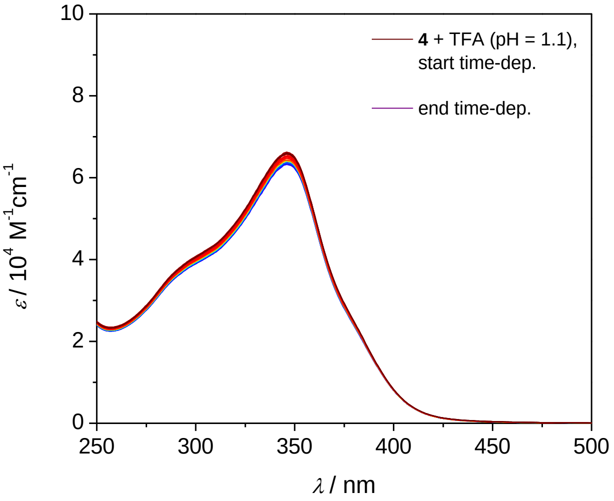

Fig. 108 Protonation studies of **4** in water/THF = 99:1 (1.5 x 10^{-5} M). The spectra show the time-dependent investigation of the solution at pH = 1.1 over a period of 20.5 hours.

These results (Fig. 107 and Fig. 108) point to a remarkable stability of the aggregates of **4** in aqueous solution at pH ~1 over the time course of around one day. Since the high aggregation tendency of **4** in water precludes the protonation of the bipyridine units in this medium, new alternatives to test its pH-responsiveness should be introduced.

Inspired by an intriguing example of phenylene ethynylene-based bipyridine derivatives by Armaroli and co-workers presented in 2009,[286] acetonitrile was chosen as solvent for the protonation studies using TFA. As the similarity of the absorption maximum of **4** in acetonitrile to the spectra in THF, chloroform and dichloromethane suggests (Fig. 94) the ligand is not aggregated in this medium. This should enable a protonation of the free bipyridine units, in contrast to their shielding in the highly aggregated state in water. The reversibility of the formation of the H^+-adducts of the bipyridines should be proven by the back titration of the system with the organic base diazabicyclo[5.4.0]undec-7-ene (DBU).

Following this procedure, a 1.5 x 10^{-5} M solution of **4** in acetonitrile was prepared. To this end, the solid was initially dissolved in 1% of THF that was completely removed to form a dry film of **4**, followed by the addition of acetonitrile. For the protonation studies, TFA was used as acid while the deprotonation should be achieved upon addition of DBU. To provide the gradual and defined (de)protonation, the concentrated acid and base were diluted with acetonitrile (TFA/acetonitrile = 1:49 and DBU/acetonitrile = 1:24, respectively) and added in microliter quantities to the system.

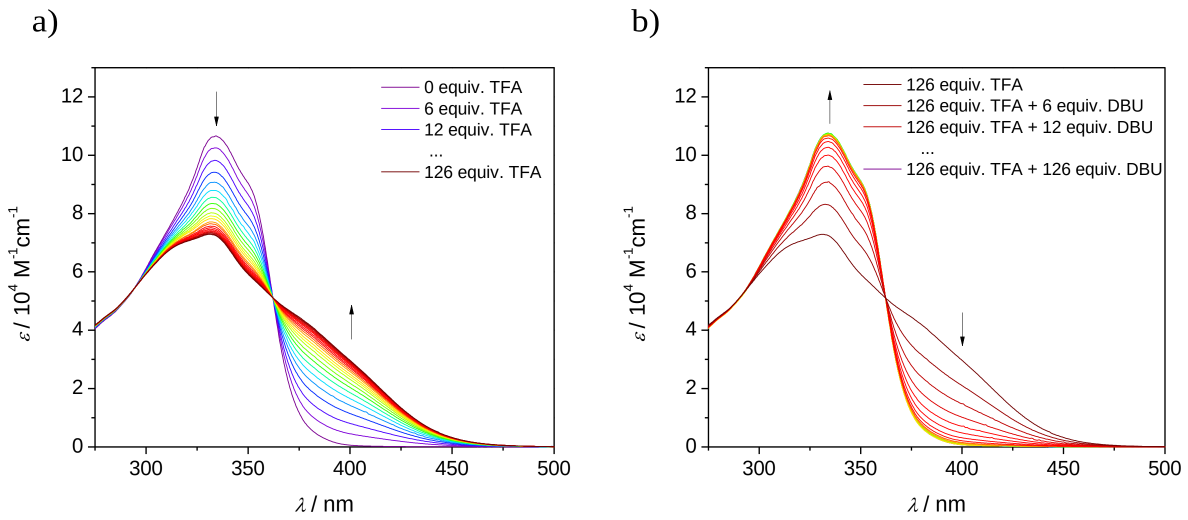

Fig. 109 a) Protonation studies of **4** in acetonitrile (1.5 x 10^{-5} M) using TFA. b) Back titration to the deprotonated state of **4** using DBU.

The gradual addition of TFA in portions of ~6 equivalents each results in significant spectral changes, as depicted in Fig. 109a. Upon addition of TFA, the band of neutral **4** at 334 nm shows a significant decrease at the expense of a new absorption shoulder at around 400 nm. While the initial changes caused by the first additions of TFA are strongly pronounced, this effect weakens upon further addition and finally levels off after ~120 equiv. At this point of saturation, the back titration with DBU was started. Similarly to the protonation process, each addition of the diluted base represents an amount of ~6 equiv. The significant spectral changes (Fig. 109b) reveal complete reversibility of the protonation that finally allows the recovery of the initial absorption features of neutral species **4**. The spectral changes are in agreement with literature[286] and clearly indicate the structural switch from the *trans*- to the *cis*-conformer upon addition of acid that results in the formation of *cis*-**4-H**$^+$ (Chart 37). The mono-protonation can be further confirmed by the presence of a single isosbestic point that is consistent with the findings observed by Armaroli and co-workers.[286] The isosbestic point clearly indicates that two distinct species (neutral **4** and mono-protonated **4-H**$^+$) are in equilibrium. In addition, the *cis*-conformation is also responsible for the broadening of the absorption band that extends significantly towards longer wavelengths. In this regard, the intramolecular N-H···N hydrogen bridge causes an increased planarization of the molecular structure that might result in an extension of the conjugated surface of the bipyridine-OPE scaffold.[286]

Chart 37 Reversible protonation step of **4** towards *cis*-**4-H**$^+$ upon addition of TFA.

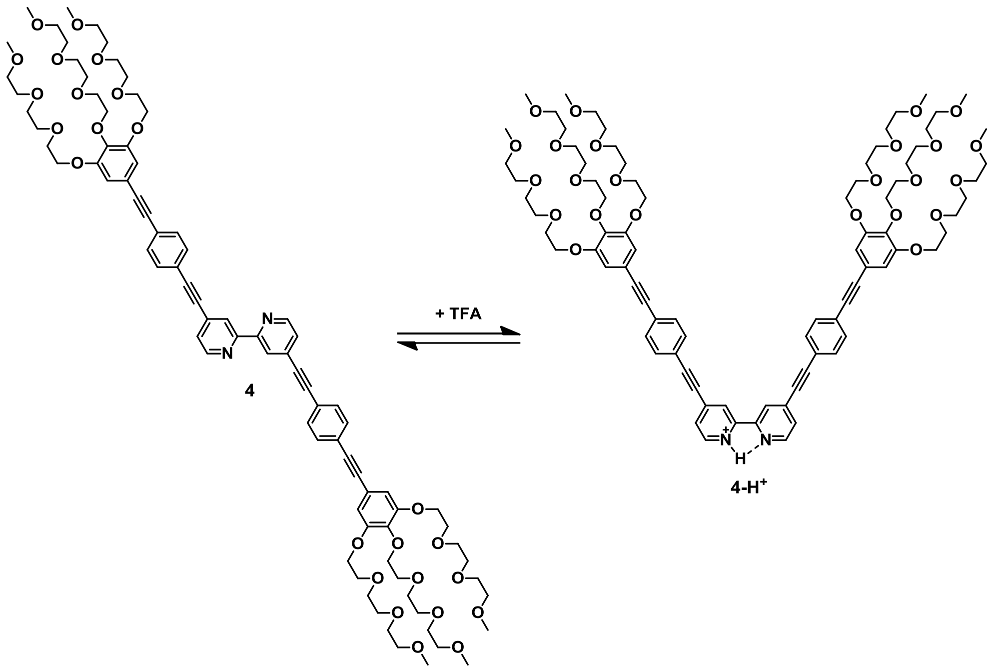

3.7.2 ^{1}H NMR studies upon protonation of 4

As the titration of **4** with TFA in acetonitrile revealed pronounced spectral changes, the protonation towards *cis*-**4-H**$^+$ was also investigated by ^{1}H NMR experiments. For this purpose, a solution of **4** at 1.5 x 10^{-4} M in acetonitirile-d$_3$ (CD_3CN) was prepared. The compound was initially dissolved in 2% of CD_2Cl_2 that was completely removed before CD_3CN was added, resulting in a stable solution of **4**. To allow relatively small addition steps, the concentrated TFA (trifluoroacetic acid-d1, CF_3COOD) was diluted with deuterated acetonitrile in a ratio of TFA/CD_3CN = 1:19.

Seven samples of **4** were prepared with varying volume of acid, resulting in titration steps from 0 up to 133 equiv. of TFA. The corresponding ^{1}H NMR titration measurements are shown in Fig. 110. The ^{1}H NMR spectrum of **4** in pure CD_3CN (red) exhibits sharp signals that partly show a significant shifting upon addition of TFA. To get deeper insight into the spectral changes, a zoom-in for the signals corresponding to the relevant protons is shown in Fig. 111 and Fig. 112.

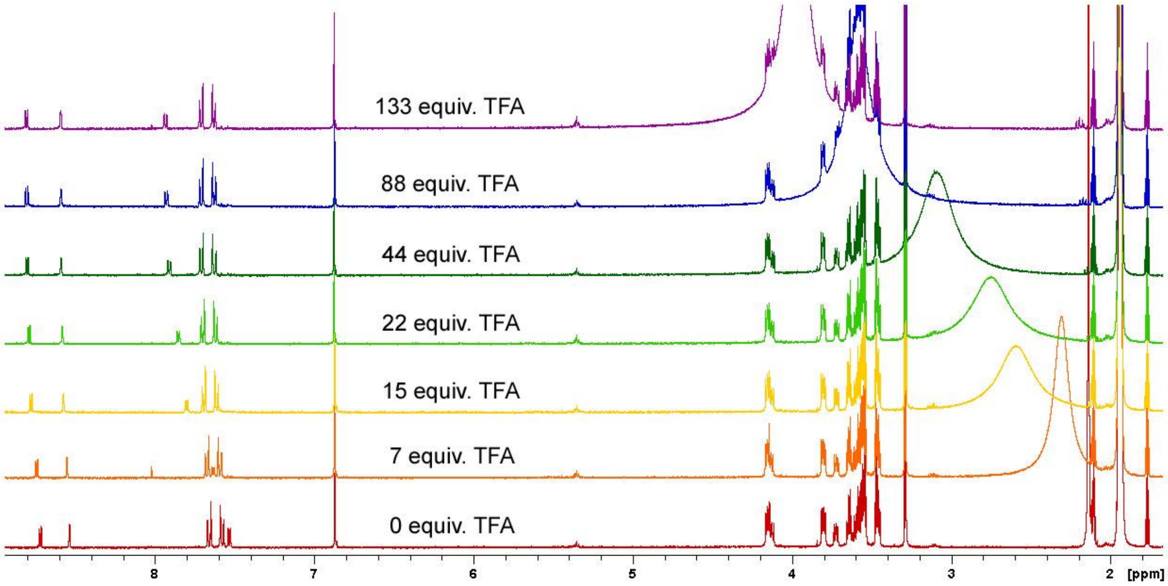

Fig. 110 ^{1}H NMR protonation studies of **4** towards **4-H**$^+$ in CD$_3$CN (400 MHz, 295 K). The spectra from bottom to top show the subsequent increase of the added amount of TFA from 0 equiv. (red) to ~133 equiv (purple).

As shown in Fig. 111, broad signals in the range of 2.1 to 4.3 ppm appear that become more and more pronounced upon increasing amount of TFA and finally overlay with the signals corresponding to the protons of the glycol chains. This shifting signal is not of relevance since it originates from the presence of water in solution becoming more intense upon increasing addition of TFA.

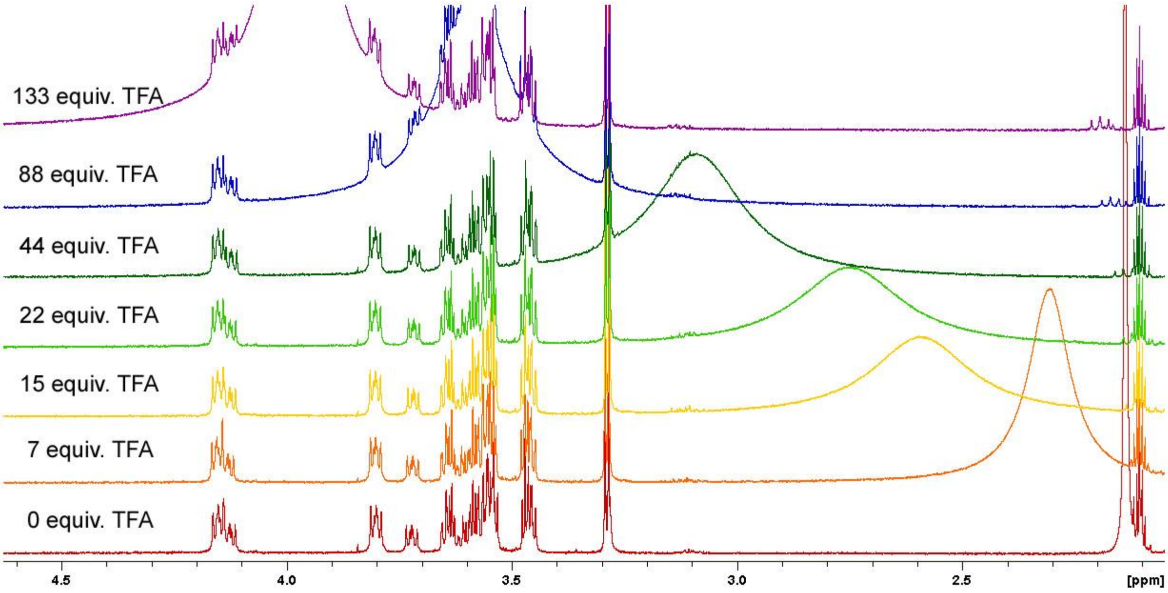

Fig. 111 ^{1}H NMR protonation studies of **4** towards **4-H**$^+$ in CD$_3$CN (400 MHz, 295 K) upon increasing amount of TFA from 0 equiv. (red spectrum) to ~133 equiv (purple spectrum). Zoom-in for the region monitoring the protons of the glycol chains.

Regarding the important regimes in Fig. 111, the signals of the glycol chains do not show any notable changes. This indicates that the protons of the terminal chains are not influenced by the addition of acid to the system.

Regarding the behaviour of compound **4** in acetonitrile solution, the molecularly dissolved state has to be considered which means that the molecules can easily coordinate to the protons. This protonation of the central bipyridine unit comes along with a change from its *trans*- to the *cis*-conformation (Chart 37). Upon closer inspection of the proton signals corresponding to the bipyridine moiety, clear changes become noticeable (Fig. 112).

Chart 38 Labelling of the aromatic protons of **4-H**$^+$ as used in Fig. 112.

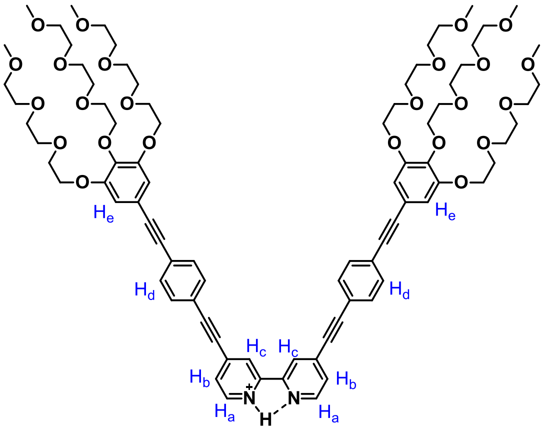

4-H$^+$

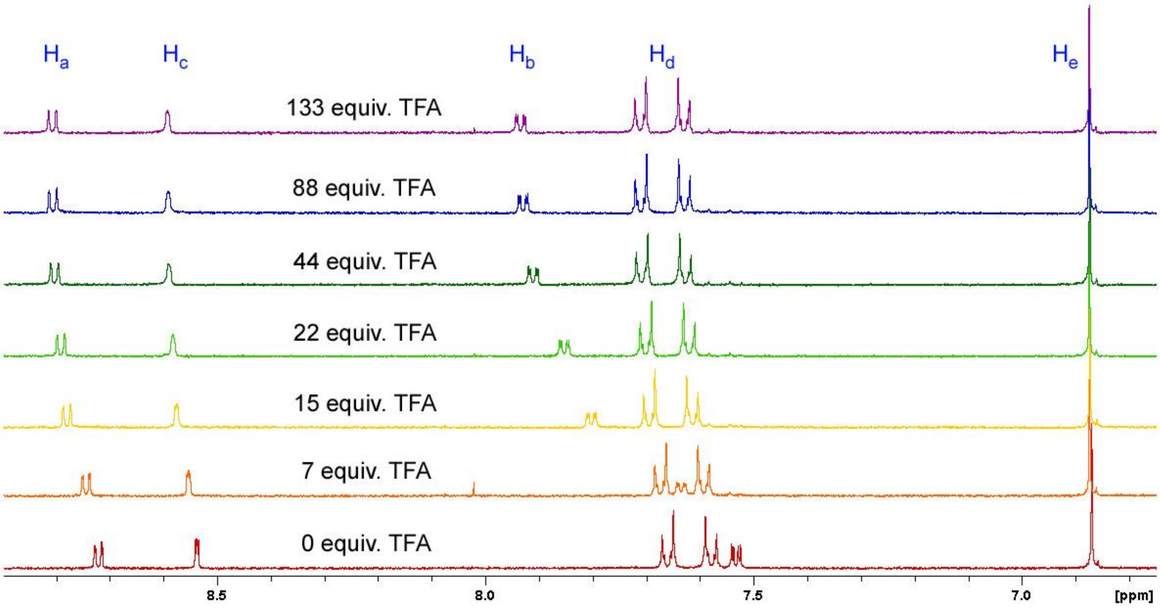

Fig. 112 ^{1}H NMR protonation studies of **4** towards **4-H**$^+$ in CD_3CN (400 MHz, 295 K) upon increasing amount of TFA from 0 equiv. (red) to ~133 equiv (purple). Zoom-in for the region monitoring the protons of the bipyridine and OPE unit.

Fig. 112 shows that the signals for protons H_a, H_b and H_c (for labelling see Chart 38) are significantly downfield shifted upon increasing addition of TFA. In particular, the shift of the signal corresponding to protons H_b is most pronounced, which is in agreement with the observations made by Armaroli and co-workers for the TFA titration of a bipyridine derivative in deuterated chloroform.[286] The effect for the remaining protons of the aromatic moiety (H_d and H_e), however, is insignificant. The signal of protons H_d shows a moderate upfield shift, while the protons H_e of the terminal phenylene ring remain completely unaffected.

The clear shift of the signals corresponding to the protons of the aromatic rings can be attributed to the change in their electronic environment upon protonation of the bipyridine unit. This effect is accompanied by the conformational switch of the bipyridine centre from *trans* to *cis* upon coordination to a proton.

3.7.3 Microscopic studies on the mono-protonated species *cis*-4-H$^+$

The absorption studies have shown that the binding constant of the self-assembled species of **4** in water is so high that disassembly of the aggregates does not occur even in the presence of TFA in excess (Fig. 107 and Fig. 108). Even at pH ~1 and over time no significant changes in aqueous solution appeared, unlike the behaviour of the system in acetonitrile, in which a clear protonation of the bipyridine unit was observed (Fig. 109).

However, in order to achieve the protonated species in aqueous media and to examine the influence of the protonation of **4** on the self-assembled structures, a new method of preparation was required. For this purpose, a highly concentrated, slightly yellow-coloured solution (4.8×10^{-3} M) of **4** in THF was initially prepared. To the THF solution an excess of concentrated TFA was added (~280 equiv.), causing an immediate intensification of the yellow colour. This change can be attributed to the protonation of the central bipyridine of **4** under the strongly acidic conditions. Subsequently, water was added to the latter solution in two different ratios and the solutions were kept with a perforated cap (evaporation of THF) for several weeks before the microscopic studies were carried out. The first measurement of the two samples (3.2×10^{-4} M and 7.1×10^{-4} M) by SEM was performed after an aging time of around 4.5 months. After this time, the lower concentrated sample (3.2×10^{-4} M) showed slight precipitation, however the solution remained intensive yellow. SEM imaging revealed rod-like assemblies of **4-H**$^+$ that show a strong tendency to agglomeration (Fig. 113).

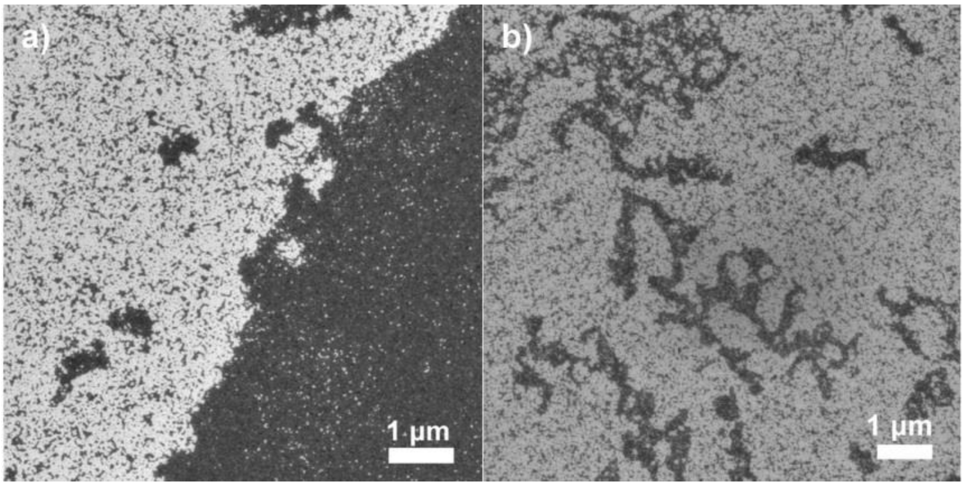

Fig. 113 SEM images of **4-H**$^+$ in aqueous solution (3.2 x 10^{-4} M) after an aging time of ~4.5 months onto silicon wafer.

The higher concentrated solution (7.1 x 10^{-4} M) remained completely stable, even after several months. In analogy to the lower concentration, one-dimensional assemblies were obtained that create an extended network on the surface (Fig. 114).

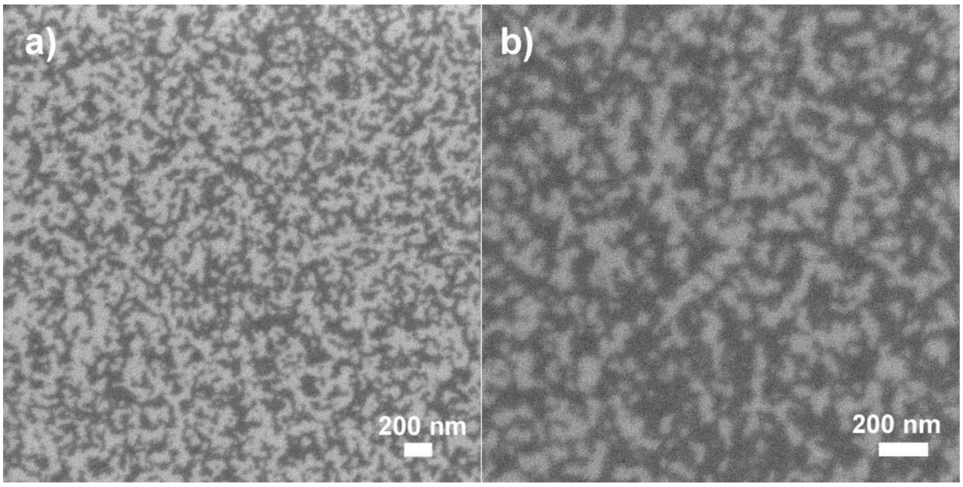

Fig. 114 SEM images of **4-H**$^+$ in aqueous solution (7.1 x 10^{-4} M) after an aging time of ~4.5 month onto silicon wafer.

Complementarily, the stable higher-concentrated solution of **4-H**$^+$ was investigated by AFM after spin-coating onto mica (Fig. 115). AFM imaging provided a better resolution and thus allowed the visualization of the individual aggregates that further self-assemble into a thin film on the hydrophilic substrate. The individual rods exhibit a diameter of 3.2±0.3 nm and a length of up to 70 nm.

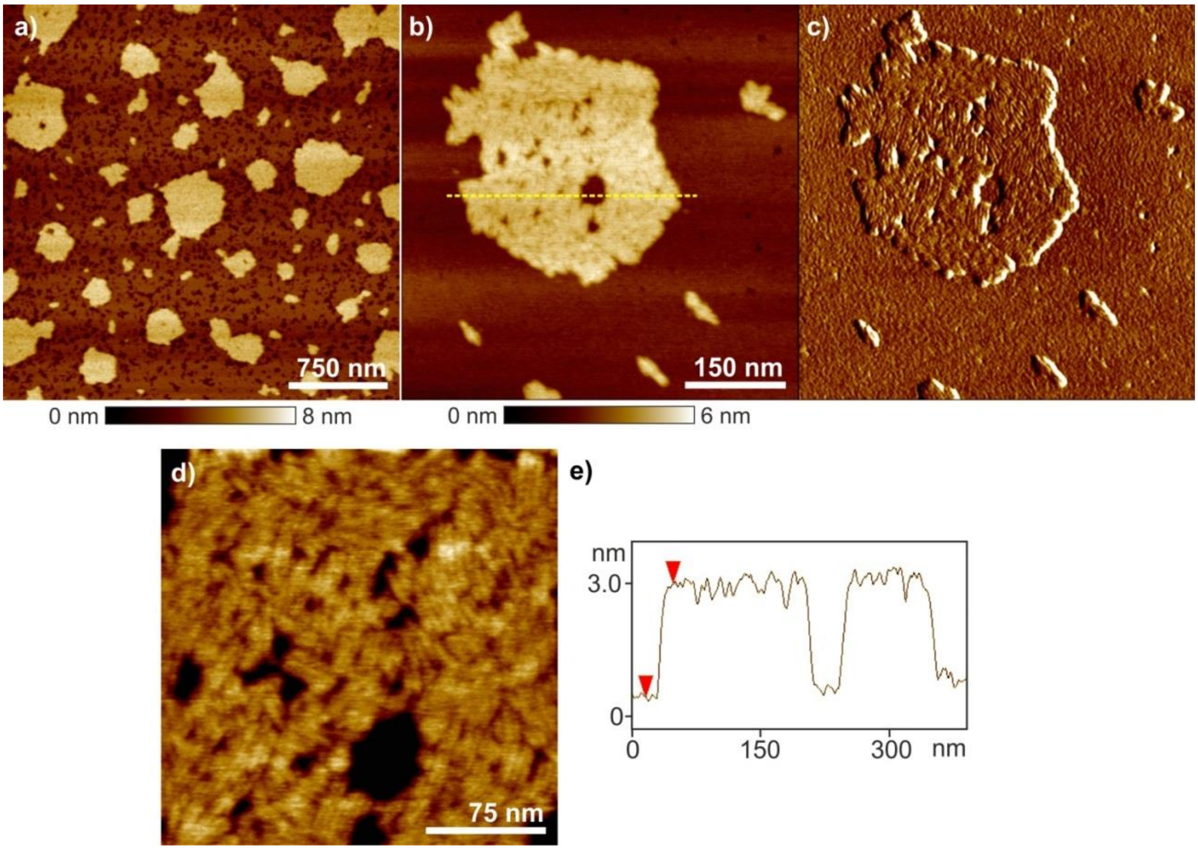

Fig. 115 AFM height (a, b, d) and phase (c) images of **4-H**$^+$ in water (7.1 x 10^{-4} M) after an aging time of ~5 months. The samples were prepared by spin-coating the solution with 7000 rpm onto mica. Image (e) shows the cross section analysis along of the yellow line in image (b).

Similarly, detailed investigation by TEM of the around six month-aged solution revealed close contact between the individual fibres (Fig. 116). Comparison of Fig. 115 and Fig. 116 furthermore shows that the structures grew further over time resulting in a length of more than 100 nm. The diameter of the one-dimensional assemblies visualized by TEM imaging could be defined to be ~3.0 nm.

To enable a comparison between the diameter of the self-assembled fibres defined by microscopic techniques and the dimension of the molecule in its *cis*-conformation AM1 calculations[241] were performed. The result is depicted in Fig. 117 with the energy minimized structure of *cis*-**4-H**$^+$.

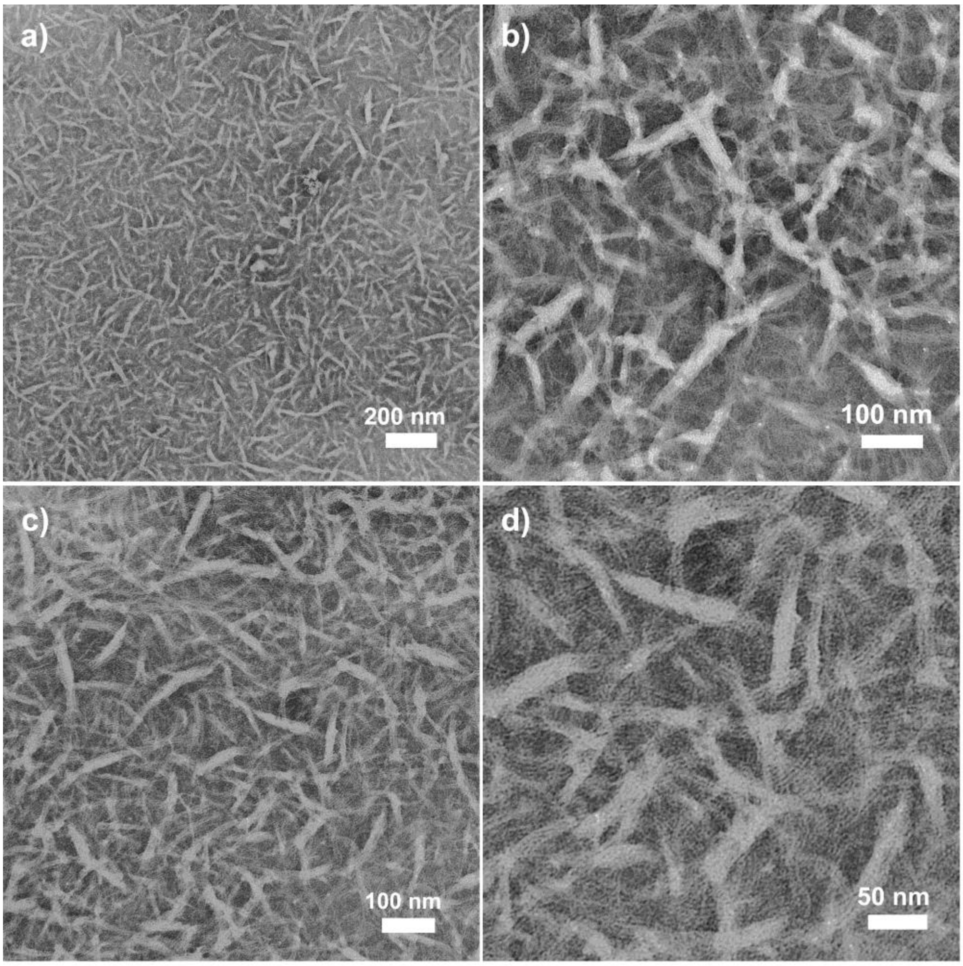

Fig. 116 TEM images of **4-H**$^+$ in water (7.1 x 10^{-4} M) after an aging time of ~6 months onto a carbon-coated copper grid. The pictures show different magnifications.

In the optimized structure (Fig. 117), the distance between the nitrogen atom (right half of the molecule) and the complexed proton is 1.01 Å, while a hydrogen bonding interaction to the second nitrogen atom (left half of the molecule) (N···H) is provided with a distance of 2.57 Å. As can be observed in Fig. 117c, the two halves of the system are twisted with respect to each other, which originates from a torsion around the C2-C2’ bond of the central bipyridine unit. However, the two individual OPE scaffolds (half of the system) adopt a planar conjugated arrangement. Similarly to the previously presented optimized structures of ligands **1** and **4** (Fig. 41 and Fig. 105), the organization of the glycol chains is not outstretched but bent due to their flexible nature. The distance between the middle glycol chains at the opposite ends of the molecule (carbon atoms highlighted in blue in Fig. 117a) can be defined to be 2.55 nm. For the dimension of one half of the molecule measured from the nitrogen atom to the glycol chains (highlighted in blue in Fig. 117b) a value of 2.00 nm can be obtained.

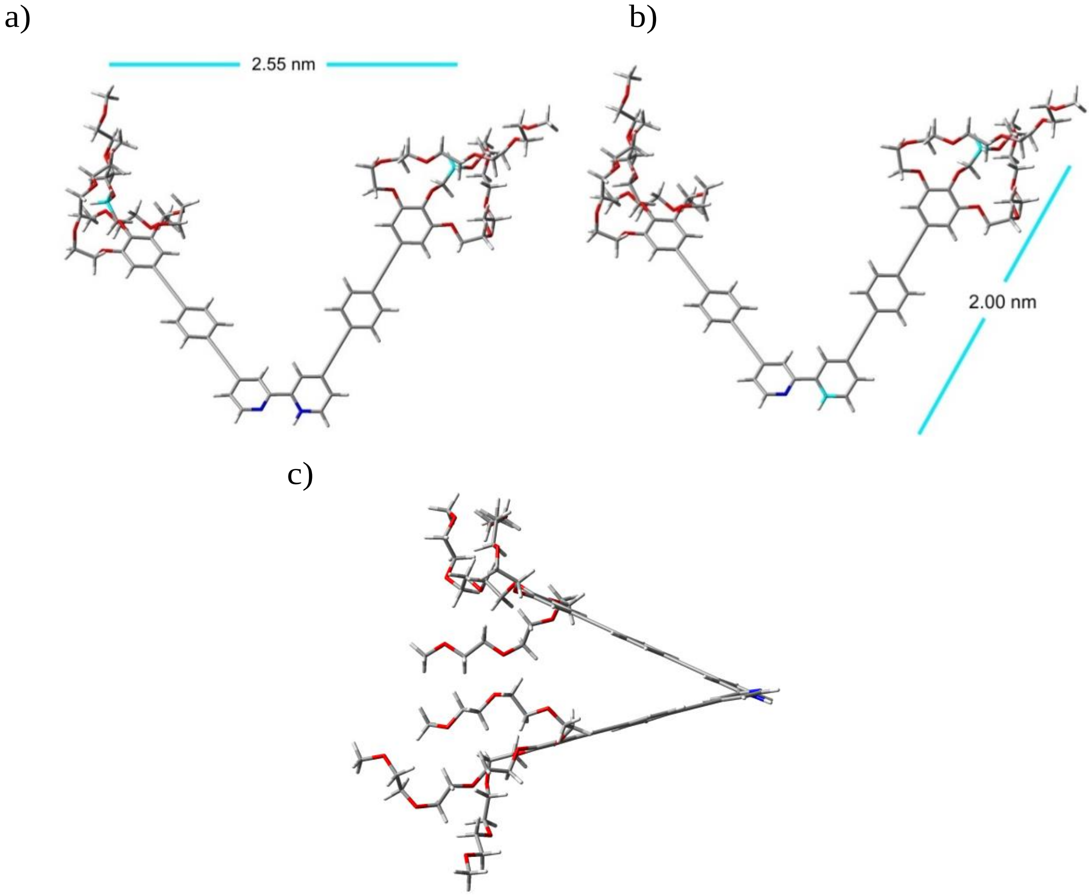

Fig. 117 Geometry optimized molecular structure of *cis*-**4-H**$^+$ by the semi-empirical approach AM1.[241] Top view (a, b) and side view (c).

Combination of the results gained by microscopic studies (Fig. 113 - Fig. 116) and molecular modelling (Fig. 117) leads to the proposed model of a *zig-zag* arrangement of *cis*-**4-H**$^+$ in aqueous medium. For the cartoon representation in Fig. 118, the minimized monomers were modified by a rotation around the C2-C2’ bond of the central bipyridine unit. This provides an almost planar aromatic core to allow close contact between the neighbouring molecules, as it is expected in aggregated solution.

In the suggested aggregation pattern (Fig. 118) the subunits adopt an opposed orientation to each other with their complexed protons directed alternatively to opposite sides. This self-assembled arrangement prohibits unfavourable repulsions between the positively charged bipyridine-H$^+$ units while providing sufficiently strong intermolecular interactions. The central OPE rings of neighbouring molecules are in close contact to stabilize the stacks by attractive aromatic interactions, supported by hydrophobic forces. Simultaneously, the flexible glycol chains can create a hydrophilic shell around the *zig-zag*-stacks to minimize unfavourable contact surface of the hydrophobic OPE-bipyridine scaffold and the surrounding aqueous medium.

This suggested self-assembly of the species *cis*-**4-H**$^+$ is in agreement with the diameter of the fibres of around 3.0 nm, determined by various microscopic techniques.

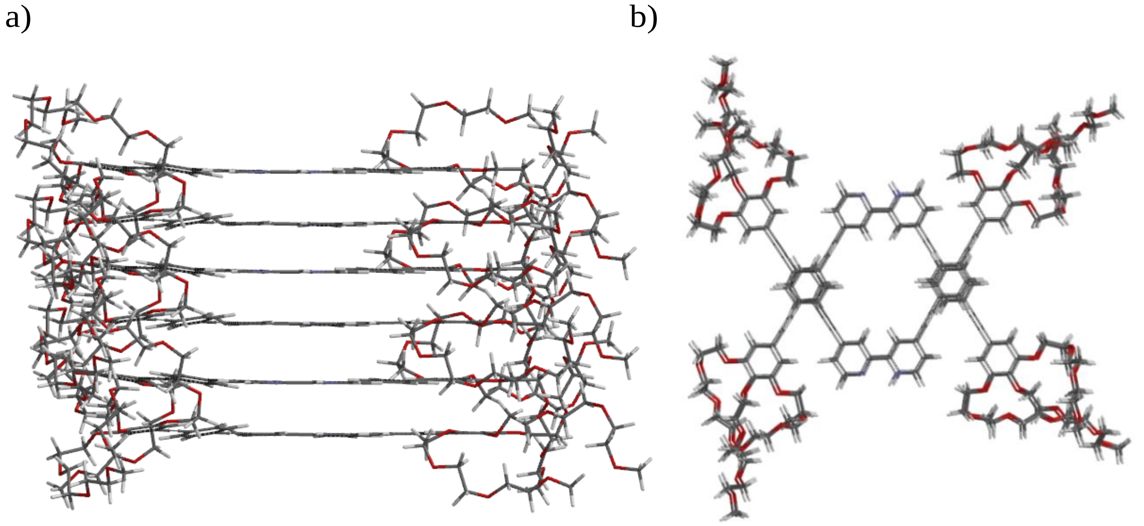

Fig. 118 Cartoon representation of the suggested *zig-zag* arrangement of **4-H**$^+$ in aqueous medium (distance between central OPE units $\leq$ 3.5 Å). Side view in a) and top view in b).

The suggested *zig-zag* arrangement of the molecules within the assemblies of **4-H**$^+$ (Fig. 118) is significantly different to the proposed model of rotated stacking presented for the neutral bipyridine derivative **4** (Fig. 106). At first glance, the stabilizing forces within the alternated stacks of **4-H**$^+$ seem to be low due to the limited contact surface for aromatic interactions. As depicted in the model in Fig. 118, in the suggested arrangement only the middle rings of the linear OPE units come sufficiently close for aromatic interactions, while in the helical stacks of neutral **4** the entire OPE scaffold seems to participate in the rotational π-stacking (Fig. 106). However, it has to be considered that in the suggested model for **4** the subunits have to adopt a rotated architecture due to the bulkiness of the glycol chains that in turn significantly reduces the contact surface for π-stacking. This sterical hindrance between the glycol units does not occur in the proposed *zig-zag* structure of **4-H**$^+$ due to the orientation of the chains towards opposite directions. Consequently, this arrangement most likely allows an even closer approximation of the OPE units of adjacent **4-H**$^+$ molecules, resulting in efficient attractive interactions between the central OPE rings. These close π-contacts seem to stabilize the entire self-assembled structures that are further supported by the hydrophobic effect and the ionic strength of the acidic aqueous solution.

3.7.4 Comparison of the spectral features for mono-protonated species *cis*-4-H$^+$ in aqueous solution and acetonitrile

To further confirm that the bipyridine derivative in the sample used for microscopic studies in section 3.7.3 existed in its protonated form **4-H$^+$**, the acidic solution was additionally investigated by UV/Vis absorption spectroscopy. In this regard, an absorption spectrum of the highly concentrated sample after an aging time of around six month was recorded, as shown in Fig. 119 (pink spectrum).

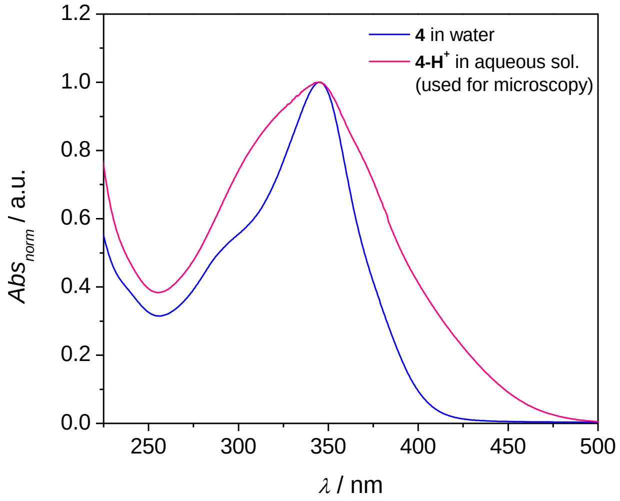

Fig. 119 Normalized UV/Vis absorption measurements: The pink spectrum corresponds to **4-H$^+$** in aqueous solution used for the microscopic studies in section 3.7.3 (7.1 x 10^{-4} M); the blue spectrum corresponds to a 1.2 x 10^{-5} M solution of **4** in water and allows a better comparison of the band shapes.

Both spectra depicted in Fig. 119 were normalized in their absorption maximum. By comparing the absorption band for **4-H$^+$** used for microscopy (pink spectrum) with the normalized band of **4** in pure water (blue spectrum), clear differences can be observed. The protonated sample is characterized by a significant broadening of the absorption band up to a wavelength of 500 nm. While the shoulder in pure water at around 290 nm becomes less obvious upon protonation, two new shoulders at around 310 nm and 375 nm appear.

Upon closer inspection, one can recognize that this behaviour in aqueous solution is similar to the characteristics upon protonation of **4** in acetonitrile. The entire TFA titration studies were already presented in Fig. 109, however for a better comparison of the band shapes in acetonitrile the normalized spectra of neutral species **4** and its protonated adduct (after addition of 126 equiv. of TFA) are shown in Fig. 120a. Finally, to compare the band shape of **4-H**$^+$ created in acetonitrile (Fig. 109) with that of **4-H**$^+$ in aqueous solution used for microscopy, both normalized absorption spectra are presented in Fig. 120b.

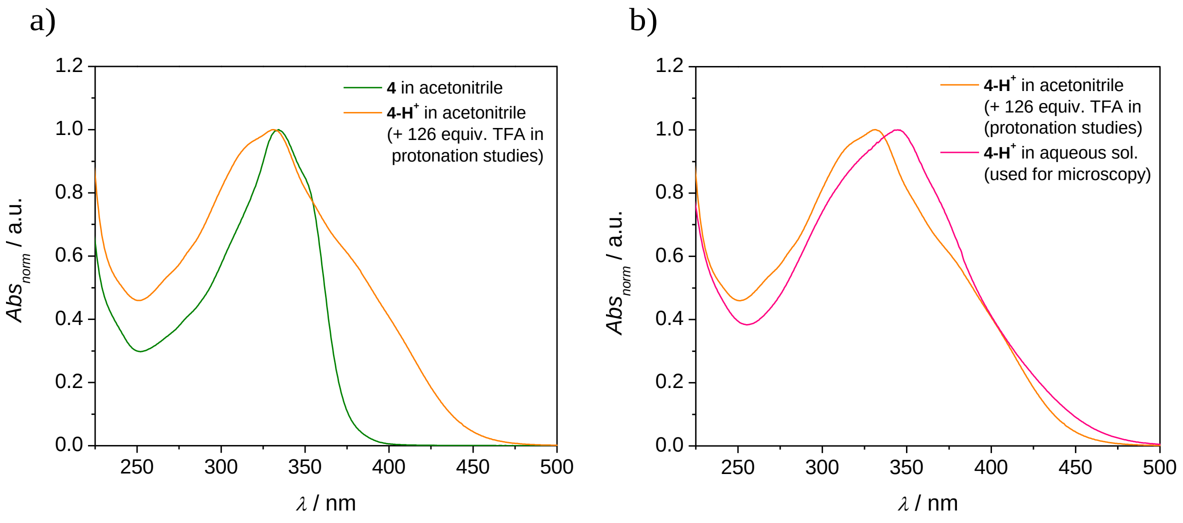

Fig. 120 a) Normalized UV/Vis absorption spectra of **4** and its protonated form **4-H**$^+$ after the addition of 126 equiv. of TFA in acetonitrile (1.5 x 10^{-5} M). b) Normalized UV/Vis absorption spectra of the protonated form **4-H**$^+$ after the addition of 126 equiv. of acid in acetonitrile and the aqueous sample used for TEM. For better comparison of the band shapes all spectra were normalized in their absorption maxima.

As mentioned previously, the spectral changes upon protonation of **4** in acetonitrile (Fig. 120a) are similar to those obtained in water (Fig. 119), both revealing a remarkable broadening of the absorption range. This effect can also be observed upon direct comparison of the samples of **4-H**$^+$ in the different media, shown in Fig. 120b. Just as observed for the water sample, the protonated species in acetonitrile is characterized by two shoulders at around 310 nm and 375 nm. As already discussed in section 3.7.1, the broadening of the spectrum towards longer wavelength in acetonitrile can be attributed to the conformational changes of **4** upon coordination to a proton.[286] Compared to the more flexible *trans*-conformer, the protonated *cis*-structure shows a stronger planarization that leads to an increased conjugation of the aromatic surface.

In water, however, stronger hydrophobic interactions are responsible for a second effect – aggregation – resulting in a slightly different UV/Vis absorption spectrum compared to less polar acetonitrile. On this basis, the similarity of the spectral changes in aqueous solution to those in acetonitrile clearly suggests the presence of the two conformers: *trans*-bipyridine in the water solution and the corresponding *cis*-conformer in the acidic sample used for microscopy. The presence of the *cis*-conformer is further supported by the microscopic studies and AM1 calculations that revealed structures of smaller diameter than those observed for the neutral ligand **4**.

3.8 Metal-ion responsiveness of bipyridine-based OPE ligand 4 towards Pt(II) complex 5

3.8.1 Synthesis of 5

Derivatives of 2,2'-bipyridine are capable to act as bidentate ligands to coordinate to a variety of metal ions. In this way, manifold complexes are created whose geometry mainly depends on the metal centre but is further influenced by the ligand structure.[9,256] Octahedral bipyridine-based Ru(II) complexes might be the most representative examples, since they have been exploited in different systems for artificial photosynthesis.[257-261] In contrast to these compounds, the characteristics of bipyridine-based platinum complexes are much less explored.[277,296]

To enrich the field of supramolecular chemistry on bipyridine-based Pt(II) complexes, molecule **5** was created by the complexation reaction of ligand **4** with bis(benzonitrile)dichloroplatinum(II) in refluxing benzene (Chart 39). The solvent was degassed and the reaction was stirred under nitrogen for several days at 87 °C.

Chart 39 Synthetic route to obtain the target complex **5**.

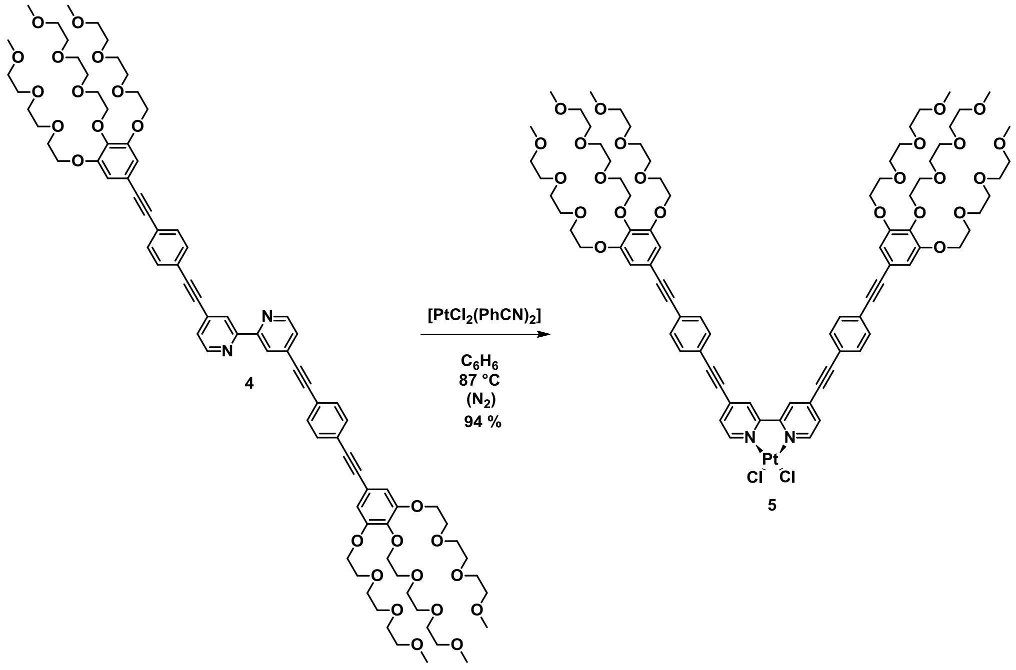

To monitor the progress of the complexation, ^{1}H NMR was used as reaction control revealing complete consumption of the starting material **4** after seven days. The complexation towards **5** is characterized by a significant shift of the protons corresponding to the bipyridine unit, as presented in Fig. 121.

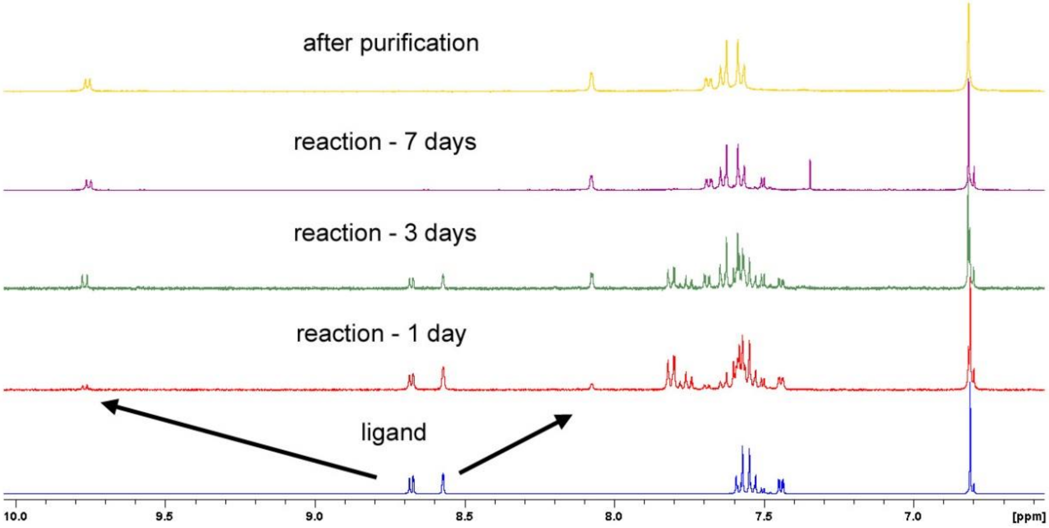

Fig. 121 ^{1}H NMR of the reaction shown in Chart 33 to achieve the target Pt(II) complex **5**.

The purification could be realized by repeated precipitation using dichloromethane for dissolution and hexane as bad solvent. This procedure gave a yield for the target complex **5** of 94%. The compound was characterized by ^{1}H NMR, ^{13}C NMR, HRMS (ESI) and elemental analysis.

3.8.2 Optical properties of 5

3.8.2.1 Solvent-dependent absorption characteristics of 5

The initial studies performed for the Pt(II) complex **5** are the solvent-dependent absorption measurements at 1 x 10^{-5} M. Due to the insolubility of **5** in pure water, an aqueous solution containing 4% of THF was investigated. To this end, the compound was initially dissolved in THF, followed by the addition of water without removal of the good solvent.

Due to the coordination of ligand **4** to the Pt(II) centre, the electronic states become more complex. This results in absorption spectra that consist of several transitions, including different predominantly ligand-centred and metal-centred orbitals.[297]

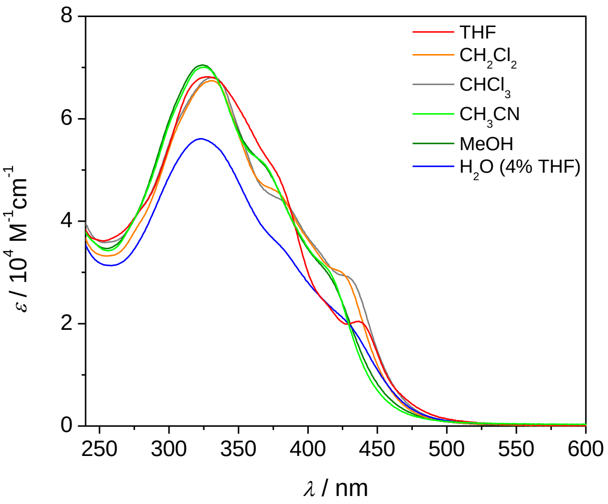

Fig. 122 Solvent-dependent UV/Vis absorption measurements of freshly prepared solutions of the bipyridine-based Pt(II) complex **5** (0.9 - 1.1 x 10^{-5} M).

As can be seen in Fig. 122, the absorption bands of **5** are relatively sharp for the organic solvents, while in water they are less defined. The highest-energy transitions of **5** are centred at 323 - 326 nm for the aqueous solution, methanol and acetonitrile while they appear at 327 - 332 nm for THF, dichloromethane and chloroform. Additionally, obvious bands at slightly lower energy are centred in the range of 370 - 385 nm for all investigated solvents. Finally, the shoulder at lowest energy shows the broadest variation and arises at 415 - 440 nm. While this transition for the THF sample is centred around 440 nm, it is blue-shifted to ~432 nm and ~426 nm for **5** in chloroform and dichloromethane, respectively. Finally, for the acetonitrile and methanol samples of **5** the centre of this shoulder appears around 415 nm, while it cannot accurately be located in aqueous solution due to the unstructured shape of the absorption band.

To elucidate the origin of the absorption characteristics of **5**, the bands were assigned to the corresponding transitions, related to a recently published work on similar Pt(II) complexes.[298] Following the spectral features presented therein, the most intense bands of **5** at 323 - 385 nm can be assigned to ligand $^1\pi \rightarrow \pi^*$ and ^{1}ILCT (intraligand charge transfer) transitions. Furthermore, the band at lower energies above 400 nm (415 - 440 nm) is characteristic of a ^{1}MLCT (metal-to-ligand charge transfer) transition. This involves predominantly metal- and predominantly ligand-centred orbitals and arises from the transition dπ(Pt) → π^*(bipy). In general, a ^{1}MLCT transition is typical for Pt(II) complexes and many examples can be found in literature.[298-301] However, as the authors mention, a relatively high intensity of this band might be due to an overlap of the ^{1}MLCT with the ^{1}ILCT transition.[298] As mentioned above this transition is located at around 440 nm for THF, while for dichloromethane and chloroform it shifts to ~430 nm and for acetonitrile and methanol to ~415 nm. The solvent-dependent differences reveal that in more polar medium this transition is centred at lower wavelength compared to less polar solvents. This is in agreement with the bipyridine-based Pt(II) complexes investigated by Sun and can be seen as further indication for a ^{1}MLCT transition.[298] Since the ^{1}MLCT state has a smaller dipole moment than the ground state, this excited state is better stabilized by less polar solvents.[298] The ^{1}MLCT characteristic becomes less obvious for **5** in aqueous medium and the centre for this transition can only be estimated to ~430 nm. However, the reduced absorption intensity and the less-structured shape of the spectrum in aqueous solution suggest an aggregated state of **5** in this medium.

3.8.2.2 Time-dependent behaviour of 5 in methanol

The spectra of **5** presented in Fig. 122 depict the absorption bands of freshly prepared solutions. Upon closer inspection of the methanol sample, it could be observed that the band shape slightly changes over time. To monitor this process, a 9.6 x 10^{-6} M solution was investigated by time-dependent UV/Vis absorption measurements. The studies were started 30 minutes after preparation and each 30 minutes a spectrum was recorded over a period of around 54 hours at 298 K (Fig. 123).

As indicated by the arrows in Fig. 123a, the changes in methanol over time concern all absorption bands. The absorption maximum of **5** slightly drops in intensity and blue-shifts by around 5 nm to 321 nm. Simultaneously, the shoulder at ~370 nm grows, while the band around 415 nm decreases in intensity. Furthermore, the absorption in the range of 475 nm slightly increases. These spectral features of **5** indicate a transition of the species in methanol solution from the initial state after dissolution to the thermodynamically stable state over time. The plot of the absorption values at 415 nm against time (Fig. 123b) shows that the changes level off after a period of around 26 hours. Furthermore, the fitting of the absorption data at 415 nm to the exponential function (red curve in Fig. 123b) reveals that this process underlies a first-order kinetics, as has also already been reported for other self-assembled systems.[171,302,303]

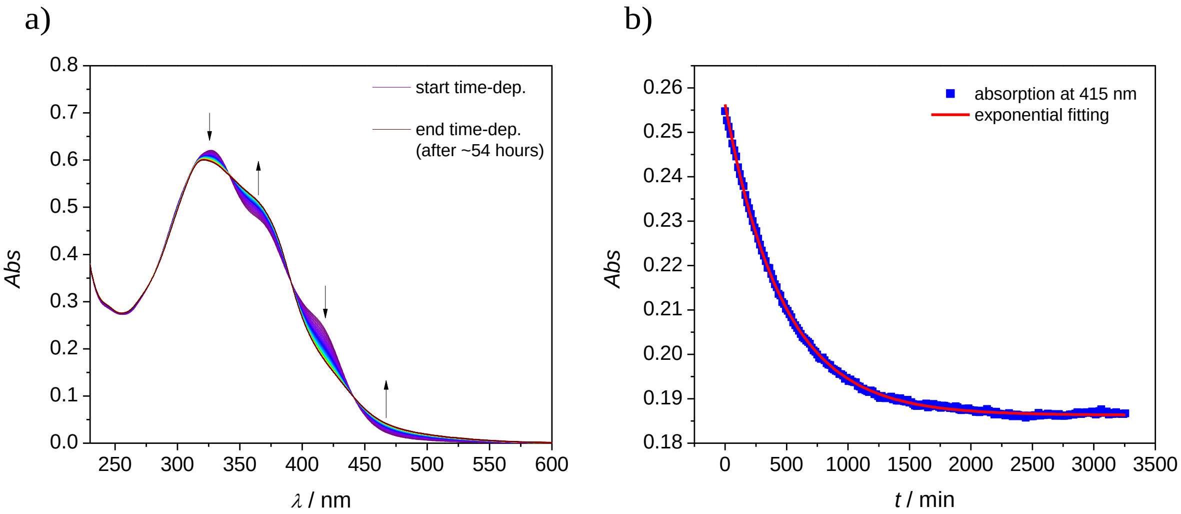

Fig. 123 a) Time-dependent UV/Vis absorption studies of **5** in methanol (9.6 x 10^{-6} M) over a period of around 54 hours, started 30 minutes after preparation. b) Corresponding plot of the absorption values at 415 nm as a function of time. The time-dependency of the absorption changes follow first-order kinetics (red curve, R^2 = 0.9994).

3.8.2.3 Solvent-dependent emission studies of 5

To further investigate the behaviour of **5** in different solvents, emission studies at 10^{-5} M were performed. The solutions were prepared one day in advance since the time-dependent measurements in methanol indicated that it takes some time to reach the thermodynamically stable state in this solvent (Fig. 123). The solutions of **5** in pure THF and in aqueous solution containing 4% of THF were omitted since increasing luminescence of the sample in pure THF indicated partial decomposition of the complex upon time in this medium. Instead of the water sample using THF as co-solvent, a solvent mixture of 20% MeOH and 80% water was investigated. To this end, the compound was initially dissolved in MeOH before water was added.

In Fig. 124 a photograph of the solutions of **5** under UV light is depicted one day after preparation. This image reveals that in none of the investigated solvents a substantial luminescence can be detected by the naked eye.

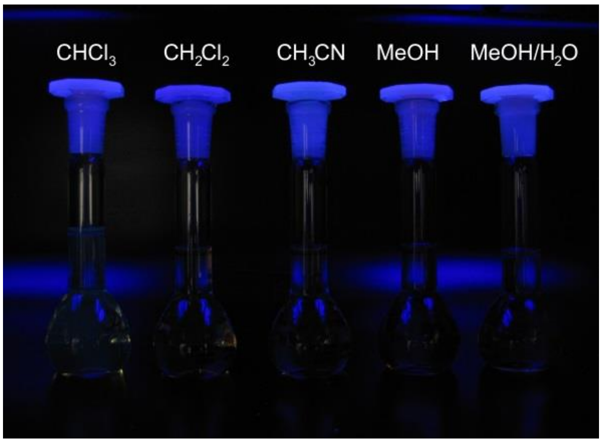

Fig. 124 Photograph of the samples of Pt(II) complex **5** in different solvents (1.0 - 1.1 x 10^{-5} M) under UV light at room temperature (wavelength of the UV lamp: 350 nm).

However, for all samples the corresponding emission spectra were recorded, as shown in the graph in Fig. 125. The spectra of **5** were normalized by division of the data with the intensity value of the maximum in chloroform.

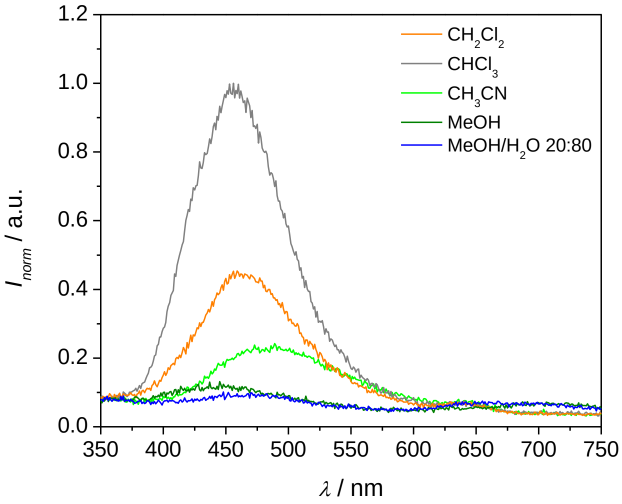

Fig. 125 Normalized solvent-dependent fluorescence spectra of Pt(II) complex **5** (1.0 - 1.1 x 10^{-5} M), (excitation wavelength: 320 nm).

As can be seen in Fig. 125, the chloroform solution of **5** exhibits the highest emission intensity with a maximum at ~455 nm. The emission band slightly loses intensity and the maximum is red-shifted to ~462 nm in dichloromethane, while for the solution of **5** in acetonitrile the emission intensity is significantly reduced and centred at around 482 nm. In methanol and the methanol/water mixture the emission is almost completely quenched, thus the centre of the bands cannot be accurately defined.

The luminescence studies of **5** were completed by the determination of the fluorescence quantum yield. For this measurement, a highly diluted solution of **5** in chloroform was prepared since this solvent showed the highest emission intensity of the investigated samples (Fig. 125). To yield an absorption value <0.05, a concentration in the order of 10^{-7} M was used. To be consistent with the solvent-dependent emission studies, the quantum yield was determined one day after preparation of the sample. However, also a freshly-prepared solution of **5** in chloroform was additionally investigated. As reference compound, quinine sulphate in 0.05 M H_2SO_4 (refractive index $\eta = 1.33$) was chosen whose quantum yield is defined as 0.52.[289,290] Using this analysis, a value for the fluorescence quantum yield of $\phi_{FL} < 0.01$ could be determined for both samples in chloroform.

Since the emission spectrum of **5** in chloroform shows the highest intensity (Fig. 125), it can be assumed that the value for the fluorescence quantum yield is below 1% for all investigated solvents. This extremely low value is in agreement with the impression of weakly-/non-emissive solutions by the naked eye (Fig. 124) and explains the rough shape of the emission spectra in Fig. 125.

3.8.3 Microscopic studies of 5

Besides the morphologies of aggregated bipyridine-based ligand **4** and its protonated form **4-H**$^+$, also the assemblies of the corresponding Pt(II) complex **5** have been examined by microscopic studies.

Due to the insolubility of **5** in pure water, samples in pure methanol and a mixture of methanol and water (20:80) were prepared. The UV/Vis absorption spectrum of **5** in aqueous solution (Fig. 122) suggested the aggregation of the complex in this medium, while the indication for its self-assembly in methanol was gained by time-dependent studies (Fig. 123). Consistent with this time-dependent absorption measurement, the sample in methanol (1.1 x 10^{-5} M) was investigated by AFM after an aging time of two days.

Upon spin-coating the solution of **5** in methanol onto mica, a thin film consisting of small nanoparticles can be observed by AFM (Fig. 126). The spherical self-assembled structures of **5** are of uniform size with a diameter of 4.2±0.3 nm. The bright structures in Fig. 126a-c represent agglomerates of several micelles that form a second layer.

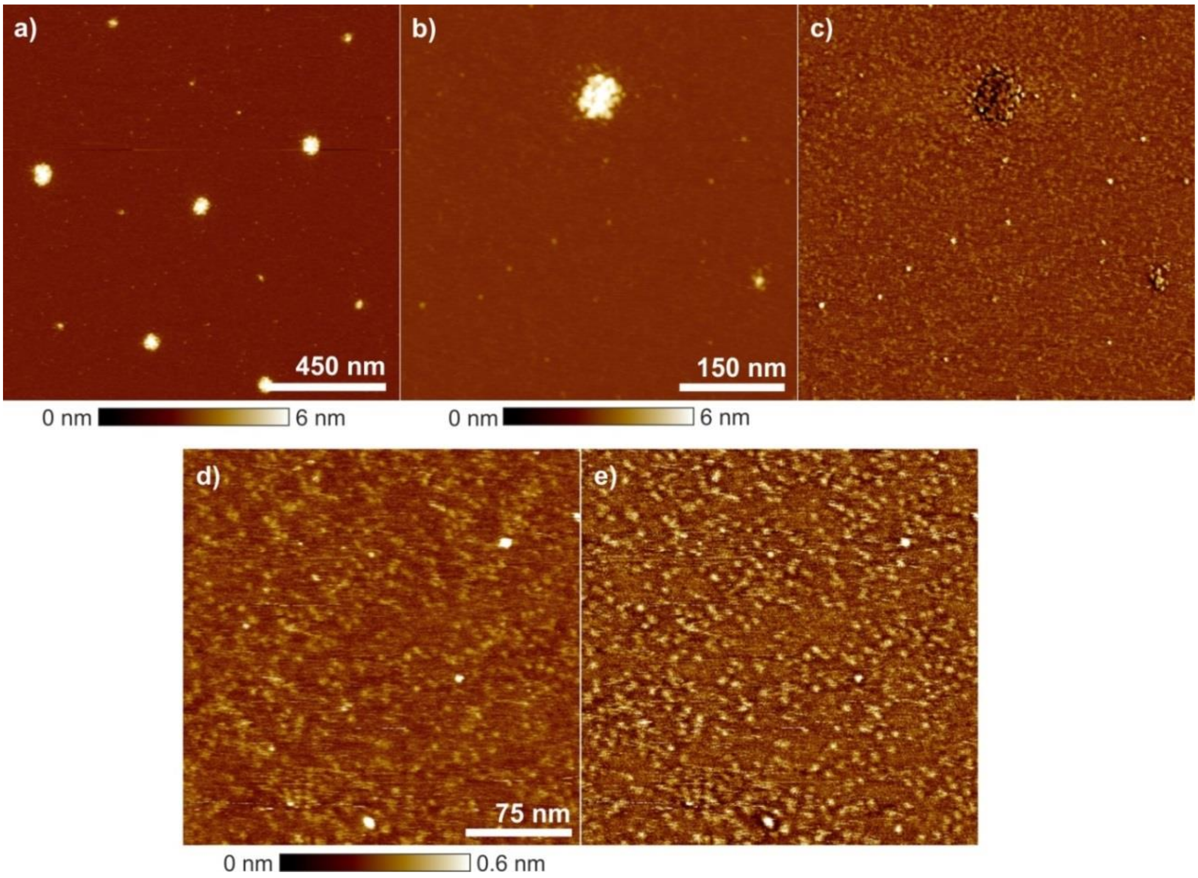

Fig. 126 AFM height (a, b, d) and phase (c, e) images of **5** in methanol (1.1 x 10^{-5} M) after an aging time of two days. The samples were prepared by spin-coating the solution with 4000 rpm onto mica.

To visualize the self-assembled structures of **5** in the methanol/water mixture (20:80), two samples with different aging-times were investigated. In analogy to the sample prepared for emission studies, the compound was dissolved in 20% of methanol before water was added.

First, similar to the methanol sample, the AFM studies of a two-days aged solution of **5** (1.1 x 10^{-5} M) are shown in Fig. 127. The images reveal spherical aggregates of uniform size, with an average diameter of 4.5±0.3 nm and a height of around 0.9±0.2 nm. These characteristics can be attributed to the formation of disc-like aggregates of micelles that flatten on the hydrophilic mica surface.

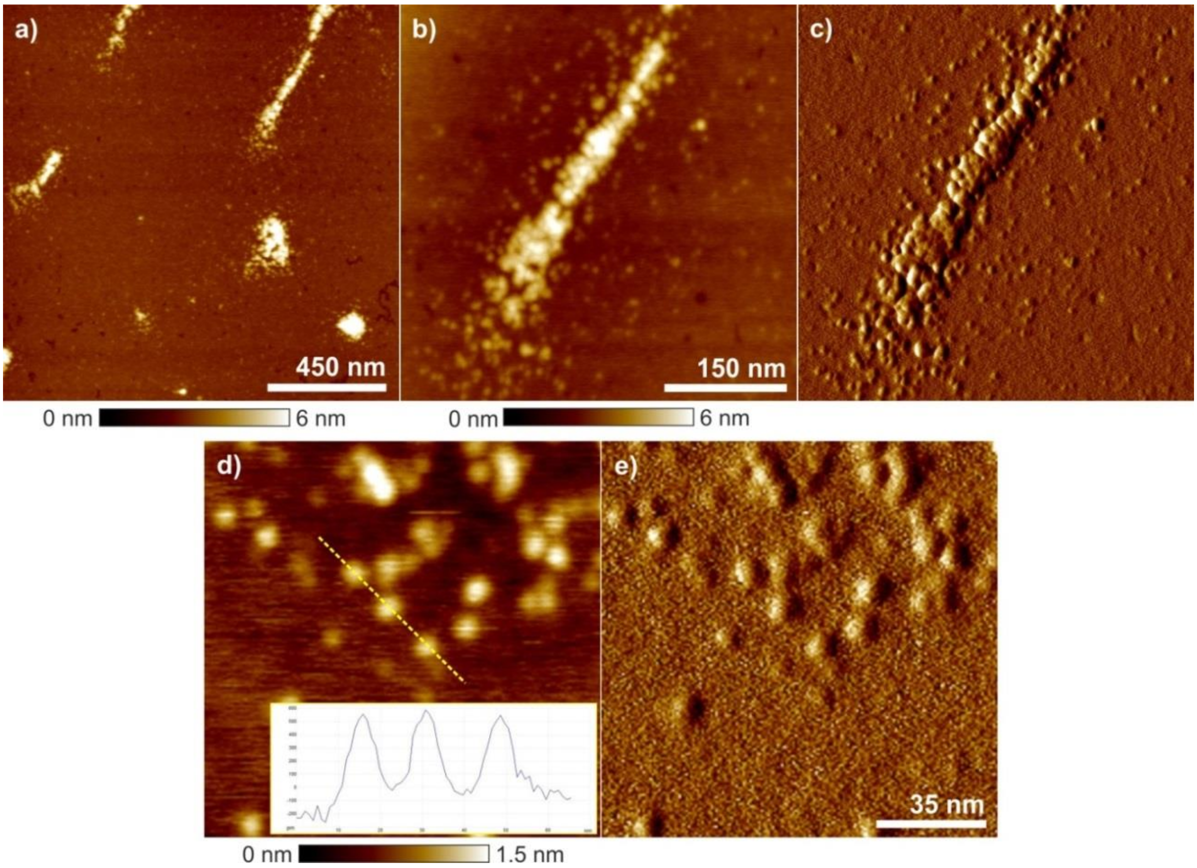

Fig. 127 AFM height (a, b, d) and phase (c, e) images of **5** in methanol/water = 20:80 (1.1×10^{-5} M) after an aging time of two days. The samples were prepared by spin-coating the solution with 4000 rpm onto mica. Inset in image (d) shows the cross section analysis along the yellow line.

To reveal potential changes in the self-assembled structure upon time, a second, six days-aged sample was investigated. Similarly to the previous measurement, the imaging of the further aged solution of **5** reveals spherical aggregates, as can be observed in Fig. 128. The nanoparticles exhibit a diameter of around 4.5±0.3 nm and a height of around 0.6±0.2 nm. These dimensions are clearly in agreement with the aggregates identified in Fig. 127. Thus, both aggregate solutions of **5** in methanol/water (20:80) after two and six days of aging provided small, spherical self-assembled structures. The similarity of the visualized aggregates clearly indicates that after the formation of the micelles no significant morphology changes occur in the investigated time scale.

To complement the results obtained by AFM imaging, the aggregate samples of **5** in methanol and methanol/water (20:80) were further used for SEM studies after an aging time of two weeks. Fig. 129 shows the SEM images of the pure methanol sample, while in Fig. 130 the self-assembled structures of **5** in methanol/water (20:80) are visualized.

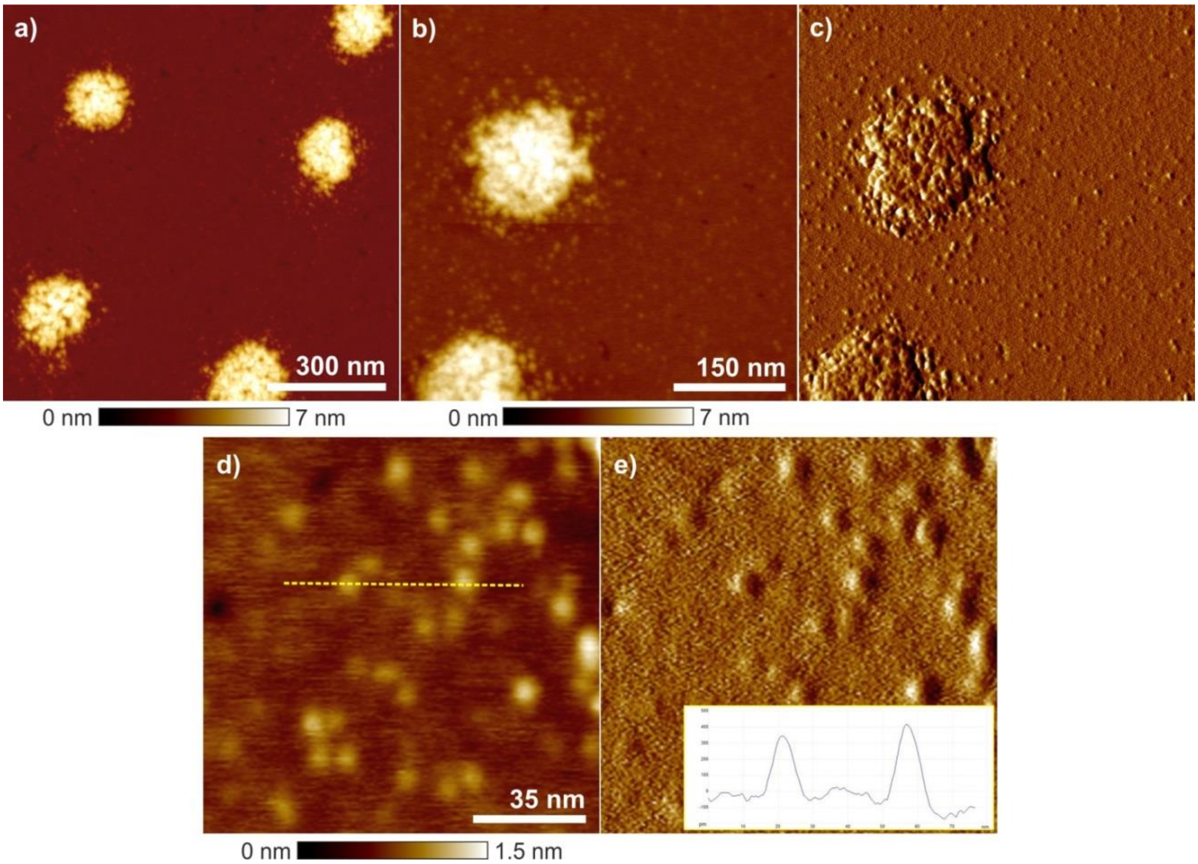

Fig. 128 AFM height (a, b, d) and phase (c, e) images of **5** in methanol/water = 20:80 (1.2 x 10^{-5} M) after an aging time of six days. The samples were prepared by spin-coating the solution with 4000 rpm onto mica. Inset in image (e) shows the cross section analysis along of the yellow line in (d).

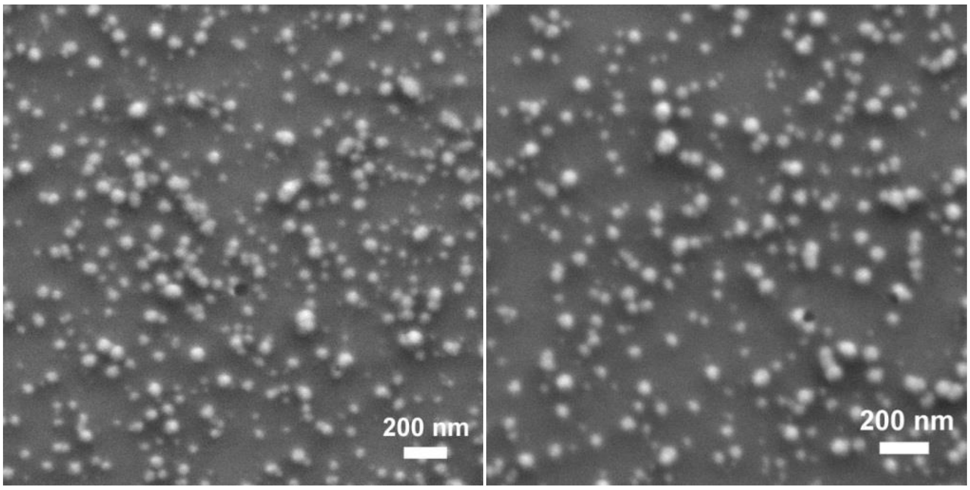

Fig. 129 SEM images of a two weeks-aged solution of **5** in methanol (1.1 x 10^{-5} M) onto silicon wafer.

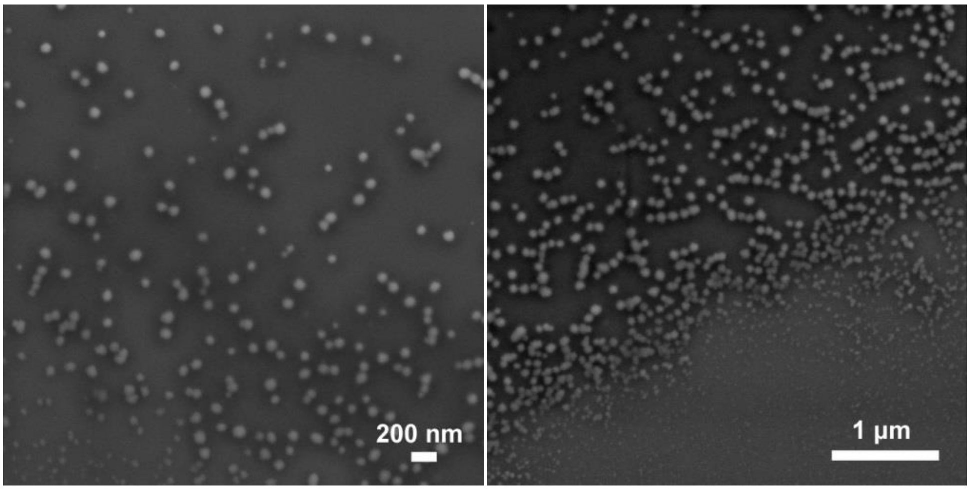

Fig. 130 SEM images of a two weeks-aged old solution of **5** in methanol/water = 20:80 (1.1×10^{-5} M) onto silicon wafer.

In agreement with the results obtained for complex **5** by AFM imaging, spherical micelles can be observed in both media. However, it becomes noticeable that their sizes are not uniform and also larger assemblies appear. This increase in size might be explained by an agglomeration process of individual nanoparticles of **5** (observed by AFM studies) into larger micellar structures.

Further information about the particles in solution should be gained by DLS measurements.[242,243] To this end, a solution of **5** in methanol/water (20:80) in the concentration range used for microscopic imaging was analysed (10^{-5} M). The sample was prepared in analogy to the previous solutions of **5** in methanol/water and investigated by DLS studies after one week. The yellow-coloured solution was filtered twice and measured at 298 K at different angles, as depicted in Fig. 131.

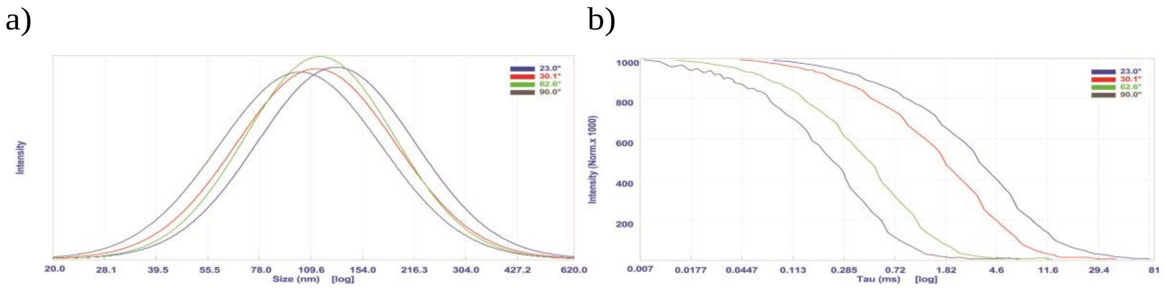

Fig. 131 Unimodal size distributions (a) from CONTIN analysis of the autocorrelation function (b) of a one-week aged solution of **5** (1.1×10^{-5} M, filtered) in methanol/water (20:80) at 298 K.

The graph for the unimodal distribution in Fig. 131a reveals for all measurements a maximum located in the range of 100 - 130 nm, indicating that this value is independent from the investigated angle. These results are clearly indicative of spherical particles of **5** in solution and in total agreement with the shape of the assemblies visualized by different microscopic techniques (Fig. 126 - Fig. 130). However, the particles detected by DLS are larger than the dimension of the individual aggregates (4 - 5 nm) visualized by AFM imaging on the mica surface. This higher value obtained by DLS studies might be attributed to an agglomeration process of the individual particles of **5** in aqueous solution, as similarly suggested by the presence of also larger particles in SEM imaging.

To suggest an appropriate model for the aggregation of **5**, the size of the molecule has to be considered. Since the Pt(II) complex **5** exists in its *cis*-conformation, its molecular structure and length is comparable to the *cis*-locked **4-H**$^+$ species, shown in the geometry optimized structure in Fig. 117. Including the Pt(II) centre, a dimension of the molecule of around 2.5 nm can be estimated. Comparison of the diameter of 4 - 5 nm for the individual micelles observed by AFM imaging with the dimension of one molecule of ~2.5 nm indicates that the assemblies possess twice the molecular length. Thus, an aggregation of the “V-shaped” Pt(II) complex **5** with a strong curvature can be proposed that results in small micellar assemblies. In this way, the aromatic part and the metal centre of the complex can be incorporated in the hydrophobic interior and thus shielded from the surrounding aqueous environment. This shielding is provided by the flexible glycol chains that create a hydrophilic shell and thus protect the aromatic core from non-favourable interactions with water molecules. A comparable aggregation pattern was observed by Würthner and co-workers in 2007 for a wedge-shaped PBI amphiphile in aqueous medium.[304] Similarly to the suggested aggregation model for **5**, they presented for the PBI derivative the formation of micelles with a high degree of curvature that exhibit a hydrophilic exterior and a hydrophobic interior.

The proposed aggregation pattern of **5** can furthermore explain the presence of larger particles in solution, as indicated by DLS studies and SEM imaging. These assemblies might result from an agglomeration of the individual micelles to reach an even stronger shielding of the hydrophobic core from the surrounding aqueous medium.

Chapter 4

-

Summary

The aim of the presented work was the synthesis and investigation of pyridine- and bipyridine-based OPE amphiphiles, decorated with terminal glycol chains to allow their analysis in polar solvents or water. The metal-ligating property of these molecules should be exploited to coordinate to Pd(II) and Pt(II) metal ions, respectively, resulting in the creation of novel *metallosupramolecular π-amphiphiles* of square-planar geometry. The (bi)pyridine-based OPE ligands and their corresponding metal complexes should be characterized in detail with focus on their self-assembly behaviour in polar and aqueous environment. In this way, the underlying aggregation mechanism (isodesmic or cooperative) should be revealed and the responsible forces and contributions elucidated.

In *Chapter 2* a detailed literature survey emphasizing the potential of cooperative phenomena in the field of supramolecular chemistry is given. To introduce the readers into the basics of self-assembly, different mechanisms of supramolecular aggregation are initially presented. The temperature-dependent isodesmic model, as well as the most frequently used cooperative models are explained. In this regard, a more detailed insight into those models is given that are in the following section (*Chapter 3*) used to describe the self-assembly of synthesized target molecules. Subsequently, an overall overview of numerous, cooperatively aggregating systems in literature is presented. The reported examples are classified by the attractive interactions and further contributions that control their self-assembly.

In *Chapter 3* the own results that were achieved during the laboratory work are presented and discussed. The creation of amphiphilic ligands substituted with a metal-coordinating unit (either pyridine (**1**) or bipyridine (**4**)), as well as of their corresponding metal complexes (**2**, **3** and **5**) could be realized. The first part of the Chapter (*Part A*) is devoted to the project dealing with the pyridine-based target compounds **1-3**. Coordination of the terminal pyridine unit of ligand **1** to a Pt(II) and Pd(II) metal centre, respectively, results in new square-planar complexes **2** and **3** in *trans*-conformation. The free ligand **1** shows an isodesmic (non-cooperative) self-assembly in water into relatively small one-dimensional structures, as can be visualized by TEM imaging. The dimension of the aggregates leads to the suggested model of linear π-stacking with a slight mutual rotation between the molecular units. In this way, the flexible glycol chains can create a hydrophilic shell protecting the aromatic scaffold from the aqueous environment. In contrast to amphiphile **1**, temperature-dependent analyses reveal that the aggregation of the related Pt(II)/Pd(II) complexes (**2** and **3**) in polar media follows a cooperative pathway. This cooperative self-assembly results in the formation of gels in different alcohols and water that consist of a three-dimensional network of fibres. For both compounds (**2** and **3**) single crystals could be obtained, whose crystal structure analysis reveals an organisation in the solid state that is comparable to the aggregation pattern of **2**/**3** in solution. The molecules adopt a slipped arrangement that is mainly stabilized by pronounced hydrogen bonding interactions between the triethylene glycol chains of adjacent subunits, in parts involving aromatic hydrogen atoms. The close contact between the terminal hydrophilic chains of neighbouring molecules results in an unprecedented, fascinating packing motif that can be termed as “molecular hand-shake”. Interestingly, close contacts between the glycol chains can also be established in solution, as ^{1}H NMR ROESY studies of samples of **2** and **3** in polar medium indicate.

In brief, this section reveals different aggregation mechanisms of target molecule **1** compared to the corresponding complexes **2** and **3**. While ligand **1** self-assembles non-cooperatively in water, for **2** and **3** in polar media a cooperative pathway occurs. Furthermore, the similarity of the characteristics of Pt(II) complex **2** and the related Pd(II) complex **3** clearly demonstrates that the nature of the metal centre only has a negligible influence within the presented system.

In the second part (*Part B*) of *Chapter 3*, the studies on the bipyridine-based ligand **4**, its protonated species **4-H**$^+$ and the corresponding Pt(II) complex **5** are presented. The investigations reveal that the self-assembly of the bipyridine derivative **4** in aqueous solution also represents a cooperative process. The temperature-dependent spectral changes upon cooling of an aqueous solution can be described by the cooperative model by van der Schoot. This behaviour can be attributed to required conformational changes (monomeric activation step) that have to be considered as additional effect in course of the aromatic aggregation of the units in *trans*-conformation. This self-assembly results in the formation of extended nanofibers of single-molecular diameter. Accordingly, a model of one-dimensional stacking is proposed with molecular subunits that adopt a mutual rotational displacement. These structures in aqueous solution exhibit a remarkable stability, even under strongly acidic conditions, most likely due to the protection of the bipyridine centres in the inner hydrophobic core. This shielding of the ligating moiety is supported by the indicated clustering of the fibers. However, the ligating properties of **4** can be exploited by the addition of acid in organic medium that comes along with a conformational change in the bipyridine centre from the free *trans*- to the mono-protonated *cis*-species **4-H**$^+$. This protonation process can be followed by UV/Vis absorption and ^{1}H NMR titration experiments in acetonitrile. Upon self-assembly of the H$^+$-adduct in aqueous solution relatively short stick-like structures are created. The proposed *zig-zag* arrangement of the molecules can minimize repulsive interactions and matches perfectly the diameter of the assemblies defined by microscopic techniques. Moreover, coordination of **4** to a Pt(II) metal centre leads to the target complex **5** with *cis*-geometry. Interestingly, the corresponding aggregates in polar solution are of spherical shape and thus exhibit an even different morphology to *trans*-**4** and *cis*-locked **4-H**$^+$. The size of the individual nanoparticles can be defined by AFM imaging and matches twice the dimension of a molecular unit. Consequently, it seems reasonable to propose the formation of micellar structures with a hydrophobic interior surrounded by a hydrophilic shell of glycol chains.

Altogether, this project in *Part B* of the thesis impressively shows how slight variations in an appropriate system can generate a variety of supramolecular assemblies, all based on a single amphiphilic ligand. Different morphologies can be created, from extended fibres for individual target molecule **4**, to thinner and shorter sticks for its protonated species **4-H**$^+$ or even spherical structures for the corresponding Pt(II) complex **5**.

In conclusion, the present thesis points out the influence of various factors on the self-assembly process in supramolecular systems. In this regard, the effect of the molecular design of the ligand, the coordination to a metal centre as well as the surrounding medium and temperature is investigated. With these detailed analyses, the work thus provides an interesting contribution to the field of supramolecular chemistry. As the investigated examples show, the non-covalent character of the stabilizing forces, allows the adaptation of the self-assembled structures towards different external stimuli, as changes in the temperature or the pH value. However, the bipyridine-based system also highlights how stable supramolecular assemblies can be. Looking ahead, the presented projects provide new perspectives in the field of *metallosupramolecular π-amphiphiles*, in particular with regard to *supramolecular architectures* in polar and aqueous environment.

Chapter 5

-

Zusammenfassung

Das Ziel der vorliegenden Arbeit war die Synthese und Untersuchung von pyridin- sowie bipyridin-basierten OPE-Amphiphilen, deren endständige Glykolketten eine Analyse in polaren Lösungsmitteln und Wasser ermöglichen sollen. Die komplexierenden Eigenschaften der Moleküle sollte ausgenutzt werden um diese an Pd(II) bzw. Pt(II) Metallionen zu koordinieren, wobei neuartige *metallosupramolekulare π-Amphiphile* von quadratisch-planarer Geometrie entstehen. Die (bi)pyridin-basierten OPE-Liganden und ihre Metallkomplexe sollten im Detail charakterisiert werden, wobei das Hauptaugenmerk auf ihrer Selbstorganisation in polarer und wässriger Umgebung liegt. Dabei sollte der zu Grunde liegende Aggregationsmechanismus (isodesmisch oder kooperativ) bestimmt und die verantwortlichen Kräfte und Beiträge erläutert werden.

Kapitel 2 gibt einen detaillierten Literaturüberblick, der das Potential von kooperativen Phänomenen im Bereich der supramolekularen Chemie hervorhebt. Um den Leser in die Grundlagen der Selbstorganisation einzuführen, werden anfänglich verschiedene Mechanismen der supramolekularen Aggregation vorgestellt. Das temperaturabhängige isodesmische Modell, sowie die am häufigsten verwendeten kooperativen Modelle werden erläutert. In diesem Zusammenhang wird ein tieferer Einblick in diejenigen Modelle gegeben, die im nachfolgenden Kapitel (*Kapitel 3*) angewendet werden um die Selbstorganisation der synthetisierten Zielmoleküle zu beschreiben. Anschließend, wird ein ausführlicher Überblick über zahlreiche, literaturbekannte Systeme gegeben, die auf kooperative Art und Weise aggregieren. Die präsentierten Beispiele sind nach den attraktiven Wechselwirkungen und weiteren Beiträge untergliedert, die ihre Selbstorganisation steuern.

In *Kapitel 3* werden die eigenen erzielten Ergebnisse präsentiert und diskutiert. Die Synthese der amphiphilen Liganden mit einer metall-koordinierenden Einheit (Pyridin (**1**) oder Bipyridin (**4**)) sowie der zugehörigen Metallkomplexe (**2**, **3** und **5**) konnte erfolgreich durchgeführt werden. Der erste Teil des Kapitels (*Teil A*) beschäftigt sich mit dem Projekt der pyridin-basierten Zielverbindungen **1**-**3**. Die Koordination der endständigen Pyridin-Einheit von Ligand **1** an ein Pt(II)- bzw. Pd(II)-Metallzentrum bringt die neuen, quadratisch-planaren Komplexe **2** und **3** in *trans*-Konformation hervor. Der freie Ligand **1** zeigt eine isodesmische (nicht-kooperative) Selbstorganisation in Wasser zu recht kleinen, eindimensionalen Strukturen, wie in TEM-Aufnahmen zu beobachten ist. Die Größe der Aggregate lässt eine lineare π-Stapelung vermuten, wobei die molekularen Einheiten leicht gegeneinander verdreht angeordnet sind. Auf diese Weise können die flexiblen Glykolketten eine hydrophile Schale bilden, die das aromatische Grundgerüst vor der wässrigen Umgebung abschirmt. Im Gegensatz zu Amphiphil **1**, zeigen temperaturabhängige Studien der zugehörigen Pt(II)-/Pd(II)-Komplexe (**2** und **3**), dass diese in polaren Medien auf kooperative Art und Weise aggregieren. Diese kooperative Aggregation führt zur Bildung von Gelen in verschiedenen Alkoholen und Wasser, die aus einem dreidimensionalen Netzwerk aus Fasern bestehen. Für beide Verbindungen (**2** und **3**) konnten Einkristalle erhalten werden, deren Kristallstrukturanalyse eine Organisation im Festkörper erkennen lässt, die vergleichbar mit dem Aggregationsmuster von **2**/**3** in Lösung ist. Die Moleküle zeigen eine versetzte Anordnung, die hauptsächlich durch ausgeprägte Wasserstoffbrückenbindungen zwischen den Triethylenglykolketten von benachbarten Einheiten (und teilweise zu den aromatischen Wasserstoffatomen) stabilisiert wird. Der enge Kontakt zwischen den endständigen, hydrophilen Ketten benachbarter Moleküle führt zu einem neuartigen, faszinierenden Packungsmuster welches als „molekularer Handschlag“ bezeichnet werden kann. Interessanterweise ist auch in Lösung ein enger Kontakt zwischen den Glykolketten möglich, wie ^{1}H NMR ROESY-Messungen von Proben von **2** bzw. **3** in polarem Medium erkennen lassen.

Kurz gesagt zeigt dieses Kapitel einen unterschiedlichen Aggregationsmechanismus für Ligand **1** im Vergleich zu den zugehörigen Komplexen **2** und **3** auf. Während **1** in

Wasser auf nicht-kooperative Art und Weise aggregiert, findet für **2** bzw. **3** ein kooperativer Prozess in polaren Medien statt. Des Weiteren lässt sich aus der Ähnlichkeit der Eigenschaften von Pt(II)-Komplex **2** und des strukturgleichen Pd(II)-Komplexes **3** schließen, dass in dem vorliegenden System die Natur des Metallzentrums einen nur unwesentlichen Einfluss hat.

Im zweiten Teil (*Teil B*) von *Kapitel 3* werden die Untersuchungen des bipyridin-basierten Liganden **4**, seiner protonierten Form **4-H**$^+$ und des zugehörigen Pt(II)-Komplexes **5** vorgestellt. Hierbei zeigt sich, dass es sich bei der Selbstorganisation des Bipyridin-Derivats **4** in wässriger Lösung ebenfalls um einen kooperativen Prozess handelt. Die temperaturabhängigen spektralen Veränderungen beim Abkühlen einer wässrigen Lösung können durch das kooperative Modell von van der Schoot beschrieben werden. Dieses Verhalten kann auf notwendige Konformationsänderungen (monomere Aktivierung) zurückgeführt werden, die als zusätzlicher Effekt im Rahmen der aromatischen Aggregation der *trans*-Spezies berücksichtigt werden müssen. Diese Selbstorganisation führt zur Bildung von ausgedehnten Nanofasern, deren Durchmesser der Länge eines Moleküls entspricht. Demnach wird ein Modell für eine eindimensionale Stapelung vorgeschlagen, in dem die molekularen Einheiten gegeneinander verdreht vorliegen. Diese Strukturen in wässriger Lösung besitzen (auch unter stark sauren Bedingungen) eine bemerkenswerte Stabilität, was höchstwahrscheinlich daran liegt, dass die Bipyridinzentren geschützt im hydrophoben Inneren vorliegen. Diese Abschirmung der komplexierenden Einheit wird durch das angedeutete Clustering der Fasern unterstützt. Die Fähigkeit von **4** als Ligand zu fungieren kann jedoch bei der Zugabe von Säure in organischem Medium ausgenutzt werden, wobei eine Konformationsänderung des Bipyridin-Zentrums von der freien *trans*- zur einfach-protonierten *cis*-Form **4-H**$^+$ stattfindet. Dieser Prozess der Protonierung kann durch UV/Vis Absorptions- sowie ^{1}H NMR-Titrationsexperimente in Acetonitril verfolgt werden. Durch Selbstorganisation des H$^+$-Addukts in wässriger Lösung entstehen relativ kurze, stäbchenförmige Strukturen. Die vorgeschlagene *Zickzack*-Anordnung der Moleküle ermöglicht es die abstoßenden Wechselwirkungen zu minimieren und ist im Einklang mit dem Durchmesser der Aggregate, der durch bildgebende Verfahren bestimmt wurde. Des Weiteren bringt die Koordinierung von **4** an ein Pt(II)-Metallzentrum Komplex **5** mit *cis*-Geometrie hervor. Interessanterweise sind die

zugehörigen Aggregate in polarer Lösung kugelförmig und besitzen somit eine nochmals andere Gestalt als *trans*-**4** und *cis*-**4-H**$^+$. Die Größe der individuellen Nanopartikel kann durch AFM-Aufnahmen bestimmt werden und entspricht der zweifachen Länge eines Moleküls. Folglich liegt die Bildung von Mizellen nahe, die ein hydrophobes Inneres und eine hydrophile Schale aus Glykolketten besitzen.
Alles in Allem zeigt dieses Projekt in *Teil B* der Arbeit auf eindrucksvolle Weise, wie leichte Veränderungen in einem geeigneten System verschiedenartige supramolekulare Strukturen hervorbringen können, die alle auf einem einzigen amphiphilen Liganden basieren. Verschiedene Morphologien können gebildet werden, von ausgedehnten Fasern für das Zielmolekül **4**, bis hin zu dünneren und kürzeren Stäbchen für die protonierte Form **4-H**$^+$ und sogar kugelförmigen Strukturen für den zugehörigen Pt(II)-Komplex **5**.

Zusammenfassend ist zu sagen, dass die vorliegende Arbeit den Einfluss verschiedener Faktoren auf den Selbstorgansisationsprozess in supramolekularen Systemen aufzeigt. Hierbei wird der Effekt des Moleküldesigns des Liganden, der Koordination an ein Metallzentrum sowie des umgebenden Mediums und der Temperatur betrachtet. Durch diese detaillierten Studien kann die Arbeit somit einen interessanten Beitrag auf dem Gebiet der supramolekularen Chemie leisten. Wie die untersuchten Beispiele zeigen, ermöglicht der nicht-kovalente Charakter der stabilisierenden Kräfte die Anpassung der selbstorganisierten Strukturen an verschiedene äußere Reize, wie Änderungen der Temperatur oder des pH-Wertes. Jedoch verdeutlicht das bipyridin-basierte System aber auch, wie stabil supramolekulare Aggregate sein können. Als Ausblick ist zu sagen, dass die vorgestellten Projekte neue Perspektiven im Bereich der *metallosupramolekularen π-Amphiphile* eröffnen, vor allem im Hinblick auf supramolekulare Formen in polarer und wässriger Umgebung.

Chapter 6

-

Experimental work

6.1 Materials and methods

Atomic Force Microscopy (AFM)

AFM studies were performed on a *Bruker AXS MultiModeTM Nanoscope IV* system using an E-scanner with a maximum scan area of 15 x 15 µm. Silicon cantilevers with a nominal spring constant of 41.0 Nm^{-1} and with resonant frequency of 300 kHz, and a typical tip radius of 7 nm (OMCL-AC160TS, Olympus) were employed. The samples were prepared by spin-coating or drop-casting onto HOPG (highly ordered pyrolytic graphite) and Mica, respectively, as mentioned for the respective studies.

Column chromatography

Purification by column chromatography was performed using glass columns and silica gel supplied by Merck and Macherey Nagel (particle size 35 - 70 µm).

For thin-layer chromatography (TLC) silica gel plates from Merck (Merck, 60 F_{254}) were used.

Dynamic Light Scattering (DLS)

Dynamic light scattering experiments were recorded on a *Beckman Coulter, N5 Submicron Particle Size Analyzer* with a 25 mW Helium-Neon laser (632.8 nm) as light source. Size distribution profile deconvolution algorithm is based on CONTIN program.[243] A conventional quartz cuvette (Helma) for fluorescence was used with a path length of 10 mm. For the sample preparation, Millipore water and commercially available solvents of spectroscopic grade were used as received.

Elemental Analysis

Elemental Analysis was provided from the Institute of Inorganic Chemistry, University of Würzburg. For the measurements a *vario MICRO cube instrument* from *Elementar* was used.

Fluorescence Spectroscopy

Steady state emission spectra were recorded on a *PTI QM4/2003 spectrofluorometer* and corrected against photomultiplier and lamp intensity. The measurements were performed using polarizers, with a polarization angle of 0° for the excitation beam and 54.7° for the emission. The fluorescence quantum yields (ϕ_{fl}) were calculated at four different excitation wavelengths using the optical dilution method (OD <0.05), the average value for ϕ_{fl} is given. As reference compound quinine sulphate in 0.05 M H_2SO_4 was used with $\phi_{fl} = 0.52$.[289,290] Conventional quartz cuvettes (Helma) for fluorescence were used with a path length of 10 mm. For the sample preparation, Millipore water and commercially available solvents of spectroscopic grade were used as received.

Mass Spectrometry

High-resolution electro spray ionization mass spectrometry (ESI-TOF) was performed with a *Bruker Daltonics micrOTOF focus instrument*. Matrix-assisted laser desorption/ionization (MALDI) spectra were recorded using an *autoflex II instrument* from *Bruker Daltonics*. As matrix DCTB (*trans*-2-[3-(4-tert-butylphenyl)-2-methyl-2-propenylidene]malononitrile) was applied.

NMR Spectroscopy

NMR spectra were recorded on a *Bruker Avance 400 MHz* (^{1}H: 400 MHz; ^{13}C: 100.6 MHz) or *Bruker DMX 600 MHz* spectrometer and calibrated to the solvent residual peaks (acetonitrile 1.94 ppm, dichloromethane 5.31 ppm, methanol 3.31 ppm). Coupling constants (J) are denoted in Hz and chemical shifts (δ) in ppm.

Multiplicities are denoted as follows: s = singlet, d = doublet, dd = doublet of doublets, t = triplet, m = multiplet.

Sample preparation for Microscopy (AFM, SEM, and TEM)

Concerning the samples of **1**, **3**, **4** and **4-H**$^+$ in aqueous medium: The samples were obtained by preparing a highly concentrated solution of the compound in THF (~15% of the end volume) and subsequent overlay of the organic solution with pure water (Millipore). The vials were closed with a perforated cap and kept under ambient conditions to enable the evaporation of the organic solvent. The aging time is referred to the date of sample preparation. Following this procedure for **3** the investigated hydrogel could be obtained after an aging time of ~2.5 month.

Scanning Electron Microscopy

SEM studies were performed on a *Ultra plus field emission scanning electron microscope (FESEM)* equipped with a GEMINI® e-Beam column (Carl Zeiss NTS GmbH) operating at an accelerating voltage of 1.5 - 3 kV. The sample was prepared by drop-casting onto silicon wafer or cover slip, as mentioned.

Transmission Electron Microscopy

All TEM samples were prepared by drop-casting on a carbon-coated copper grid (300 mesh), followed by negative staining with 0.5% aqueous solution of uranyl acetate. TEM studies were performed on a *Siemens Elmiskop 101 Electron Microscope,* with an accelerating voltage of 80 kV.

UV/Vis Spectroscopy

UV/Vis absorption spectra were recorded on a *Perkin Elmer Lambda 35*, *Perkin Elmer Lambda 40*, *Perkin Elmer Lambda 950* and *Jasco V-670* spectrophotometer with a scan rate of ~200 nmmin^{-1}. Unless otherwise specified, the measurements were recorded at room temperature or 298 K. Temperature control was provided by a *Perkin Elmer PTP-1+1 Peltier System* for the Perkin Elmer instruments. For the Jasco device, a *Julabo Temperature Programmer F 250* was used. Conventional quartz cuvettes (Helma) were used with a path length of 0.1, 1 and 10 mm. For the sample preparation, commercially available solvents of spectroscopic grade were used as received.

X-Ray Diffraction Analysis

Single crystal X-ray diffraction data were collected at 100 K on a *Bruker D8 Quest* diffractometer with a Bruker photon area detector (for Pt(II) complex **2**) or a *Bruker X8Apex-II* diffractometer with a CCD area detector (for Pd(II) complex **3**) utilizing multi-layer mirror monochromated $Mo_{K\alpha}$ radiation (α = 0.71073 Å). The structures were solved using direct methods, expanded with Fourier techniques and refined with Olex 2[305] (for **2**) or the Shelx[306] (for **3**) software package. All non-hydrogen atoms were refined anisotropically. Hydrogen atoms were included in the structure factor calculation on geometrically idealized positions.

Crystallographic data have been deposited at the Cambridge Crystallographic Data Centre, deposition number CCDC 955619 (**2**) and CCDC 1018057 (**3**). These data can be obtained free of charge from The CCD centre via www.ccdc.cam.ac.uk/data_request/cif.

Chemicals

The solvents and reagents were ordered from commercial suppliers (abcr, Acros, Alfa Aesar, Fluka, Grüssing, Sigma Aldrich, TCI, VWR) and used as received, unless otherwise stated. For analytical studies, organic solvents of spectroscopic grade were used as received. Water was used as ultrapure water, purified by a *Milli-Q water system* from Merck Millipore.

6.2 Synthesis and characterization of the target molecules

Synthesis of ligand 1[*]:

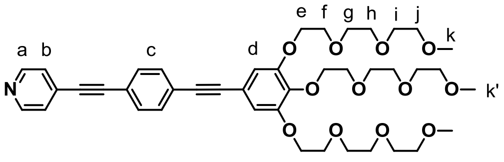

Chemical Formula: $C_{42}H_{55}NO_{12}$
Molecular Weight: 765.88560

1

5-((4-ethynylphenyl)ethynyl)-1,2,3-tris(2-(2-(2-methoxyethoxy)ethoxy)ethoxy)-benzene (**119**) (917 mg, 1.33 mmol), 4-iodopyridine (**120**) (274 mg, 1.34 mmol), tetrakis(triphenylphosphine)palladium(0) (92 mg, 0.08 mmol) and copper(I)iodide (12 mg, 0.06 mmol) were dissolved in triethylamine (20 ml). The mixture was subjected to five vacuum/argon cycles and additionally flushed with argon for 20 min. Afterwards, the reaction mixture was stirred at 80 °C for five hours. After evaporation of the solvent under reduced pressure the residue was purified by column chromatography (silica gel, (1) CH_2Cl_2/MeOH = 95:5 and (2) diethyl ether/MeOH = 90:10) affording **1** as a yellow oil (860 mg, 1.12 mmol, yield: 84 %).

As already reported previously, the yellow oil turns dark brown upon time due to partial decomposition of the ligand **1** into unidentified products.[234] However, a simple (re)purification step by flash column chromatography (silica gel) using CH_2Cl_2/MeOH (95:5) provided good fractions of **1** for its investigation and subsequent complexation reactions.

^{1}H NMR (400 MHZ, CD_2Cl_2, 298 K):

δ (in ppm) = 8.59 - 8.58 (m, 2H, H_a), 7.56 - 7.51 (m, 4H, H_c), 7.39 - 7.38 (m, 2H, H_b), 6.80 (s, 2H, H_d), 4.17 - 4.14 (m, 6H, H_e), 3.85 - 3.48 (m, 30H, $H_{f\text{-}j}$), 3.33 (s, 3H, $H_{k'}$), 3.32 (s, 6H, H_k).

---

[*] Synthesis towards ligand **1** was initially elaborated and described in the bachelor thesis of A. Martin[234] under the supervision of C. Rest, Prof. Dr. G. Fernández and Prof. Dr. F. Würthner, Julius-Maximilians-Universität Würzburg, 2012.

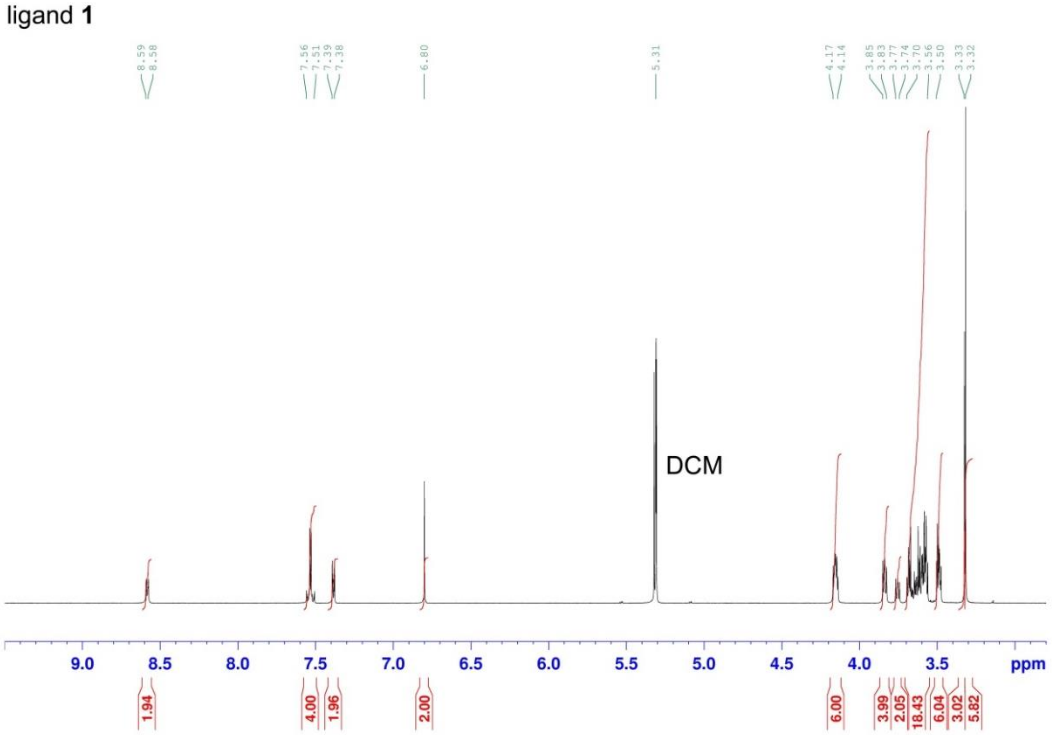

Fig. 132 ^{1}H NMR (400 MHz, CD_2Cl_2, 300 K) of ligand **1**.

^{13}C NMR (100.6 MHz, CD_2Cl_2, 300 K):

δ (in ppm) = 153.0, 150.3, 140.0, 132.3, 131.9, 131.4, 125.8, 124.6, 122.2, 117.9, 111.4, 93.6, 92.3, 88.7, 88.2, 72.9, 72.4, 71.2, 71.0, 70.9, 70.8, 70.0, 69.3, 59.0.

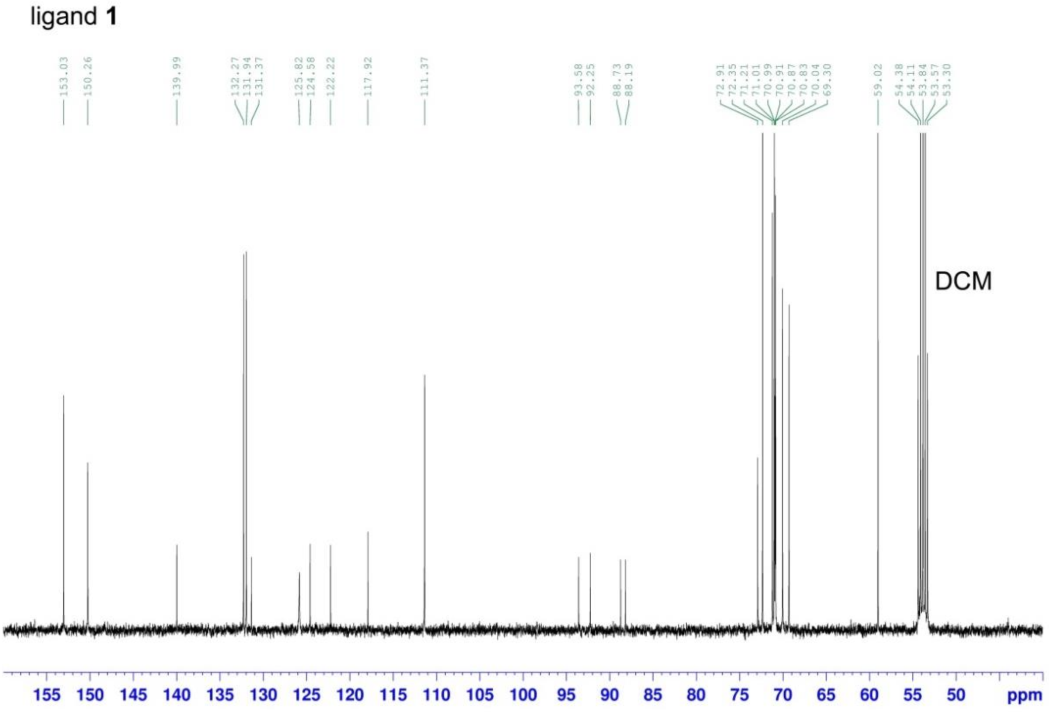

Fig. 133 ^{13}C NMR (100.6 MHz, CD_2Cl_2, 300 K) of ligand **1**.

MS (MALDI-TOF-MS):

m/*z*: calculated for $[C_{42}H_{55}NO_{12}Na]^+$ $[M+Na]^+$: 788.362; found: 788.421.

HRMS (ESI, pos. Mode), (acetonitrile/chloroform 1:1):

m/*z*: calculated for $[C_{42}H_{56}NO_{12}]^+$ $[M+H]^+$: 766.3797; found: 766.3800.

Synthesis of Pt(II) complex 2:

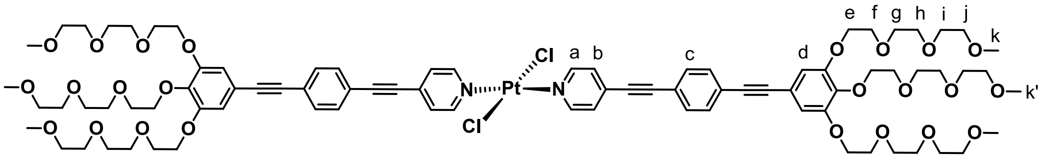

Chemical Formula: $C_{84}H_{110}Cl_2N_2O_{24}Pt$
Molecular Weight: 1797.76120

2

In advance benzene was subjected to five vacuum/argon cycles and additionally flushed with argon for 20 min. The reactant 4-((4-((3,4,5-tris(2-(2-(2-methoxyethoxy)ethoxy)ethoxy)phenyl)ethynyl)phenyl)ethynyl)pyridine (**1**) was freshly purified by a flash chromatography column (silica gel) using CH_2Cl_2/MeOH = 95:5 as eluent.

Ligand **1** (495 mg, 0.65 mmol) and dichlorobis(benzonitrile)platinum(II) (154 mg, 0.33 mmol) were dissolved in dried benzene (60 ml) and subjected to five vacuum/argon cycles. Afterwards the mixture was stirred at 87 °C under argon for six days. After evaporation of the solvent under reduced pressure the residue was purified by column chromatography (silica gel, CH_2Cl_2/MeOH = 95.5:4.5) affording **2** as a yellow solid (402 mg, 0.22 mmol, yield: 69 %).

^{1}H NMR (400 MHz, CD_2Cl_2, 300 K):

δ (in ppm) = 8.87 - 8.85 (m, 4H, H_a), 7.59 - 7.53 (m, 8H, H_c), 7.41 - 7.39 (m, 4H, H_b), 6.81 (s, 4H, H_d), 4.17 - 4.15 (m, 12H, H_e), 3.85 - 3.48 (m, 60H, $H_{f\text{-}j}$), 3.33 (s, 6H, $H_{k'}$), 3.32 (s, 12H, H_k).

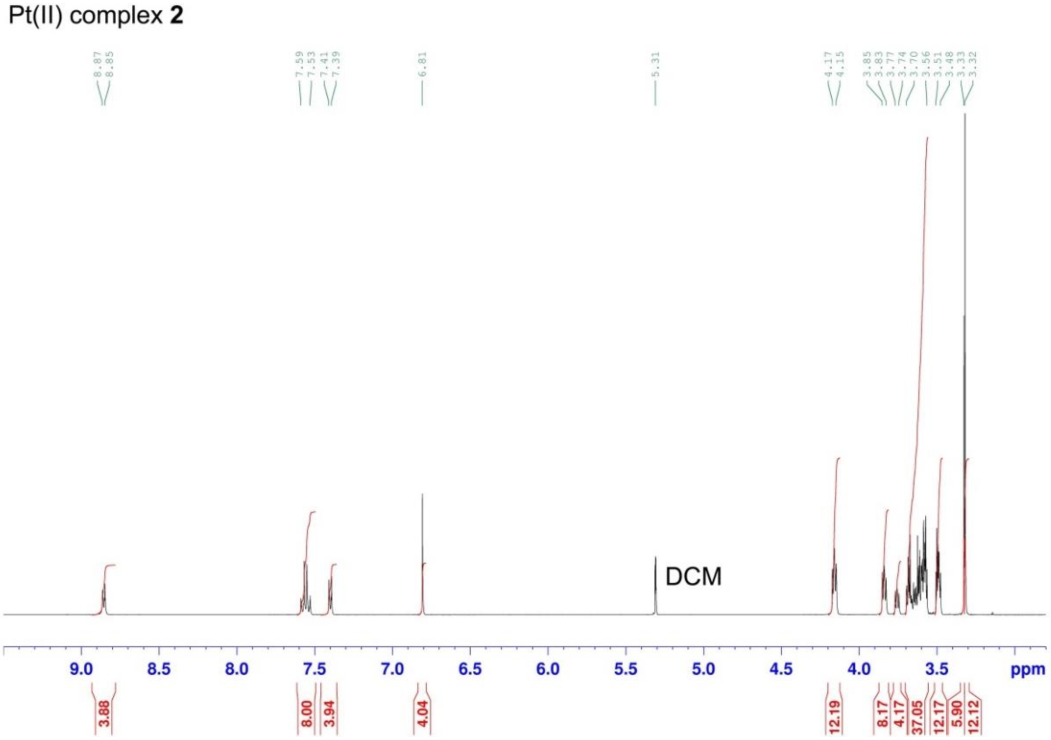

Fig. 134 ^{1}H NMR (400 MHz, CD_2Cl_2, 300 K) of Pt(II) complex **2**.

^{13}C NMR (150.9 MHz, CD_2Cl_2, 300 K):

δ (in ppm) = 153.5, 152.9, 139.8, 134.3, 132.5, 132.0, 127.3, 125.3, 121.3, 117.8, 111.1, 97.9, 92.7, 88.1, 87.4, 72.8, 72.3, 71.1, 70.9, 70.8, 69.9, 69.1, 59.0.

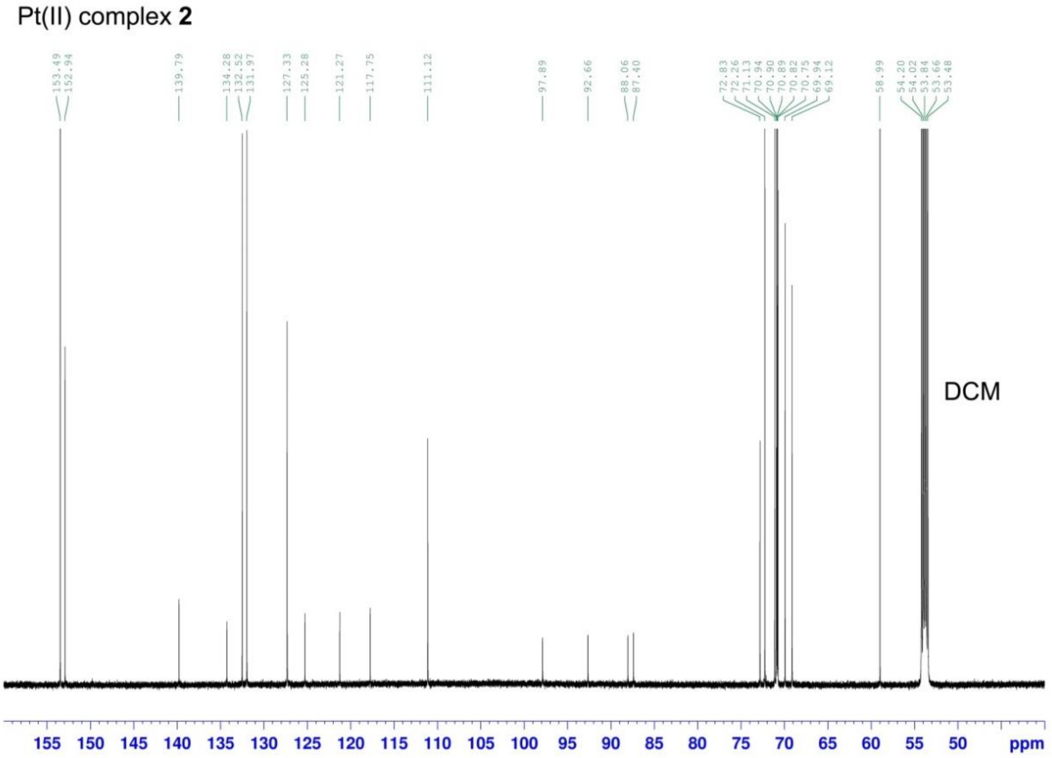

Fig. 135 ^{13}C NMR (150.9 MHz, CD_2Cl_2, 293 K) of Pt(II) complex **2**.

HRMS (ESI, pos. Mode), (dichloromethane/methanol 1:1):
m/*z*: calculated for [X+4] of $[C_{84}H_{110}Cl_2N_2O_{24}PtNa]^+$ ([X+4] of $[M+Na]^+$): 1819.6373; found: 1819.6366.

Elemental analysis: calculated for $C_{84}H_{110}Cl_2N_2O_{24}Pt$: C 56.12; H 6.17; N 1.56; found: C 55.97; H 6.33; N 1.54.

Synthesis of Pd(II) complex 3[*]:

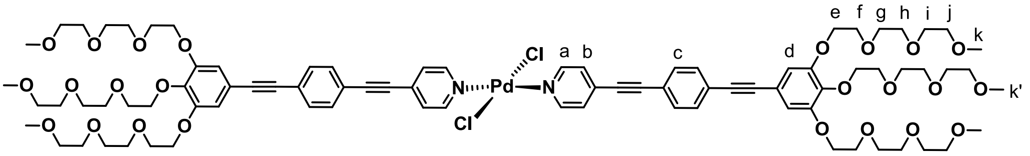

Chemical Formula: $C_{84}H_{110}Cl_2N_2O_{24}Pd$
Molecular Weight: 1709.09720
3

In advance, the reactant 4-((4-((3,4,5-tris(2-(2-(2-methoxyethoxy)ethoxy)ethoxy)-phenyl)ethynyl)phenyl)ethynyl)pyridine (**1**) was freshly purified by a flash chromatography column (silica gel) using CH_2Cl_2/MeOH = 95:5 as eluent. Afterwards, **1** (315 mg, 0.41 mmol) was dissolved in 30 ml dichloromethane (Uvasol) and subjected to vacuum/argon cycles. Similarly, a solution of dichlorobis(benzonitrile)palladium(II) (79 mg, 0.21 mmol) in dichloromethane (Uvasol) (65 ml) was prepared and subjected to vacuum/argon cycles. The Pd(II) solution was added dropwise (over 1 hour) under argon to the solution of **1** while stirring at room temperature. Afterwards, the dropping funnel was flushed with additional 10 ml of CH_2Cl_2 to avoid loss of the Pd(II) reactant. The reaction mixture was stirred over night at room temperature under argon. The next day, reaction control by ^{1}H NMR indicated complete consumption of **1** and consequently the solvent was evaporated under reduced pressure. After filtration of the crude product in

---

[*] Synthesis towards Pd(II) complex **3** was initially elaborated and described in the bachelor thesis of A. Martin[234] under the supervision of C. Rest, Prof. Dr. G. Fernández and Prof. Dr. F. Würthner, Julius-Maximilians-Universität Würzburg, 2012. The reaction conditions were modified insofar as the complexation presented herein was performed under argon atmosphere. Thus, the yield could be improved from 17%[234] to 80%.

dichloromethane through Celite, it was purified by repeated precipitation of the solid using dichloromethane and hexane, affording **3** as a yellow solid (281 mg, 0.16 mmol, yield: 80 %).

^{1}H NMR (400 MHz, CD_2Cl_2, 300 K):

δ (in ppm) = 8.80 - 8.78 (m, 4H, H_a), 7.58 - 7.53 (m, 8H, H_c), 7.44 - 7.42 (m, 4H, H_b), 6.81 (s, 4H, H_d), 4.17 - 4.14 (m, 12H, H_e), 3.85 - 3.48 (m, 60H, H_{f-j}), 3.33 (s, 6H, $H_{k'}$), 3.32 (s, 12H, H_k).

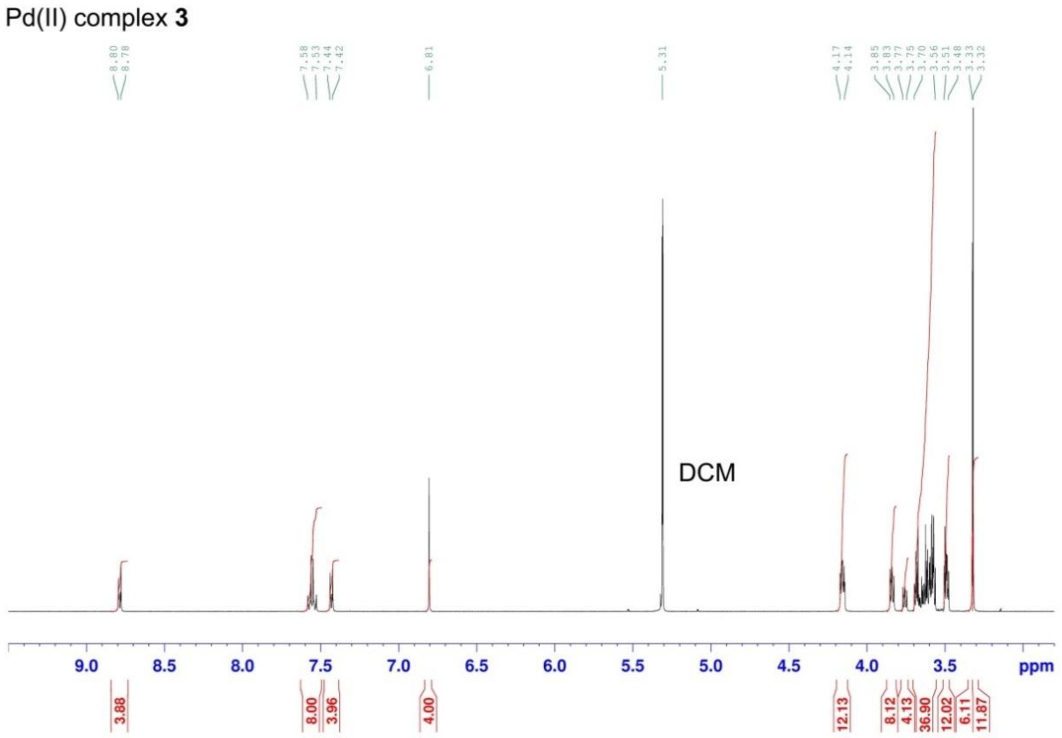

Fig. 136 ^{1}H NMR (400 MHz, CD_2Cl_2, 300 K) of Pd(II) complex **3**.

^{13}C NMR (100.6 MHz, CD_2Cl_2, 300 K):

δ (in ppm) = 153.3, 153.0, 140.0, 134.7, 132.6, 132.0, 127.1, 125.4, 121.3, 117.8, 111.3, 97.8, 92.7, 88.1, 87.4, 72.9, 72.3, 71.2, 71.0, 70.9, 70.8, 70.0, 69.3, 59.0.

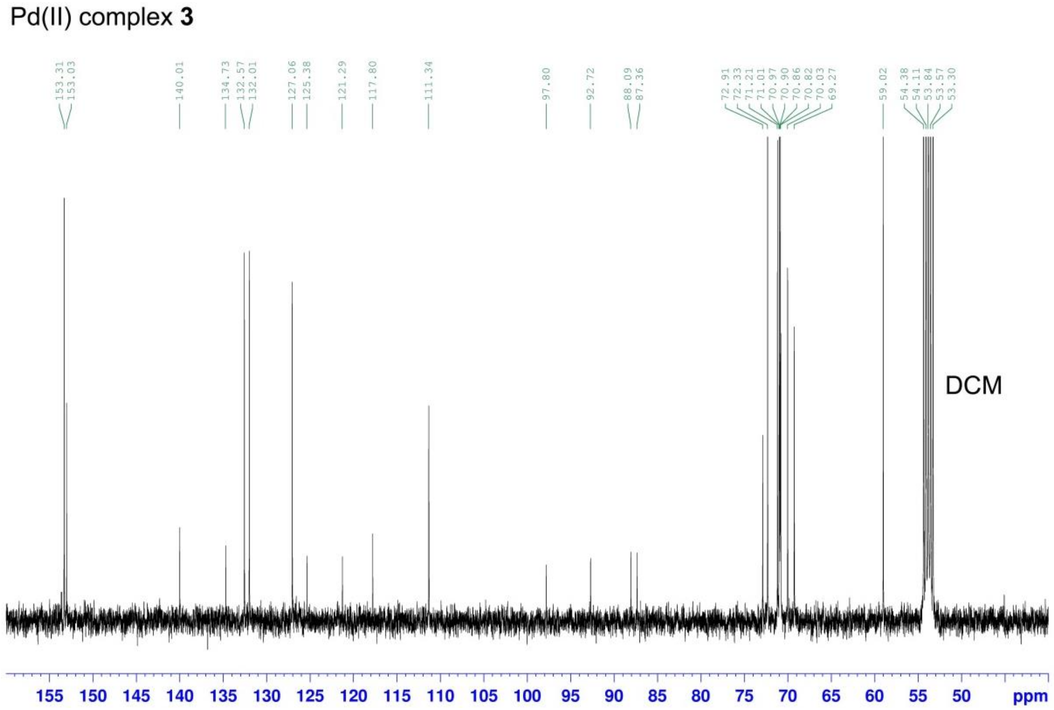

Fig. 137 ^{13}C NMR (100.6 MHz, CD_2Cl_2, 300 K) of Pd(II) complex **3**.

HRMS (ESI, pos. Mode), (dichloromethane/methanol 1:1):
m/*z*: calculated for [X+6] of $[C_{84}H_{110}Cl_2N_2O_{24}Pd+NH_4]^+$ ([X+6] of $[M+NH_4]^+$): 1726.6215; found: 1726.6225.

Due to the isotopic distribution over a broad m/z region caused by chlorine and palladium the signal of the monoisotopic signal can be too small for some compounds in intensity for an accurate mass measurement. Therefore, the most intense signal (X+6) of this isotopic distribution was taken as described and compared with the respective calculated value.

Elemental analysis: calculated for $C_{84}H_{110}Cl_2N_2O_{24}Pd$: C 59.03; H 6.49; N 1.64; found: C 58.90; H 6.61; N 1.59.

Synthesis of ligand 4:

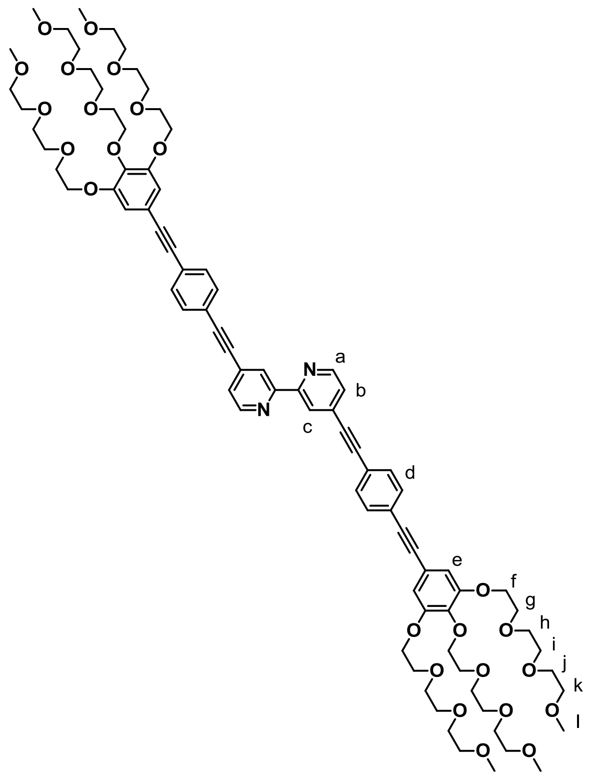

Chemical Formula: $C_{84}H_{108}N_2O_{24}$
Molecular Weight: 1529.75532
4

In advance, triethylamine (NEt_3) was freshly distilled under nitrogen and tetrahydrofuran (THF) was purified by a solvent purification system.

A 50 ml three-necked flask, equipped with septum and tap, was charged with 4,4'-dibromo-2,2'-bipyridine **121** (116 mg, 0.37 mmol), tris(dibenzylideneacetone)dipalladium(0) (35 mg, 0.04 mmol) and triphenylarsine (3.9 mg, 0.01 mmol). The flask was rejected to a vacuum/nitrogen cycle prior to the addition of 10 ml triethylamine and 2 ml of THF. The mixture was heated under nitrogen to 70 °C.

Additionally, a solution of 5-((4-ethynyl-phenyl)ethynyl)-1,2,3-tris(2-(2-(2-methoxyethoxy)ethoxy)ethoxy)benzene **119** (555 mg, 0.81 mmol) in THF is prepared by dissolution of **119** under nitrogen in 4.5 ml dried THF. This solution of the alkyne is added to the reaction mixture and after further addition of 1.2 ml THF, the reaction mixture was stirred at 75 °C under nitrogen.

When the reaction seemed to pause after two hours (reaction control by TLC), a spatula tip of tetrakis(triphenylphosphine)palladium(0) was added and the temperature increased to 85 °C for around 1 hour. Finally, after further addition of the alkyne reactant 5-((4-ethynyl-phenyl)ethynyl)-1,2,3-tris(2-(2-(2-methoxyethoxy)ethoxy)-ethoxy)benzene (**119**) the reaction was stirred at 95 °C for additional 1.5 hours.

After evaporation of the solvent under reduced pressure, the crude product was purified by column chromatography (CH_2Cl_2/MeOH = 96:4) affording **4** as a yellow solid (111 mg, 0.07 mmol, yield: 20 %).

^{1}H NMR (400 MHz, CD_2Cl_2, 300 K):

δ (in ppm) = 8.68 (dd, ^3J = 5.0 Hz, ^5J = 0.9 Hz, 2H, H_a), 8.57 (dd, ^4J = 1.6 Hz, ^5J = 0.9 Hz, 2H, H_c), 7.59 - 7.53 (m, 8H, H_d), 7.44 (dd, ^3J = 5.0 Hz, ^4J = 1.6 Hz, 2H, H_b), 6.81 (s, 4H, H_e), 4.18 - 4.14 (m, 12H, H_f), 3.86 - 3.48 (m, 60H, $H_{g\text{-}k}$), 3.33 (s, 6H, $H_{l'}$), 3.32 (s, 12H, H_l)

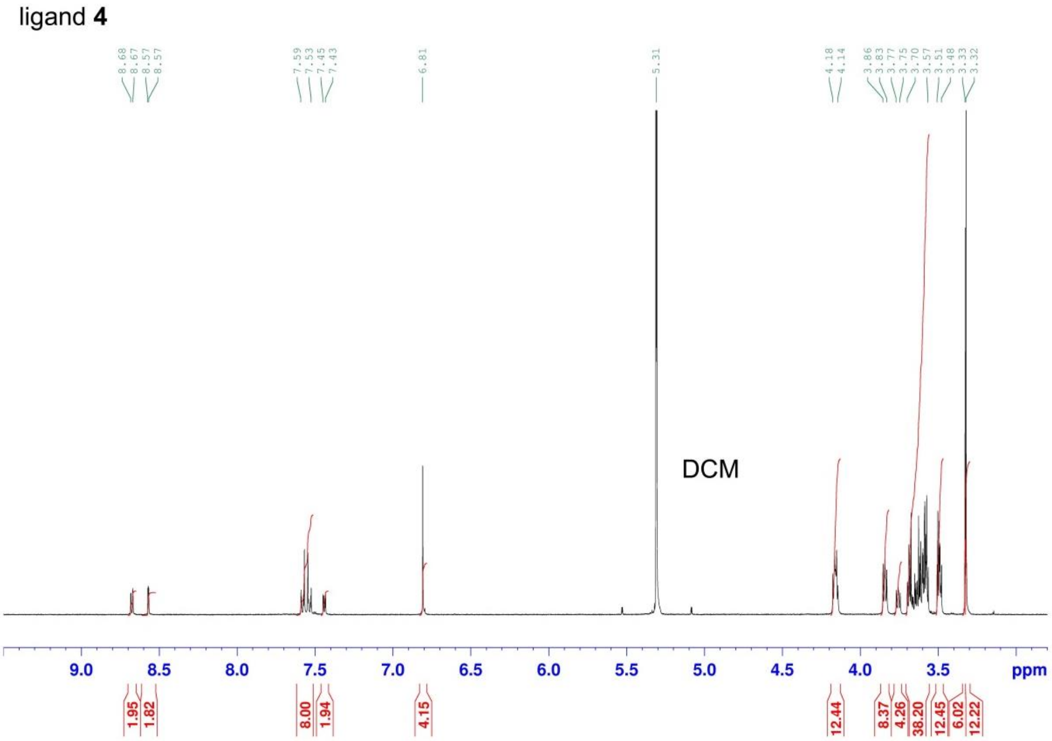

Fig. 138 ^{1}H NMR (400 MHz, CD_2Cl_2, 300 K) of ligand **4**.

^{13}C NMR (100.6 MHz, CD_2Cl_2, 300 K):

δ (in ppm) = 156.1, 153.0, 149.7, 140.0, 132.5, 132.3, 131.9, 125.9, 124.6, 123.3, 122.3, 117.9, 111.3, 93.7, 92.2, 89.1, 88.2, 72.9, 72.3, 71.2, 71.0, 70.9, 70.8, 70.0, 69.3, 59.0.

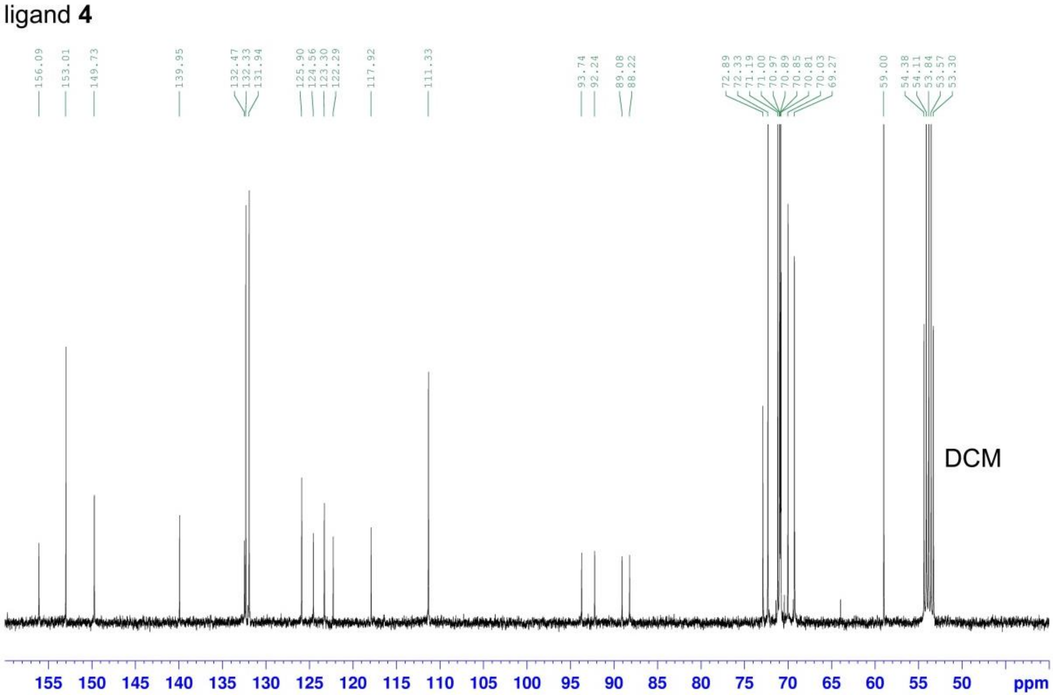

Fig. 139 ^{13}C NMR (100.6 MHz, CD_2Cl_2, 300 K) of ligand **4**.

MS (MALDI-TOF-MS, pos.):

m/*z*: calculated for $[C_{84}H_{108}N_2O_{24}Na]^+$ $[M+Na]^+$: 1551.718; found: 1551.709.

HRMS (ESI, pos. Mode), (acetonitrile/chloroform 1:1):

m/*z*: calculated for $[C_{84}H_{108}N_2O_{24}Na]^+$ ($[M+Na]^+$): 1551.7184; found: 1551.7190.

Elemental analysis: calculated for $C_{84}H_{108}N_2O_{24}$: C, 65.95; H, 7.12; N, 1.83; found (++V_2O_5): C 65.60; H 7.37; N 1.89.

Synthesis of Pt(II) complex 5:

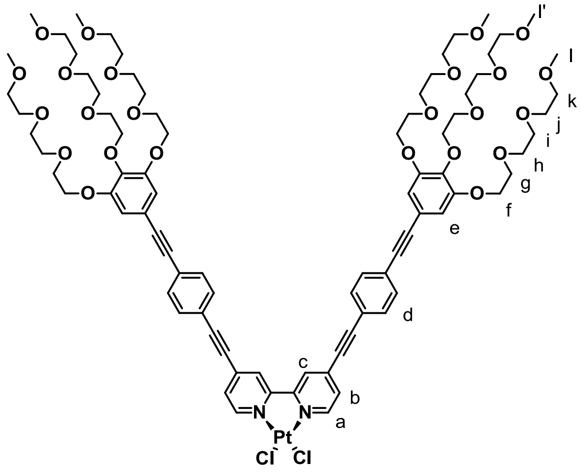

Chemical Formula: $C_{84}H_{108}Cl_2N_2O_{24}Pt$
Molecular Weight: 1795.74532

5

In advance benzene was subjected to five vacuum/nitrogen cycles and additionally flushed with argon for one hour. A 50ml-three-necked flask was charged with 4,4'-bis((4-((3,4,5-tris(2-(2-(2-methoxyethoxy)ethoxy)ethoxy)phenyl)ethynyl)phenyl)-ethynyl)-2,2'-bipyridine (**4**) (99.8 mg, 0.07 mmol) and dichlorobis(benzonitrile)-platinum(II) (31.7 mg, 0.07 mmol) and subsequently subjected carefully to three vacuum/nitrogen cycles. Under nitrogen 35 ml degassed benzene was added and the mixture again subjected to three vacuum/nitrogen cycles. The complexation mixture stirred at 87 °C under nitrogen until reaction control by ^{1}H NMR indicated complete consumption of the ligand **4** after seven days. After evaporation of the solvent, the crude product was purified by several precipitation steps using dichloromethane and hexane.

^{1}H NMR (400 MHz, CD_2Cl_2, 300 K):

δ (in ppm) = 9.76 (d, ^3J = 6.2 Hz, 2H, H_a), 8.07 (d, 2H, H_c), 7.68 (dd, ^3J = 6.2 Hz, 2H, H_b), 7.64 - 7.56 (m, 8H, H_d), 6.82 (s, 4H, H_e), 4.18 - 4.15 (m, 12H, H_f), 3.86 - 3.48 (m, 60H, $H_{g\text{-}k}$), 3.33 (s, 6H, $H_{l'}$), 3.32 (s, 12H, H_l).

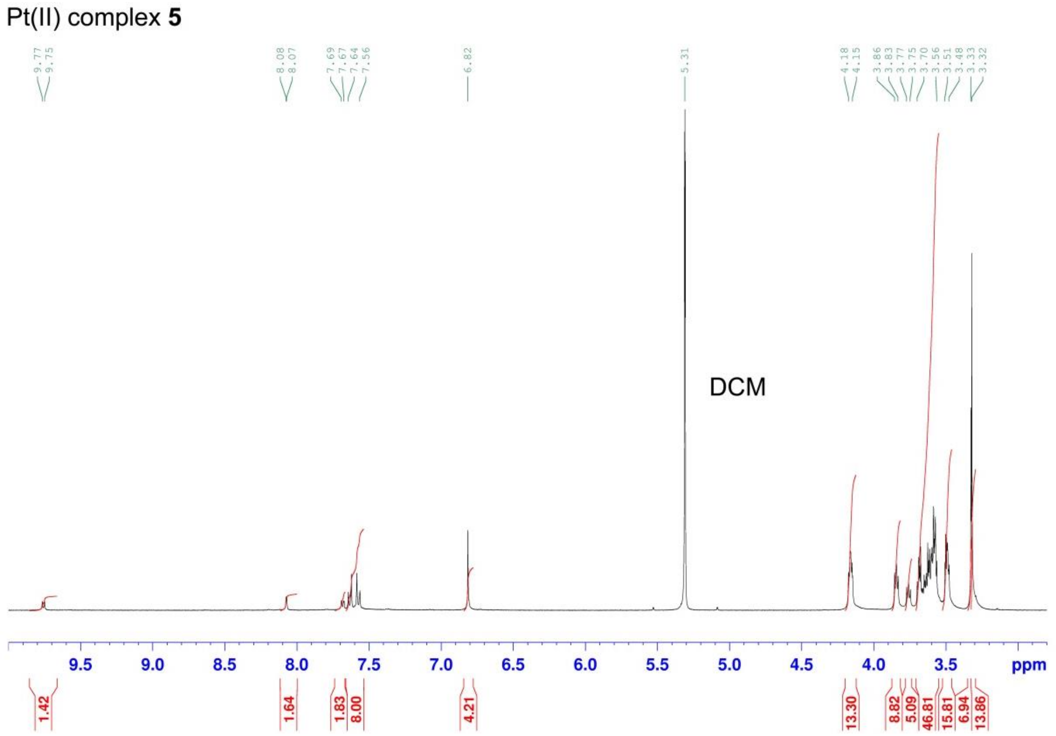

Fig. 140 ^{1}H NMR (400 MHz, CD_2Cl_2, 300 K) of Pt(II) complex **5**.

^{13}C NMR (100.6 MHz, CD_2Cl_2, 295 K):

δ (in ppm) = 156.8, 153.0, 149.5, 140.0, 135.3, 132.6, 132.1, 129.3, 125.9, 125.0, 120.9, 117.7, 111.2, 99.9, 93.1, 88.0, 87.6, 72.9, 72.3, 71.2, 71.0, 70.9, 70.8, 70.0, 69.2, 59.0.

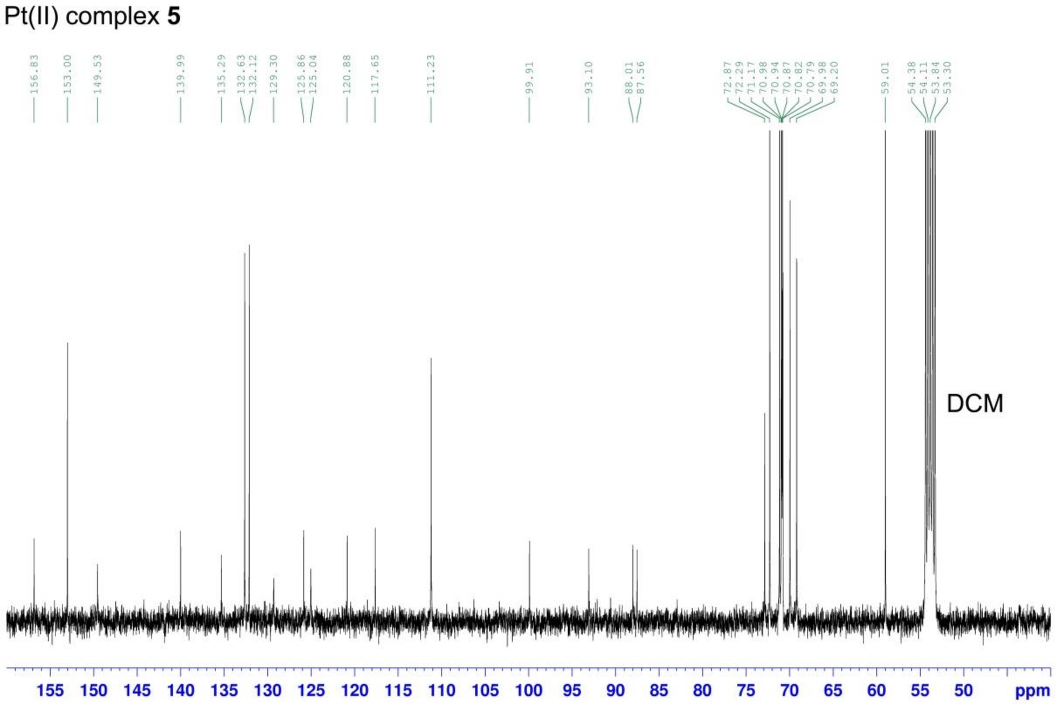

Fig. 141 ^{13}C NMR (100.6 MHz, CD_2Cl_2, 295 K) of Pt(II) complex **5**.

HRMS (ESI, pos. Mode), (dichloromethane/methanol 1:1):
m/*z*: calculated for [X+4] of $[C_{84}H_{108}Cl_2N_2O_{24}Pt+NH_4]^+$ ([X+4] of $[M+NH_4]^+$): 1812.6663; found: 1812.6669.

Elemental analysis: calculated for $C_{84}H_{108}Cl_2N_2O_{24}Pt$: C, 56.18; H, 6.06; N, 1.56; found: C 56.04; H 6.02; N 1.63.

6.3 Crystallographic data

Crystal structure analysis of the Pt(II) complex 2:

Table 11 Crystallographic data for **2**.

Parameter	
Formula	$C_{84}H_{110}Cl_2N_2O_{24}Pt$
Mr	1797.79
Crystal system	triclinic
Space group	$P\bar{1}$
T (K)	100
a (Å)	12.7037(6)
b (Å)	13.0474(6)
c (Å)	14.3967(7)
α (°)	64.542(2)
β (°)	83.775(2)
γ (°)	80.805(2)
V (Å^3)	2124.75(18)
Z	1
density (calc, g/cm^{-3})	1.4049
wavelength (Å)	0.71073
abs. coef (mm^{-1})	1.788
F(000)	931.1454
crystal size (mm^{-3})	0.191 x 0.082 x 0.047
theta range for data collection	2.31 - 26.00
index ranges	$-16 < h < 16$
	$-16 < k < 16$
	$-18 < l < 18$
reflections collected	49896
independent reflections	8347
refinement method	full-matrix least-squares on F^2
data/restraints/parameters	8347/0/513
goodness of fit on F^2	1.0509

final *R* indices	$R_1 = 0.0257$
[I>2σ(I)]	$wR_2 = 0.0609$
largest diff peak and hole [eÅ^{-3}]	1.0805 and -0.8143

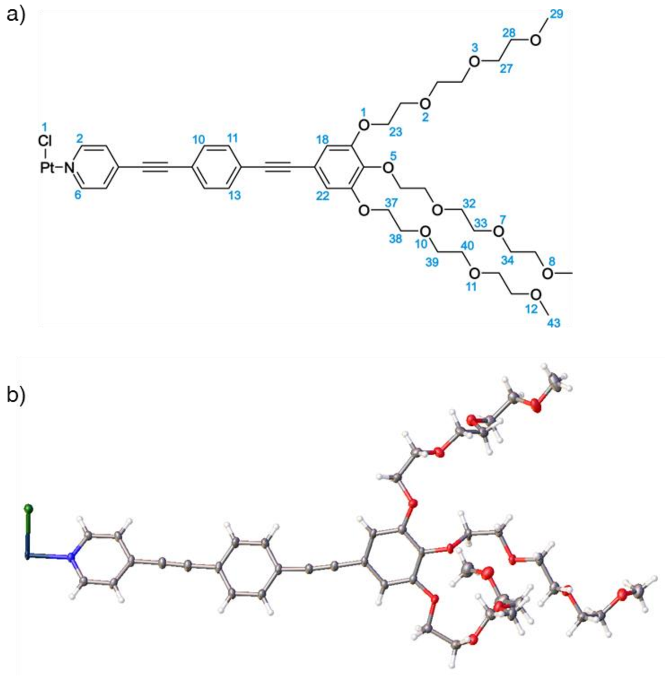

Fig. 142 a) Scheme of the asymmetric unit of Pt(II) complex **2** with atom numbering scheme of the hydrogen bond donating and accepting atoms and b) molecular structure of the asymmetric unit.

Table 12 CH···Cl and CH···O hydrogen bond distances in the crystal structure of **2**.

Hydrogen bond	Distance (D···A) [Å]	Angle (D-H···A) [°]
C2-H2···O5	3.375(3)	148.90(6)
C10-H10···O8	3.256(3)	162.34(8)
C11-H11···O7	3.289(3)	122.74(6)
C18-H18···O12	3.313(3)	120.24(6)
C22-H22···O3	3.632(3)	174.21(6)
C23-H23b···O12	3.486(3)	151.13(7)
C23-H23b···O11	3.179(3)	126.77(8)
C27-H27b···Cl1	3.896(3)	162.48(6)
C29-H29a···O1	3.404(4)	155(2)[a]
C32-H32b···O8	3.105(3)	127.15(8)

C34-H34b···O10	3.635(3)	152.52(7)
C37-H37b···O2	3.579(3)	169.36(6)
C40-H40a···O10	3.604(3)	155.78(7)
C43-H43c···Cl1	3.928(3)	171.1(8)

---

[a] the relatively large error on the angle is due to larger mobility of the terminal CH_3-group compared to the remaining CH_2-groups in the ethylene glycol chain.

Crystal structure analysis of the Pd(II) complex 3:

Table 13 Crystallographic data for **3**.

Parameter	
Formula	$C_{84}H_{110}Cl_2N_2O_{24}Pd$
Mr	1709.03
Crystal system	triclinic
Space group	$P\overline{1}$
T (K)	100
a (Å)	12.7142(5)
b (Å)	13.0337(5)
c (Å)	14.4284(5)
α (°)	64.8840(11)
β (°)	83.6590(12)
γ (°)	81.0220(12)
V (Å^3)	2135.77(14)
Z	1
density (calc, g/cm^{-3})	1.329
wavelength (Å)	0.71073
abs. coef (mm^{-1})	0.354
F(000)	900
Crystal size (mm^{-3})	0.18 x 0.12 x 0.12
theta range for data collection	3.167 - 26.407
index ranges	$-15 < h < 15$
	$-16 < k < 16$
	$-18 < l < 18$

reflections collected	28964
independent reflections	8699
refinement method	full-matrix least-squares on F^2
data/restraints/parameters	8699/0/514
goodness of fit on F^2	1.024
final R indices	$R_1 = 0.0296$
[I>2σ(I)]	$wR_2 = 0.0651$
largest diff peak and hole [eÅ^{-3}]	0.439 and -0.590

References

[1] J. M. Lehn, *Pure Appl. Chem* **1978**, *50*, 871 - 892.

[2] J. M. Lehn, *J. Inclusion Phenom: Nobel Lecture*, **1988**, *6*, 351 - 396.

[3] D. Philp, J. F. Stoddart, *Angew. Chem. Int. Ed. Engl.* **1996**, *35*, 1154 - 1196.

[4] G. M. Cooper, *The Cell - A Molecular Approach*, Second Edition, Sunderland (MA): Sinauer Associates; **2000**.

[5] B. Alberts, A. Johnson, J. Lewis, M. Raff, K. Roberts, P. Walter, *Molecular Biology of the Cell*, Fourth Edition, New York: Garland Science; **2002**.

[6] D. A. Uhlenheuer, K. Petkau, L. Brunsveld, *Chem. Soc. Rev.* **2010**, *39*, 2817 - 2826.

[7] A. Sorrenti, O. Illa, R. M. Ortuño, *Chem. Soc. Rev.* **2013**, *42*, 8200 - 8219

[8] M. J. Mayoral Muñoz, G. Fernández, *Chem. Sci.* **2012**, *3*, 1395 - 1398.

[9] E. Riedel, *Anorganische Chemie*, 6. Auflage, Walter de Gruyter, Berlin, New York; **2004**.

[10] K. M.-C. Wong, V. W.-W. Yam, *Acc. Chem. Res.* **2011**, *44*, 424 - 434.

[11] I. Eryazici, C. N. Moorefield, G. R. Newkome, *Chem. Rev.* **2008,** *108*, 1834 - 1895.

[12] R. Chakrabarty, P. S. Mukherjee, P. J. Stang, *Chem. Rev.* **2011**, *111*, 6810 - 6918.

[13] A. Juris, V. Balzani, *Coord. Chem. Rev.* **1988**, *84*, 85 - 277.

[14] V. W.-W. Yam, K. M.-C. Wong, *Chem. Commun.* **2011**, *47*, 11579 - 11592.

[15] N. Liu, B. Wang, W. Liu, W. Bu, *J. Mater. Chem. C* **2013**, *1*, 1130 - 1136.

[16] C. Po, A. Y.-Y. Tam, K. M.-C. Wong, V. W.-W.Yam, *J. Am. Chem. Soc* **2011**, *133*, 12136 - 12143.

[17] W. Lu, Y. Chen, V. A. L. Roy, S. S.-Y. Chui, C.-M. Che, *Angew. Chem. Int. Ed.* **2009**, *48*, 7621 - 7625.

[18] S. Y.-L. Leung, A. Y.-Y. Tam, C.-H. Tao, H. S. Chow, V. W.-W. Yam, *J. Am. Chem. Soc.* **2012**, *134*, 1047 - 1056.

[19] K. C. Chang, J.-L. Lin, Y.-T. Shen, C.-Y. Hung, C.-Y. Chen, S.-S. Sun, *Chem. Eur. J.* **2012**, *18*, 1312 - 1321.

[20] V. W.-W. Yam, *Pure Appl. Chem.* **2013**, *85*, 1321 - 1329.

[21] M. Levitus, K. Schmieder, H. Ricks, K. D. Shimizu, U. H. F. Bunz, M. A. Garcia-Garibay, *J. Am. Chem. Soc.* **2001**, *123*, 4259 - 4265.

[22] A. Whitty, *Nature Chem. Biol.* **2008**, *4*, 435 - 439

[23] D. E. Sleat, P. C. Turner, J. T. Finch, P. J. G. Butler, T. M. A. Wilson, *Virology* **1986**, *155*, 299 - 308.

[24] A. Klug, *Phil. Trans. R. Soc. Lond. B* **1999**, *354*, 531 - 535.

[25] A. Hernandez-Garcia, D. J. Kraft, A. F. J. Janssen, P. H. H. Bomans, N. A. J. M. Sommerdijk, D. M. E. Thies-Weesie, M. E. Favretto, R. Brock, F. A. de Wolf, M. W. T. Werten, P. van der Schoot, M. Cohen Stuart, R. de Vries, *Nat. Nanotechnol.*, **2014**, *9*, 698 - 702.

[26] W. A. Eaton, E. R. Henry, J. Hofrichter, A. Mozzarelli, *Nat. Struct. Biol.* **1999**, *6*, 351 - 358.

[27] C. Bohr, K. Hasselbalch, A. Krogh, *Skand. Arch. Physiol.* **1904**, *15*, 401 - 412.

[28] J. M. Berg, J. L. Tymoczko, L. Stryer, *Stryer Biochemie*, 7. Auflage, Springer-Verlag Berlin Heidelberg; **2013**.

[29] G. Ercolani, *J. Am. Chem. Soc.* **2003**, *125*, 16097 - 16103.

[30] C. A. Hunter, H. L. Anderson, *Angew. Chem. Int. Ed.*, **2009**, *48*, 7488 - 7499.

[31] A. Ciferri, *Macromol. Rapid. Commun.* **2002**, *23*, 511 - 529.

[32] D. Zhao, J. S. Moore, *Org. Biomol. Chem.*, **2003**, *1*, 3471 - 3491.

[33] Z. Chen, A. Lohr, C. R. Saha-Möller, F. Würthner, *Chem. Soc. Rev.*, **2009**, *38*, 564 - 584.

[34] T. F. A. de Greef, M. M. J. Smulders, M. Wolffs, A. P. H. J. Schenning, R. P. Sijbesma, E. W. Meijer, *Chem. Rev.*, **2009**, *109*, 5687 - 5754.

[35] M. M. J. Smulders, M. M. L. Nieuwenhuizen, T. F. A. de Greef, P. van der Schoot, A. P. H. J. Schenning, E. W. Meijer, *Chem. Eur. J.* **2010**, *16*, 362 - 367.

[36] R. B. Martin, *Chem. Rev.* **1996**, *96*, 3043 - 3064.

[37] T. Aida, E. W. Meijer, S. Stupp, *Science*, **2012**, *335*, 813 - 817.

[38] C. Kulkarni, S. Balasubramanian, S. J. George, *ChemPhysChem* **2013**, *14*, 661 - 673.

[39] R. F. Goldstein, L. Stryer, *Biophys. J.* **1986**, *50*, 583 - 599.

[40] T. E. Kaiser, V. Stepanenko, F. Würthner, *J. Am. Chem. Soc.* **2009**, *131*, 6719 - 6732.

[41] P. van der Schoot in *Supramolecular Polymers*, A. Ciferri, Second Edition, CRC Press, Baton Rouge, LA; **2005**.

[42] P. Jonkheijm, P. van der Schoot, A. P. H. J. Schenning, E. W. Meijer, *Science* **2006**, *313*, 80 - 83.

[43] M. M. J. Smulders, A. P. H. J. Schenning, E. W. Meijer, *J. Am. Chem. Soc.* **2008**, *130*, 606 - 611.

[44] H. M. M. ten Eikelder, A. J. Markvoort, T. F. A. de Greef, P. A. J. Hilbers, *J. Phys. Chem. B* **2012**, *116*, 5291 - 5301.

[45] A. J. Markvoort, H. M. M. ten Eikelder, P. A. J. Hilbers, T. F. A. de Greef, E.W. Meijer, *Nat. Commun.*, **2011**, *2*, 509 - 517.

[46] MATLAB scripts for fitting melting curves of one-component supramolecular polymerizations, attached to ref. 44.

[47] L. F. Lindoy, I. M. Atkinson, *Self-Assembly in Supramolecular Systems*, J. F. Stoddart, The Royal Society of Chemistry: Cambridge; **2000**.

[48] H. Umeyama, K. Morokuma, *J. Am. Chem. Soc.* **1977**, *99*, 1316 - 1332.

[49] G. R. Desiraju, *Acc. Chem. Res.* **2002**, *35*, 565 - 573.

[50] G. R. Desiraju, *Angew. Chem. Int. Ed.* **2011**, *50*, 52 - 59.

[51] L. Saroléa-Mathot, *Trans. Faraday Soc*. **1953**, *49*, 8 - 20.

[52] F. Weinhold, *J. Mol. Struc. – Theochem*. **1997**, *398-399*, 181 - 197.

[53] T. Steiner, *Angew. Chem. Int. Ed.* **2002**, *41*, 48 - 76.

[54] P. Vishweshwar, A. Nangia, V. M. Lynch *Chem. Commun.* **2001**, 179 - 180.

[55] N.Kobko, L. Paraskevas, E. del Rio, J. J. Dannenberg, *J. Am Chem. Soc.* **2001**, *123*, 4348 - 4349.

[56] N.Kobko, J. J. Dannenberg *J. Phys. Chem. A* **2003**, *107*, 10389 - 10395.

[57] J. Kříž, J. Dybal, *J. Phys. Chem. B* 2007, **111**, 6118 - 6126.

[58] K. S. Birdi, *Handbook of Surface and Colloid Chemistry*, Second Edition (Chapter 2.6), CRC Press; **2002**.

[59] G. Gilli, F. Bellucci, V. Ferretti, V. Bertolasi, *J. Am. Chem. Soc.* **1989**, *111*, 1023 - 1028.

[60] V. Bertolasi, P. Gilli, V. Ferretti, G. Gilli, *J. Am. Chem. Soc.* **1991**, *113*, 4917 - 4925.

[61] P. Gilli, V. Bertolasi, V. Ferretti, G. Gilli, *J. Am. Chem. Soc.* **2000**, *122*, 10405 - 10417.

[62] G. Song, L. Zhang, C. He, D.-C. Fang, P. G. Whitten, H. Wang, *Macromolecules* **2013**, *46*, 7423 - 7435.

[63] R. Q. Albuquerque, A. Timme, R. Kress, J. Senker, H.-W. Schmidt, *Chem. Eur. J.* **2013**, *19*, 1647 - 1657.

[64] A. P. H. J. Schenning, P. Jonkheijm, E. Peeters, E. W. Meijer, *J. Am. Chem. Soc.* **2001**, *123*, 409 - 416.

[65] P. Jonkheijm, F. J. M. Hoeben, R. Kleppinger, J. van Herrikhuyzen, A. P. H. J. Schenning, E. W. Meijer, *J. Am. Chem. Soc.* **2003**, *125*, 15491 - 15949.

[66] A. Gesquière, P. Jonkheijm, F. J. M. Hoeben, A. P. H. J. Schenning, S. de Feyter, F. C. de Schryver, E. W. Meijer, *Nano Lett.* **2004**, *4*, 1175 - 1179.

[67] F. Oosawa, M. Kasai, *J. Mol. Biol.* **1962**, *4*, 10 - 21.

[68] S. J. George, Ž. Tomović, M. M. J. Smulders, T. F. A. de Greef, P. E. L. G. Leclère, E. W. Meijer, A. P. H. J. Schenning, *Angew. Chem. Int. Ed.* **2007**, *46*, 8206 - 8211.

[69] P. J. M. Stals, J. F. Haveman, R. Martín-Rapún, C. F. C. Fitié, A. R. A. Palmans, E. W. Meijer, *J. Mater. Chem.* **2009**, *19*, 124 - 130.

[70] P. J. M. Stals, M. M. J. Smulders, R. Martín-Rapún, A. R. A. Palmans, E. W. Meijer, *Chem. Eur. J.* **2009**, *15*, 2071 - 2080.

[71] Y. Nakano, T. Hirose, P. J. M. Stals, E. W. Meijer, A. R. A. Palmans, *Chem. Sci.* **2012**, *3*, 148 - 155.

[72] T. Mes, M. M. J. Smulders, A. R. A. Palmans, E. W. Meijer, *Macromolecules* **2010**, *43*, 1981 - 1991.

[73] P. J. M. Stals, J. C. Everts, R. de Bruijn, I. A. W. Filot, M. M. J. Smulders, R. Martín-Rapún, E. A. Pidko, T. F. A. de Greff, A. R. A. Palmans, E. W. Meijer, *Chem. Eur. J.* **2010**, *16*, 810 - 821.

[74] D. Ogata, T. Shikata, K. Hanabusa, *J. Phys. Chem. B* **2004**, *108*, 15503 - 15510.

[75] Y. Matsunaga, N. Miyajima, Y. Nakayasu, S. Sakai, M. Yonenaga, *Bull. Chem. Soc. Jpn.* **1988**, *61*, 207 - 210.

[76] A. J. Wilson, M. Masuda, R. P. Sijbesma, E. W. Meijer, *Angew. Chem. Int. Ed.* **2005**, *44*, 2275 - 2279.

[77] M. M. J. Smulders, M. M. L. Nieuwenhuizen, M. Grossman, I. A. W. Filot, C. C. Lee, T. F. de Greef, A. P. H. J. Schenning, A. R. A. Palmans, E. W. Meijer, *Macromolecules* **2011**, *44*, 6581 - 6587.

[78] T. Mes, S. Cantekin, D. W. R. Balkenende, M. M. M. Frissen, M. A. J. Gillissen, B. F. M. de Waal, I. K. Voets, E. W. Meijer, A. R. A. Palmans, *Chem. Eur. J.* **2013**, *19*, 8642 - 8649.

[79] H.-J. Lee, Y.-S. Choi, K.-B. Lee, J. Park, C.-J. Yoon, *J. Phys. Chem. A* **2002**, *106*, 7010 - 7017.

[80] G. Fernández, F. García, F. Aparicio, E. Matesanz, L. Sánchez, *Chem. Commun.* **2009**, 7155 - 7157.

[81] F. García, G. Fernández, L. Sánchez, *Chem. Eur. J.* **2009**, *15*, 6740 - 6747.

[82] F. García, L. Sánchez, *Chem. Eur. J.* **2010**, *16*, 3138 - 3146.

[83] F. García, J. Buendía, L. Sánchez, *J. Org. Chem.* **2011**, *76*, 6271 - 6276.

[84] J. Buendía, L. Sánchez, *Org. Lett.* **2013**, *15*, 5746 - 5749.

[85] F. Aparicio, F. García, L. Sánchez, *Chem. Eur. J.* **2013**, *19*, 3239 - 3248.

[86] F. García, P. M. Viruela, E. Matesanz, E. Ortí, L. Sánchez, *Chem. Eur. J.* **2011**, *17*, 7755 - 7759.

[87] M. M. J. Smulders, I. A. W. Filot, J. M. A. Leenders, P. van der Schoot, A. R. A. Palmans, A. P. H. J. Schenning, E. W. Meijer, *J. Am. Chem. Soc.* **2010**, *132*, 611 - 619.

[88] M. M. J. Smulders, P. J. M. Stals, T. Mes, T. F. E. Paffen, A. P. H. J. Schenning, A. R. A. Palmans, E. W. Meijer, *J. Am. Chem. Soc.* **2010**, *132*, 620 - 626.

[89] F. García, L. Sánchez, *J. Am. Chem. Soc.* **2012**, *134*, 734 - 742.

[90] F. García, P. A. Korevaar, A. Verlee, E. W. Meijer, A. R. A. Palmans and L. Sánchez, *Chem. Commun.* **2013**, *49*, 8674 - 8676.

[91] F. Wang, M. A. J. Gillissen, P. J. M. Stals, A. R. A. Palmans, E. W. Meijer, *Chem. Eur. J.* **2012**, *18*, 11761 - 11770.

[92] F. Aparicio, E. Matesanz, L. Sánchez, *Chem. Commun.* **2012**, *48*, 5757 - 5759.

[93] F. Aparicio, L. Sánchez, *Chem. Eur. J.* **2013**, *19*, 10482 - 10486.

[94] F. Würthner, *Chem. Commun.* **2004**, 1564 - 1579.

[95] F. Würthner, T. E. Kaiser, C. R. Saha-Möller, *Angew. Chem. Int. Ed.* **2011**, *50*, 3376 - 3410.

[96] D. Görl, X. Zhang, F. Würthner, *Angew. Chem. Int. Ed.* **2012**, *51*, 6328 - 6348.

[97] Z. Chen, B. Fimmel, F. Würthner, *Org. Biomol. Chem.* **2012**, *10*, 5845 - 5855.

[98] T. E. Kaiser, H. Wang, V. Stepanenko, F. Würthner, *Angew. Chem. Int. Ed.*, **2007**, *46*, 5541 - 5544.

[99] F. Fennel, S. Wolter, Z. Xie, P.-A. Plötz, O. Kühn, F. Würthner, S. Lochbrunner, *J. Am. Chem. Soc.* **2013**, *135*, 18722 - 18725.

[100] T. Seki, A. Asano, S. Seki, Y. Kikkawa, H. Murayama, T. Karatsu, A. Kitamura, S. Yagai, *Chem. Eur. J.* **2011**, *17*, 3598 - 3608.

[101] C. Shao, M. Stolte, F. Würthner, *Angew. Chem. Int. Ed.* **2013**, *52*, 10463 - 10467.

[102] R. van der Weegen, P. A. Korevaar, P. Voudouris, I. K. Voets, T. F. A. de Greef, J. A. J. M. Vekemans, E. W. Meijer, *Chem. Commun.* **2013**, *49*, 5532 - 5534.

[103] F. Würthner, C. Thalacker, S. Diele, C. Tschierske, *Chem. Eur. J.* **2001**, *7*, 2245 - 2253.

[104] Z. Chen, V. Stepanenko, V. Dehm, P. Prins, L. D. A. Siebbeles, J. Seibt, P. Marquetand, V. Engel, F. Würthner, *Chem. Eur. J.* **2007**, *13*, 436 - 449.

[105] S. Yagai, M. Suzuki, X. Lin, M. Gushiken, T. Noguchi, T. Karatsu, A. Kitamura, A. Saeki, S. Seki, Y. Kikkawa, Y. Tani, K.-i. Nakayama, *Chem. Eur. J.* **2014**, *20*, 16128 - 16137.

[106] M. Yamauchi, S. Kubota, T. Karatsu, A. Kitamura, A. Ajayaghosh, S. Yagai, *Chem. Commun.* **2013**, *49*, 4941 - 4943.

[107] T. Seki, X. Lin, S. Yagai, *Asian. J. Org. Chem.* **2013**, *2*, 708 - 724.

[108] S. Yagai, M. Gushiken, T. Karatsu, A. Kitamura, Y. Kikkawa, *Chem. Commun.* **2011**, *47*, 454 - 456.

[109] S. Yagai, M. Usui, T. Seki, H. Murayama, Y. Kikkawa, S. Uemura, T. Karatsu, A. Kitamura, A. Asano, S. Seki, *J. Am. Chem. Soc.* **2012**, *134*, 7983 - 7994.

[110] S. Boileau, L. Bouteiller, F. Lauprêtre, F. Lortie, *New. J. Chem.* **2000**, *24*, 845 - 848.

[111] F. Lortie, S. Boileau, L. Bouteiller, C. Chassenieux, B. Demé, G. Ducouret, M. Jalabert, F. Lauprêtre, P. Terech, *Langmuir* **2002**, *18*, 7218 - 7222.

[112] V. Simic, L. Bouteiller, M. Jalabert, *J. Am. Chem. Soc.* **2003**, *125*, 13148 - 13154.

[113] O. Colombani, L. Bouteiller, *New. J. Chem.* **2004**, *28*, 1373 - 1382.

[114] L. Bouteiller, O. Colombani, F. Lortie and P. Terech, *J. Am. Chem. Soc.* **2005**, *127*, 8893 - 8898.

[115] P. van der Schoot, M. A. J. Michels, L. Brunsveld, R. P. Sijbesma, A. Ramzi, *Langmuir* **2000**, *16*, 10076 - 10083.

[116] J. van Gestel, P. van der Schoot, M. A. J. Michels, *J. Phys. Chem. B* **2001**, *105*, 10691 - 10699.

[117] B. Isare, M. Linares, L. Zargarian, S. Fermandjian, M. Miura, S. Motohashi, N. Vanthuyne, R. Lazzaroni, L. Bouteiller, *Chem. Eur. J.* **2010**, *16*, 173 - 177.

[118] M. Amelia, L. Zou, A. Credi, *Coord. Chem. Rev.* **2010**, *254*, 2267 - 2280.

[119] M. Higuchi, *J. Mater. Chem. C* **2014**, *2*, 9331 - 9341.

[120] B. Happ, A. Winter, M. D. Hager, U. S. Schubert, *Chem. Soc. Rev.* **2012**, *41*, 2222 - 2255.

[121] J. K.-H. Hui, M. J. MacLachlan, *Coor. Chem. Rev.* **2010**, *254*, 2363 - 2390.

[122] M. Mauro, A. Aliprandi, D. Septiadi, N. S. Kehr, L. de Cola, *Chem. Soc. Rev.* **2014**, *43*, 4144 - 4166.

[123] A. Y.-Y. Tam, V. W.-W. Yam, *Chem. Soc. Rev.* **2013**, *42*, 1540 - 1567.

[124] C.-M. Che, S.-W. Lai, *Coord. Chem. Rev.* **2005**, *249*, 1296 - 1309.

[125] A. Kishimura, T. Yamashita, T. Aida, *J. Am. Chem. Soc.* **2005**, *127*, 179 - 183.

[126] A. Kishimura, T. Yamashita, K. Yamaguchi, T. Aida, *Nature* **2005**, *4*, 546 - 549.

[127] Y. Li, D. P.-K. Tsang, C. K.-M. Chan, K. M.-C. Wong, M.-Y. Chan, V. W.-W. Yam, *Chem. Eur. J.* **2014**, *20*, 13710 - 13715.

[128] C. Y.-S. Chung, V. W.-W. Yam, *Chem. Eur. J.* **2014**, *20*, 13016 - 13027.

[129] C. A. Strassert, C.-H. Chien, M. D. G. Lopez, D. Kourkoulos, D. Hertel, K. Meerholz, L. de Cola, *Angew. Chem. Int. Ed.* **2011**, *50*, 946 - 950.

[130] N. K. Allampally, M. Bredol, C. A. Strassert, L. de Cola, *Chem. Eur. J.* **2014**, *20*, 16863 - 16868.

[131] I. Stengel, C. A. Strassert, L. de Cola and P. Bäuerle, *Organometallics* **2014**, *33*, 1345 - 1355.

[132] X.-S. Xiao, W. Lu, C.-M. Che, *Chem. Sci.* **2014**, *5*, 2482 - 2488.

[133] G. Cheng, S. C. F. Kui, W.-H. Ang, M.-Y. Ko, P.-K. Chow, C.-L. Kwong, C.-C. Kwok, C. Ma, X. Guan, K.-H. Low, S.-J. Su, C.-M. Che, *Chem. Sci.* **2014**, *5*, 4819 - 4830.

[134] Y. Chen, W. Lu, C.-M. Che, *Organometallics* **2013**, *32*, 350 - 353.

[135] N. K. Allampally, C.-G. Daniliuc, C. A. Strassert, L. de Cola, *Inorg. Chem.* **2015**, *54*, 1588 - 1596.

[136] M. J. Mayoral, C. Rest, V. Stepanenko, J. Schellheimer, R. Q. Albuquerque, G. Fernández, *J. Am. Chem. Soc.* **2013**, *135*, 2148 - 2151.

[137] Y.-J. Tian, E. W. Meijer, F. Wang, *Chem. Commun.* **2013**, *49*, 9197 - 9199.

[138] X.-D. Xu, J. Zhang, L.-J. Chen, X.-L. Zhao, D.-X. Wang, H.-B. Yang, *Chem. Eur. J.* **2012**, *18*, 1659 - 1667.

[139] M. T. Stone, J. S. Moore, *J. Am. Chem. Soc.* **2005**, *127*, 5928 - 5935.

[140] J. Wm. Wackerly, J. S. Moore, *Macromolecules* **2006**, *39*, 7269 - 7276.

[141] J. C. Nelson, J. G. Saven, J. S. Moore, P. G. Wolynes, *Science* **1997**, *227*, 1793 - 1796.

[142] R. B. Prince, J. G. Saven, P. G. Wolynes, J. S. Moore, *J. Am. Chem. Soc.* **1999**, *121*, 3114 - 3121.

[143] D. Poland, H. A. Scheraga, *Theory of Helix-Coil Transitions in Biopolymers*, Academic Press: New York; **1970**.

[144] K. Matsuda, M. T. Stone, J. S. Moore, *J. Am. Chem. Soc.* **2002**, *124*, 11836 - 11837.

[145] C. G. Spike, R. W. Parry, *J. Am. Chem. Soc.* **1953**, *75*, 3770 - 3772.

[146] A. W. Adamson, *J. Am. Chem. Soc.* **1954**, *76*, 1578 - 1579.

[147] A. Lohr, M. Lysetska, F. Würthner, *Angew. Chem. Int. Ed.* **2005**, *44*, 5071 - 5074.

[148] A. Lohr, F. Würthner, *Chem. Commun.* **2008**, 2227 - 2229.

[149] J. Seibt, A. Lohr, F. Würthner, V. Engel, *Phys. Chem. Chem. Phys.* **2007**, *9*, 6214 - 6218.

[150] A. Lohr, T. Gress, M. Deppisch, M. Knoll, F. Würthner, *Synthesis* **2007**, *19*, 3073 - 3082.

[151] A. Lohr, F. Würthner, *Angew. Chem. Int. Ed.* **2008**, *47*, 1232 - 1236.

[152] A. Lohr, S. Uemura, F. Würthner, *Angew. Chem. Int. Ed.* **2009**, *48*, 6165 - 6168.

[153] A. Lohr, F. Würthner, *Isr. J. Chem.* **2011**, *51*, 1052 - 1066.

[154] A. Lohr, M. Grüne, F. Würthner, *Chem. Eur. J.* **2009**, *15*, 3691 - 3705.

[155] F. Würthner, S. Yao, U. Beginn, *Angew. Chem. Int. Ed.* **2003**, *42*, 3247 - 3250.

[156] G. Fernández, M. Stolte, V. Stepanenko, F. Würthner, *Chem. Eur. J.* **2013**, *19*, 206 - 217.

[157] R. Schmidt, S. Uemura, F. Würthner, *Chem. Eur. J.* **2010**, *16*, 13706 - 13715.

[158] C. Schmuck, *Eur. J. Org. Chem.* **1999**, 2397 - 2403.

[159] C. Schmuck, *J. Org. Chem.* **2000**, *65*, 2432 - 2437.

[160] C. Schmuck, *Tetrahedron* **2001**, *57*, 3063 - 3067.

[161] C. Schmuck, W. Wienand, *J. Am. Chem. Soc.* **2003**, *125*, 452 - 459.

[162] S. Schlund, C. Schmuck, B. Engels, *J. Am. Chem. Soc.* **2005**, *127*, 11115 - 11124.

[163] C. Schmuck, T. Rehm, F. Gröhn, K. Klein, F. Reinhold, *J. Am. Chem. Soc.* **2006**, *128*, 1430 - 1431.

[164] C. Schmuck, *Coord. Chem. Rev.* **2006**, *250*, 3053 - 3067.

[165] T. H. Rehm, C. Schmuck, *Chem. Soc. Rev.* **2010**, *39*, 3597 - 3611.

[166] M. T. Fenske, W. M.-Zaika, H.-G. Korth, H. Vieker, A. Turchanin, C. Schmuck, *J. Am. Chem. Soc.* **2013**, *135*, 8342 - 8349.

[167] P. J. M. Stals, P. A. Korevaar, M. A. J. Gillissen, T. F. A. de Greef, C. F. C. Fitié, R. P. Sijbesma, A. R. A. Palmans, E. W. Meijer, *Angew. Chem. Int. Ed.* **2012**, *51*, 11297 - 11301.

[168] F. Aparicio, F. García, G. Fernández, E. Matesanz, L. Sánchez, *Chem. Eur. J.* **2011**, *17*, 2769 - 2776.

[169] T. Haino, M. Tanaka, Y. Fukazawa, *Chem. Commun.* **2008**, 468 - 470.

[170] F. Garcia, F. Aparicio, G. Fernández, L. Sánchez, *Org. Lett.* **2009**, *11*, 2748 - 2751.

[171] C. Shao, M. Stolte, F. Würthner, *Angew. Chem. Int. Ed.* **2013**, *52*, 7482 - 7486.

[172] Ž. Tomović, J. van Dongen, S. J. George, H. Xu, W. Pisula, P. Leclère, M. M. J. Smulders, S. de Feyter, E. W. Meijer, A. P. H. J. Schenning, *J. Am. Chem. Soc.* **2007**, *129*, 16190 - 16196.

[173] P. Ball, *Chem. Rev.* **2008**, *108*, 74 - 108.

[174] T. Lazaridis, in *eLS*, John Wiley & Sons, **2013**.

[175] K. A. Dill, *Biochemistry* **1990**, *29*, 7133 - 7155.

[176] D. Chandler, *Nature* **2005**, *437*, 640 - 647.

[177] R. Ludwig, *Angew. Chem.* **2001**, *113*, 1856 - 1876; *Angew. Chem. Int. Ed.* **2001**, *40*, 1808 - 1827.

[178] J.-H. Ryu, D.-J. Hong, M. Lee, *Chem. Commun.* **2008**, 1043 - 1054.

[179] H.-J. Kim, T. Kim, M. Lee, *Acc. Chem. Res.* **2011**, *44*, 72 - 82.

[180] W. Li, Y. Kim, J. Li, M. Lee, *Soft Matter* **2014**, *10*, 5231 - 5242.

[181] G. V. Oshovsky, D. N. Reinhoudt, W. Verboom, *Angew. Chem. Int. Ed.* **2007**, *46*, 2366 - 2393.

[182] T. Rehm, C. Schmuck, *Chem. Commun.* **2008**, 801 - 813.

[183] E. Krieg, B. Rybtchinski, *Chem. Eur. J.* **2011**, *17*, 9016 - 9026.

[184] C. Rest, M. J. Mayoral, G. Fernández, *Int. J. Mol. Sci.* **2013**, *14*, 1541 - 1565.

[185] J. B. Matson, S. I. Stupp, *Chem. Commun.* **2012**, *48*, 26 - 33.

[186] X. Ma, H. Tian, *Acc. Chem. Res.* **2014**, *47*, 1971 - 1981.

[187] X. Zhang, D. Görl, F. Würthner, *Angew. Chem.* **2014**, *126*, 1294 - 1298; *Angew. Chem. Int. Ed.* **2014**, *53*, 1270 - 1274.

[188] M. J. Mayoral, C. Rest, J. Schellheimer, V. Stepanenko and G. Fernández, *Chem. Eur. J.* **2012**, *18*, 15607 - 15611.

[189] N. K. Allampally, A. Florian, M. J. Mayoral, C. Rest, V. Stepanenko, G. Fernández, *Chem. Eur. J.* **2014**, *20*, 10669 - 10678.

[190] E. Krieg, H. Weissman, E. Shimoni, A. B. O. Ustinov, B. Rybtchinski, *J. Am. Chem. Soc.* **2014**, *136*, 9443 - 9452.

[191] P. Besenius, G. Portale, P. H. H. Bomans, H. M. Janssen, A. R. A. Palmans, E. W. Meijer, *Proc. Nat. Acad. Sci.* **2010**, *107*, 17888 - 17893.

[192] P. Besenius, K. P. van den Hout, H. M. H. G. Albers, T. F. A. de Greef, L. L. C. Olijve, T. M. Hermans, B. F. M. de Waal, P. H. H. Bomans, N. A. J. M. Sommerdijk, G. Portale, A. R. A. Palmans, M. H. P. van Genderen, J. A. J. M. Vekemans, E. W. Meijer, *Chem. Eur. J.* **2011**, *17*, 5193 - 5203.

[193] H. Frisch, J. P. Unsleber, D. Lüdeker, M. Peterlechner, G. Brunklaus, M. Waller, P. Besenius, *Angew. Chem. Int. Ed.* **2013**, *52*, 10097 - 10101.

[194] K. Ariga, T. Kunitake, *Supramolecular Chemistry - Fundamentals and Applications* (Advanced Textbook), Springer-Verlag Berlin Heidelberg; **2006**.

[195] J. P. Hill, L. K. Shrestha, S. Ishihara, Q.Ji, K. Ariga, *Molecules* **2014**, *19,* 8589 - 8609.

[196] T. G. Barclay, K. Constantopoulos, J. Matisons, *Chem. Rev.* **2014**, *114*, 10217 - 10291.

[197] Y.-b. Lim, K.-S. Moon, M. Lee, *J. Mater. Chem.* **2008**, *18*, 2909 - 2918.

[198] J. N. Israelachvili, *Intermolecular and Surface Forces*, Third Edition, Chapter 19, Elsevier; **2011**.

[199] J. N. Israelachvili, D. J. Mitchell, B. W. Ninham, *J. Chem. Soc., Faraday Trans. 2* **1976**, *72*, 1525 - 1568.

[200] G. L. Mosley, C. D. Yamanishi, D. T. Kamei, *J. Lab. Autom.* **2013**, *18*, 34 - 45.

[201] S. Song, A. Song, J. Hao, *RSC Adv.* **2014**, *4*, 41864 - 41875.

[202] H. Frisch, P. Besenius, *Macromol. Rapid Commun.* **2015**, *36*, 346 - 363.

[203] K. R. Raghupathi, J. Guo, O. Munkhbat, P. Rangadurai, S. Thayumanavan, *Acc. Chem. Res.* **2014**, *47*, 2200 - 2211.

[204] Y. Wang, H. Xu, X. Zhang, *Adv. Mater.* **2009**, *21*, 2849 - 2864.

[205] Q. Lin, B. Sun, Q.-P. Yang, Y.-P. Fu, X. Zhu, T.-B. Wei, Y.-M. Zhang, *Chem. Eur. J.* **2014**, *20*, 11457 - 11462.

[206] R. Afrasiabi, H.-B. Kraatz, *Chem. Eur. J.* **2013**, *19*, 17296 - 17300.

[207] M. Lee, S.-J. Lee, L.-H. Jiang, *J. Am. Chem. Soc.* **2004**, *126*, 12724 - 12725.

[208] S. Fleming, R. V. Ulijn, *Chem. Soc. Rev.* **2014**, *43*, 8150 - 8177.

[209] L. Kelland, *Nat. Rev. Cancer* **2007**, *7*, 573 - 584.

[210] B. Rosenberg, *Naturwissenschaften* **1973**, *60*, 399 - 406.

[211] B. Lippert, W. Beck, *Chemie in unserer Zeit* **1983**, *6*, 190 - 199.

[212] D. A. Juckett, B. Rosenberg, *Cancer Res.* **1982**, *42*, 3565 - 3573.

[213] G. Y. Park, J. J. Wilson, Y. Song, S. J. Lippard, *Proc. Natl. Acad. Sci.* **2012**, *109*, 11987 - 11992.

[214] N. J. Wheate, J. G. Collins, *Coord. Chem. Rev.* **2003**, *241*, 133 - 145.

[215] D. Lebwohl, R. Canetta, *Eur. J.Cancer* **1998**, *34*, 1522 - 1534.

[216] E. Wong, C. M. Giandomenico, *Chem. Rev.* **1999**, *99*, 2451 - 2466.

[217] K. M.-C. Wong, V. W.-W. Yam, *Coord. Chem. Rev.* **2007**, *251*, 2477 - 2488.

[218] M. Orchin , P. J. Schmidt, *Inorg. Chim. acta rev.* **1968**, *2* , 123 - 135.

[219] N. Farrell, T. T. B. Ha, J.-P. Souchard, F. L. Wimmer, S. Cros, N. P. Johnson, *J. Med. Chem.* **1989**, *32*, 2240 - 2241.

[220] Y. Zou, B. van Houten, N. Farrell, *Biochemistry* **1993**, *32*, 9632 - 9638.

[221] M. D. Levin, P. J. Stang, *J. Am. Chem. Soc.* **2000**, *122*, 7428 - 7429.

[222] T. Weilandt, N. L. Löw, G. Schnakenburg, J. Daniels, M. Nieger, C. A. Schalley, A. Lützen, *Chem. Eur. J.* **2012**, *18*, 16665 - 16676.

[223] M. Chen, C. Wei, J. Tao, X. Wu, N. Huang, G. Zhang, L. Li, *Chem. Eur. J.* **2014**, *20*, 2812 - 2818.

[224] T. Colacot, *RSC Catalysis Series - New Trends in Cross-Coupling: Theory and Applications*, Royal Society of Chemistry; **2014**.

[225] A. S. Abu-Surrah, H. H. Al-Sa'doni, M. Y. Abdalla, *Cancer Therapy* **2008**, *6*, 1 - 10.

[226] A. Garoufis, S. K. Hadjikakou, N. Hadjiliadis, *Coord. Chem. Rev.* **2009**, *253*, 1384 - 1397.

[227] A. R. Kapdi, I. J. S. Fairlamb, *Chem. Soc. Rev.* **2014**, *43*, 4751 - 4777.

[228] M. Tominaga, K. Suzuki, M. Kawano, T. Kusukawa, T. Ozeki, S. Sakamoto, K. Yamaguchi, M. Fujita, *Angew. Chem. Int. Ed.* **2004**, *43*, 5621 - 5625.

[229] M. Tominaga, K. Suzuki, T. Murase, M. Fujita, *J. Am. Chem. Soc.* **2005**, *127*, 11950 - 11951.

[230] S. Sato, J. Iida, K. Suzuki, M. Kawano, T. Ozeki, M.Fujita, *Science* **2006**, *313*, 1273 - 1276.

[231] K. Suzuki, K. Takao, S. Sato, M. Fujita, *Angew. Chem. Int. Ed.* **2011**, *50*, 4858 - 4861.

[232] T. Ichijo, S. Sato, M. Fujita, *J. Am. Chem. Soc.* **2013**, *135*, 6786 - 6789.

[233] C. J. Bruns, D. Fujita, M. Hoshino, S. Sato, J. F. Stoddart, M. Fujita, *J. Am. Chem. Soc.* **2014**, *136*, 12027 - 12034.

[234] A. Martin, Bachelorarbeit: *Synthese und Untersuchung des Aggregationsverhaltens von metallorganischen supramolekularen Amphiphilen*, Julius-Maximilians-Universität Würzburg; **2012**.

[235] M. Schmittel, H. Ammon, *Synlett* **1999**, *6*, 750 - 752.

[236] A. Florian, M. J. Mayoral, V. Stepanenko, G. Fernández, *Chem. Eur. J.* **2012**, *18*, 14957 - 14961.

[237] D. Velasco, V. Jankauskas, J. Stumbraite, J. V. Grazulevicius, V. Getautis, *Synthetic Met.* **2009**, *159*, 654 - 658.

[238] C. Gentilini, M. Boccalon, L.Pasquato, *Eur. J. Org. Chem.* **2008**, *19*, 3308 - 3313.

[239] H. Maeda, Y. Ito, Y. Haketa, N. Eifuku, E. Lee, M. Lee, T. Hashishin, K. Kaneko, *Chem. Eur. J.* **2009**, *15*, 3706 - 3719.

[240] S. P. Jagtap, S. Mukhopadhyay, V. Coropceanu, G. L. Brizius, J.-L. Brédas, D. M. Collard, *J. Am. Chem. Soc.* **2012**, *134*, 7176 - 7185.

[241] M. J. S. Dewar, E. G. Zoebisch, E. F. Healy, J. J. P. Stewart, *J. Am. Chem. Soc.* **1985**, *107*, 3902 - 3909.

[242] B. J. Berne, R. Pecora, *Dynamic Light Scattering,* New York Wiley; **1976**.

[243] Handbook (PCS Software Help Manual) for the *N5 Submicron Particle Size Analyzer,* Beckman Coulter Inc.; **2003**.

[244] A. Walther, M. Drechsler, A. H. E. Müller, *Soft Matter* **2009**, *5*, 385 - 390.

[245] J. J. McKinnon, A. S. Mitchell, M. A. Spackman, *Chem. Eur. J.* **1998**, *4*, 2136 - 2141.

[246] M. A. Spackman, J. J. McKinnon, *CrystEngComm.* **2002**, *4*, 378 - 392.

[247] M. A. Spackman, D. Jayatilaka, *CrystEngComm*. **2009**, *11*, 19 - 32.

[248] J. J. McKinnon, D. Jayatilaka, M. A. Spackman, *Chem. Commun.* **2007**, 3814 - 3816.

[249] A. D. Martin, J. Britton, T. L. Easun, A. J. Blake, W. Lewis, M. Schröder, *Cryst. Growth Des.* **2015**, *15*, 1697 - 1706.

[250] C. R. Smith, *J. Am. Chem. Soc.* **1924**, *46*, 414 - 419.

[251] H. Müller, *Mikrochemie*, **1933**, *12*, 307 - 314.

[252] R. A. Koenig, C. R. Johnson, *J. Biol. Chem.* **1942**, *143*, 159 - 163.

[253] F. H. Case, *J. Am. Chem. Soc*. **1946**, *68*, 2574 - 2577.

[254] F. Wm. Cagle, Jr., G. F. Smith, *J. Am. Chem. Soc.* **1947**, *69*, 1860 - 1862.

[255] P. Krumholz, *Nature* **1949**, *163*, 724 - 725.

[256] E. A. Moore, R. Janes, *Metal-Ligand Bonding*, First Edition, Royal Society of Chemistry, **2004**.

[257] L. Sun, L. Hammarström, B. Åkermark, S. Styring, *Chem. Soc. Rev.* **2001**, *30*, 36 - 49.

[258] Y.-Z. Hu, S. H. Bossmann, D. van Loyen, O. Schwarz, H. Dürr, *Chem. Eur. J.* **1999**, *5*, 1267 - 1277.

[259] J. J. Concepcion, J. W. Jurss, M. K. Brennaman, P. G. Hoertz, A. O. T. Patrocinio, N. Y. M. Iha, J. L. Templeton, T. J. Meyer, *Acc. Chem. Res.* **2009**, *42*, 1954 - 1965.

[260] M. Yagi, M. Toda, S. Yamada, H. Yamazaki, *Chem. Commun.* **2010**, *46*, 8594 - 8596.

[261] L. Kohler, N. Kaveevivitchai, R. Zong, R. P. Thummel, *Inorg. Chem.* **2014**, *53*, 912 - 921.

[262] P. Zhang, L. Pei, Y. Chen, W. Xu, Q. Lin, J. Wang, J. Wu, Y. Shen, L. Ji, H. Chao, *Chem. Eur. J.* **2013**, *19*, 15494 - 15503.

[263] R. Zhang, B. Song, Z. Dai, Z. Ye, Y. Xiao, Y. Liu, J. Yuan, *Biosens. Bioelectron.* **2013**, *50*, 1 - 7.

[264] J. Lehr, T. Lang, O. A. Blackburn, T. A. Barendt, S. Faulkner, J. J. Davis, P. D. Beer, *Chem. Eur. J.* **2013**, *19*, 15898 - 15906.

[265] S. Das, S. Karmakar, S. Mardanya, S. Baitalik, *Dalton Trans.* **2014**, *43*, 3767 - 3782.

[266] S. Gago, J. González, S. Blasco, A. J. Parola, M. T. Albelda, E. García-España, F. Pina, *Dalton. Trans.* **2014**, *43*, 2437 - 2447.

[267] C. Chen, L.-X. Cai, B. Tan, Y.-J. Zhang, X.-D. Yang, J. Zhang, *Chem. Commun.* **2015**, *51*, 8189 - 8192.

[268] H. Le Bozec, T. Renouard, *Eur. J. Inorg. Chem.* **2000**, 229 - 239.

[269] C. Feuvrie, O. Maury, H. Le Bozec, I. Ledoux, J. P. Morrall, G. T. Dalton, M. Samoc, M. G. Humphrey, *J. Phys. Chem. A* **2007**, *111*, 8980 - 8985.

[270] H. M. Kim, B. R. Cho, *J. Mater. Chem.* **2009**, *19*, 7402 - 7409.

[271] A.-J. Attias, C. Cavalli, B. Bloch, N. Guillou, C. Noël, *Chem. Mater.* **1999**, *11*, 2057 - 2068.

[272] B. W. Smucker, J. M. Hudson, M. A. Omary, K. R. Dunbar, *Inorg. Chem.* **2003**, *42*, 4714 - 4723.

[273] M. J. Lundqvist, E. Galoppini, G. J. Meyer, P. Persson, *J. Phys. Chem. A* **2007**, *111*, 1487 - 1497.

[274] W. Zhao, B. Tong, Y. Pan, J. Shen, J. Zhi, J. Shi, Y. Dong, *Langmuir* **2009**, *25*, 11796 - 11801.

[275] U. S. Schubert, C. Eschbaumer, *Angew. Chem. Int. Ed.* **2002**, *41*, 2892 - 2926.

[276] V. Balzani, G. Bergamini, F. Marchioni, P. Ceroni, *Coord. Chem. Rev.* **2006**, *250*, 1254 - 1266.

[277] W. Otani, K. Kinbara, T. Aida, *Faraday Discuss.* **2009**, *143*, 335 - 343.

[278] M. Wang, Y.-R. Zheng, K. Ghosh, P. J. Stang, *J. Am. Chem. Soc.* **2010**, *132*, 6282 - 6283.

[279] X. Zhu, P. Duan, L. Zhang, M. Liu, *Chem. Eur. J.* **2011**, *17*, 3429 - 3437.

[280] G. Wu, P. Verwilst, J. Xu, H. Xu, R. Wang, M. Smet, W. Dehaen, C. F. J. Faul, Z. Wang, X. Zhang, *Langmuir* **2012**, *28*, 5023 - 5030.

[281] P. Yin, T. Li, R. S. Forgan, C. Lydon, X. Zuo, Z. N. Zheng, B. Lee, D. Long, L. Cronin, T. Liu, *J. Am. Chem. Soc.* **2013**, *135*, 13425 - 13432.

[282] J. Wang, V. Safarifard, A.-Y. Wang, Y. Shen, J.-M. Cai, H.-P. Xiao, A. Morsali, *Inorg. Chim Act.* **2013**, *407*, 216 - 222.

[283] Q. Miao, C. Yin, M. Xie, Y. Luo, Z. Hai, Q. Yuan, J. Jiang, G. Liang, *Chem. Commun.* **2015**, *51*, 11045 - 11047.

[284] K. Szabó, N. Marek, *J. Biochem. Biophys. Methods* **2006**, *69*, 223 - 226.

[285] T. Ohtake, *J. Photopolym. Sci. Technol.* **2005**, *18*, 711 - 713.

[286] P. V. James, K. Yoosaf, J. Kumar, K. G. Thomas, A. Listorti, G. Accorsi, N. Armaroli, *Photochem. Photobiol. Sci.* **2009**, *8*, 1432 - 1440.

[287] K. Nakamoto, *J. Phys. Chem.* **1960**, *64*, 1420 - 1425.

[288] S. T. Howard, *J. Am. Chem. Soc.* **1996**, *118*, 10269 - 10274.

[289] S. R. Meech, D. Phillips, *J. Photochem.* **1983**, *23*, 193 - 217.

[290] W. H. Melhuish, *J. Phys. Chem.* **1960**, *64*, 762 - 764.

[291] C. L. Cheng, D. S. N. Murthy, G. L. D. Ritchie, *J. Chem. Soc., Faraday Trans. 2* **1972**, *68*, 1679 - 1690.

[292] P. V. James, P. K. Sudeep, C. H. Suresh, K. G. Thomas, *J. Phys. Chem. A* **2006**, *110*, 4329 - 4337.

[293] W. Hu, Q. Yan, D. Zhao, *Chem. Eur. J.* **2011**, *17*, 7087 - 7094.

[294] C.-J. Lin, S. K. Kundu, C.-K. Lin, J.-S. Yang, *Chem. Eur. J.* **2014**, *20*, 14826 - 14833.

[295] J. Kwak, S.-Y. Lee, *Colloids Surf., B Biointerfaces* **2014**, *115*, 406 - 411.

[296] B. Brusilowskij, E. V. Dzyuba, R. W. Troff, C. A. Schalley, *Chem. Commun.* **2011**, *47*, 1830 - 1832.

[297] V. Balzani, P. Ceroni, A. Juris, *Photochemistry and Photophysics: Concepts, Research, Applications*, First Edition, Wiley-VCH Verlag GmbH & Co. KGaA; **2014**.

[298] R. Liu, Y. Li, J. Chang, E. R. Waclawik, W. Sun, *Inorg. Chem.* **2014**, *53*, 9516 - 9530.

[299] F. N. Castellano, I. E. Pomestchenko, E. Shikhova, F. Hua, M. L. Muro, N. Rajapakse, *Coord. Chem. Rev.* **2006**, *250*, 1819 - 1828.

[300] S.-K. Chung, Y.-R. Tseng, C.-Y. Chen, S.-S. Sun, *Inorg. Chem.* **2011**, *50*, 2711 - 2713.

[301] A. A. Melekhova, D. V. Krupenya, V. V. Gurzhiy, A. S. Melnikov, P. Y. Serdobintsev, S. I. Selivanov, S. P. Tunik, *J. Organomet. Chem.* **2014**, *763 - 764*, 1 - 5.

[302] P. Jonkheijm, A. Miura, M. Zdanowska, F. J. M. Hoeben, S. De Feyter, A. P. H. J. Schenning, F. C. De Schryver, E. W. Meijer, *Angew. Chem. Int. Ed.* **2004**, *43*, 74 - 78.

[303] Q. Chen. S. C. Bae, S. Granick, *Nature* **2011**, *469*, 381 - 385.

[304] X. Zhang, Z. Chen, F. Würthner, *J. Am. Chem. Soc.* **2007**, *129*, 4886 - 4887.

[305] O. V. Dolomanov, L. J. Bourhis, R. J. Gildea, J. A. K. Howard, H. Puschmann, *J. Appl. Cryst.* **2009**, *42*, 339 - 341.

[306] G. M. Sheldrick, *Acta Crystallogr. A* **2008**, *64*, 112 - 122.